

AN X-RAY DIFFRACTION STUDY OF THE STRUCTURE
OF ARGON IN THE DENSE LIQUID REGION

Thesis by
Stephen C. ^{Hester} Smelser

In Partial Fulfillment of the Requirements
For the Degree of
Doctor of Philosophy

California Institute of Technology

Pasadena, California

1969

(Submitted February 7, 1969)

ACKNOWLEDGMENTS

I wish to express my sincere appreciation to Professor C. J. Pings for his helpful guidance and his encouragement during the course of this investigation.

Special thanks go to Dr. Wallace Honeywell, who was responsible for the design and construction of the apparatus; to Dr. Paul Mikolaj, who documented the β -filter data processing technique; to Dr. George Chang, who contributed to equipment modifications and the collecting of data; to George Griffith, Chic Nakawatase, and to June Gray. I would like to acknowledge conversations with Dr. Sten Samson, Dr. Ernest Henninger, Dr. George Wignall, Paul Fehder, Paul Morrison, and Joe Karnicky.

During my graduate studies, I have been the recipient of financial support from the California Institute of Technology and the National Science Foundation. The funds for this investigation were contributed by the Air Force Office of Scientific Research. Hewlett Packard Company donated counting equipment. I wish to express my appreciation for all these forms of support.

Finally, I wish to thank my parents and especially my wife, Theresa, for their sacrifice and continuous encouragement.

ABSTRACT

X-ray diffraction measurements were made on argon at six states in the general liquid region below the critical pressure at densities between 0.910 to 1.261 gm/cc and at temperatures between 108 to 143 °K. The intensity patterns exhibited three distinct maxima at s values of $1.91 \pm .02$, $3.68 \pm .06$ and $5.43 \pm .16 \text{ \AA}^{-1}$. The intensity patterns were Fourier transformed to the net radial distribution function and the direct correlation function. The functions, $4\pi r^2 \bar{\rho} h(r)$, showed 3 maxima at low densities and 4 at the high densities at values of r of 3.85 ± 0.05 , $7.29 \pm .10$, $10.75 \pm .45$ and $14.1 \pm .5 \text{ \AA}$. A subsidiary maximum between the first and second main peaks was observed to increase in prominence and disappear systematically as the density increased. It was not noticeably evident at either the lowest or highest density. The first zero of the direct correlation function was at an r value of $3.34 \pm .03 \text{ \AA}$, whereas the first maximum was at $3.78 \pm .06 \text{ \AA}$. Unlike previous determinations of $C(r)$ in this laboratory, the direct correlation function exhibited secondary features on the shoulder of the main peak. At the highest density the direct correlation function goes negative near 6 \AA . The intermolecular potential function was calculated from the data using the Percus-Yevick equation. At the lowest density the potential predicted in this way closely resembled the Lennard-Jones 12-6 potential for argon. However, the well-depths of these predicted potentials diminished rapidly with increasing density and decreasing temperature from 118.0 °K at $\bar{\rho} = .910$ to 68.6 °K at $\bar{\rho} = 1.261 \text{ gm/cc}$.

Comparisons of the direct correlation function and the radial distribution function with analytic predictions based on the Lennard-Jones potential and the P-Y equation indicated internal consistency at the lower densities. A comparison of the experimental radial distribution function at the highest density, with one calculated by molecular dynamics, indicated substantial agreement.

TABLE OF CONTENTS

<u>PART</u>	<u>TITLE</u>	<u>PAGE</u>
	ACKNOWLEDGMENTS	ii
	ABSTRACT	iii
	TABLE OF CONTENTS	v
	LIST OF FIGURES	viii
	LIST OF TABLES	xiii
	NOMENCLATURE	xv
I.	INTRODUCTION	1
II.	EXPERIMENTAL	9
	A. General	9
	B. Sample Confinement	11
	C. Optics and Optical Alignment	15
	D. X-ray Measurement	19
	E. A Typical Run	19
III.	TREATMENT OF EXPERIMENTAL DIFFRACTION DATA	24
	A. General	24
	B. Preliminary Calculations	27
	C. Absorption Factors	29
	D. Atomic and Incoherent Scattering Factors	33
	E. Data Smoothing	35
	F. Normalization	38
	G. Divergence Correction	39
	H. The Transform Calculation	41

<u>PART</u>	<u>TITLE</u>	<u>PAGE</u>
	I. Uncertainty Bands	43
	J. Calculation of P-Y Potentials	44
IV.	RESULTS	46
	A. General	46
	B. Intensity Curves	47
	C. Net Radial Distribution Functions	51
	D. Direct Correlation Functions	53
	E. Percus-Yevick Potential Functions	54
V.	DISCUSSION OF RESULTS	55
	A. Intensity Curves	55
	B. Net Radial Distribution Functions	57
	C. Direct Correlation Functions	59
	D. Percus-Yevick Potential Functions	61
	E. First Coordination Numbers	62
VI.	CONCLUSIONS	63
	REFERENCES	65
	FIGURES	68
	TABLES	112
	APPENDICES	155
	1. THE BASIC SCATTERING EQUATION	155
	2. THE BASIC DATA REDUCTION EQUATION	172
	3. DERIVATION OF THE CONFIDENCE INTERVAL FOR THE BASIC DATA REDUCTION EQUATION	181

<u>PART</u>	<u>TITLE</u>	<u>PAGE</u>
	4. THE BREIT-DIRAC FACTOR FOR INCOHERENT SCATTERING DETECTED BY A SCINTILLATION COUNTER	185
	5. THE DUAL FILTER SPECTRUM	193
	6. CALIBRATION OF THE PRESSURE GAGE	201
	7. THERMOMETER CALIBRATION	209
	8. CALCULATION OF ABSORPTION CORRECTION FACTORS	220
	9. THE CORRECTION FOR HORIZONTAL DIVERGENCE	231
	PROPOSITIONS	241
	1.	241
	2.	255
	3.	267
	4.	282

LIST OF FIGURES

<u>FIGURE</u>	<u>TITLE</u>	<u>PAGE</u>
1.	Argon P, ρ , T Diagram Showing Locations of the Experimental States	68
2.	Cross Section of Cryostat	69
3.	Pictorial Illustration of the X-ray Optical System (Figure taken from Mikolaj ¹⁰)	70
4.	Scattering Geometry used in the Argon Experiments	71
5.	Vertical Cell Alignment Data	72
6.	Horizontal Cell Alignment Data	72
7.	Normalized Cell Scattering Intensity for One Scan (Δ , β -Filter Intensity; \odot , α -Filter Intensity)	73
8.	Normalized Cell and Sample Scattering Intensities for One Scan (Δ , β -Filter Intensity; \odot , α -Filter Intensity)	74
9.	Comparison of Atomic Scattering f_d^2 , for Ag $K\alpha$ Radiation. — — Gingrich and Tompson ⁶ ; — — — Lark-Horowitz and Miller ⁵ ; — — — f_d^2 Berghuis et. al. ⁵⁴ with $f' = 0.13$ and $f'' = 0.16$ ⁵⁵	75
10.	Comparison of Atom Scattering, f_d^2 , for MoK Radiation. — — Eisenstein and Gingrich ⁸ ; — — — Harris and Clayton ⁷ ; — — — f_d^2 Berghuis et. al. ⁵⁴ with $f' = 0.18$ and $f'' = 0.24$ ⁵⁵	76
11.	Experimental $j(s)$: — — Henshaw ² with Neutrons; — — — Gingrich and Tompson with X-rays. Figure taken from Rahman. ⁵⁶	77
12.	Experimental $j(s)$: — — Henshaw ² — — — Estimated from Gingrich and Tompson Data ⁶ using f_d^2 from Berghuis et. al. ⁵⁴ with $f' = 0.13$ and $f'' = 0.16$ ⁵⁵	78
13.	Net Normalized Scattering Intensities (Δ , β -Filter Intensity Minus α -Filter Intensity, Average for Three Scans of Cell and Sample; \odot β -Filter Intensity Minus α -Filter Intensity,	79

<u>FIGURE</u>	<u>TITLE</u>	<u>PAGE</u>
	Argon for Five Scans of Cell)	
14.	Argon Scattering Curve for Run No. 2 with the 90% Confidence Interval, Scaled to the Total Gas Scattering Function (●, Preliminary Estimate of the Sample Intensity; ○, Data; ∅, Rejected Data; — — —, Confidence Interval; — — — Extrapolation)	80
15.	The Normalized Scattering Curve for Argon Run No. 2, before the Divergence Correction (----- Indicates the Incoherent Portion of the Total Gas Scattering Function)	81
16.	The Argon Intensity Function, $j(s)$, depicting the Divergence Correction for Argon Run No. 2 (●, before the Correction; — after the Divergence Correction; — — — Extrapolation to the Compressibility Limit)	82
17.	The Argon Intensity Function, $j(s)$, for Argon Runs 1, 3 and 4	83
18.	The Argon Intensity Function, $j(s)$, for Argon Runs 5 and 6	84
19.	The Effect of Temperature and Bulk Density on the Width of the Main Intensity Peak in the Argon Intensity Function, $j(s)$ at $j(s) = 1$ (Full Symbols, this work; Open Symbols, Mikolaj ¹⁰)	85
20.	The Effect of Temperature and Bulk Density on the Height of the Main Peak in the Argon Intensity Function, $j(s)$ (Full Symbols, this work; Open Symbols, Mikolaj ¹⁰)	86
21.	The Radial Atomic Density Function of Argon for Runs 1, 2 and 3 (The Parabola at small r is $4\pi r^2 \bar{\rho}$)	87
22.	The Radial Atomic Density Function of Argon for Runs 4, 5 and 6 (The Parabola at small r is $4\pi r^2 \bar{\rho}$)	88
23.	The Effect of the Divergence Correction on $h(r)$ and $C(r)$ (— after the Correction; — — before the Correction)	89

<u>FIGURE</u>	<u>TITLE</u>	<u>PAGE</u>
24.	The Estimated Net Radial Distribution Function of Argon for Runs 1, 2 and 3	90
25.	The Estimated Net Radial Distribution Function of Argon for Runs 4, 5 and 6	91
26.	The Estimated Direct Correlation Function of Argon for Runs 1, 2 and 3	92
27.	The Estimated Direct Correlation Function of Argon for Runs 4, 5 and 6	93
28.	The Estimated Small r Behavior of the Direct Correlation Function of Argon for Runs 1, 3, 4, 5 and 6	94
29.	The Potential Function of Liquid Argon Calculated from the Percus-Yevick Equation for the Six States	95
30.	The Argon Intensity Function, $j(s)$ at $\rho = 0.780$ gm/cc and $T = -110^{\circ}\text{C}$ (— Verlet's Function Calculated from the P-Y Equation using the Leonard-Jones Potential; •, Mikolaj ¹⁰). This figure taken from Levesque and Verlet ¹⁵	96
31.	The Argon Intensity Function, $j(s)$ for Run No. 2 (— this work; •, Mikolaj and Pings ¹¹)	97
32.	r_0 as a Function of $\rho\sigma^3$. (♦ this work; All Others from Verlet ¹⁷) "s" is the Value s_{max} where $j(s_{\text{max}})$ is Maximum	98
33.	The Net Radial Distribution Function of Argon for Run No. 2. (— this work; •, Mikolaj and Pings ¹¹)	99
34.	The Net Radial Distribution Function for Run No. 2. (— this work; •, Watts ¹⁹)	100
35.	The Net Radial Distribution Function of Argon for Run No. 6. (— this work; •, Molecular Dynamics of Verlet ¹⁷ , same density but a higher temperature)	101
36.	Two Dimensional Molecular Dynamics Calculation of $g(r)$ at a Relative Packing Density of 0.5406 (from Fehder ²¹), $T = 137.56^{\circ}\text{K}$	102

<u>FIGURE</u>	<u>TITLE</u>	<u>PAGE</u>
37.	Two Dimensional Molecular Dynamics Calculation of $g(r)$ at a Relative Packing Density of 0.6237 (from Fehder ²¹), $T = 132.12$ °K	103
38.	Two Dimensional Molecular Dynamics Calculation of $g(r)$ at a Relative Packing Density of 0.7274 (from Fehder ²¹), $T = 120.74$ °K	104
39.	The Direct Correlation Function of Argon Run No. 2. (—— Indicates Best Estimate of Subatomic Behavior; — — Direct Results from Transform of $i(s)$)	105
40.	The Direct Correlation Function of Argon Run No. 2. (—— this work; •, Mikolaj and Pings ¹³)	106
41.	The Direct Correlation Function of Argon Run No. 2. (—— this work; •, Lennard-Jones Potential, Percus-Yevick Approximation of Watts ¹⁹)	107
42.	The Direct Correlation Function of Argon (—— Run 1, this work; •, Watts ¹⁹ , same density but 5° higher temperature)	108
43.	The Calculated Percus-Yevick Potential for Argon 2 with Error Bands vs the Lennard-Jones Potential (O)	109
44.	Depth of the Argon Potential Well as Predicted from the Percus-Yevick Equation (Open Symbols, this work; •, Mikolaj and Pings ¹³)	110
45.	First Coordination Number of Liquid Argon (Open Symbols, Calculated by Method A for this work, All Others from Mikolaj and Pings ¹⁴ . Methods A, B, C and D Described in Text)	111
4-1.	Solid Curve Represents Coherent, Incoherent with $1/B^3$ Recoil Correction, and Total Scattering from Helium. The Broken Curve Represents Total Scattering with No Recoil Correction. These Theoretical Curves Are According to Herzog. The Circles Indicate Experimental Values Obtained by Wollan	188
5-1.	β -Filter and Dual Filter Spectra	196

<u>FIGURE</u>	<u>TITLE</u>	<u>PAGE</u>
6-1.	Schematic Diagram of the Pressure Calibration Equipment	203
6-2.	Deviations from the Least Squares Fit (Pressure Calibration)	206
7-1.	Schematic of Temperature Calibration Apparatus	211
7-2.	Wiring Diagram (Thermometer Calibration)	213
7-3.	Deviation from Least Squares Fit (Thermometer Calibration)	217
8-1.	Cell, Sample and Beam Geometry (For Absorption Factor Program)	222
9-1.	Three Limiting Cases for Maximum Horizontal Divergence	232
9-2.	Upper Limits to Horizontal Divergence for the Three Situations Depicted in Figure 9-1	235
9-3.	Scattering Geometry as Viewed Along the Axis of the Line Source	236
9-4.	A Typical Scattering Cone as Seen on Plane AB of Figure 9-3	239
9-5.	Diagram of the Arc Length Approximation	240

LIST OF TABLES

<u>TABLE</u>	<u>TITLE</u>	<u>PAGE</u>
I.	Summary of Argon Thermodynamic States and Experimental Uncertainty Limits	112
II.	Summary of the Experimental Argon Diffraction Data	113
III.	Atomic and Incoherent Scattering Factors for Argon	121
IV.	Atomic and Incoherent Scattering Factors for Beryllium	122
V.	Absorption Factors	123
VIa.	Summary of the Smooth Intensity Functions	129
VIb.	Summary of the Smooth Intensity Functions After Correction for Horizontal Divergence	132
VII.	Extrapolation Coefficients, Normalization Constants and Truncation Limits Used in the Fourier Inversion	135
VIII.	Summary of Features in the Experimental Argon Intensity Patterns	137
IX.	Estimates of the Net Radial Distribution Functions, $h(r) = g(r) - 1$	138
X.	Summary of Features in the Atomic Density Distribution of Argon	144
XI.	Summary of Features in the Argon Distribution Function, $h(r)$	145
XII.	Estimates of the Direct Correlation Functions, $C(r)$	146
XIII.	Summary of Features in the Direct Correlation Function of Argon	153
XIV.	Summary of Features in the Predicted PY Potential Functions	154

<u>TABLE</u>	<u>TITLE</u>	<u>PAGE</u>
5-1.	Dual Filter Spectrum Corresponding to Circles in Figure 5-1, Background Radiation	197
5-2.	Dual Filter Spectrum Corresponding to Circles in Figure 5-1, K_{α} and K_{β} Regions	198
6-1.	Pressure Calibration Data	207
7-1.	Temperature Calibration Data	218
8-1.	A Comparison of Calculated Absorption Coefficients with Ritter, et. al.	229
9-1.	Calculated Values of Divergence Limits	234

NOMENCLATURE

English Symbols

ACC	total absorption factor for scattering from the cell and self-absorption within the cell
ACSC	total absorption factor for scattering from the cell and absorption in the sample and the cell
ASSC	total absorption factor for scattering from the sample and absorption in the sample and the cell
\AA	Angstrom unit
a	parameter in the intensity smoothing function
a_2	parameter in low angle extrapolation of $i(s)$
a_4	parameter in low angle extrapolation of $i(s)$
atm	atmosphere, 14.696 pounds per square inch
B	Breit-Dirac factor
b	parameter in the intensity smoothing function
(C/N)	normalization constant
C(r)	direct correlation function
c	parameter in the intensity smoothing function, speed of light
E	voltage
e	charge of electron
F(θ)	incoherent scattering correction factor
f(θ) , f(s)	atomic scattering factor
G(θ)	incoherent scattering correction factor
g	gravitational acceleration
g(r)	atomic radial distribution function

$h(r)$	net atomic radial distribution function, $g(r) - 1$
$I(\theta)$, $I(s)$	scattered intensity
I_0	incident intensity; average scattering power
$I_0(s)$	intensity of zero-angle scattering
ΔI_s	confidence interval
$I_T(\theta)$	scattering function for electron
i	index notation
$i(s)$	kernel of the Fourier integral
I.D.	inside diameter
j	index notation
$j(\theta)$, $j(s)$	scattered intensity function, $i(s) + 1$
K	temperature, degrees Kelvin
K_T	isothermal compressibility
K_v	kilovolts
k	Boltzmann constant
k_j	statistical confidence parameter
l	optical path length
m	mass of electron
Mean	statistical mean of
N	number of counts; number of atoms
N_1	first coordination number
O.D.	outside diameter
P	pressure
$P(\theta)$	polarization factor

PAD,PHD	pulse amplitude distribution
PHS	pulse-height selector
P-Y	Percus Yevick
Q	intensity scaling factor
R	intensity ratio; resistance
R_0	ice point resistance of platinum thermometer
r	radial coordinate
r_0	location of intermolecular potential well
S,s	scattering parameter, $(4\pi/\lambda) \sin \theta$
s_{\max}	limit of the Fourier integral
Δs	width of main intensity peak
T	temperature
t	thickness
t_{PHS}	PHS transmission factor
$u(r)$	intermolecular potential function
V	volume
var	variance of
ΔV	volume element
W	characteristic width of the PAD

Greek Symbols

α	Callender-Van-Deusen equation constant
β	Callender-Van-Deusen equation constant
γ	fraction of total radiation scattered coherently
δ	Callender-Van-Deusen equation constant

ϵ	parameter in the intermolecular potential function, $\epsilon/K = 119.8$ °K for argon
θ	half of the total scattering angle
λ	radiation wavelength
μ	linear x-ray absorption coefficient
ρ	density
$\rho(r)$	radial density
$\bar{\rho}$	number density
σ	standard deviation of the Gaussian distribution; parameter in the intermolecular potential function, $\sigma = 3.405$ Å for argon
τ	counting time
ω	circular frequency of incident radiation
ψ	polarization angle for incident radiation
ψ_i	Hartree-Fock wave function for the i^{th} atom
$\psi_{\text{PHS}}^{\text{inc}}$	relative PHS transmission factor for incoherent scattering

Subscripts

a	atomic
c	cell
c + s	cell-plus-sample
d	corrected for dispersion
e.u.	electron units
exp	experimental
p	penumbra

Subscripts (cont)

ref	reference angle
s	sample
u	umbra

Superscripts

α	with α filter on incident beam
β	with β filter on incident beam
coh	coherent
E	experimental
inc	incoherent
n	background noise, electronic
smh	smooth
*	complex conjugate

I. INTRODUCTION

The atomic radial distribution function in fluid argon has been the subject of several investigations using both neutron and x-ray diffraction techniques. The neutron experiments, three in number, were made near the triple point: the first by Henshaw, Hurst and Pope,¹ the second a repeat of the first experiment by Henshaw² using improved techniques, and the third by Dasannacharya and Rao.³ Structure in this region has also been investigated with x-rays by Eisenstein and Gingrich,⁴ Lark-Horowitz and Miller,⁵ and more recently by Gingrich and Tompson,⁶ and Harris and Clayton.⁷ These experiments represent seven measurements of the intensity patterns of scattered radiation which were Fourier transformed to the radial distribution function, $g(r)$.

The most extensive measurements of the intensity patterns for argon were made by Eisenstein and Gingrich,⁸ at 26 different temperatures and densities. Unfortunately, only six patterns were subjected to Fourier inversion to obtain the radial distribution function. The associated thermodynamic states were along the coexistence curve, five of the six on the liquid side.

A systematic investigation of the atomic distributions of argon was initiated by Honeywell⁹ and Mikolaj.¹⁰ This work, encompassing 13 thermodynamic states in the general vicinity of the critical region, represents the largest internally consistent set of experimental radial distribution functions for argon. The intensity patterns measured in these two thesis studies were augmented to include theoretical small angle scattering. The new intensity patterns were

transformed and the results were reported by Mikolaj and Pings.^{11,12} The direct correlation function, and the first coordination numbers (calculated in four different ways) were investigated for this data.^{13,14}

Calculated radial distribution functions are qualitatively similar, but they are different in detail. The discrepancies are partially attributable to systematic errors that are evident in most of the aforementioned intensity kernels. However, in addition to this complication, direct comparisons of radial distribution functions can not be made with complete rigor because an estimate of the uncertainty in each distribution due to the statistics inherent in the scattering process itself, is not presented. In this paper, a method to estimate these uncertainties will be presented for both the radial distribution function and the direct correlation function.

Based on the simple physical argument that two atoms cannot be arbitrarily close, ripples in the calculated radial distribution functions at small values of r are known to be spurious. This fact has clouded the issue of whether or not a subsidiary maximum between the first and second peaks in the distribution functions is real or not. Evidence presented herewithin supports the claim that this subsidiary peak does exist, but its prominence and its position, like the basic features in the radial distribution function are state dependent.

Extending the temperature-density grid of Honeywell and Mikolaj, the purpose of this x-ray investigation was to determine the structure of liquid argon at six thermodynamic states: six states in

the liquid region, below the critical pressure, and somewhat removed from the triple point, the critical point and the coexistence curve. The 13 previous states and these six are depicted on a P, ρ, T diagram for argon. See Figure 1. The present study includes densities (in grams/cc) of 0.982, 0.910, 1.049, 1.116, 1.200, and 1.261 with the states at the respective temperatures 138.15 °K, 143.15 °, 133.15 °, 127.15 °, 117.093 °, and 108.18 °.

With a few modifications, the Mikolaj-Honeywell apparatus was used. Only one change directly affects the quality of the results. A more monochromated incident x-ray beam was achieved by performing a Zirconium-Yttrium dual filter experiment rather than a Zr β -filter experiment as previously done. This improvement was analyzed by repeating the measurements of one of the states measured by Honeywell and transformed by Mikolaj. A comparison of the two independently measured intensity patterns indicates a moderate discrepancy; a discrepancy which, incidentally, was anticipated by Levesque and Verlet.¹⁵ The details of the intensity discrepancy and the changes it effected in the radial distribution function will be discussed as the thesis develops.

In this investigation, emphasis was placed on the quantitative determination of structure functions for all six states, including estimated uncertainty bands. Since one of the most important applications of the experimental structure functions is to test models or theories of the liquid state, comparisons will be made to radial distribution functions determined by two techniques: those calculated

by Verlet^{16,17,18} using three dimensional molecular dynamics, and those mathematically deduced by Watts^{19,20} from the Lennard-Jones potential and the Percus-Yevick equation. Furthermore, a few radial distributions calculated by Fehder²¹ using two dimensional molecular dynamics will be presented to support the claim of the existence of the subsidiary peak.

Before reviewing the technique of x-ray diffraction analysis, it should be pointed out that x-ray and neutron studies on a large number of liquids have been completed. A review of similar studies will not be presented as several review articles are available, for example, see Gingrich,²² Furukawa,²³ or Kruh.²⁴

The general approach that relates the scattering intensity data to the radial distribution function can be found in James,²⁵ Filipovich²⁶ or Paalman and Pings.²⁷ The Paalman and Pings' treatment applicable to fluids composed of spherically-symmetric atoms is presented in Appendix 1. The equations therein have been modified slightly. Familiarity with one of these treatments is assumed.

The radial distribution function is related to the intensity pattern by the following Fourier transform

$$4\pi r^2 \rho^{-1} h(r) = \frac{2r}{\pi} \int_0^{\infty} s i(s) \sin sr ds \quad (1)$$

where

$$i(s) = \frac{I(s)}{Nf_d^2(s)} - 1 \quad (2)$$

and

$$s = \frac{4\pi}{\lambda} \sin \theta \quad (3)$$

The net correlation function, $h(r)$, is $g(r) - 1$. For a scattering experiment in the Debye-Scherrer geometry²⁸ and a monochromatic source of x-rays of wavelength, λ , the scattering parameter, s , is uniquely determined by θ (θ is one-half of the scattering angle between the direction of the incident beam and the scattered beam). $I(s)$ is the fully corrected coherent scattering observable at 2θ for an irradiated group of N spherically-symmetric atoms. Corrections are made for polarization, absorption and incoherent scattering. $f_d(s)$ is the dispersion corrected atomic scattering factor. The Fourier intensity kernel $i(s)$ is short-ranged, since $I(s)$ rapidly approaches $Nf_d^2(s)$ for moderate s . Representing the distance from an atom at the origin to another point in the fluid, r is a scalar quantity. $\bar{\rho}$ is the number density which is equivalent to the bulk density of the fluid. In an actual experiment, the upper limit on the integral is satisfied by a finite s beyond which $i(s)$ is zero. Scattering can not be measured at small angles because the high intensity x-ray beam interferes with the measurement. The low angle limit is satisfied by extrapolating $i(s)$ to a theoretical value at $s = 0$.

The direct correlation function as proposed by Ornstein and Zernike²⁹ may be defined by the following equation

$$c(\vec{r}_{12}) = h(\vec{r}_{12}) - \bar{\rho} \int c(\vec{r}_{13}) h(\vec{r}_{23}) d\vec{r}_3 \quad (4)$$

where subscript two refers to the atom at the origin and subscripts one and three to other points in the fluid. Fisher³⁰ provides the interpretation that the correlation $h(r)$ between "atoms" 1 and 2 can be regarded as caused by (i), a direct influence of 1 on 2, described by the so-called direct correlation function, $C(\vec{r}_{12})$, which should be short-ranged, and (ii), an indirect influence propagated directly from 1 to a third atom at \vec{r}_3 , which in turn exerts its influence on atom 2. For a monotonic fluid $C(r)$ is related, as pointed out by Goldstein,³¹ to the intensity pattern by this expression:

$$4\pi r^2 \rho C(r) = \frac{2r}{\pi} \int_0^\infty s \frac{i(s)}{1+i(s)} \sin sr \, ds \quad (5)$$

and therefore, is also available from the intensity data.

The direct correlation function was computed¹³ for the 13 states of Honeywell and Mikolaj. Reetz and Lund³² performed computations of $C(r)$ for four states using the data of Eisenstein and Gingrich.⁸ The short range character of $C(r)$ is evident in both of these computations. Although the latter computations contain suggestions of secondary peaks, monotonic decay of the main peak was observed in the former where all 13 direct correlation functions exhibited the same characteristic shape, negative at distances less than the atomic diameter, rising steeply through zero towards a single positive maximum and then decaying monotonically.

The direct correlation function can also be investigated via a double Fourier transform of a molecular dynamics radial

distribution function. This technique was used by Hutchinson³³ to produce a direct correlation function that was short-ranged relative to the potential function used to generate $g(r)$. The density and temperature of this mathematical experiment was 1.407 gm/cc at 85.5 °K. The maximum in $C(r)$ was slightly larger than the maximum in $h(r)$, and $C(r)$ was negative between r values of 6.5 to 8.0 Å.

The Percus-Yevick theory for predicting the distribution functions of fluid is based on a fundamental assumption regarding the relationship of $C(r)$, $g(r)$ and the intermolecular potential. The assumption, called the Percus-Yevick equation,^{34,35} is

$$C(r) = g(r) (1 - e^{-\mu(r)/kT}) \quad (6)$$

Since both correlation functions are available experimentally, the validity of this assumption can be tested. Mikolaj and Pings' study¹³ of this assumption using argon diffraction data indicated that the potential function well-depth decreased linearly with increasing density, which was contradictory to the assertion that the potential was independent of state. The density dependence evident in the Mikolaj and Pings' study was greater than that predicted by Copeland and Kestner³⁶ using an effective two body interaction. The validity of the Percus-Yevick assumption will be subjected to analysis with the data contained herein.

The experimental problem is to determine $i(s)$ from a scattering experiment, where argon is confined in a sample cell at low

temperature and at moderate pressures. In order to irradiate the argon, the cell is unavoidably irradiated. The quantitative removal of cell scattering has been treated by Mikolaj.¹⁰ Two experiments must be performed: one experiment determines the scattering from cell and sample, the other, the scattering from the empty cell. These two patterns via the proper subtraction (See Appendix 2) produces the total (coherent and incoherent) scattering function, $I_s(s)$, for argon. This particular subtraction corrects for absorption and includes the correction for polarization. The coherent scattering function, $I(s)$ is deduced from $I_s(s)$.

The uncertainty, $\Delta I_s(s)$, in $I_s(s)$ is derived (See Appendix 3) from the assumption³⁷ that x-ray scattering is governed by Poisson statistics, for which the square of the standard deviation is proportion to the mean. $\Delta I_s(s)$ will be used to reject data and to calculate the uncertainty bands for the structure functions.

Before presenting the net radial distribution functions and the direct correlation functions obtained for the six states investigated, the details of the experimental method, and the data reduction scheme will be summarized. A significant portion of the thesis will then be devoted to discussing the results. Finally, the conclusions will be noted. An effort has been made to keep derivations and other miscellaneous details in appendices.

II. EXPERIMENTAL

A. General

The experimental x-ray diffraction patterns were obtained by irradiating an argon sample confined in a cylindrical beryllium cell with a collimated beam of x-rays and measuring the scattering intensity as a function of the scattering angle, 2θ . To obtain the low temperatures desired, the sample cell was mounted within a thermal control annulus which was positioned in a vacuum chamber. Both the annulus and the cryostat were slotted to pass the incident and scattered radiation.

Cooling was supplied by passing the vapor of liquid nitrogen through cooling tubes in the thermal annulus. For each state of argon investigated, the annulus was cooled a few degrees below the desired temperature by selecting the proper flow rate of cooling vapor. The final temperature was reached and maintained by varying the current to heater wires in the annulus.

The six thermodynamic states were selected to be on isotherms in either of two PVT measurements, those of Levelt³⁸ or those of Van Itterbeek, Verbeke and Staes.³⁹ To obtain the desired density of argon it was then only necessary to select the proper pressure. The six states were selected to match T, P data points in the PVT measurements, thereby reducing the uncertainty in knowing the density for a given pressure and temperature.

The sample cell was filled from a high pressure reservoir of argon through a microflow valve to the desired pressure. Pressure was monitored continuously and controlled manually. The microflow valve was

adjusted to bleed argon into the cell to counterbalance small leaks in the fittings. A manually operated trimmer injector was used to adjust the volume of the sample system, thus providing the fine pressure control.

The source of x-rays was a molybdenum target operated at 55 Kv and 20 milliamps. The optical slit defining the incident beam was positioned at a take off angle of 5.8° so that the effective target was a line source, 10.0 mm. long (parallel to the cylindrical sample cell) and 0.12 mm. high.

Selective monochromatization of the incident beam was accomplished by the use of "balanced" dual filters⁴⁰ which isolated a narrow band of wavelengths spanning the $K\alpha$ doublet of the molybdenum source. The dual filter technique requires two measurements to determine the scattering intensity at each angle. One measurement is the intensity scattered at 2θ with a zirconium β -filter in the incident beam. The other is the intensity scattered at 2θ with an yttrium α -filter in the incident beam. For the argon sample and Be cell scattering, the experimental intensity is

$$I_{c+s}^E(\theta) = I_{c+s}^\beta(\theta) - I_{c+s}^\alpha(\theta) \quad (7)$$

and for the empty cell measurements

$$I_c^E(\theta) = I_c^\beta(\theta) - I_c^\alpha(\theta) \quad (8)$$

Governed by a Poisson distribution, x-ray scattering is a statistical process. Although the uncertainty in a measurement of the scattering at one angle depends only on the total counting time, several scans through angle space from 1.5° to 120° (2θ) were made in steps of 0.5° . Three scans of cell and sample (100 seconds for each filter at each angle) and five scans of the empty cell (300 seconds for each filter) were made. Statistical arguments could then be used to reject data points. The scattering data were accumulated in 101 days of around the clock measurements.

In order to eliminate fluctuations of the intensity of the incident beam, fluctuations which would occur as 1-3% changes over several hours, the scattering data were normalized to the scattering at a reference angle. The intensity scattered at the reference angle was measured several times during each scan. Linear interpolation between reference angle measurements was used to normalize each scan point.

Before developing the data reduction scheme, the sample confinement and the optical geometry will be described in detail.

B. Sample Confinement

The argon used in this investigation was obtained from the Linde Rare Gas division of Union Carbide. The maximum impurity was reported to be less than 15 parts per million as follows:

Nitrogen	<	5 ppm
Hydrogen	<	1 ppm
Oxygen	<	5 ppm
Hydrocarbons	<	1 ppm
Moisture	<	3 ppm

The beryllium cell confining the argon was similar to the

cell described by Paalman and Pings.⁴¹ The cell is depicted in cross-section in Figure 2 (Part H) and pictorially in Figure 3. The dimensions of that portion of the cell irradiated by the incident beam were:

length	1.000 cm.
outside diameter	0.179 cm.
inside diameter	0.093 cm.

The inner and outer surfaces of the cell were not concentric, the centerlines being 0.0127 cm. apart. The cell was positioned so that the thinnest wall was in the direction of scattering for two theta of 90° .

The cryostat has been described in detail elsewhere.^{9,42} This equipment, as modified, is depicted in cross-section in Figure 2. The cross-section is perpendicular to the incident beam, with the x-ray target 17.7 cm. behind that portion of the cell which is exposed by the slot.

The vacuum chamber, C, a $6\frac{1}{2}$ inch I. D. brass can with a $\frac{1}{4}$ inch wall thickness, was positioned so that its flat end was perpendicular to the goniometer shaft, indicated by the centerline, G. The other end of the chamber was closed with a removable flat end plate, T. Whenever scattering measurements were being taken, this chamber was evacuated through port, Q, to less than 5×10^{-5} torr. Port R was not used.

Electrical leads from the chamber passed through port O. The cap used on this port contained ²⁴, 1/16 inch copper rods that were epoxied into slip fit holes in a $\frac{1}{4}$ inch lucite plate.

The cell, H, was positioned in the cell holder, I, which was slip fitted into the temperature control annulus, J. A $7/16$ inch slot was machined into the cell holder, the temperature annulus as well as the vacuum chamber, to pass the incident and scattered radiation. The slot which extends 280 degrees around the wall of the vacuum chamber was covered with quarter-mil Mylar film. A vacuum seal was achieved with an o-ring under a compression ring, B. The brass thermal block surrounding the Be cell was sectioned into two parts by this slot.

An aluminized Mylar heat shield, F, reduced radiation heat transfer to the exposed portion of the cell. The quarter-mil aluminized strip was wrapped around a recess in the cell holder and held in place with a pair of split rings. Other heat shields, D and S, were also used.

Support for the thermal block was provided by two $\frac{1}{4}$ inch lucite plates, M, that were bolted to the temperature control annulus. Each plate contacted the chamber wall at only three places, with three $1\frac{1}{2}$ inch wide equally spaced legs. These plates were lapped to slip fit the vacuum chamber. Longitudinal placement of this assembly was achieved when the right plate was butted against a step in the chamber bore.

Around the outer surface of the control annulus were soldered two sets of $1/8$ inch copper tubes, L, that carried the cooling gas. These tubes, which were installed to provide counter current flow, joined into common inlet and outlet lines. Thin walled stainless steel tubing and teflon spacers provided thermal standoffs for the

inlet and outlet lines.

Just inside the cooling coils were the heater wires, K, which provided the fine temperature control. These nylon-insulated # 30 manganin wires were wound in grooves on the outside of a brass annulus. One heater-wire was wound on each side of the slot. After cementing the wires in place, the grooves were packed with indium to provide better heat transfer. This annulus was then force fit into the portion containing the coolant tubes. The two heaters were operated independently to control the temperature gradient across the irradiated portion of the cell. The current to the heater in the larger section of the annulus was controlled to maintain the temperature detected by that platinum thermometer, N. This thermometer was in the non-irradiated portion of the cell and immersed in the argon. The other heater was controlled by the differential thermocouple, E, (Cu-Constantan wires).

The beryllium cell was held in position by the closure nut extension, P. Argon was fed into the cell through a stainless steel capillary (0.025 inch I. D., 0.042 inch O. D.). One end of the spiralled capillary was silver soldered to the closure nut, the other was connected with a Swagelok fitting to the stainless steel pressure manifold.

The pressure manifold contained the trimmer injector, W, argon feed line, V, and the pressure tap, X. The pressure was measured with a calibrated Texas Instrument model # 141, precision pressure gage using a steel bourdon spiral rated at 5000 psi.

C. Optics and Optical Alignment

The optical system has not been altered from that previously used in this lab. A pictorial illustration can be found in Figure 3 (This figure was taken from Mikolaj's thesis¹⁰). The molybdenum x-ray source was stationary. Both the incident beam and receiving beam collimating slits were attached to the goniometer in such a way that the goniometer could be raised, lowered or slightly tilted to confine the intersection of the incident beam to the extended centerline of the goniometer. These adjustments of the goniometer were accomplished by using the three screw-legs on the goniometer. The goniometer was positioned so that the distance from the x-ray target to the centerline was 6.97 inches. Final alignment of the goniometer was checked using a lithium fluoride crystal. With this crystal the measurement of theta was ascertained to be accurate to within ± 0.02 degrees, by checking the angular positions of silicon Bragg peaks for molybdenum $K\alpha$ radiation.

Collimated by vertical Soller slits, the incident beam was defined by the $1/6^\circ$ divergence slit (0.0062 inches) placed 3.3 inches from the target at a takeoff angle of 5.8° . If a line is drawn from the target through the center of the divergence slit, the takeoff angle is measured between this line and the horizontal plane passing through the rectangular target. In this way, the width of the target (10 mm. by 1.2 mm.) is foreshortened, effectively creating a line source (10 mm. by 0.12 mm.). The vertical Soller slits on the incident beam were constructed from 2.5 mil foils that were 1 and $1/8$ inches long and spaced eighteen mils apart.

Since the line source has width and only one divergence slit was used, the incident beam intensity distribution was trapazoidal: the umbra being 0.2 mm. across and the penumbra 0.52 mm. The width of this beam was less than the I. D. of the sample cell. The final geometry was such that the lower edge of the penumbra was above the centerline of the hole in the cell.

The viewing beam was collimated by horizontal Soller slits, and defined by a receiving slit (0.111 inches) selected so that this beam spanned the width of the scattering regions. Constructed from 2.4 mil foils spaced 5 mils apart, the Soller slits were 1.131 inches long.

The angular resolution is given by the horizontal and vertical divergence of the detected radiation. The maximum divergence is defined as the largest difference between the diffracted angle of any scattered ray and the nominal scattering angle, θ . This behavior will be discussed in section III-G, where a correction procedure that limits the maximum horizontal divergence to less than 0.35 degrees will be applied. Some values of the divergence before the correction are listed below. Vertical divergence was $\pm 0.375^\circ$ and independent of theta.

Nominal Angle, θ	Maximum Horizontal Divergence
1.5 degrees	1.71 degrees
2.5	1.28
5.0	0.75
7.5	0.50
10.0	0.39
15.0	0.25
30.0	0.10
45.0	0.03
60.0	-0.06

The alignment problem was to place the cell in the incident

beam so that the upper edge of the umbra was just below the top edge of the argon sample, as Mikolaj did. This geometry as well as the beam definitions are depicted in Figure 4. This alignment was accomplished as follows.

When the end of the cryostat was placed perpendicular to the axis of the goniometer, the cell axis and target were parallel. The slot in the cryostat was visually positioned in front of the target. Then, the final vertical and horizontal positioning of the cell could be achieved by moving the cryostat either up or down, and either closer to or farther from the target, using adjustment screws to move the cradle supporting the cryostat.

Vertical alignment was accomplished by taking a "shadow picture". A large divergence slit was used so that the x-ray beam was wider than the cell. Then with a very narrow receiving slit, the beam was scanned. The upper and lower edges of the cell could be easily located (See Figure 5). By this method, vertical positioning closer than 0.001 inch was realized.

Horizontal alignment was designed to place the centerline of the sample directly below the axis of the goniometer. To achieve this placement, the goniometer centerline was "made" into a scattering center. A very narrow divergence slit defined a very narrow incident beam that passed through the goniometer centerline. Then, the scintillation counter was positioned at 2θ of 90° and a very narrow receiving slit placed in front of it, such that scattering would only be detected if a portion of the beryllium cell was on the centerline. The cradle

was moved so that the entire cell passed horizontally through this scattering region. A plot of intensity versus the number of turns of the adjustment screws then showed two maxima, one for each wall. The center of the cell was determined from this plot (See Figure 6) to an accuracy approaching one thousandth of an inch.

Due to thermal contraction of the sample cell supports, the cell was aligned vertically at the operating temperature for each state of argon investigated. The cell was maintained at this temperature for at least twelve hours before the alignment was performed.

The final cell and beam geometry was:

cell I. D.	0.0370 \pm 0.0005 inches
cell O. D.	0.0700 \pm 0.0003 inches (actual measurement)
cell O. D. axis	0.0050 \pm 0.0005 inches below cell I. D. axis
incident beam centerline	0.0122 \pm 0.0002 inches above cell I. D. axis
height of umbra	0.0077 \pm 0.0002 inches
height of penumbra	0.0183 \pm 0.0002 inches
horizontal displacement of cell I. D.	0.0000 \pm 0.0010 inches from goniometer axis toward x-ray target
target to goniometer	17.7 cm.
nearest edge of vertical Soller slits to goniometer ϕ	9.6 cm.
divergence slit to goniometer ϕ	9.2 cm.
goniometer ϕ to receiving slit	14.3 cm.

goniometer ϕ to horizontal Soller slits	10.5 cm.
goniometer ϕ to detector	14.8 cm.

D. X-ray Measurement

The intensity of the scattered radiation was detected with a sodium iodide (thallium activated) scintillation counter. The crystal was $1/8$ inch thick and $\frac{1}{2}$ inch square. A one mil beryllium window served as a light shield. The output signal from the phototube multiplier was fed through amplifiers to a pulse-height selector. The output from the PHS was counted by an electronic scaler-timer. The resolution of this system was 46% (FWHM). The pulse-height distribution was discovered to shift its position when the count rate changed. To compensate for this, the voltage window was set to pass 99.5% of the PHD measured at one of the beryllium Bragg peaks.

The fact that the intensities were recorded in counts per second instead of the normal units, alters^{43,44} the Breit-Dirac correction factor^{45,46} for incoherent scattering from B^3 to B^2 (See Appendix 4).

The Zr-Y dual filter was experimentally balanced (See Appendix 5). The thicknesses of the balanced filters were 3.5 mils (Zr) and 5.5 mils (Y). Ninety per cent of the integrated intensity lies between 0.704 \AA and 0.718 \AA . The effective monochromatic wavelength of the source was assumed to be 0.7107 \AA .

E. A Typical Run

Argon state number 2 will be described. The density desired was 0.910 grams/cc and the temperature, $143.15 \text{ }^\circ\text{K}$. It will be

assumed that the cryostat has been positioned, and the cell aligned at room temperature.

The oil diffusion vacuum pump was turned on, and the cryostat evacuated. A 157 liter liquid nitrogen dewar was connected to the inlet to the cryostat, via a coolant transfer tube. In less than $\frac{1}{2}$ hour, the cryostat was cooled below 142°K by activating a variable a. c. heater in the dewar.

At this time, the proportional-integral controller regulating the main heater in the larger half of the slotted annulus was operated manually to warm the annulus to 143 degrees, then switched to automatic. In order to establish this preliminary temperature control, the input to the controller was the net emf from a calibrated thermocouple in the annulus, less a bucking potential equivalent to 143.15°K .

A second proportional controller was then activated to heat the smaller side of the annulus. For input, the desired control emf (taken from Honeywell's thesis) for the differential thermocouple was bucked against the differential thermocouple voltage. The cell was kept at 143.15°K for a period of twelve hours, then was vertically aligned.

The scintillation counter was positioned at 2θ of 23.62° , on the largest beryllium peak. The x-ray tube shutter was opened and the Zr filter placed in the incident beam. With the high voltage to the phototube set at the midpoint of the high voltage plateau, the PHD was measured. The average voltage, V , and the width, W , at half maximum were determined from a plot of the PHD, a Gaussian distribution.

For this curve, σ is related to W

$$W = 2.355 \sigma \quad (9)$$

The voltage base line and the voltage window were set for 99.5% transmission of the Mo $K\alpha$ radiation. Since the shifting of the PHD with intensity changes was small compared to W , the transmission was assumed constant. Typical values for the Hewlett Packard detector system were

V	3.122 volts
W	1.445
base line	1.397
window	3.450

The counter was then positioned at 2θ of 38° and the empty cell reference intensity was measured, and the electronic noise level recorded.

Using Levelts' data, the desired control pressure was determined to be 39.92 atm. Referring to the calibration (See Appendix 6) equation for the pressure gage, the gage setting equivalent to this pressure was calculated. Next, referring to Honeywell's thesis the platinum thermometer control temperature was calculated applying two corrections to the temperature sensed by the platinum resistance thermometer. This control temperature was equal to the desired temperature plus the temperature gradient correction minus the pressure times the thermometer pressure coefficient. Knowing the control temperature, the resistance of the platinum thermometer at this temperature was calculated from the Callender Van Deusen constants that were obtained in a calibration experiment (See Appendix 7).

With the pressure gage in servo, argon was bled into the

cell through the microflow valve until the pressure was close (10% below) to the control pressure. The platinum resistance thermometer current was activated and measured. The bucking voltage was calculated from the control resistance and this current. Control of the main heater was switched from the thermocouple to the platinum resistance sensor. When temperature control was obtained, more argon was added until the control pressure was reached.

The initial reference intensity was measured for the argon and cell. Then the dual filter scan was started at 2θ of 1.50 and data points were taken: β -filter followed by the α -filter; the counter was advanced 0.5° and the next two filter measurements were recorded; and so on. The scan was interrupted several times (about two hours apart) to monitor the reference angle intensity. When the scan was completed, the reference angle intensity was measured again, the argon removed, and the cell evacuated. Then, the empty cell reference intensity was measured. To be certain that the cell had not moved, the alignment was checked.

This completed the first scan. The dewar of nitrogen was refilled and scan two, then similarly scan three followed. The data were plotted during the run and questionable points were immediately checked.

During each scan the pressure was manually kept at the control pressure ± 0.2 psi. Once the argon bleed rate to balance leaks had been established, small trimmer injector corrections had to be made about every 20 minutes. The current to the platinum thermometer was

checked regularly and if corrections were needed, the bucking voltage was changed.

At 99.5% transmission of the $K\alpha$ wavelength, up to 40% of the radiation detected with a β -filter on the incident beam is not the desired radiation. Typical β and α -patterns are depicted in Figure 7 for the empty cell measurements, and in Figure 8 for the cell and sample measurements. The actual dual filter intensity patterns are the difference between the curves in each figure.

III. TREATMENT OF EXPERIMENTAL DIFFRACTION DATA

A. General

The radial distribution functions and the direct correlation functions are obtained by Fourier transforming intensity kernels which must be obtained from the experimental diffraction patterns. The method by which the Fourier intensity kernels were produced from the cell and sample scattering pattern will be presented. Since the experimental data were recorded in θ -space, the computations preceding the transformation were performed with θ as the independent variable rather than the scattering parameter, s .

In order to obtain the total scattering function originating from the confined argon, the scattering from the empty cell must be subtracted using the Basic Data Reduction Equation (derived in Appendix 2):

$$I_s(\theta) = \frac{1}{P(\theta) F(\theta) ASSC(\theta)} \left[I_{c+s}^E(\theta) - G(\theta) \frac{ACSC(\theta)}{ACC(\theta)} I_c^E(\theta) \right] \quad (10)$$

where

$P(\theta)$ is a polarization correction, $\frac{1}{2} [1 + \cos^2(2\theta)]$

$ASSC(\theta)$, the sample absorption factor, corrects the sample scattering for absorption in both the sample and cell

$F(\theta)$ is a correction term that arises from the fact that the fractions of coherent and incoherent sample scattering are absorbed differently

$I_{c+s}^E(\theta)$, the average cell and sample scattering obtained from the three data scans

$I_C^E(\theta)$, the average cell scattering obtained from five data scans

$G(\theta)$ is a correction term that arises from the fact that the fractions of coherent and incoherent cell scattering are absorbed differently

ACSC(θ), one of two cell absorption factors, for scattering from the cell and absorption in cell and sample

ACC(θ), the second cell absorption factor, for scattering from the cell and absorption in the cell

and

$I_S(\theta)$ is the total scattering from the sample, i.e., the sum of the coherent, which contain the structure information, and the incoherent scattering.

The Fourier intensity kernel is obtained from $I_S(\theta)$ by normalizing to the total gas scattering function (the sum of the atomic coherent and incoherent scattering determined from theory), subtracting the gas scattering function and then dividing by the atomic coherent scattering factor, $f_d^2(s)$. Namely

$$i(\theta) = \frac{(C/N) I_S(\theta) - \frac{\text{Inc}(\theta)}{B^2(\theta)} - f_d^2(\theta)}{f_d^2(\theta)} \quad (11)$$

where (C/N) is determined by requiring $I_S(\theta)$ to be equal to the sum of $\text{Inc}(\theta)/B^2(\theta)$ and $f_d^2(\theta)$ at large values of θ where coherent constructive and destructive interference is small

$$(C/N) = \frac{I_S}{\frac{\text{Inc}}{B^2} + f_d^2} \quad \text{at large } \theta. \quad (12)$$

This normalization will be discussed later.

Experimentally, $i(\theta)$ would contain fluctuations which are inherent in the statistics of scattering. To eliminate the difficulty in transforming $i(\theta)$ in this form, $I_s(\theta)$ is smoothed before $i(\theta)$ is calculated.

The smoothing technique is improved by comparing estimates of $I_s^{\text{smh}}(\theta)$ plus the confidence interval with $I_s(\theta)$ data points. The confidence interval (derived in Appendix 3) is calculated from the data as follows:

$$(\Delta I_s)_j = \frac{\pm k_j}{P(\theta) F(\theta) \text{ASSC}(\theta) \sqrt{\tau_{c+s}}} * \left[\frac{I_{c+s}^{\beta}(\theta) + I_{c+s}^{\alpha}(\theta)}{n_{c+s}} + \frac{G^2(\theta) \text{ACSC}^2(\theta) \tau_{c+s}}{\text{ACC}^2(\theta) \tau_c} \frac{I^{\beta}(\theta) + I^{\alpha}(\theta)}{n_c} \right]^{\frac{1}{2}} \quad (13)$$

where τ_{c+s} is the time interval (100 seconds) for each data point in each cell and sample scan

n_{c+s} is the number (3) of cell and sample scans

τ_c is the time interval (300 seconds) for each data point in each cell scan

n_c is the number (5) of each empty cell scans

k_j is a constant for each confidence level.

Whenever $I_s(\theta)$ is considerably outside the 90% confidence band about $I_s^{\text{smh}}(\theta)$, and this is not obviously due to one measurement, the data at this angle are rejected and $I_s^{\text{smh}}(\theta)$ recomputed.

The intensity kernel $i(s)$ is extrapolated to s of zero as Mikolaj did, using

$$j(s) = i(s) + 1 = \frac{j(0)}{1 + a_2 s^2 + a_4 s^4} \quad (14)$$

where

$$j(0) = k T \rho K_T \quad (15)$$

The s^2 dependence at small s has been experimentally verified for argon near the critical state by Thomas and Schmidt.⁴⁷ The s^4 term is included to allow a smooth transition from the region of s^2 behavior to the value at the smallest experimentally obtainable s . Even powers of s are used since $i(s)$ is an even function. $j(0)$ was calculated from the PVT data, whereas a_2 and a_4 were determined by the magnitude and slope of the experimental $i(s)$ at the smallest s .

The details of the data reduction will now be summarily presented. With the exception of the uncertainty band for the structure functions, the technique is Mikolaj's.

B. Preliminary Calculations

All measured intensities were obtained as follows:

$$I(\theta) = \frac{N(\theta) - n}{\tau} \quad (16)$$

where

$N(\theta)$ is the number of experimental counts recorded at θ during the counting time τ .

n is the average number of electronic background counts determined with the x-ray shutter closed.

The Fourier transform of $i(s)$ is based on the assumption that the scattering is obtained with the intensity of the main beam held constant. That is, the experimental intensities in Eq. (10) are assumed to be measured relative to one common incident intensity, I_0 , a constant. Since each measurement is proportional to the incident beam intensity, fluctuations in the incident beam intensity were removed by scaling the observed intensities to a reference scattering intensity which was selected to be the scattering intensity at 38° (2θ).

$$I^E(\theta) = \frac{I^\beta(\theta) - I^\alpha(\theta)}{I^{\text{ref}}(\theta)} \quad (17)$$

The subscripts, either c or c+s, do not appear here as the equation is similar for the cell and sample, and cell scans. $I^{\text{ref}}(\theta)$ is obtained by calculating the intensity of the reference angle scattering, assuming it varied linearly between two monitorings. Suppose that for a particular scan that the reference angle intensity had been measured by interrupting the data sequence at 20° and 30° , and the reference intensity at 24.5° was desired. Then this intensity is:

$$I^{\text{ref}}(24.5) = I^{\text{ref}}(20) + \frac{4.5}{10} \left[I^{\text{ref}}(30) - I^{\text{ref}}(20) \right] \quad (18)$$

To increase the accuracy of this scaling, the reference angle intensities were measured at least seven times and statistically analyzed to reject points before an average was calculated.

The empty cell data points were normalized by the reference angle intensity measured at 38° during an empty cell scan. The cell and sample data points were normalized by the reference angle intensity measured during a cell and sample scan. In order to subtract these two intensities as suggested by Eq. (10), it is now necessary to scale the cell and sample data by the ratio of the cell and sample reference intensity to the cell reference angle intensity. This ratio, Q , was experimentally determined at the start of each cell and sample scan. Since the quantitative calculation of I_s depends on the accuracy to which Q is known, the initial measurements of reference angle intensities with and without argon in the cell were repeated until the standard deviation in Q was less than 0.2%. To determine the effect of an error in Q on $I_s(\theta)$, a test case was computed for argon Run # 2. When Q was in error by +0.2% the main peak intensity after normalization would be reduced 0.4%.

C. Absorption Factors

Absorption of x-rays is governed by the mass absorption coefficient which is a function of wavelength. The technique of applying this correction to coherent scattering from a sample confined in a cylindrical cell, originally treated by Paalman and Pings,⁴⁸ has been modified to include the trapezoidal intensity distribution of the incident beam and the non-concentricity of the beryllium cell (See

Appendix 8). In addition, the technique was applied to the incoherent scattering where the wavelength of the scattered radiation is longer than the incident wavelength, to calculate the incoherent absorption factors which are needed to evaluate $F(\theta)$ and $G(\theta)$.

The wavelength behavior of the mass absorption coefficient has been taken from the International Crystallographic Tables,⁴⁰ that contains an empirical correlation which was taken from Victoreen.⁴⁹ The magnitude of the mass absorption coefficients for incoherent and coherent scattering from argon are greater by about 7% from those used by Mikolaj, who used the values experimentally determined by Chipman and Jennings.⁵⁰ Victoreens' correlations were used in preference to the measured values for two reasons. First, Victoreen stated that the disagreement between observers of mass absorption coefficients is sufficiently great as to make any single observed value doubtful. Second, the tabular values represent the systematic correlation of a large set of measurements. The effect of the uncertainty in the mass absorption coefficient was investigated by comparing I_s curves calculated for absorption coefficients 5% below that used by Mikolaj with those 5% above Victoreens, a range of 17%. After normalization, the magnitudes of peaks and valleys were altered less than 2%, primarily the first valley and the main peak. Since an order of magnitude less error results from an error in the mass absorption coefficients, it will be assumed that a possible systematic error related to the absorption coefficients is negligible.

The basic data reduction equation includes the use of the

coherent absorption factors directly and the incoherent factors indirectly in the evaluation of the two terms, $F(\theta)$ and $G(\theta)$, which are defined as follows:

$$F(\theta) = \gamma_s^{\text{coh}}(\theta) + \gamma_s^{\text{inc}}(\theta) \frac{\text{ASSC}^{\text{inc}}(\theta)}{\text{ASSC}^{\text{coh}}(\theta)} \quad (19)$$

and

$$G(\theta) = \frac{\gamma_c^{\text{coh}}(\theta) + \gamma_c^{\text{inc}}(\theta) \frac{\text{ACSC}^{\text{inc}}(\theta)}{\text{ACSC}^{\text{coh}}(\theta)}}{\gamma_c^{\text{coh}}(\theta) + \gamma_c^{\text{inc}}(\theta) \frac{\text{ACC}^{\text{inc}}(\theta)}{\text{ACC}^{\text{coh}}(\theta)}} \quad (20)$$

where the superscripts, coh and inc, relate to the scattering which occurs coherently and incoherently. (The absorption factors are then the correction terms which apply to either scattering, respectively.) The term, γ_c , is the fraction of the intensity scattered, coherently or incoherently, from the cell, and γ_s the corresponding fraction for the argon sample.

Assuming that $G(\theta)$ can be calculated, the fractions of coherent and incoherent scattering from the argon sample can be determined by an iterative technique. The first estimates are obtained from the coherent and incoherent scattering, f_d^2 and I^{inc}/B^2 respectively. Once I_s is normalized, the incoherent portion (I^{inc}/B^2) can be subtracted leaving the next estimate of the coherent scattering. This is repeated until successive estimates of γ_s^{coh} are identical.

Unfortunately this technique can not be applied to γ_c because destructive and constructive interference of the coherent scattering from the beryllium crystals in the cell occurs at all values of θ . This is unlike the scattering from the liquid argon where interference effects do not occur at large θ .

This difficulty was overcome by selecting a scattering geometry which makes $G(\theta)$ insensitive to γ_c , a geometry which minimizes the absorption in argon of incoherent scattering from beryllium. This is the reason why the incident beam was kept at the top of the argon sample. With this geometry, $ACSC^{inc}/ACSC^{coh}$ and ACC^{inc}/ACC^{coh} are very close to one. As a consequence, $G(\theta)$ is very close to one irrespective of γ_c . For purposes of reducing the data, γ_c was determined from the atomic scattering factor and the incoherent scattering predicted from quantum-mechanical electron wave functions for beryllium.

Inherent in the definitions of $F(\theta)$ and $G(\theta)$ is the assumption that the electronic transmission for incoherent scattering is the same as the transmission for coherent scattering. The angular dependence of the incoherent wavelength is given²⁸ by

$$\lambda^{inc} = \lambda^{coh} + 0.0243 (1 - \cos 2\theta) \quad (21)$$

This means that the energy of incoherent scattering is less than the energy of the coherent scattering and the difference increases with increasing θ . At 2θ of 120° , the largest angle investigated, the largest change for $\lambda^{coh} = 0.7107 \text{ \AA}$ is less than 5%. The associated PHD for

incoherent scattering should shift a maximum of 5% and the net result is that the electronic transmissions, because of the wide voltage window, are essentially constant within 0.1%.

D. Atomic and Incoherent Scattering Factors

The incoherent scattering factors for Be was obtained by LaGrange polynomial interpolation⁵¹ of the ten calculated values of I^{inc} published by Freeman.⁵² These values were given only to s of 13.8. A plot of these ten points was extrapolated to s of 15.3 to obtain the necessary values to complete the data reduction scheme.

At the time the data were analyzed, incoherent scattering factors including exchange effects were not available for argon. The values that were used were interpolated from those⁵² of Ca^{++} , K^+ and Cl^- , which did include exchange. Extrapolation from s of 13.8 to 15.3 was required. Recently, Cromer and Mann⁵³ published values of these factors including exchange effects which agree with the interpolated values over the range of theta for which the intensity kernel showed interference. At larger angles, the discrepancy increased slowly to 3% at two theta of 120° .

The atomic scattering factors, including exchange effects, were obtained from Berghuis et. al.⁵⁴ The values for Be were reported to agree well with previous calculations, but the inclusion of the exchange effects indicated changes of up to 10% with previous results for argon. This discrepancy will be elaborated upon shortly.

The calculation of atomic scattering factors is made with the assumption that the circular frequency of the incident radiation

is not close to any natural modes of the electron system of the atom. The corrections to make the factors applicable for any given wavelength are called dispersion corrections, and the applicable dispersion corrected atomic scattering factor takes the following form

$$f_d(s) = f(s) + \Delta f' + i\Delta f'' \quad (22)$$

The values of $\Delta f' = 0.18$ and $\Delta f'' = 0.24$ for Mo $K\alpha$ radiation were obtained from Cromer.⁵⁵

The nature of discrepancies between the dispersion corrected atomic scattering, f_d^2 , and values used by others in reducing x-ray diffraction for argon are depicted in Figures 9 and 10. Systematic errors in $i(s)$ would result if the proper values of the atomic scattering are not selected. Two pieces of evidence which support the use of the values calculated by Berghuis will now be mentioned.

Rahman⁵⁶ compared two Fourier intensity kernels, one obtained with x-rays, the other with neutrons. A plot from his paper is reproduced here. (See Figure 11). Using a new criteria to test the validity of these intensity kernels, Rahman concluded that the neutron data were more reliable than the x-ray data. In order to show what the effect of the uncertainty in the atomic scattering factor would do to the x-ray data, the x-ray intensity kernel was recalculated using the dispersion corrected values of Berghuis et. al. and the new x-ray kernel was compared to the neutron kernel in Figure 12. Within the accuracy with which the published figures could be interpolated to make the

calculations, the two curves now show substantial agreement.

Secondly, the atomic scattering factor of argon has been measured by Chipman and Jennings.⁵⁰ The values of $f(s)$, obtained on an absolute basis with an accuracy of about $\frac{1}{4}\%$, agree with the values of Berghuis et. al. within 0.1 e.u. Since Chipman and Jennings reduced their data using dispersion corrections and subtracted incoherent scattering that included exchange effects, it is reasonable to assume that the Berghuis values are an accurate estimate of the atomic scattering factor.

E. Data Smoothing

The sample intensity data, $I_s(\theta)$, were smoothed by fitting a second order polynomial in θ to short segments of the scattering curve. The form of the fitting polynomial was

$$I_s^{\text{smh}}(\theta) = a(\theta) + b(\theta) * \theta + c(\theta) * \theta^2 \quad (23)$$

The coefficients were evaluated by least squares, and a separate set of coefficients were determined for each value of θ (with the exception of data points near the apex of the main peak which were not smoothed).

The range of data points used to smooth the data at each θ is summarized below.

θ	No. of pts. on each side of θ
1.50 to 4.00	3,4,5,5,4,4,4,3,3,3
5.25 to 8.00	3,3,4,4,4,4,4,4,4,4,4
8.25 to 12.25	5,5,...5
12.50 to 16.25	5,6,6,7,7,8,8,8,8,8,8,8,8
16.50 up	8,8,9,9,10,10,... to a maximum of 40,40

These ranges of fittings were the last set used, with many other combi-

nations having been examined.

The smoothing process itself was a lengthy, systematic analysis, which will be briefly summarized, step by step.

The first analysis was the effect of the 17% range of the mass absorption coefficient. $I_s(\theta)$ for all six states was evaluated for seven values of this coefficient. After it was discovered that only small changes in $i(s)$ would result from any two different mass absorption coefficients in this range, a decision was made to use the coefficient from the International Crystallographic Tables.

Next, a qualitative study of effect of Q on I_s was undertaken. For each run, eight values of Q spanning an arbitrarily selected 8% fluctuation in Q were used to check to see if the experimental Q was reasonable. This technique was based on the beryllium Bragg peaks which are present in both the cell pattern and the cell and sample pattern. The argument is this: if the value of Q being tested is too large, the peaks in $I_s(\theta)$ will all lie above basic argon intensity pattern, and similarly, if the value of Q is too small, the peaks in $I_s(\theta)$ will all be below the basic argon pattern. The net result of this investigation was that the six experimentally measured Q 's were more narrowly defined than any value of Q which could be derived by examining the behavior of the peaks.

Now, the experimentally measured Q 's, and the argon mass absorption coefficient were used to calculate $I_s(\theta)$ for all six states, and plots of these six functions were studied to ascertain whether or not any of the empty cell beryllium peaks were consistently too large

or too small. The first step was to construct a table where, at each θ corresponding to a peak, entries were made which described to what extent $I_s(\theta)$ was above or below the basic pattern at that angle. Whenever the six table entries indicated that the $I_c^E(\theta)$ was probably in error, the five β -filter and the five α -filter measurements used to compute this intensity were checked to eliminate one pair of measurements, if this pair deviated significantly from the other four. If a pair was eliminated, the average cell intensity at this angle was then recalculated.

Following this, a preliminary smoothing was performed, the 90% confidence band was calculated, and a plot of I_s , and $I_s^{\text{smh}} \pm \Delta I_s$ was made. All points of I_s falling outside the 90% confidence band were investigated just as the empty cell data points as beryllium peaks were. Individual pairs of β and α -filter cell and sample measurements were rejected only where the pair significantly contributed to the discrepancy. When it did, a new average cell and sample intensity was calculated from the remaining two pairs at the angle. In this step, for each argon state investigated, less than eight pairs out of 711 were discarded. When this was completed, the average intensities, at each angle in the cell measurements and at each angle in the cell and sample measurements, were considered to be "the experimental data." No further rejection of individual β -filter- α -filter pairs was attempted. Figure 13 depicts the cell pattern and the cell and sample pattern for Run # 2.

Two additional refinements were necessary to complete the

smoothing process. The first was simple to apply. Any I_s point which remained outside a confidence band of 99.5% was rejected and replaced by the preliminary estimate, $I_s^{\text{smh}}(\theta)$.

Then, a large number of variations in the smoothing ranges were tested to determine the maximum number of oscillations which could be statistically identified in the six state patterns being investigated. Three criteria were used. First, a maximum or minimum was said to be identifiable, if the distance between the normalized pattern, $(C/N) I_s^{\text{smh}}$ and the gas scattering function, $f_d^2 + I^{\text{inc}}/B^2$, was greater than the width of the 50% confidence band. Second, this maxima or minima must exist at approximately the same angle in all intensity patterns at higher densities. And third, a continuous set of oscillations must be identifiable at all angles smaller than that angle where an oscillation could be identified. Within these criteria, only three maxima could be identified at each temperature and density investigated. (Refer to the smoothing curve plotted in Figure 14 for argon Run # 2.)

Once this fact had been established, the smoothing range previously listed was used to complete the smoothing process. Fluctuations in I_s^{smh} beyond θ of about 22° were considered random.

F. Normalization

The kernel of the Fourier integral is calculated from the smoothed intensity patterns by subtracting the total gas scattering from I_s^{smh} as follows:

$$i(\theta) = \frac{(C/N) I_s^{\text{smh}}(\theta) - f_d^2(\theta) - I^{\text{inc}}(\theta)/B^2}{f_d^2(\theta)} \quad (24)$$

where the constant, C/N, normalizes the smoothed intensity to the electron unit.

The proper value of C/N is that which allows $i(\theta)$ to vanish as θ increases. This normalization was accomplished by a least squares fit of the ratio

$$\frac{I_s^{\text{smh}}(\theta)}{f_d^2(\theta) + I^{\text{inc}}(\theta)/B^2} \quad (25)$$

One hundred values of I_s^{smh} from θ of 20° to 45° were used to calculate C/N within a maximum estimated error of 0.3%. A typical fit of the normalized smoothed curve for Run # 2 is depicted in Figure 15.

With C/N determined, $i(\theta)$ was calculated.

G. Divergence Correction

As previously described, the maximum horizontal divergence of the experimentally scattered radiation is a function of angle. A correction procedure to limit the maximum divergence to less than 0.35 degrees has been developed. Since the details of this correction are carefully outlined in Appendix 9, only the reason for the correction will be presented here.

When the scattering geometry was analyzed, it was discovered that the horizontal divergence was primarily contributable to the width of the horizontal Soller slits. If the receiving beam had been collimated vertically as well as horizontally, the horizontal divergence would have been considerably reduced.

The incident beam was defined by a set of vertical Soller

slits. Because of the length and the narrow spacing of the vertical foils, an incident ray could not deviate more than 0.825 degrees from intercepting the sample at 90° to the axis of the goniometer. Therefore, within this small angular deviation, it was assumed that all scattered radiation resulted from parallel incident radiation, where each incident ray would be scattered in a diffraction cone defined by the scattering angle 2θ .

The receiving Soller slit system can be considered to be a set of detectors, each one looking at a portion of the sample, each one 0.005 inches high and about 0.400 inches wide. Since the foils of the Soller slit assembly are parallel, the nominal angle 2θ is applicable to each, and the correction was developed for only one of these detectors. The two dimensions of the detector will be called the window, the length being parallel to the target and sample. The face of the window moves about the sample on an arc of radius R in steps of 0.25° in θ , thus defining a set of observations of the intensity measurements at 237 values of θ . For this analysis the narrow target and the portion of sample being viewed will be considered to be a line source and a line sample respectively.

Consider scattering from the line sample which is defined by a scattering angle 2θ . Each point in the line sample generates a scattering cone. A portion of each cone will certainly be detected at the nominal angle equal to the angle of the cone. The question then becomes, is the $2\theta_k$ cone detected at any other angle, $2\theta_1$, besides that specific angle, $2\theta_k$? The answer is yes, when the counter is at angles

smaller than $2\theta_k$ and where the maximum horizontal divergence at $2\theta_k$ is greater than $2\theta_k - 2\theta_1$. That is, only at small angles.

Therefore, the measured scattering intensity at small angles is actually greater than it should be if the viewing beam were properly collimated. Using the procedure outlined in Appendix 9, a correction was made to $I_s^{\text{smh}}(\theta)$ and $i(s)$ recalculated from the divergence corrected smooth scattering function. Figure 16 depicts the argon intensity function, $j(s)$ [$j(s) = i(s) + 1$], for Run # 2, before and after the divergence correction.

This correction did not significantly alter the calculated radial distribution functions, nor the direct correlation functions beyond r of 3.2. However, the calculated values of $C(r)$ at small values of r were more negative than those calculated from the uncorrected argon intensity patterns.

H. The Transform Calculation

Before the net radial distribution function and the direct correlation function could be calculated, it was necessary to extrapolate the dispersion corrected intensity kernels to s of zero (See Eq. (14)). Since no systematic oscillations were detected beyond the third maximum in $i(s)$, the experimental intensity kernels were truncated after the third maximum. This truncation limit is labeled s_{max} .

The net radial distribution function was calculated by integrating the intensity kernel from s of zero to the truncation limit.

$$4\pi r^2 \rho_h(r) = \frac{2r}{\pi} \int_0^{s_{\text{max}}} s i(s) \sin sr \, ds \quad (26)$$

Fifth degree LaGrange interpolating polynomials were calculated for the discrete values of $i(s)$, six points at a time, and the powers of s with the appropriate coefficient were analytically integrated with $\sin sr$, such that:

$$4\pi r^2 \bar{\rho} h(r) = \frac{2r}{\pi} \sum_j \sum_{i=0}^5 (a_i)_j s^{i+1} \sin sr ds \Big]_{s_j}^{s_{j+1}} \quad (27)$$

where $(a_i)_j$ is the coefficient of the i^{th} power of s for the LaGrange polynomial over the interval (s_j, s_{j+1}) . The subscript j counts the intervals required to fit $i(s)$ from zero to the truncation limit.

Similarly, the direct correlation function was calculated from

$$4\pi r^2 \bar{\rho} C(r) = \frac{2r}{\pi} \int_0^{s_{\max}} \frac{i(s)}{1+i(s)} \sin sr ds \quad (28)$$

where the polynomial interpolation coefficients were calculated for the intensity kernel, $i(s)/(1+i(s))$. For $r < 3.2 \text{ \AA}$, the procedure developed by Mikolaj and Pings¹³ was used to calculate more accurate estimates of $C(r)$ than available from the direct transform. At these values of r , the radial distribution is zero and $h(r) = -1$. Therefore, equations (26) and (28) may be subtracted to produce

$$4\pi r^2 \bar{\rho} (C(r) + 1) = \frac{-2r}{\pi} \int_0^{s_{\max}} s \frac{i^2(s)}{1+i(s)} \sin sr ds \quad (29)$$

which could be evaluated using another set of interpolating polynomials.

I. Uncertainty Bands

The confidence interval for $i(s)$ can be calculated as follows:

$$\delta i(s) = \frac{(C/N) \Delta I_s(s)}{f_d^2(s) \sqrt{N(s)-3}} \quad (30)$$

where

C/N is the previously determined normalization constant to convert to electron units

ΔI_s is the previously determined confidence interval for the data

$f_d(s)$ is the dispersion corrected atomic scattering factor

$N(s)-3$ represents the number of degrees of freedom that are inherent in the quadratic (3 constant) smoothing process. If the data at a particular value of s were not smoothed, $N(s)-3$ was set to one; otherwise, $N(s)$ was taken to be the total number of data points used to calculate I_s^{smh} at s .

For the purpose of estimating the uncertainty in structure, the values of ΔI_s at the 50% confidence interval (that is, k_j was taken to be 0.675), were used.

An uncertainty band for the net radial distribution function has been estimated as follows:

$$4\pi r^2 \bar{\rho} \Delta h(r) = \frac{2r}{\pi} \int_0^{s_{\text{max}}} s \delta i(s) | \sin sr | ds \quad (31)$$

To simplify the calculation, the absolute value of $\sin sr$ was replaced by the constant, one. In this sense, $\Delta h(r)$ represents an uncertainty band in $h(r)$ that is based on the fact that over the range of s that $i(s)$ has been determined, the exact value of $i(s)$ is uncertain.

For $r > 3.2$, the uncertainty band for the direct correlation function has been estimated using

$$4\pi r^2 \bar{\rho} \Delta C(r) = \frac{2r}{\pi} \int_0^{s_{\max}} s \frac{\delta i(s)}{1+i(s)} ds \quad (32)$$

For r less than 3.2, the following definition for $\Delta C(r)$ was used

$$4\pi r^2 \bar{\rho} \Delta C(r) = \frac{2r}{\pi} \int_0^{s_{\max}} \frac{s i(s)(2+i(s))\delta i(s)}{(1+i(s))^2} ds \quad (33)$$

The uncertainty bands, $\Delta h(r)$ and $\Delta C(r)$, are a statement of the fact that the ability to calculate $h(r)$ and $C(r)$ depends on the total time allotted to measure the scattering intensities.

J. Calculation of P-Y Potentials

Once the radial distribution function and the direct correlation function had been calculated, the potential predicted by the Percus-Yevick equation could be calculated by rearranging the P-Y equation to

$$\frac{1}{k} \left[u(r) \right]_{\text{P-Y}} = T \ln \left[\frac{g(r) - C(r)}{g(r)} \right] \quad (34)$$

This equation can be used when neither the numerator nor the denominator of the logarithm are zero.

The uncertainty bands for the structure functions were used to estimate the uncertainty in $u(r)$, namely

$$\frac{1}{k} \Delta[u(r)]_{P-Y} = T \sqrt{\left(\frac{\Delta g(r)}{g(r)}\right)^2 + \left(\frac{\Delta(g(r) - C(r))}{g(r) - C(r)}\right)^2} \quad (35)$$

where

$$\Delta g(r) = \Delta h(r) \quad (36)$$

$$g(r) = h(r) + 1 \quad (37)$$

and where $\Delta(g(r) - C(r))$ is calculated using the right hand side of Eq. (33).

IV. RESULTS

A. General

The six thermodynamic states investigated, including the experimental uncertainties, are summarized in Table I. The values of temperature and pressure are absolute relative to the primary standards, an NBS calibrated platinum resistance thermometer and the Hart dead weight tester, whereas the densities quoted are based on the PVT measurements of Levelt³⁸ and Van Itterbeek.³⁹ $\Delta\rho$ is based on ΔT and ΔP .

The uncertainty in the temperature includes uncertainties in the thermometer pressure coefficient, the temperature gradient between the irradiated sample and the argon in which the thermometer is immersed, the inaccuracy of the thermometer calibration, and the maximum fluctuation of temperature during the three scans of θ -space. In addition to this, an uncertainty that relates to the thermometer calibration device itself was included to insure the absolute measurement. That is, the respective terms are

$$\Delta T = \Delta T_{P.C.} + \Delta T_{T.G.} + \Delta T_{T.C.} + \Delta T_{Fluc} + \Delta T_{C.D.} \quad (38)$$

Typical values for Run # 1 are:

$$\Delta T = 0.005 + 0.015 + 0.0023 + 0.0007 + 0.015 = \pm 0.038 \text{ } ^\circ\text{K} \quad (39)$$

The maximum temperature fluctuation was 1.2 millidegrees for Run # 2.

The uncertainty in the pressure includes the precision of the pressure calibration data, the uncertainty of the primary standard (1 part in 10,000), the experimental fluctuation, and a zero drift correction (0.05%) for the Texas Instrument.

$$\Delta P = \Delta P_{P.C.} + \Delta P_{P.S.} + \Delta P_{Fluc} + \Delta P_{Z.D.} \quad (40)$$

Typical values for Run # 1 are:

$$\Delta P = 0.005 + 0.050 + 0.200 + 0.264 = \pm 0.519 \text{ psi} \quad (41)$$

The experimental fluctuation of 0.2 psi was the same for all runs. The zero drift correction was taken from the literature accompanying the precision pressure gage, and must be included whenever the gage is pressurized for long periods of time. The hysteresis behavior of the bourdon spiral was carefully avoided by never pressurizing the gage above the measuring pressure.

B. Intensity Curves

The average experimental cell and cell plus sample experimental intensities, normalized by the reference angle intensity, are listed in Table II. Each number in the cell intensity data represents at least fifty minutes total counting time, 1500 seconds with the β -filter on the incident beam and 1500 seconds with the α -filter on the incident beam, accumulated in five θ -space scans. In the other six columns, each number in the cell and sample intensity data represents 10

minutes counting time, 300 seconds for each filter accumulated in three θ -space scans. The average empty cell checkpoint intensity was 42.16 counts/sec. In order to subtract the cell intensity from the cell and sample intensity, the latter must be scaled by Q , the ratio of the cell plus sample reference angle intensity to the empty cell reference angle intensity. The six experimentally determined ratios for the six states are 1.5300, 1.4890, 1.5201, 1.4737, 1.4237, 1.4274 and 1.3454, for Runs 1 to 6 respectively.

A typical plot of the normalized data has been presented in Figure 13. Note that over 40 of the 237 angle measurements have been made on beryllium Bragg peaks. The lines connecting data points in this figure are not meant to imply the actual shape of the more than fifteen peaks which are outlined. The first peak and the right shoulder of the second peak of the argon scattering curve are clearly discernable at six degrees and to the right of 13° .

The values of the dispersion corrected atomic scattering factor and the incoherent scattering factor used to deduce $i(s)$ from the experimental data are listed in Table III. The last two entries of the incoherent scattering have been obtained by extrapolation. The relative amount of incoherent scattering in the total scattering is depicted in Figure 15. The total gas scattering intensity drops monotonically from 330.57 electron units at the origin to 25.8 at theta of 60° . As pointed out in the data reduction scheme, the relative amounts of incoherent and coherent scattering from beryllium need not be known for this scattering geometry. Nonetheless, since the fractions

of coherent and incoherent scattering were approximated by the Be atomic scattering function and the Be incoherent scattering factor, selected values of these functions are presented in Table IV.

Before the data could be subtracted, values of the absorption coefficients, ASSC, ACSC and ACC for both incoherent and coherent scattering were calculated for each angle where scattering data was taken. The wavelength dependence of the mass absorption factor is presented in Appendix 8. The density of the beryllium cell was taken from Mikolaj's thesis, 1.82 gm/cc and the density of argon used to calculate the linear absorption coefficient from the mass absorption coefficient was the appropriate experimental sample density. Representative values of the absorption coefficients for each run, estimated to be accurate to three significant figures, are listed in Table V.

Using the methods of data analysis described in the preceding section, x-ray scattering curves were obtained at the six different thermodynamic states. The results of these calculations, the argon intensity curves ($j(s) = i(s) + 1$), are presented in Table VIa before the divergence correction was made, and in Table VIb after this correction. Since the general features of the argon intensity curves are more clearly shown in $j(s)$ rather than I^{smh} (Figure 15), the divergence corrected data are presented in terms of $j(s)$ in Figure 16 (Run 2), Figure 17 (Runs 1, 3 and 4), and Figure 18 (Runs 5 and 6). The order of increasing density and decreasing temperature is Run 2, 1, 3, 4, 5, then 6. The values of $j(0)$, a_2 and a_4 used to extrapolate these curves to s of zero, the normalization constant, and the trunca-

tion limit are listed in Table VII. Two sets of extrapolation parameters are given, one for $j(s)$ before the divergence correction, one after the correction.

Each $j(s)$ curve shows three maxima at s values of 1.92 ± 0.02 , 3.68 ± 0.06 and 5.43 ± 0.16 , and three minima. The position of the first minimum is between s of 0.55 and 0.69 for the first five runs but shifts considerably towards the origin to s of about 0.14 for the highest density. The second minimum occurs at s of 2.73 ± 0.04 and the third at s of 4.48 ± 0.18 . The precise values for each run are listed in Table VIII. In general, the depth of the first minimum decreases with increasing density from 0.20 to 0.09 and the height of the first peak increases markedly with increasing density from 1.45 at $\rho = 0.910$ gm/cc to 2.26 at a density of 1.261 gm/cc. The other features do not show marked changes with change of state, except that the third peak at a density of 1.116 gm/cc (Run 4) is at a larger s than any other state, a fact that is consistent with the intensity patterns measured by Eisenstein and Gingrich.

The width of the first peak in $j(s)$ [at $j(s) = 1$] is reasonably constant in this density range (See Figure 19) between s of 0.70 to 0.74, but considerably narrower than the width of the $j(s)$ functions measured by Mikolaj at lower densities in a β -filter experiment. The effect of the dual filter monochromatization was to reduce the magnitude of the first peak, thereby reducing the peak width. Compare the dual filter data with the β -filter data at 143 °K and a density of 0.982 gm/cc in this figure.

The height of the first peak systematically increases with density as is depicted in Figure 20, with the exception of the height of the first peak at 1.116 gm/cc which appears to be 8 to 10% lower than the trend of the other five states would indicate. It should be pointed out that the data for this run was the only set taken while the air conditioning in the lab was not working (The room temperature was 15° hotter in the daytime and 5° cooler at night than the normal 68 ± 2 °F). Even though the scatter in the data was increased by an increase in the electronic noise in the detector system, the statistically predicted uncertainty band about this peak height is not large enough to be able to claim that this lower peak height is within statistical fluctuations. This lower peak height is an experimental fact.

C. Net Radial Distribution Functions

The net radial distribution functions were calculated at 155 values of r as follows:

<u>range of r</u>	<u>increment in r</u>
0.1 to 7.0 Å	0.1 Å
7.0 to 24.0	0.2

The results of this calculation for $r > 3.0$ Å, including the uncertainty band based on the 50% confidence interval are listed in Table IX.

These functions show three distinct maxima. In order to show the nature of the functions being calculated before the uncertainty band is added, the radial atomic density, $4\pi r^2 \bar{\rho}_h(r)$ is depicted for all six states in Figures 21 and 22. Without the uncertainty bands, it would be extremely difficult to judiciously report the structure. However,

the basic features, the three major peaks, are discernable. (These peaks positions and magnitudes are listed in Table X.) In general, the height of the first peak increases with increasing density from 2.78 to 4.98 atoms/Å. Note that the height of the first peak for Run 4 is lower than the trend with increasing density by Runs 2, 1, 3, 5 and 6, respectively. The ripples at small r are presumed to be spurious.

Before presenting the net radial distribution functions calculated from the divergence corrected intensity functions, it is significant to note that the effects of the divergence correction have a small effect on $h(r)$. In the lower half of Figure 23, the effect of the correction is seen to be so small that the two $h(r)$ curves are almost identical.

The tabularized net radial distribution functions (Table XI) are depicted in Figures 24 and 25. These functions are shown as bands because it is not reasonable to imply that they can be determined more precisely than this. The first zero in $h(r)$ was observed at r of 3.34 ± 0.03 Å, and the first maximum at 3.38 ± 0.06 Å. The height of the first maximum varies from 1.09 to 1.44 over the density range, with Run # 4 lower than the trend. These properties are summarized in Table XI. A second peak is clearly visible and upon closer examination a third peak exists at the higher densities.

However, unexpectedly, the transition region between the first peak and the second is not always smooth. Based on the confidence bands the existence of a secondary feature in this region is probable. This behavior will be discussed later.

The first coordination number, an estimate of the average number of nearest neighbors, was calculated by determining the area under the function $4\pi r^2 [r g(r)]_{\text{sym}}$. The subscript sym means that the function $r g(r)$ was made symmetric at the vertical line through the maximum of the first peak by producing the mirror image of the leading edge as the second half of the peak. The experimental coordination numbers, for Runs 1 to 6 respectively, are 5.1 ± 0.3 , 4.3 ± 0.2 , 5.7 ± 0.2 , 5.3 ± 0.2 , 6.4 ± 0.2 and 6.5 ± 0.2 .

D. Direct Correlation Function

The direct correlation function was calculated from the divergence corrected intensity pattern using Equation (28) for $r > 3.2 \text{ \AA}$ and Equation (29) for $r < 3.2$.

The basic features in $C(r)$ for $r > 3.2$ are not altered by the divergence correction, although the main peak is slightly reduced (See Figure 23). The results (Table 12) are depicted in Figures 22 and 23 for $r > 3.2$. These functions are short-ranged, with no discernable features beyond nine angstroms. Each function rises steeply from the first zero at r of $3.46 \pm 0.03 \text{ \AA}$ to a maximum at $3.91 \pm 0.06 \text{ \AA}$ and then decays somewhat irregularly to zero. With the exception of Run 4, the height of this peak, 1.14 ± 0.05 does not change significantly with increasing density. The peak in Run 4 is 20% shorter (0.91) and broader than the other five peaks. Based on the 50% uncertainty bands, secondary features are evident in the curves for Runs 1, 3, 5 and 6, with $C(r)$ for Run 6 actually going negative.

The low r behavior of $C(r)$ is depicted in Figure 23 (Run 2)

and Figure 28. The error band about $C(r)$ diverges rapidly as r approaches zero. Therefore, the estimate of $C(r)$ at r of zero was obtained by extrapolation. These intercepts decreased rapidly with increasing density from -8.93 to -17.93 at the highest density investigated. The intercepts, first zeros, first maxima, and the value of $C(r)$ at the maxima are summarized for all six thermodynamic states in Table XIII.

E. Percus-Yevick Potential Functions

Once the radial distribution function and the direct correlation functions were known, the potential function predicted by the Percus-Yevick equation was calculated using Equation 34. Since $g(r)$ is presumed to be zero for r less than the hard core diameter, the calculation was made starting at r of 3.0 angstroms. The results of these calculations are depicted in Figure 29. All six functions drop rapidly from over 100°K through zero at r of $3.46 \pm 0.03 \text{ \AA}$ to a negative minimum at r of $3.99 \pm 0.04 \text{ \AA}$ and then rise quite irregularly to zero. The range of the potential function is about 8 angstroms. With the exception of Run # 4, the minimum is well defined. The well depth decreases rapidly with increasing density from $-118.0 \pm 3.5^\circ$ at $\rho = 0.910 \text{ gm/cc}$ to -68.6 ± 2.1 at 1.261 gm/cc . The attractive portions of these functions are quite irregular, with the exception of the curve for the lowest density which remarkably resembles the L-J 12-6 potential ($\sigma = 3.405 \text{ \AA}$, $\epsilon/k = 119.8^\circ\text{K}$). A few features of these potentials are listed in Table XIV.

V. DISCUSSION OF RESULTS

A. Intensity Curves

In April, 1968, Levesque and Verlet¹⁵ published a note, wherein they stated:

"The experimental structure factor $[j(s)$ of Mikolaj and Pings,¹¹ See Figure 30] seems too high for low and intermediate "s". In the high "s" region the oscillations of the experimental structure factor are not regular. This contrasts with the regular behavior of the theoretical structure factor. ...The question can then be raised of the precision of the x-ray scattering experiment..."

These statements were based on molecular dynamic computations of the radial distribution and the P-Y theory. A computer experiment at several densities in the general critical region had been performed in which the validity of the P-Y equation to within 1% had been verified, and then the intensity functions were calculated by Fourier transforming the structure functions. The conclusion that the intensity functions were probably in error by 10% was based not only on the L-J potential (well depth 120°) but also on Kihara potentials (well depths of 143° and 163°). The figure reproduced here was selected as it depicted the largest discrepancy between Verlet¹⁵ and Mikolaj.¹¹

As mentioned earlier, this x-ray experiment was calibrated by repeating the measurement of the scattering function of one of the states investigated by Mikolaj¹⁰ and Honeywell,⁹ the one at 0.910 gm/cc and 143 °K. Because the incident beam was more monochromatic, differences in the two independently measured intensity curves were expected, and there were differences (See Figure 31). If one compares the curves in Figure 31 with those in Figure 30, the improvement in the experiment

can be seen to correct the intensity patterns in just the way to make the new patterns more consistent with the molecular dynamic predictions. The structure factor at low and intermediate s is lower, the right half of the second peak is higher, and the third peak is not changed.

The validity of the truncation of the intensity patterns after the third maximum can be tested by referring to the approximate asymptotic behavior of $i(s)$ empirically correlated by Verlet,¹⁷ namely

$$i(s) \propto \frac{e^{-\alpha s}}{s} \quad (42)$$

where α is on the order of 0.1 for densities near 1 gm/cc. If there was a fourth peak near s of 7.2, its magnitude relative to the height of the third peak at s of 5.4 would be predicted to be

$$\frac{I_4}{I_3} = \frac{e^{-.72}}{7.2} \bigg/ \frac{e^{-.54}}{5.4} = 0.629 \quad (43)$$

or that is, about 63% as large as the third peak. With this fact in mind, the smoothed curves were carefully re-examined. It was not possible to identify a peak of this magnitude in any of the six intensity patterns. Since the inclusion of additional portions of $i(s)$ might decrease the reliability of the transforms, the data were truncated.

The position in s -space of the maximum in $i(s)$ has been predicted from the Percus-Yevick theory and the Lennard-Jones potential as well as for the hard spheres by Verlet,¹⁷ using

$$s_{\max} \left[\text{where } i(s) \text{ a maximum} \right] = \frac{2\pi}{r_0} \quad (44)$$

where r_0 is very close to σ but depends on density (See Figure 32 for the density correlation). Within experimental accuracy, the positions of the maximum in the six intensity patterns produce an r_0 which agrees with this model.

B. Net Radial Distribution Functions

The net radial distribution function for Run # 2 has been compared to the one determined at the same thermodynamic state by Mikolaj and Pings (See Figure 33). The first and second peaks calculated from the intensity pattern obtained in the dual filter experiment are higher and more narrow than the corresponding peaks calculated from the intensity pattern obtained in the β -filter experiment. In addition, the position of the maximum of second peak occurs at a smaller value of r . The other features are remarkably similar.

The net radial distribution function for this thermodynamic state has been predicted by Watts¹⁹ using the Percus-Yevick approximation in conjunction with the Lennard-Jones potential. The numerically predicted function is compared to the experimentally determined function in Figure 34. Within the experimental uncertainty, the functions agree at all values of r , except where the main peak in the predicted function is higher than the main peak in the experimental function. It is possible that a portion of this peak height discrepancy is experimental error. If Verlet's asymptotic prediction for $i(s)$ is

true, then a fourth maxima in the intensity pattern would exist. Gingrich and Tompson in their study of argon scattering near the triple point have pointed out that if the intensity pattern is prematurely truncated, the height of the main peak is reduced and shifted to smaller values of r .

A comparison of the net radial distribution function for Run # 6 with one calculated by Verlet using molecular dynamics is depicted in Figure 35. The densities are the same, but the molecular dynamics experiment was carried out at 128.19 °K. The height of the main peak in this thermodynamic region is sensitive to temperature. Therefore, only the other features, which agree well, can be quantitatively compared. If the temperature of the molecular dynamics experiment was lowered to agree with the one measured here, the height of the first peak would increase and the position of the maximum would shift to larger values of r .

The presence of a small subsidiary maximum located between the first and second peaks in $h(r)$ has been the subject of considerable discussion. This maximum was reported by Eisenstein and Gingrich,⁸ and also by Honeywell,⁹ but not by Mikolaj¹¹ when he reprocessed Honeywell's data. Finbak,⁵⁷ after analyzing several monatomic fluids, concluded that this maximum was spurious and caused by experimental errors in the intensity data. In a comprehensive analysis of transforms of $i(s)$ and $g(r)$, Kahn⁵⁸ stated the major cause of this irregularity in the distribution function was inherent in the experimental intensity curves and not the truncation error. If the truncation error is not responsible, and if no systematic error has been perpetrated, then the radial

distributions that have been presented for Runs 1, 3 and 5 must contain a subsidiary feature.

Further insight to this question can be gained by reviewing three radial distribution functions calculated by Fehder²¹ using two dimensional molecular dynamics (See Figures 36, 37 and 38). The two dimensional relative packing densities, 0.5406, 0.6237 and 0.7274, almost spans the relative packing density of the six argon states which extends from 0.565 to 0.776. At the lowest packing density (0.5406) a subsidiary feature between 5.2 and 6.2 Å is evident. At the intermediate packing density, the transition between the first peak and the second peak is not symmetrical enough to argue that a subsidiary feature is not evident, whereas, at the highest relative packing density the transition region is quite symmetrical and bowl-like. The secondary feature is thus seen to be density dependent.

There is one additional state dependent feature in the two dimensional molecular dynamic radial distribution functions that should be observed. The height of the first peak in these states does not increase uniformly as the density increases and the temperature decreases.

<u>Temperature</u>	<u>Density</u>	<u>Peak height in $g(r)$</u>
137.56 °K	0.5406	2.42
132.12 °K	0.6237	2.35
120.74 °K	0.7274	2.55

This is quite similar to the behavior of the lower peak height of Run 4 relative to the increasing peak height of the other five states.

C. Direct Correlation Functions

The experimental direct correlation function is defined by

the transform of $i(s)/(1 + i(s))$ given in Equation (28). If this kernel were used to calculate the low r behavior of $C(r)$ spurious ripples would appear, ripples whose amplitudes increase as r decreases. The technique developed by Mikolaj and Pings, expressed by Equation (29), significantly improves the subatomic behavior of $C(r)$ (See Figure 39).

The calibration experiment, comparing Run 2 with the same state measured by Mikolaj,¹⁰ indicates significant changes in $C(r)$ result from the improvement in the monochromatization of the incident beam (See Figure 40). The first peak height is higher, the leading edge of this peak is steeper and the subatomic values of $C(r)$ are lowered significantly (See Figure 40). In addition, there is a suggestion of subsidiary structure in the trailing edge of the first peak that did not appear in the 13 β -filter investigations of Mikolaj and Pings.¹³

Two of the direct correlation functions, Runs 2 and 1, at the lowest densities are compared with those analytically predicted by Watts from the P-Y approximation (See Figures 41 and 42). The magnitudes of the two main peaks in the experimental direct correlation functions are smaller than the predicted magnitudes and the positions of the experimental maxima are at larger values of r . However, the pairs of curves are quite similar. In particular, the estimated behavior of $C(r)$ at small r agrees in magnitude and shape with the analytical curves.

D. Percus-Yevick Potential Functions

In their published note on the intensity patterns of Mikolaj and Pings,¹¹ Levesque and Verlet¹⁵ claimed on the basis of their molecular dynamics calculations, that the P-Y equation was applicable in the general vicinity of the critical region. The calculated P-Y potential for Run 2 closely resembles the L-J potential (See Figure 43). In addition to this, the experimental $h(r)$ and $C(r)$ agree with Watts' functions that were predicted from the P-Y equation and the L-J potential. The internal consistency of this experimental state with the Watts' study, plus the molecular dynamics work, all support the validity of the Percus-Yevick equation at densities around the critical state.

The significant density effect on the predicted P-Y potential function along with the density effect predicted by Mikolaj and Pings is depicted in Figure 44. Two curves are not expected to be colinear since the former was based on the dual filter and the latter on the β -filter monochromator. Since the radial distribution functions calculated from the dual filter experiments are more sharply defined than the β -filter distributions, the well depths for this work are much deeper. However, the significant fact is that the well depth decreases significantly with increasing density, which means that the Percus-Yevick equation can not be applied in the high-density-low-temperature region of the PVT diagram. Since only one measurement was made at each density, no statement about the slope of this line being independent of temperature can be made. The well depth of Run 4 does not follow the

trend of the other five. This is consistent with the fact that the height of the first peak of $h(r)$ for Run 4 is lower than the trend indicated for the other five densities.

E. First Coordination Numbers

The use of the radial distribution function, $g(r)$ to compute a coordination number for argon has been discussed by Mikolaj and Pings¹⁴ for four different methods:

<u>Method</u>	<u>Description</u>
A	symmetrizing the first peak in $r g(r)$
B	symmetrizing the first peak in $r^2 g(r)$
C	decomposition of $r^2 g(r)$ into shells
D	computation of the area to the first minimum in $r^2 g(r)$

The magnitude of the first coordination number depends on which method was used to compute it. Successively larger values would be predicted for the different methods from A to D respectively. The first coordination numbers calculated by Method A for the six states investigated correlate well with the results published by Mikolaj and Pings (See Figure 45).

VI. CONCLUSION

One approach to the understanding of the properties of fluids is based on attempts to calculate the radial distribution function, $g(r)$. For simple molecular fluids an accurate knowledge of $g(r)$ for all temperatures and densities and accurate knowledge of the state-independent intermolecular potential function would provide the thermodynamic properties, via the volumetric equation of state and the caloric equation of state:

$$P = \rho kT - \frac{\rho^2}{6} \int_0^{\infty} g(r) r \frac{du(r)}{dr} 4\pi r^2 dr \quad (45)$$

$$U = \frac{3}{2} N_0 kT - \frac{N_0}{2} \rho \int_0^{\infty} g(r) u(r) 4\pi r^2 dr \quad (46)$$

where U is the internal energy per mole and N_0 is Avogadro's number.

Efforts are being made to determine $u(r)$ from a diffraction experiment.⁵⁹ Once this function is available, the radial distribution functions determined in this work will be used to evaluate the thermodynamic properties of argon in the liquid region.

However, the significant breakthrough will not come until a theory of fluids is developed that will predict $g(r)$ and $C(r)$ from the pair potential, at which time, the complete thermodynamic properties will be derivable from the pair potential.

It is to this end that this experiment was performed: the radial distribution functions and the direct correlation functions

must be known at a few states in the liquid region before theories can be demonstrated to be valid. Within this framework several conclusions have been drawn.

1. Since the well-depths of the pair potentials (predicted by substituting the experimental distribution functions into the Percus-Yevick equation) are state dependent, the P-Y equation rapidly becomes invalid as the density increases from 0.910 to 1.261 gm/cc. The fact that the predicted potential at 0.910 gm/cc closely resembles the Lennard-Jones potential for argon probably implies, in correlation with Verlet's work, that the limiting density for using the P-Y equation is near 0.910 gm/cc.

2. The radial distribution functions for argon contain secondary features between the first two main peaks. Since this fact has been previously contested in the literature, it is significant to note that the technique of calculating confidence bands about $g(r)$ firmly resolves this question. The existence of these peaks has been suggested by Fehder's molecular dynamics calculations, by Monte Carlo calculations and by early solutions of the Yvon-Born-Green equation.

3. Secondary features are observed on the right shoulder of the main peak in the direct correlation function. This is the first evidence of this behavior for a van der Waals fluid.

4. This study indicates that the structure of liquid argon near a density of 1.116 gm/cc and 127.05 °K may be anomalous. The maximum in $g(r)$ is lower than the trend of neighboring density-state distribution

functions. The first maximum in $i(s)$ is lower than the trend in density, and the width of the third peak is greater than others at lower and higher densities.

5. Confidence bands about the smoothed intensity functions have been used with care to show that a fourth peak in the intensity kernel is not detectable. Within the accuracy of the data and the data reduction scheme, the validity of the asymptotic form of $i(s)$ proposed by Verlet is dubious.

Several other conclusions which relate more to the experimental technique are noted.

6. Within the arguments given here, the atomic scattering factor for argon given by Berghuis et. al. seems to be more reasonable than other factors used by different investigators. Quantitative comparisons of structure functions determined by two different x-ray investigators should not be made unless the effect of probably different structure factors is eliminated.

7. The accuracy of $C(r)$ at low r is directly related to increasing the accuracy of $i(s)$ at low s . To accomplish this, divergence of the incident and scattered beam must be minimized.

REFERENCES

1. D. G. Henshaw, D. G. Hurst, and N. K. Pope, Phys. Rev. 92, 1229(1953).
2. D. G. Henshaw, Phys. Rev. 105, 976(1957).
3. B. A. Dasannacharya and K. R. Rao, Phys. Rev. 137, A417(1965).
4. A. Eisenstein and N. S. Gingrich, Phys. Rev. 58, 307(1940).
5. K. Lark-Horowitz and E. P. Miller, Nature 147, 460(1940).
6. N. S. Gingrich and C. W. Tompson, J. Chem. Phys. 36, 2398(1963).
7. R. W. Harris and G. T. Clayton, Phys. Rev. 153, 229(1967).
8. A. Eisenstein and N. S. Gingrich, Phys. Rev. 62, 261(1942).
9. W. I. Honeywell, "X-Ray Diffraction Studies of Dense Fluids," doctoral thesis, California Institute of Technology, Pasadena, California(1964).
10. P. G. Mikolaj, "An X-Ray Diffraction Study of the Structure of Fluid Argon," doctoral thesis, California Institute of Technology, Pasadena, California(1965).
11. P. G. Mikolaj and C. J. Pings, J. Chem. Phys. 46, 1401(1967).
12. Tables of intensity patterns and structure functions can be found in:
H. L. Frisch and Z. W. Salsburg, Simple Dense Fluids, Academic Press, N. Y.(1968).
13. P. G. Mikolaj and C. J. Pings, J. Chem. Phys. 46, 1412(1967).
14. P. G. Mikolaj and C. J. Pings, J. Phys. and Chem. of Liq. 1, 93(1968).
15. D. Levesque and L. Verlet, Phys. Rev. Letters 20, 905(1968).
16. L. Verlet, Phys. Rev. 159, 98(1967).
17. L. Verlet, Phys. Rev. 165, 201(1968).
18. L. Verlet, Physica 30, 95(1964).
19. R. O. Watts, The Percus Yevick Approximation Applied to Argon, preprint, personal communication(1963).

20. R. O. Watts, personal communication, tables of functions depicted in reference 19 (1968).
21. P. L. Fehder, "Microscopic Properties of Dense Fluids," doctoral thesis, California Institute of Technology, Pasadena, California(1969).
22. N. S. Gingrich, Rev. Mod. Phys. 15, 90(1943).
23. K. Furukawa, Rept. Progr. Phys. 25, 395(1962).
24. R. F. Kruh, Chem. Rev. 62, 319(1962).
25. R. W. James, The Optical Principles of the Diffraction of X-Rays, G. Bell and Sons, London, England(1962).
26. V. N. Filipovich, Soviet Phys.-Tech. Phyd. 1, 391, 409(1956).
27. H. H. Paalman and C. J. Pings, Rev. Mod. Phys. 35, 398(1963).
28. B. D. Cullity, Elements of X-Ray Diffraction, Addison-Wesley Pub. Co., Inc., Reading, Mass.(1956).
29. L. S. Ornstein and F. Zernicke, Proc. Acad. Sci. (Amsterdam) 17, 793(1914).
30. M. E. Fisher, J. Math. Phys. 5, 944(1964).
31. L. Goldstein, Phys. Rev. 84, 466(1951).
32. A. Reetz and L. H. Lund, J. Chem. Phys. 26, 518(1957).
33. P. Hutchinson, Disc. of the Faraday Society 43, 53(1967).
34. J. K. Percus and G. J. Yevick, Phys. Rev. 110, 1(1958).
35. J. K. Percus, in "The Equilibrium Theory of Classical Fluids," K. L. Frisch and J. L. Lebowitz, Eds. (W. A. Benjamin, Inc., New York, 1964), p.II 33.
36. D. A. Copeland and N. R. Kestner, Accurate "Effective" Intermolecular Pair Potentials in Gaseous Argon, preprint, personal communication (1968).
37. W. Parrish, "X-ray Intensity Measurements with Counter Tubes," Philips Technical Review 17, 206(1956).

38. J. M. H. Levelt, "Measurements of the Compressibility of Argon in the Gaseous and Liquid Phase," doctoral thesis, Amsterdam (1958). This work also reported in A. Michels, J. M. H. Levelt and G. J. Wolkers, *Physica* 24, 769(1956).
39. A. Van Itterbeek, O. Verbeke and K. Staes, *Physica* 29, 742(1963).
40. International Tables for X-ray Crystallography, Vol. III, ed. by C. H. MacGillavry and G. D. Rieck, The International Union of Crystallography (Kynock Press, Birmingham, England, 1962).
41. H. H. Paalman and C. J. Pings, *Rev. Sci. Instr.* 33, 496(1962).
42. W. I. Honeywell, C. M. Knobler, B. L. Smith and C. J. Pings, *Rev. Sci. Instr.* 35, 1216(1964).
43. C. B. Walker, *Phys. Rev.* 103, 558(1956).
44. D. R. Chipman and L. D. Jennings, *Phys. Rev.* 132, 728(1963).
45. G. Breit, *Phys. Rev.* 27, 362(1926).
46. P. A. M. Dirac, *Proc. Roy. Soc. (London)* 111A, 405(1926).
47. J. E. Thomas and P. W. Schmidt, *J. Chem. Phys.* 39, 2506(1963).
48. H. H. Paalman and C. J. Pings, *J. Appl. Phys.* 33, 2635(1962).
49. J. A. Victoreen, *J. Appl. Phys.* 20, 1141(1949).
50. D. R. Chipman and L. D. Jennings, *Phys. Rev.* 132, 728(1963).
51. L. Lapidus, Digital Computation for Chemical Engineers, McGraw-Hill Book Co., N. Y. (1962).
52. A. J. Freeman, *Acta. Cryst.* 13, 190(1960).
53. D. T. Cromer and J. B. Mann, *J. Chem. Phys.* 47, 1892(1967).
54. J. Berghuis, I. M. Haanappel and M. Potters, *Acta. Cryst.* 8, 478(1955).
55. D. T. Cromer, *Acta. Cryst.* 18, 17(1965).
56. A. Rahman, *J. Chem. Phys.* 10, 3540(1965).
57. C. Finbak, *Acta. Chem. Scand.* 3, 1293(1949).
58. A. A. Kahn, *Phys. Rev.* 136, A367(1964).

59. C. J. Pings, Disc. of the Faraday Society 43, (1967).

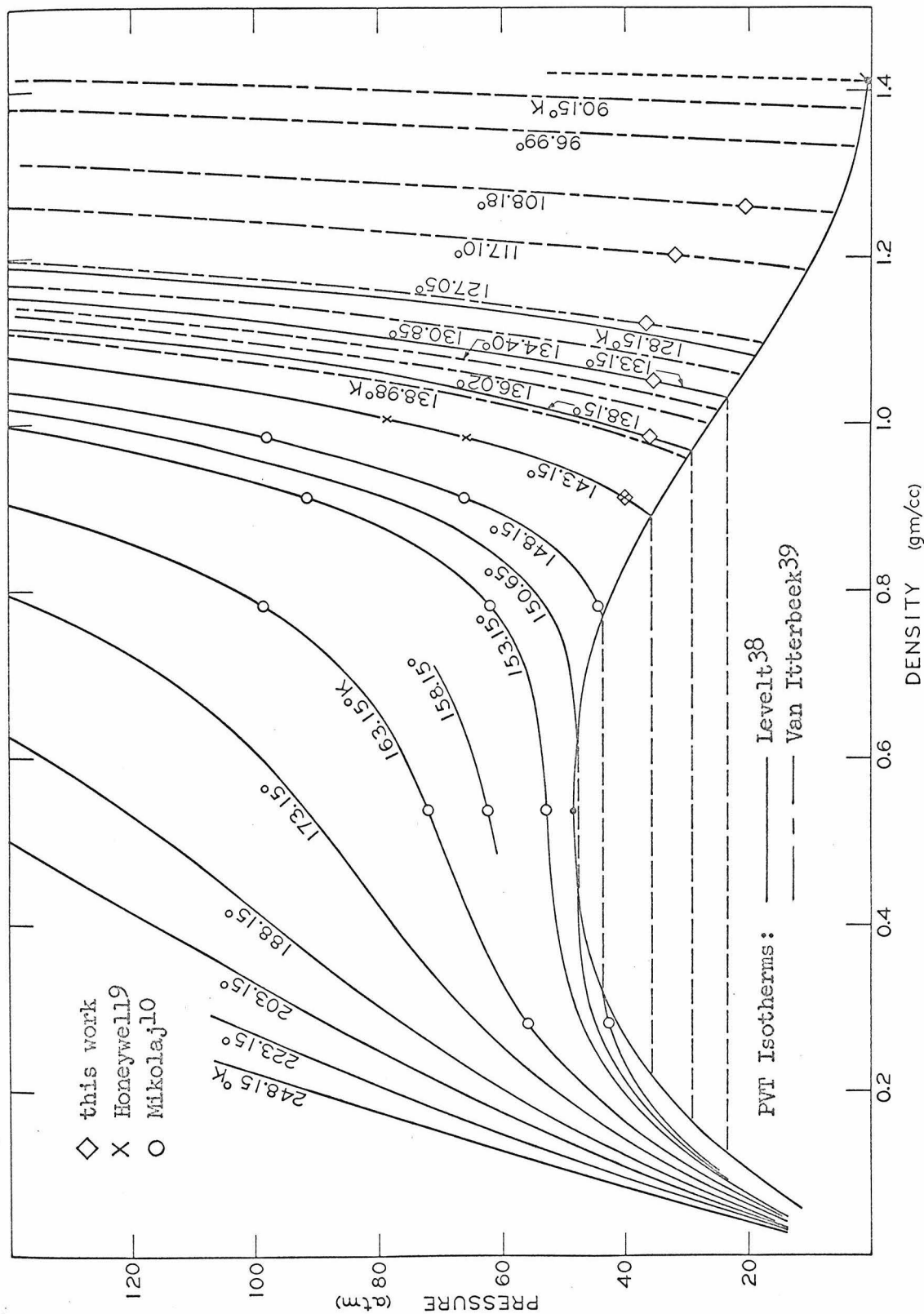


Figure 1. Argon P, ρ , T Diagram Showing Locations of the Experimental States

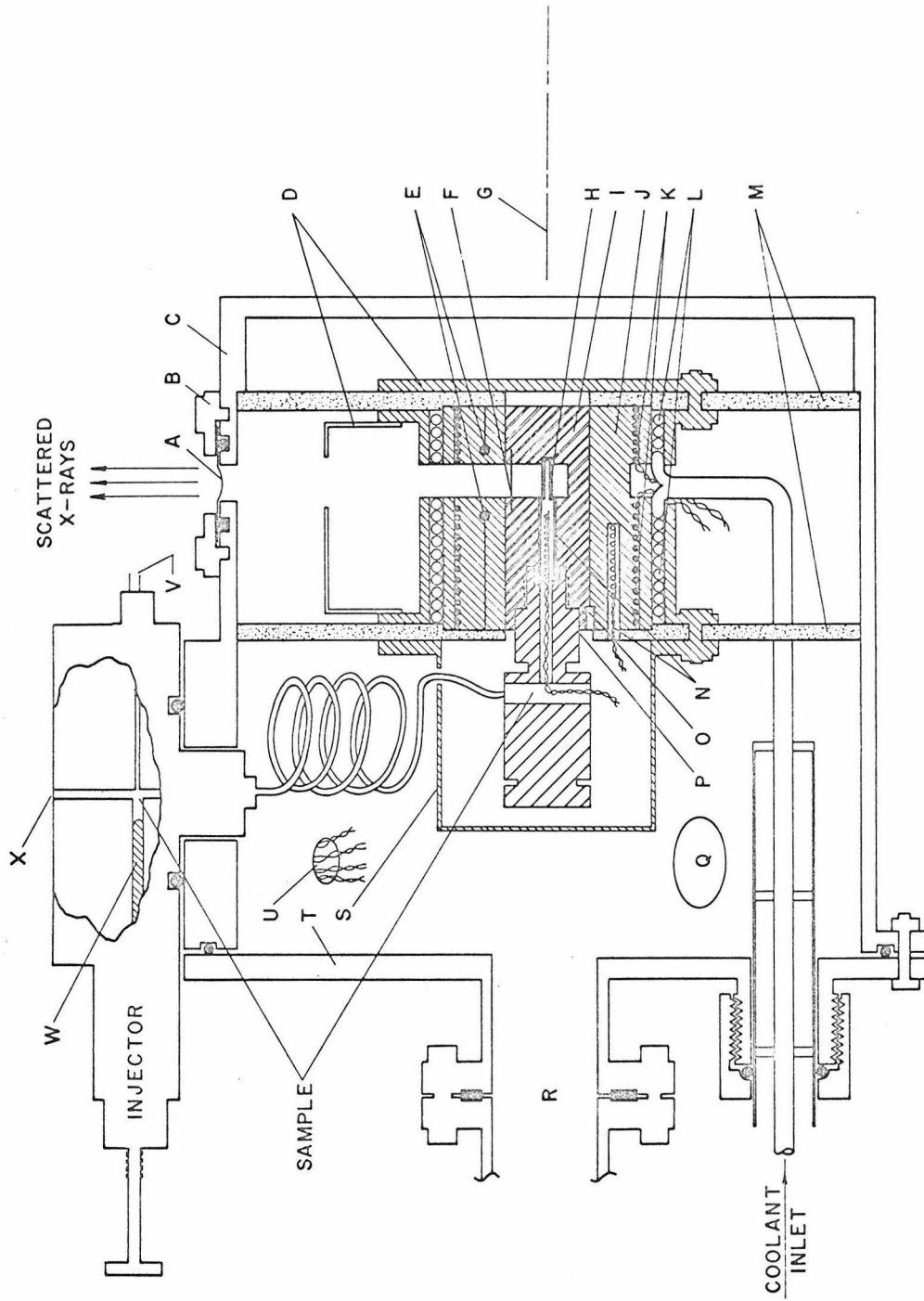


Figure 2. Cross Section of Cryostat

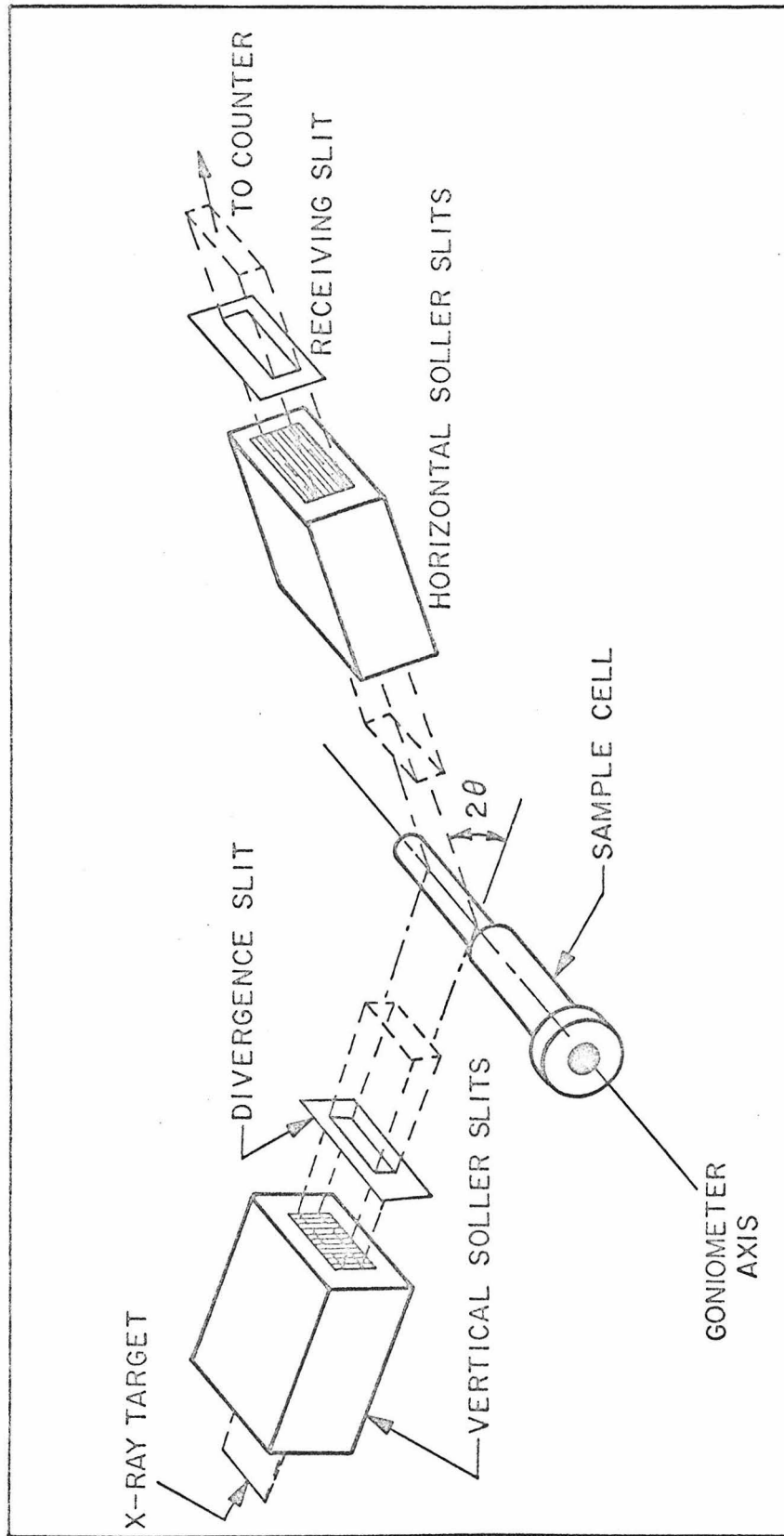


Figure 3. Pictorial Illustration of the X-Ray Optical System (Figure taken from Mikolaj¹⁰)

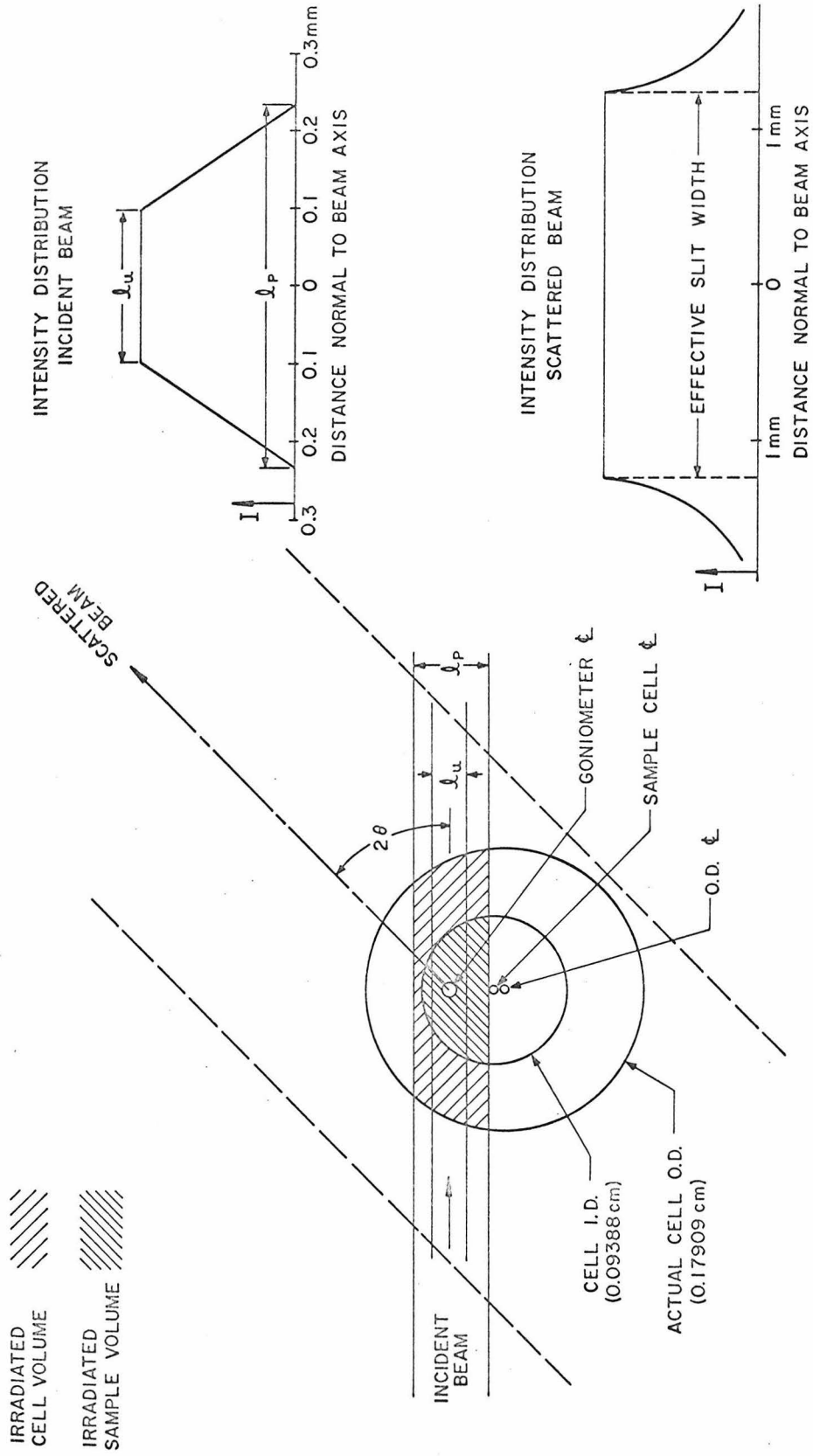


Figure 4. Scattering Geometry used in the Argon Experiments

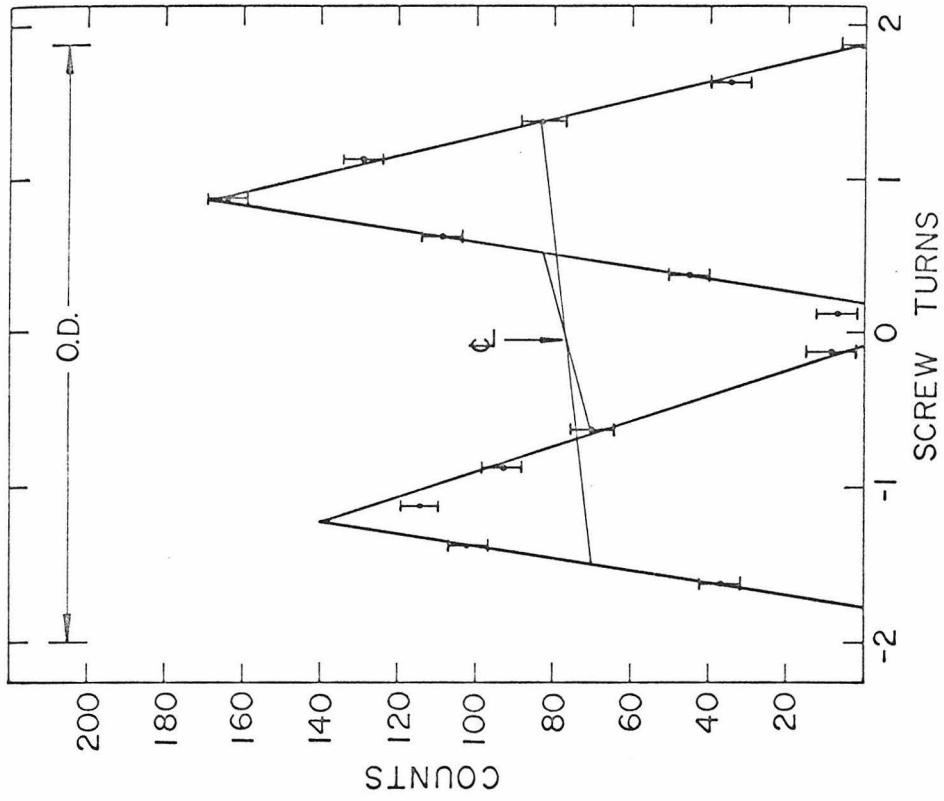


Figure 6. Horizontal Cell Alignment Data

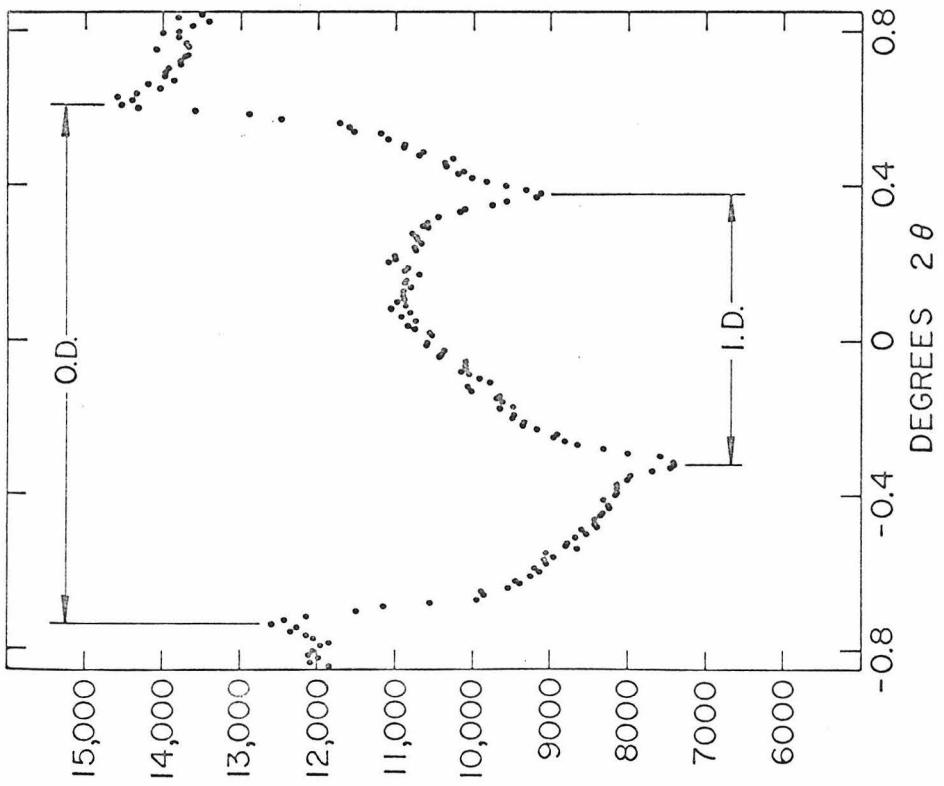


Figure 5. Vertical Cell Alignment Data

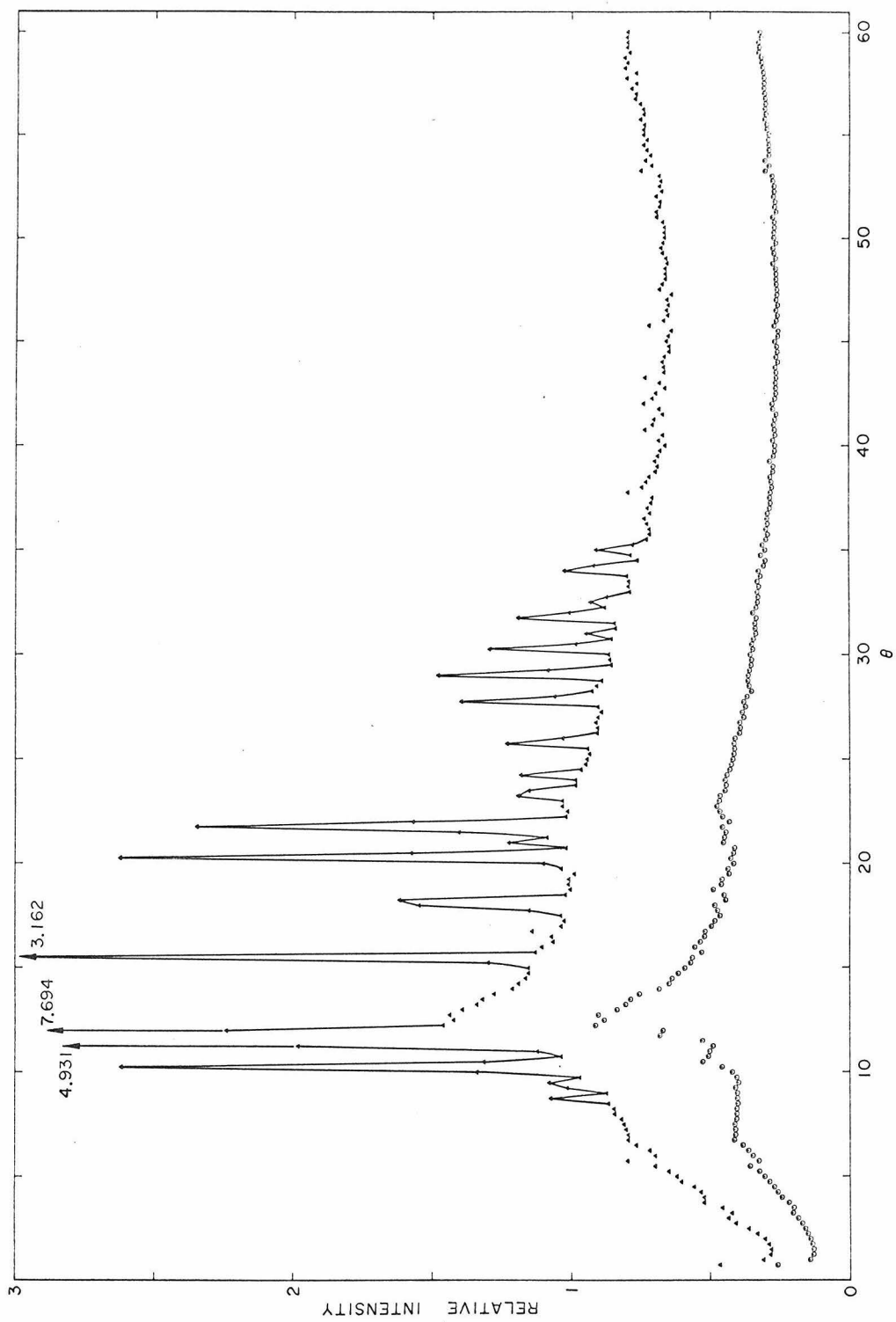


Figure 7. Normalized Cell Scattering Intensity for One Scan (Δ , β -Filter Intensity; \circ , α -Filter Intensity)

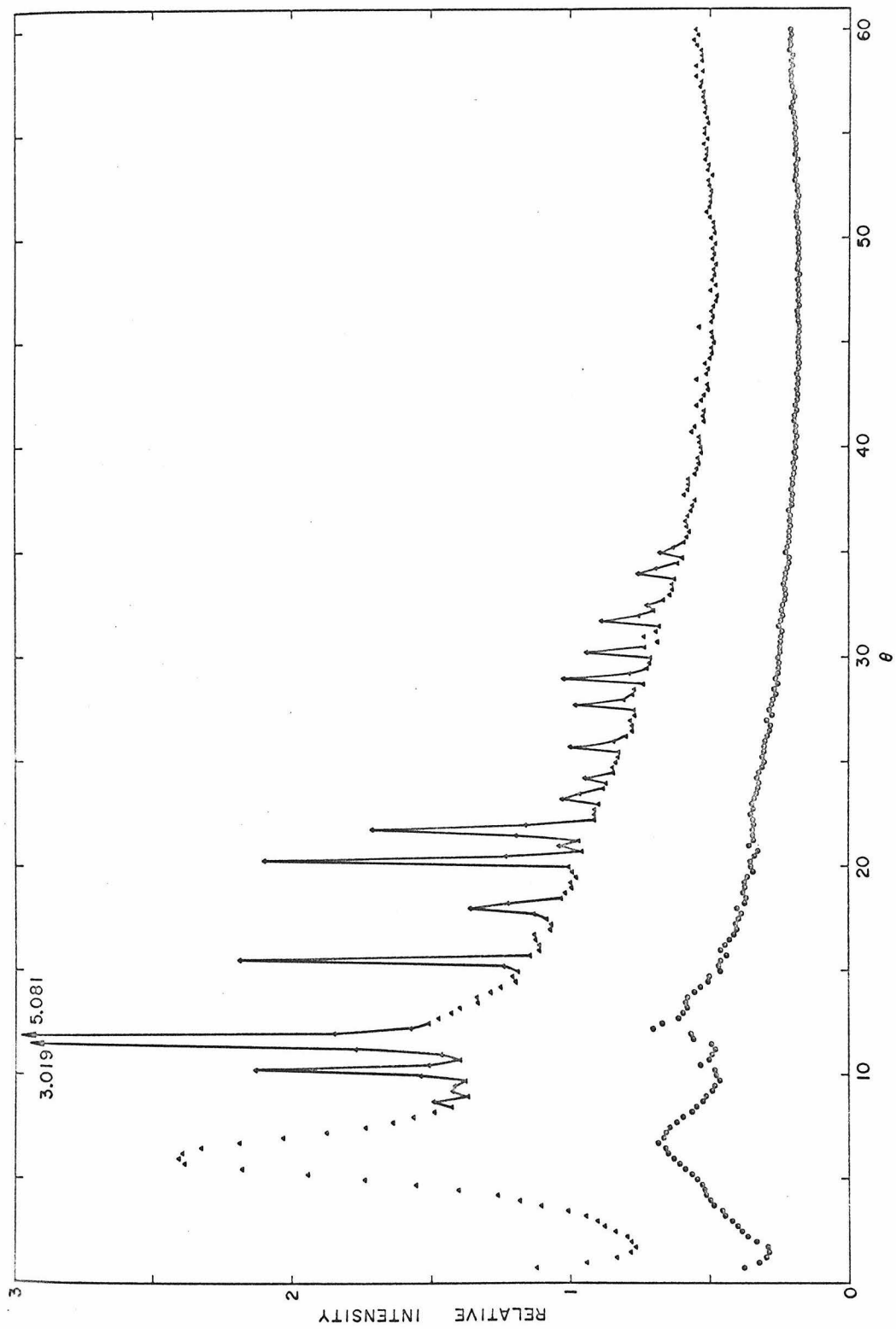


Figure 8. Normalized Cell and Sample Scattering Intensities for One Scan (Δ , β -Filter Intensity; \circ , α -Filter Intensity)

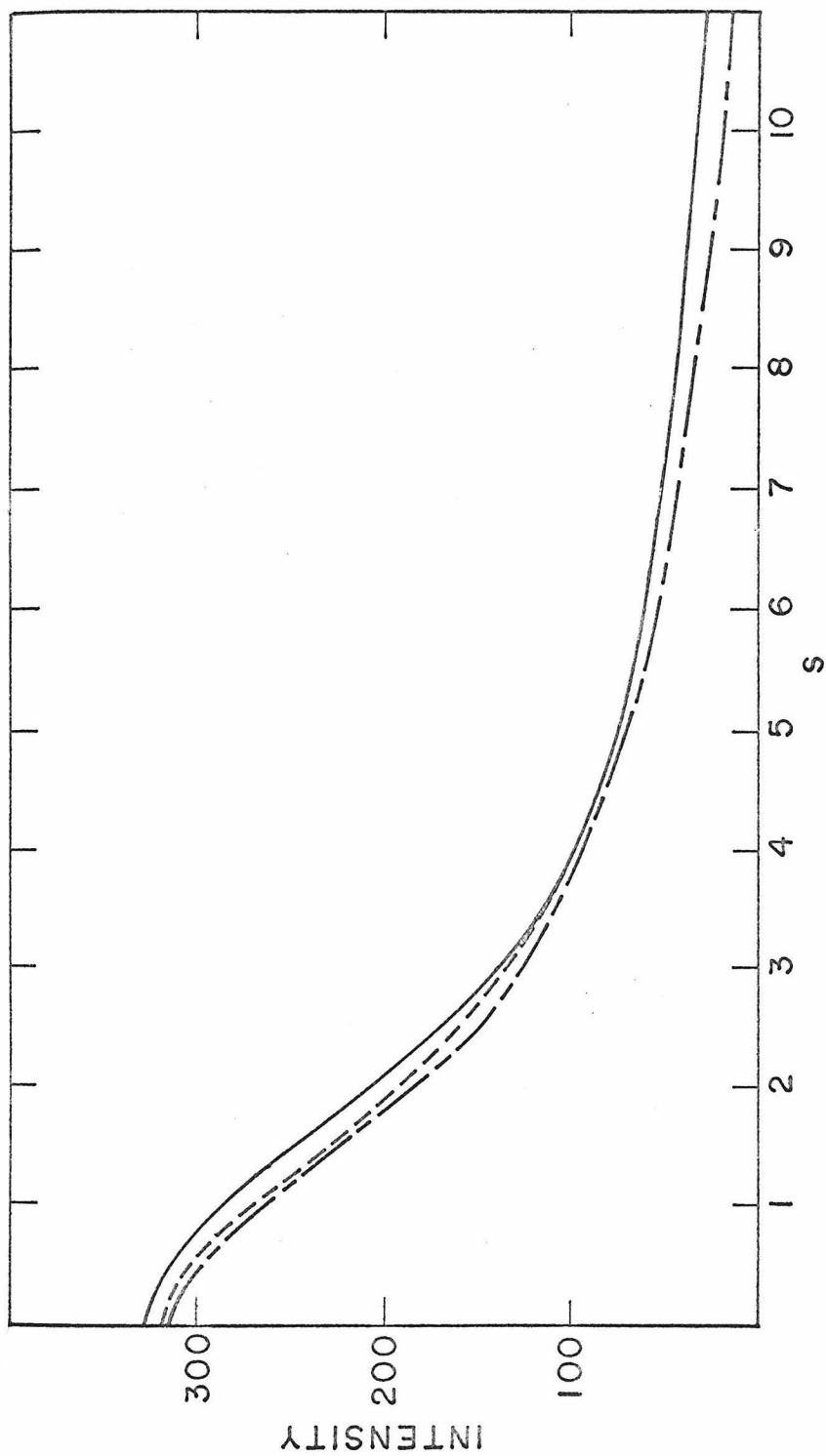


Figure 9. Comparison of Atomic Scattering f_d^2 , for Ag Kx Radiation. ——— Gingrich and Tompson⁶; - - - Lark-Horowitz and Miller⁵; - · - f_d^2 Berghuis et. al.⁵⁴ with $\Delta f' = 0.13$ and $\Delta f'' = 0.1655$

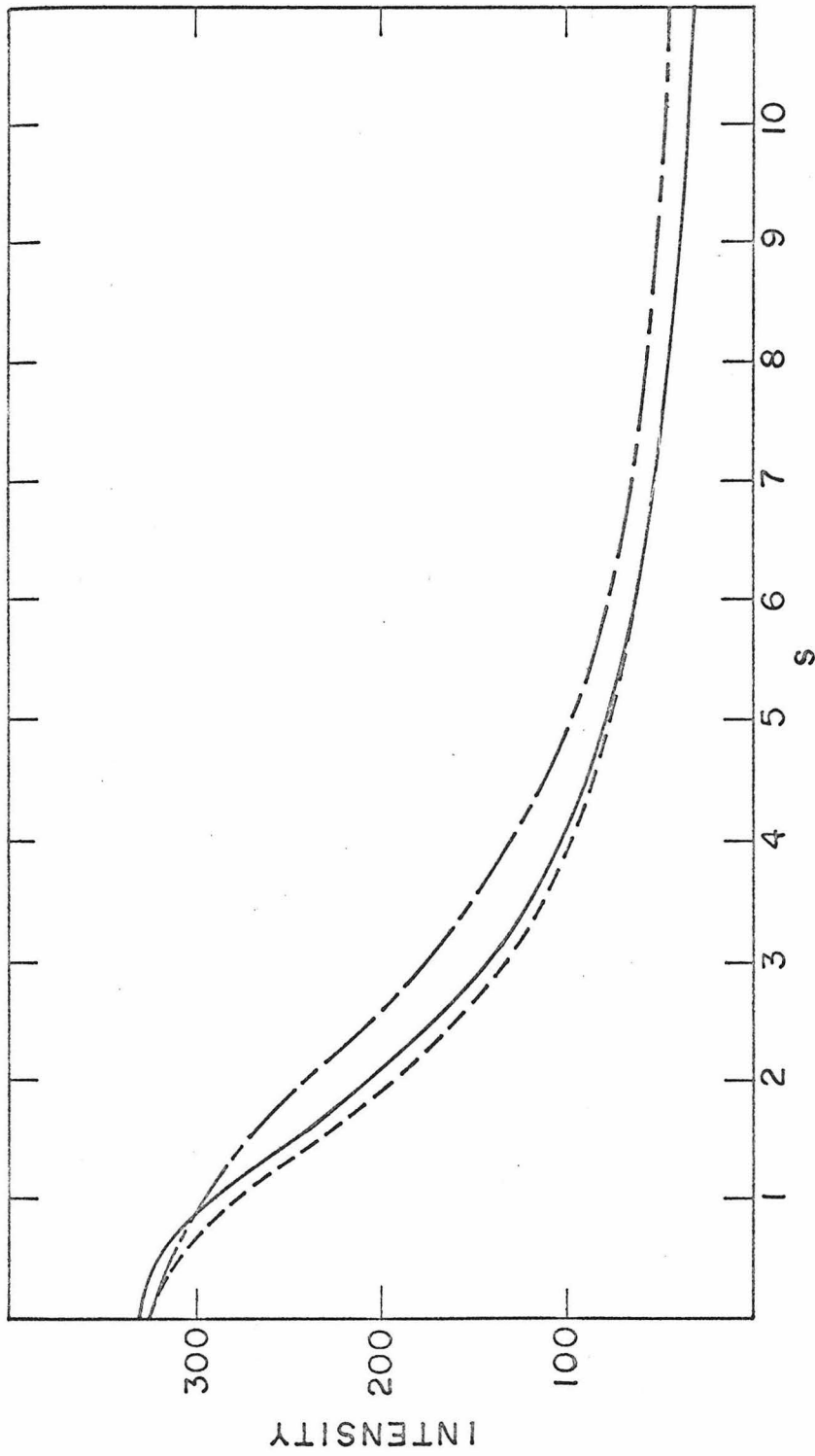


Figure 10. Comparison of Atom Scattering, f_d^2 , for Mo K α Radiation. --- Eisenstein and Gingrich⁸; - - - Harris and Clayton⁷; - - - f_d^2 Berghuis et. al.⁵⁴ with $\Delta f' = 0.18$ and $\Delta f'' = 0.24$ ⁵⁵

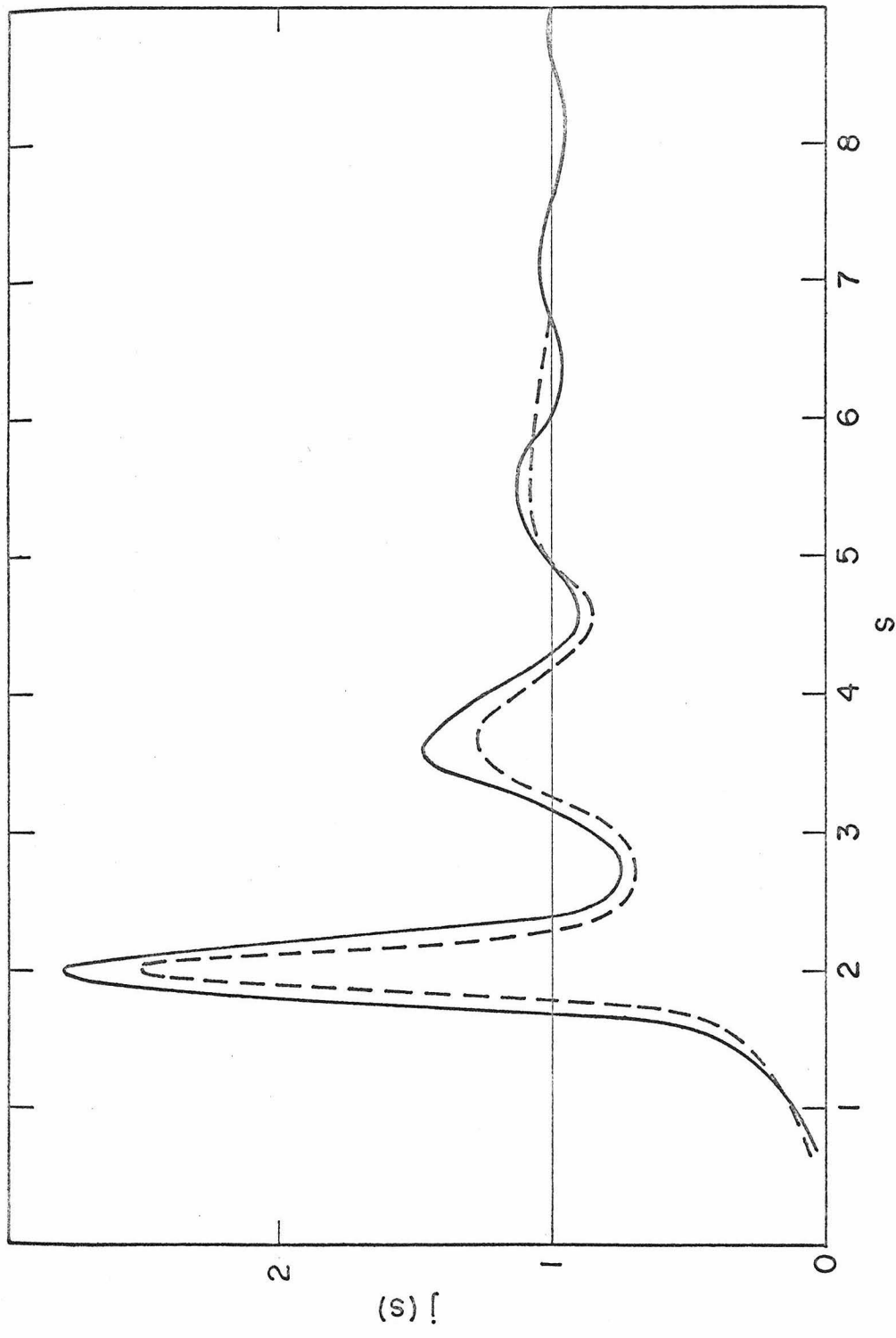


Figure 11. Experimental $j(s)$: --- Henshaw² with Neutrons: — Gingrich and Tompson⁶ with X-Rays. Figure taken from Rahman⁵⁶

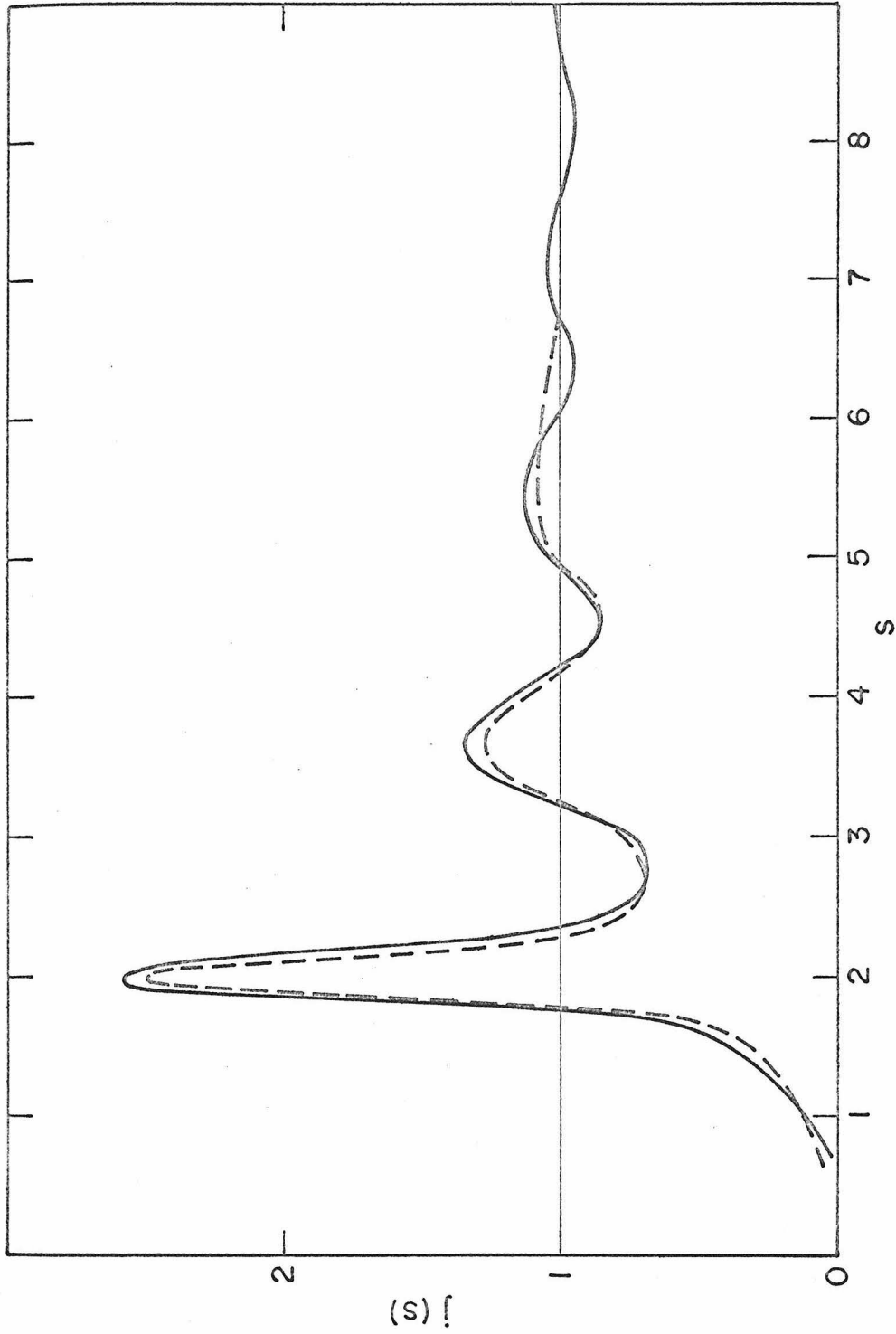


Figure 12. Experimental $j(s)$: — Henshaw² — — Estimated from Gingrich and Tompson⁶ data using f_d^2 from Berghuis et. al.⁵⁴ with $\Delta f' = 0.13$ and $\Delta f'' = 0.1655$

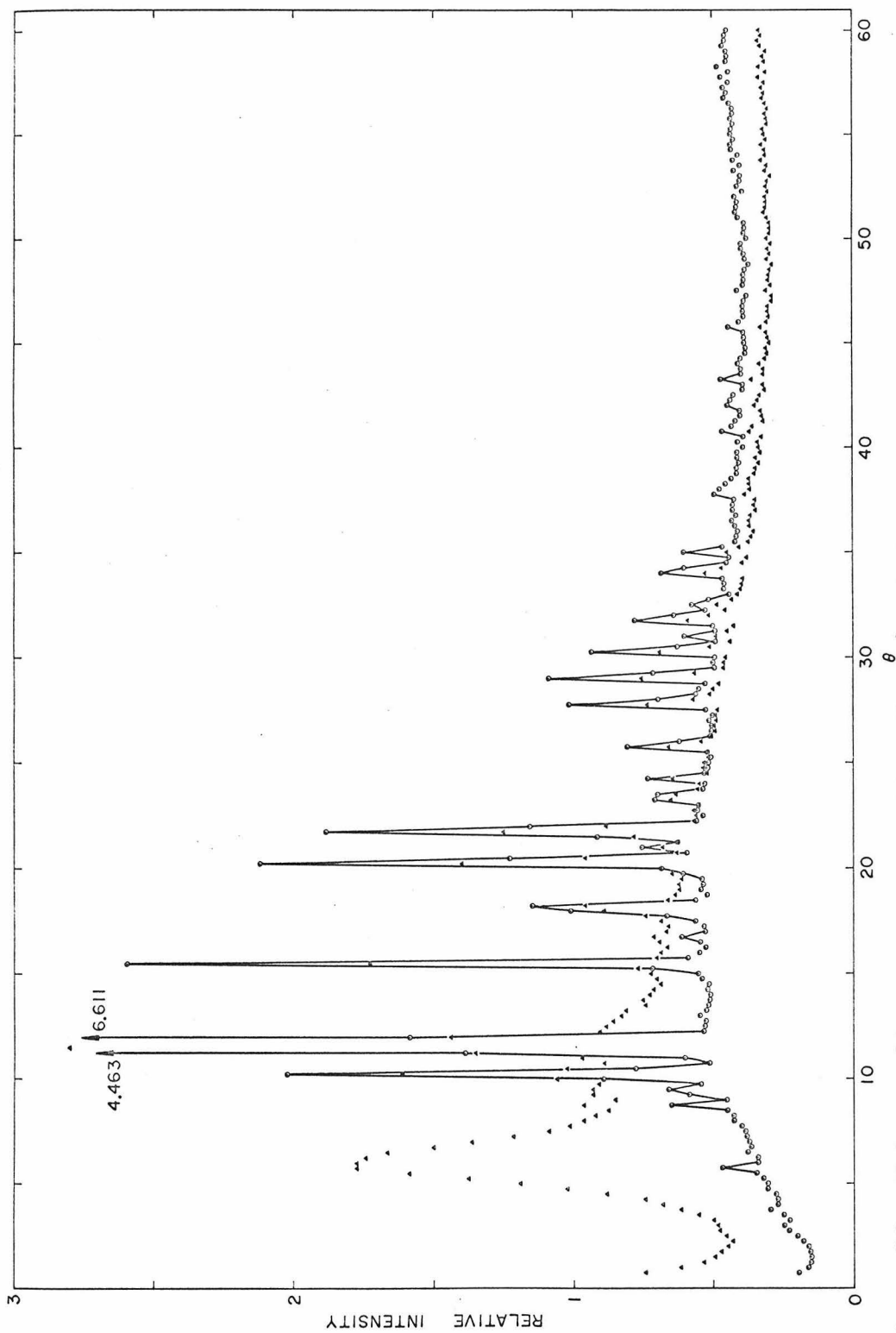


Figure 13. Net Normalized Scattering Intensities (A, β -Filter Intensity Minus α -Filter Intensity, Average for Three Scans of Cell and Sample; O, β -Filter Intensity Minus α -Filter Intensity, Average for Five Scans of Cell)

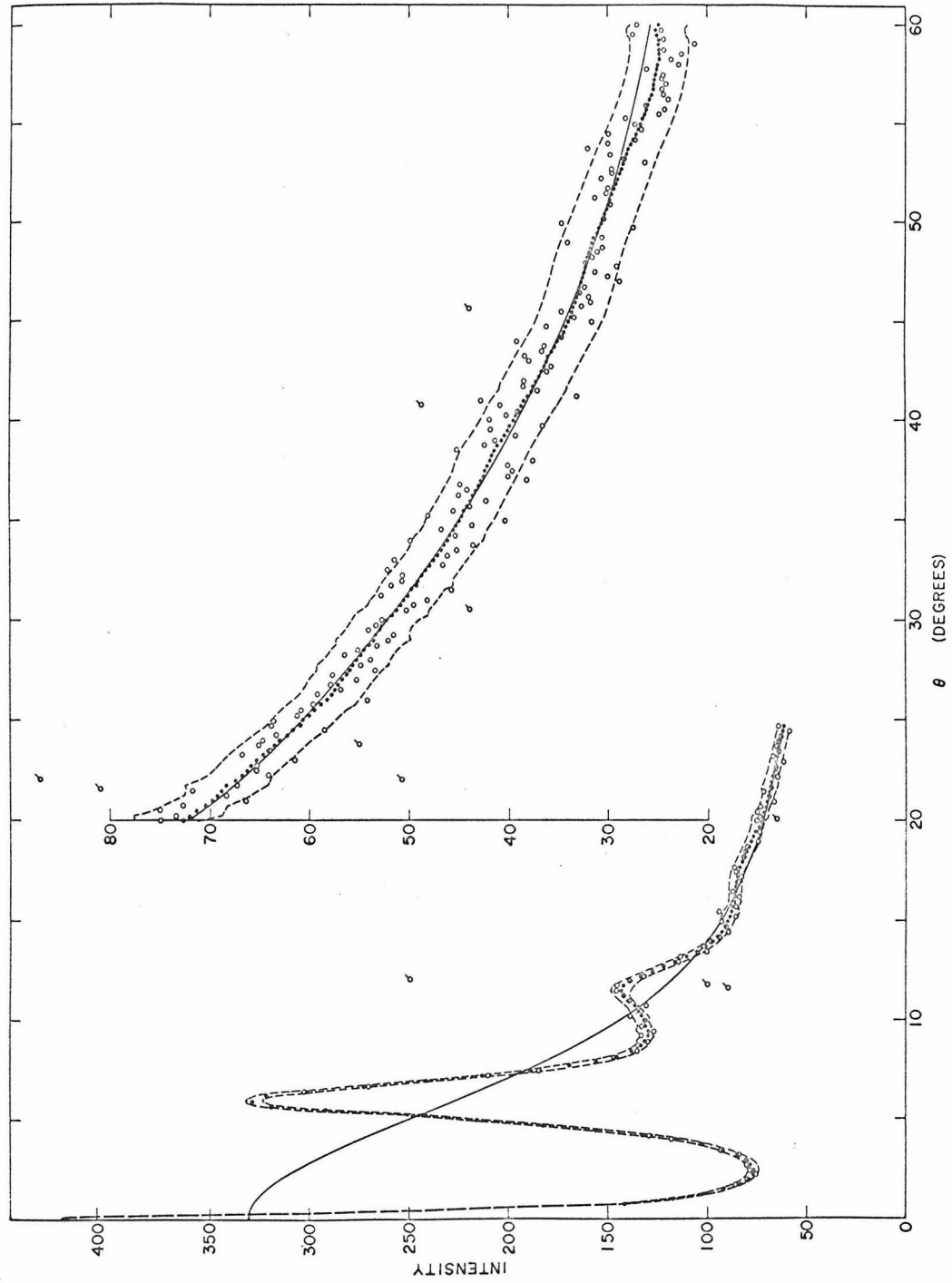


Figure 14. Argon Scattering Curve for Run No. 2 with the 90% Confidence Interval, Scaled to the Total Gas Scattering Function (\bullet , Preliminary Estimate of the Sample Intensity; \circ , Data; \circ , Rejected Data; --- Confidence Interval; — — Extrapolation)

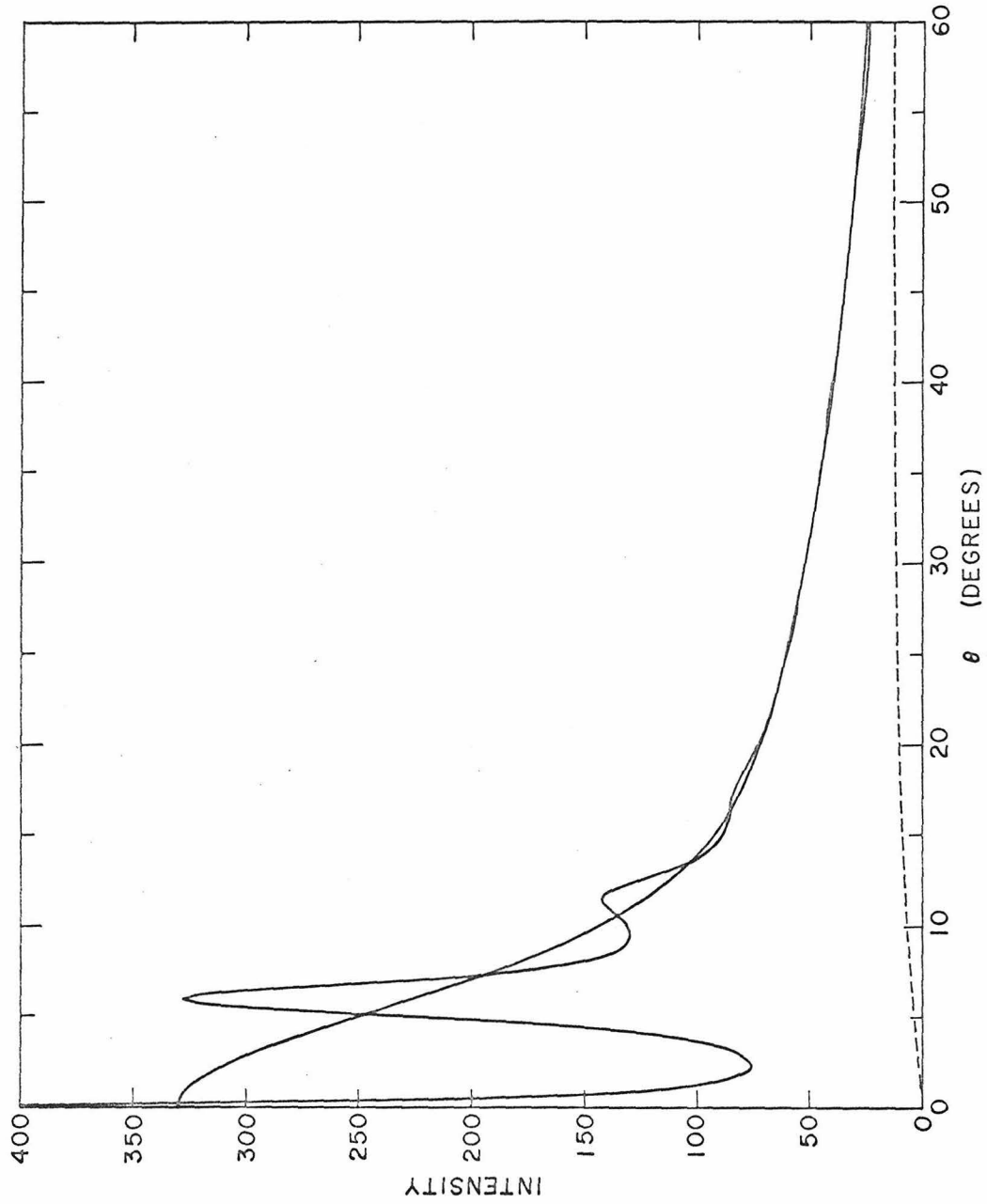


Figure 15. The Normalized Scattering Curve for Argon Run No. 2, before the Divergence Correction (----- Indicates the Incoherent Portion of the Total Gas Scattering Function)

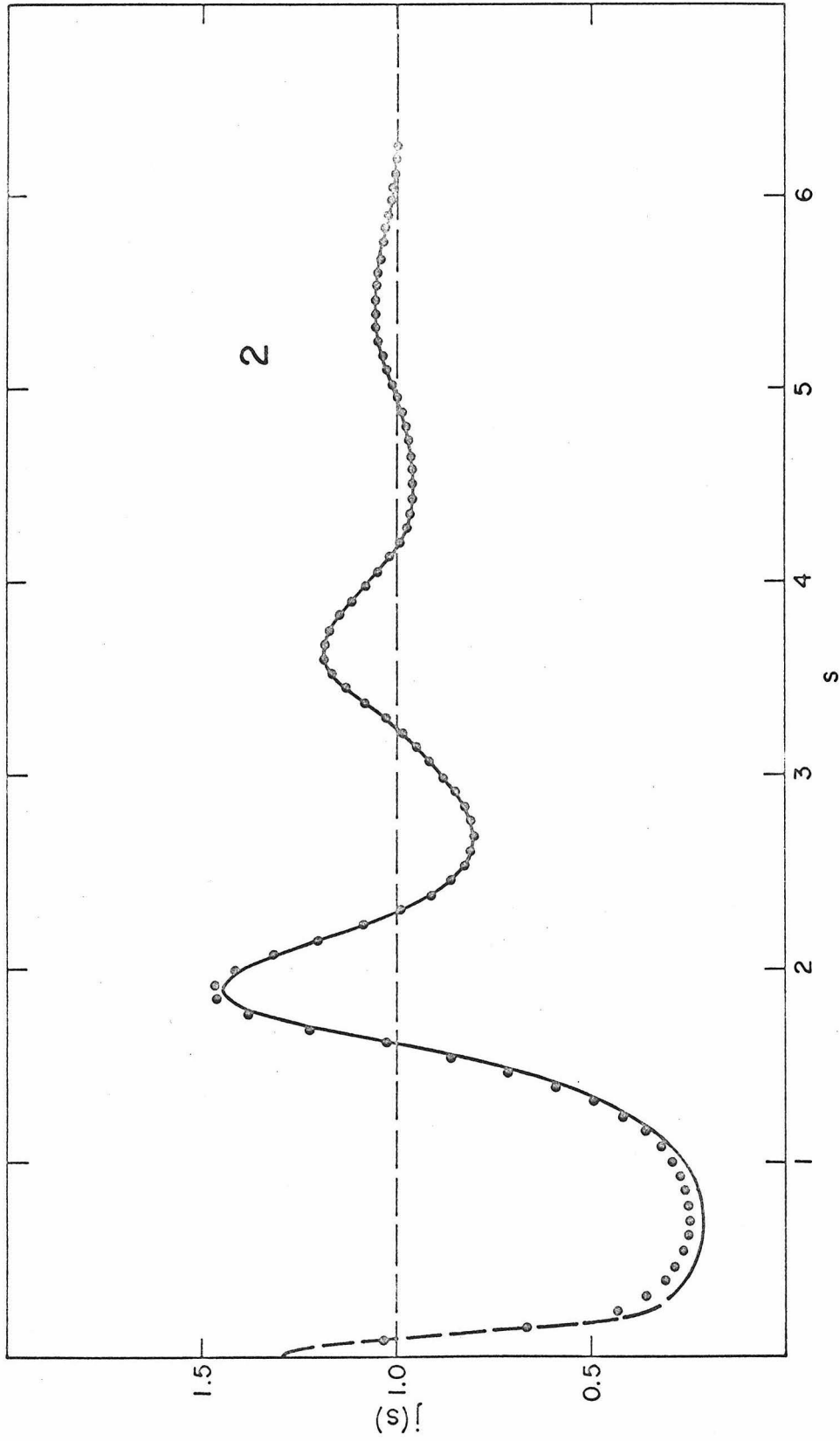


Figure 16. The Argon Intensity Function $j(s)$ depicting the Divergence Correction for Argon Run No. 2 (•, before the correction; — after the Divergence Correction; — — — Extrapolation to the Compressibility Limit)

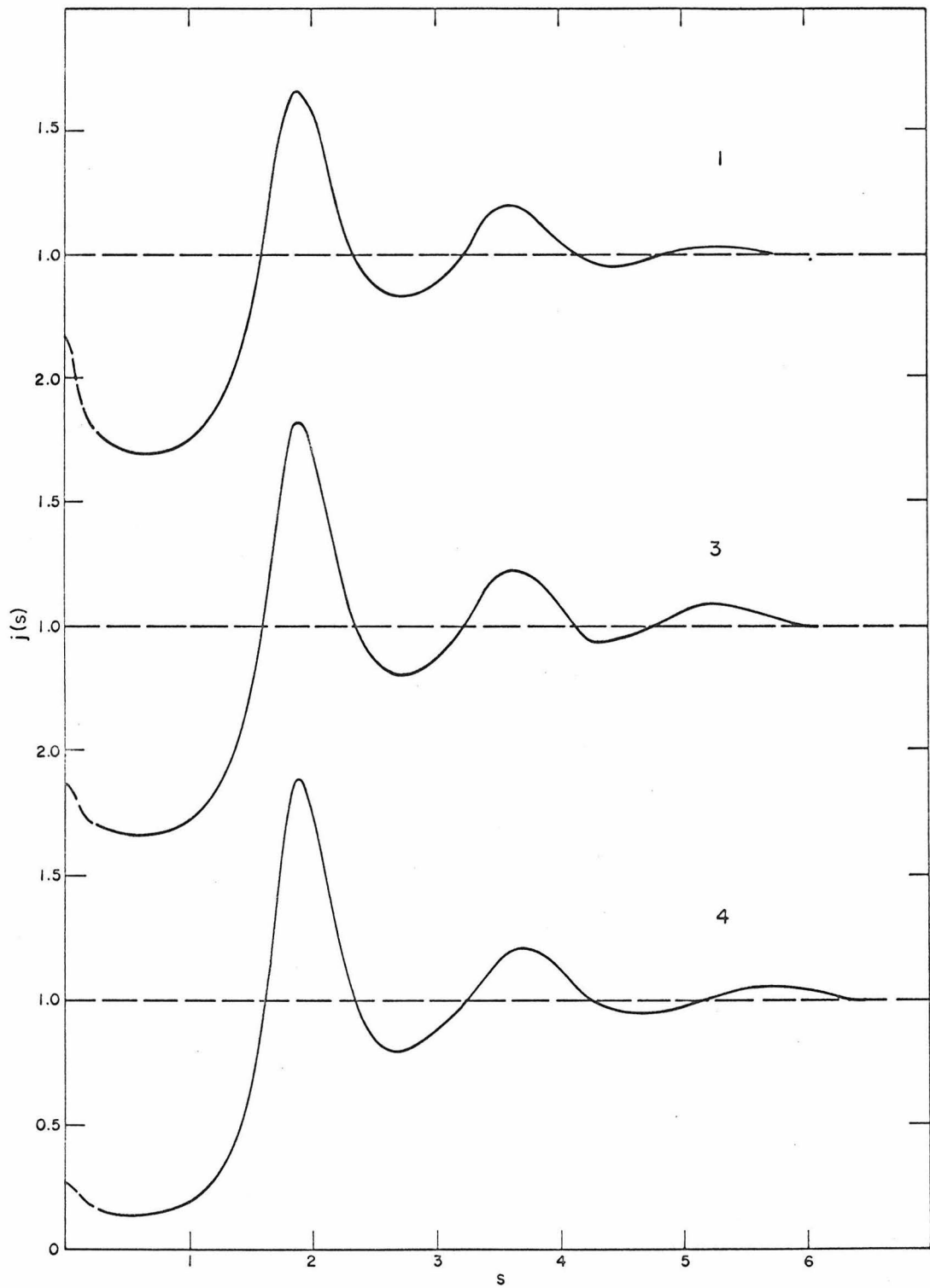


Figure 17. The Argon Intensity Function $j(s)$, for Argon Runs 1, 3, and 4

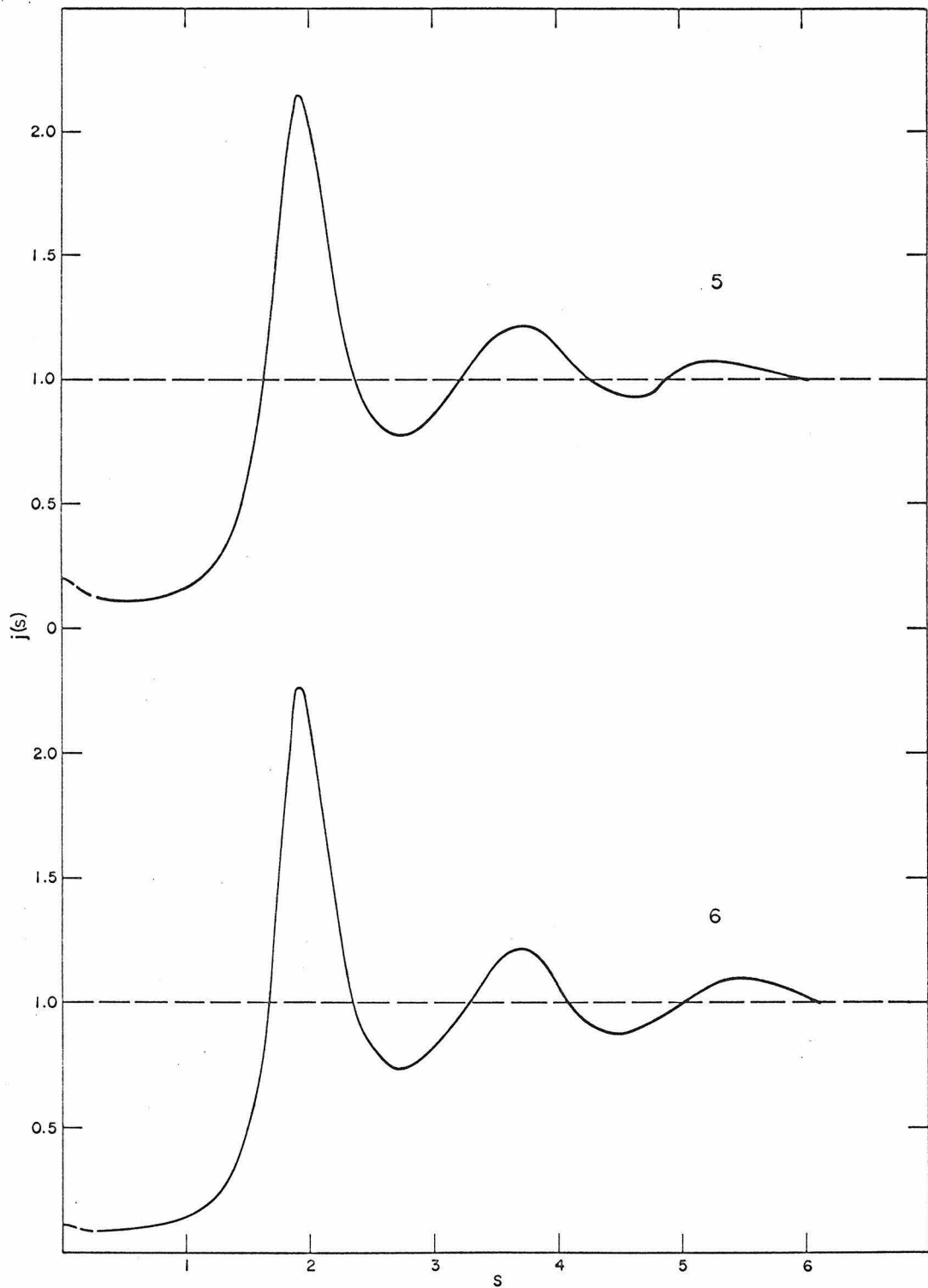


Figure 18. The Argon Intensity Function, $j(s)$, for Argon Runs 5 and 6

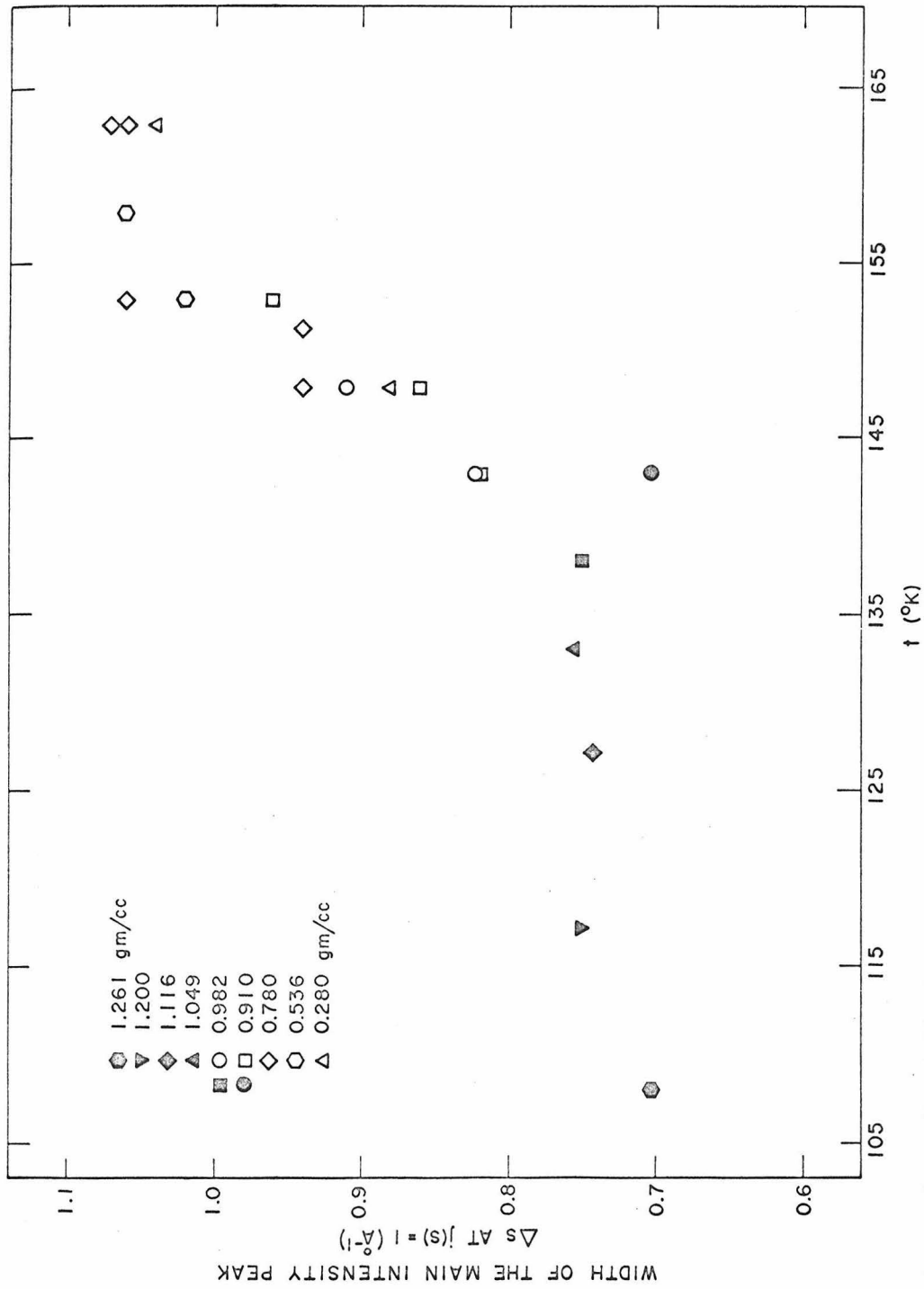


Figure 19. The Effect of Temperature and Bulk Density on the Width of the Main Intensity Peak in the Argon Intensity Function, $j(s)$ at $j(s) = 1$ (Full symbols, this work; Open symbols, Mikola,¹⁰)

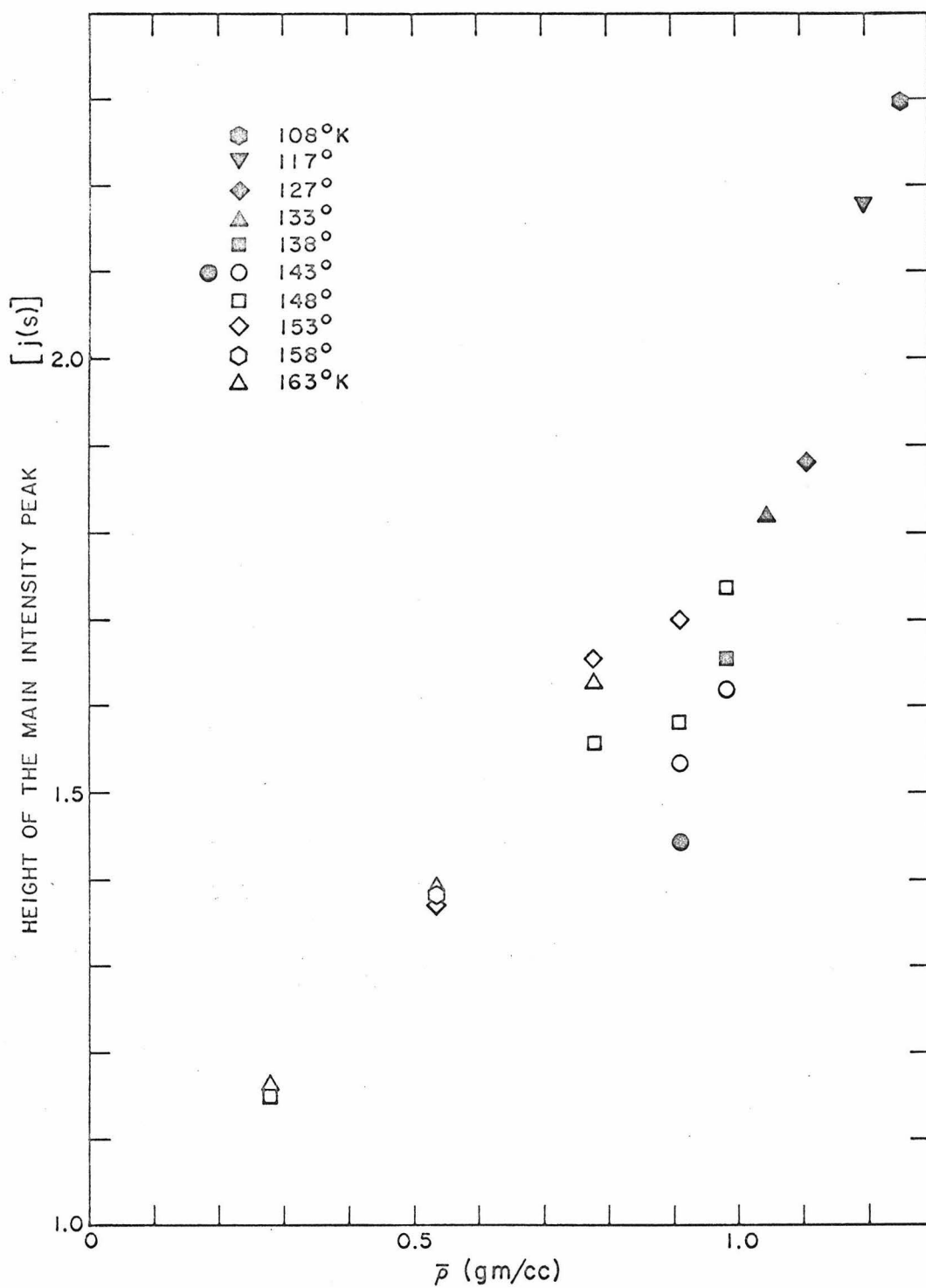


Figure 20. The Effect of Temperature and Bulk Density on the Height of the Main Peak in the Argon Intensity Function, $j(s)$ (Full symbols, this work; Open symbols, Mikolaj¹⁰)

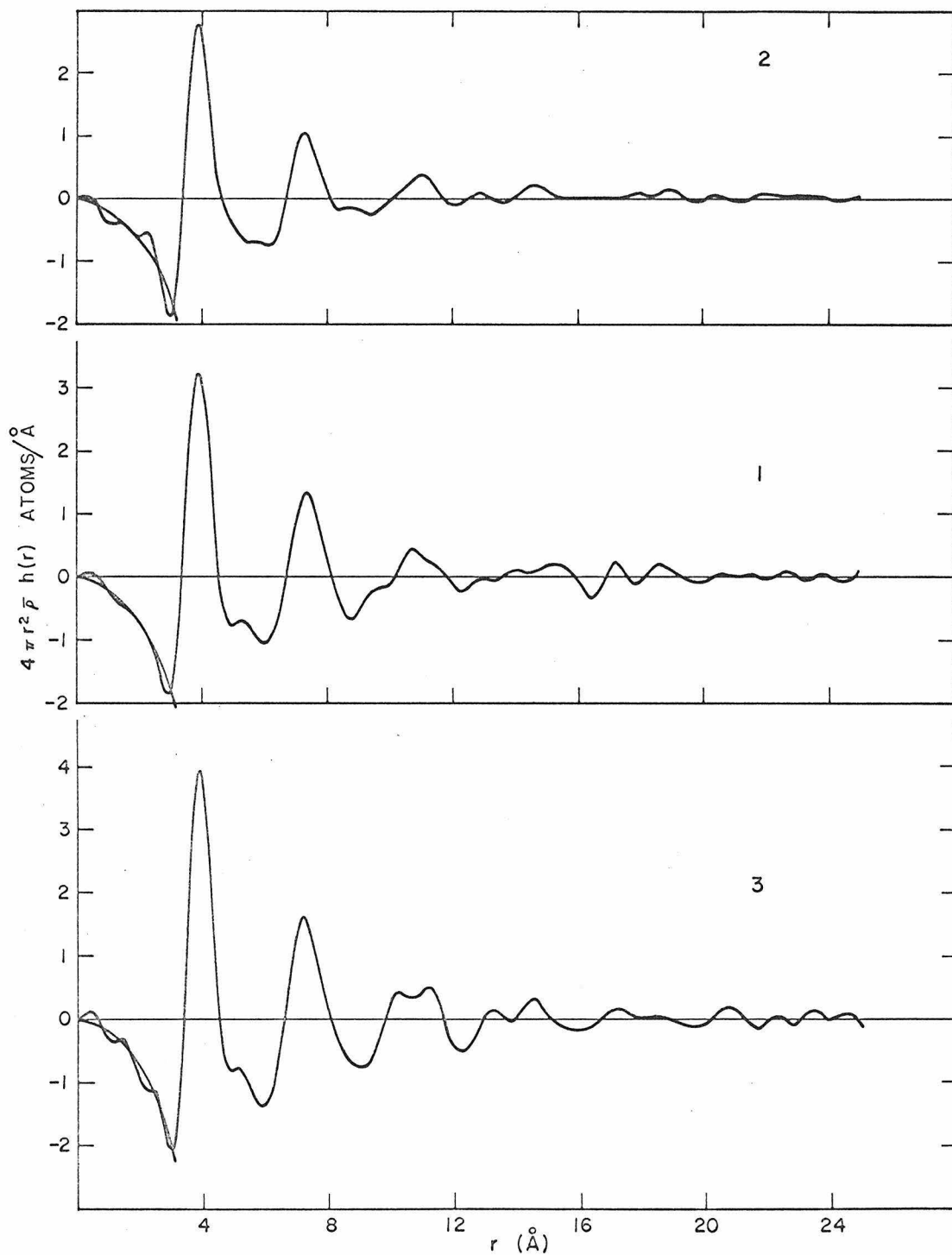


Figure 21. The Radial Atomic Density Function of Argon for Runs 1, 2, and 3 (The Parabola at small r is $4\pi r^2 \bar{\rho}$)

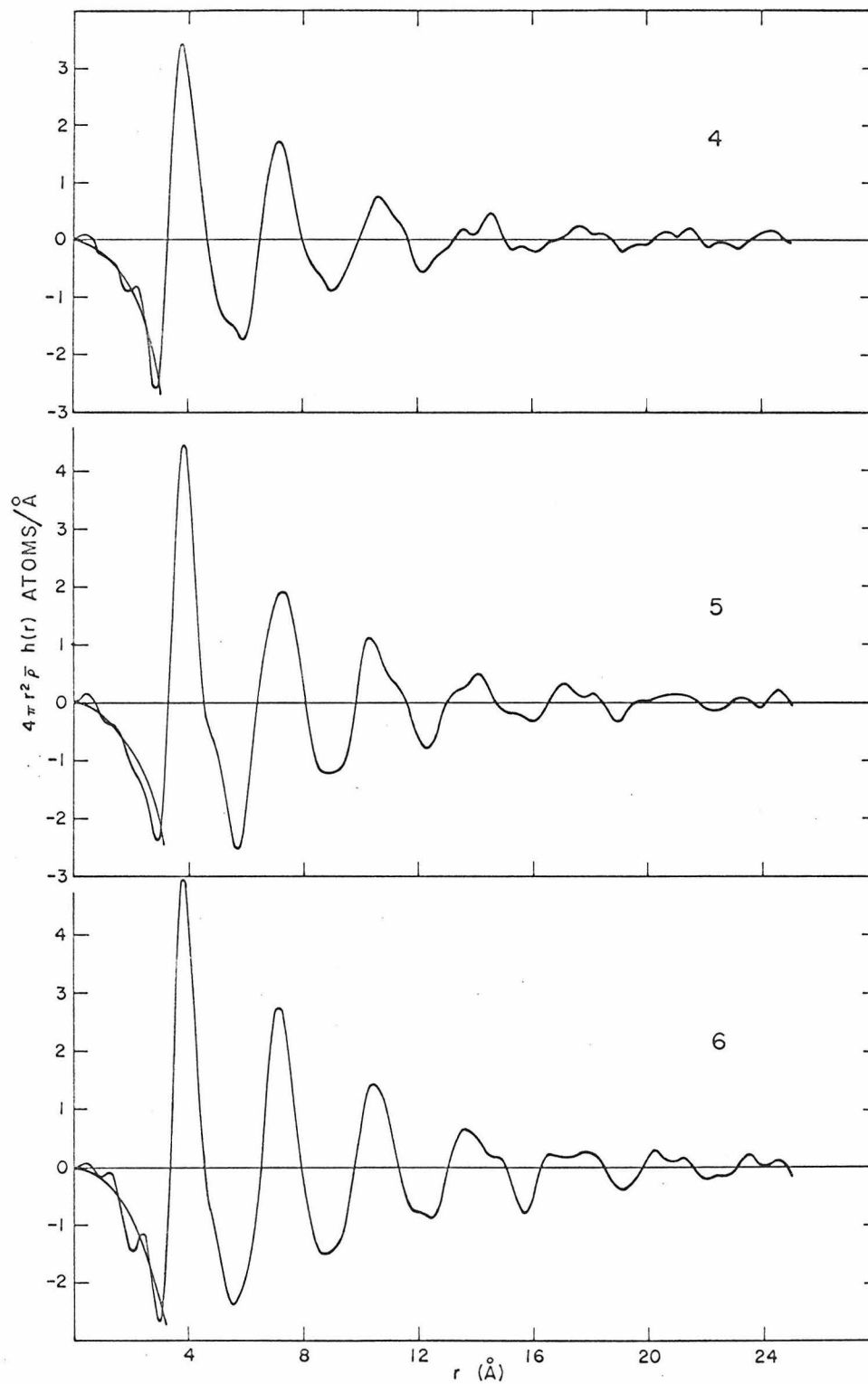


Figure 22. The Radial Atomic Density Function of Argon for Runs 4, 5, and 6 (The Parabola at small r is $4\pi r^2 \bar{\rho}$)

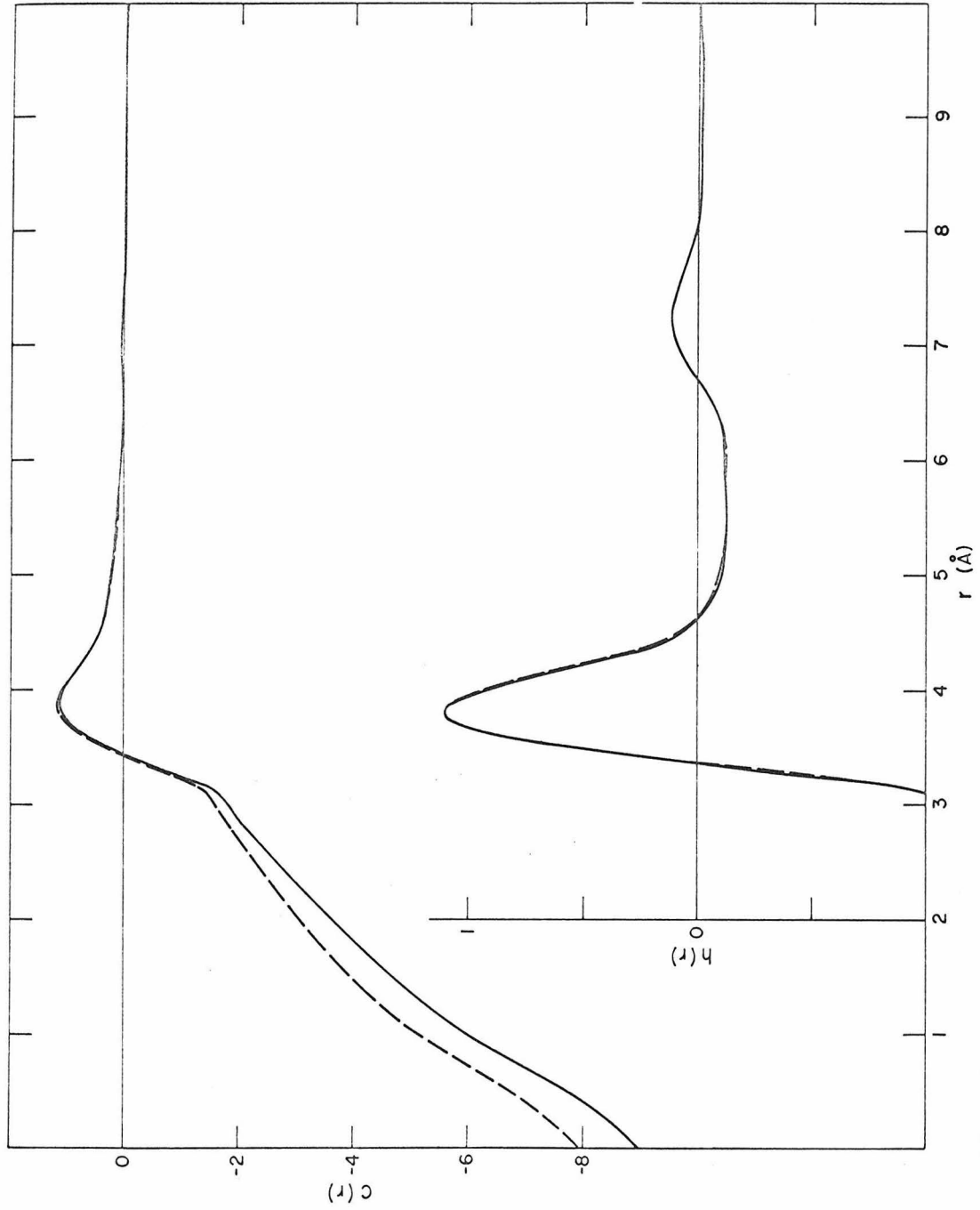


Figure 23. The Effect of the Divergence Correction on $h(r)$, and $C(r)$ (——— after the Correction; - - - before the Correction)

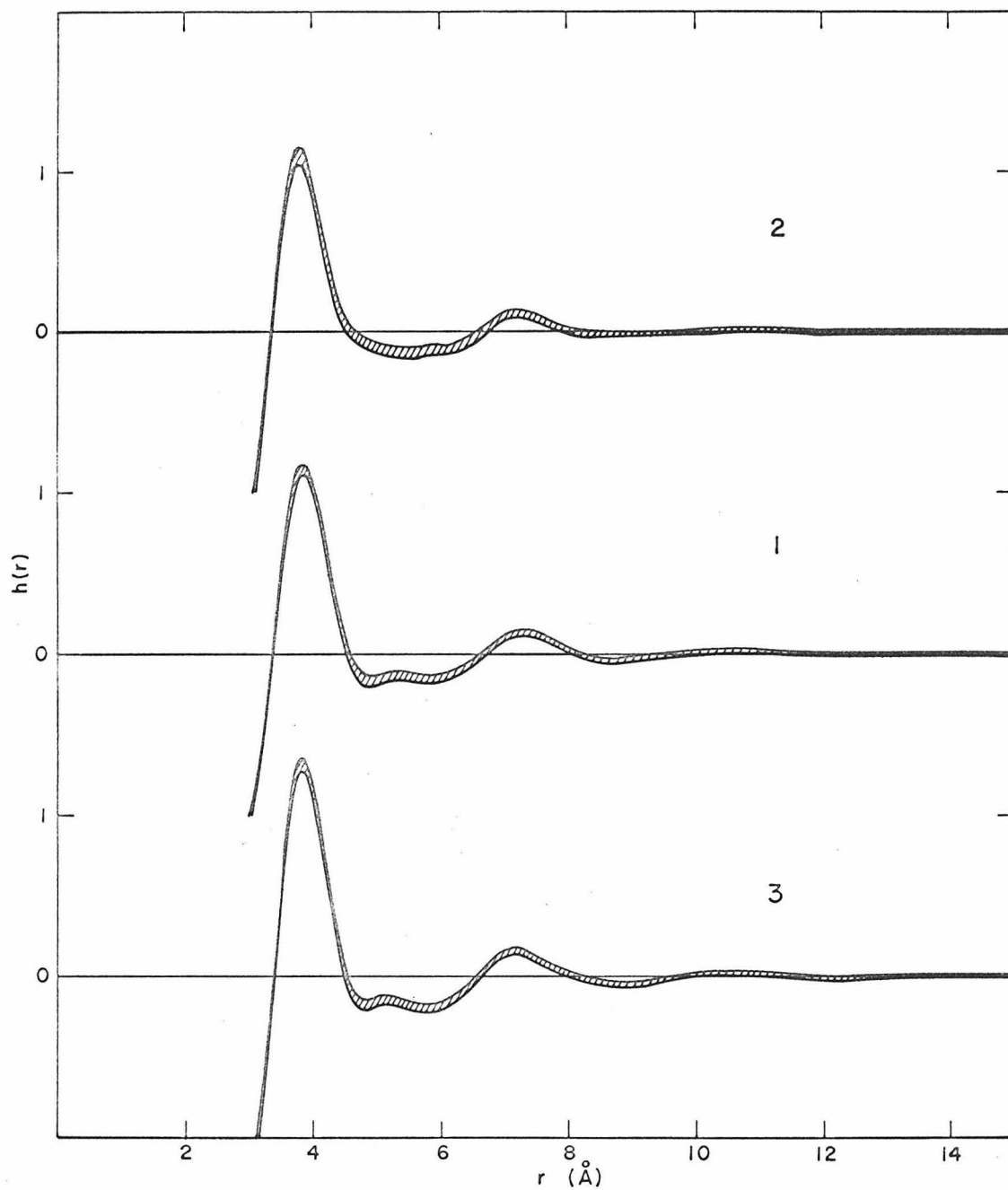


Figure 24. The Estimated Net Radial Distribution Function of Argon for Runs 1, 2, and 3

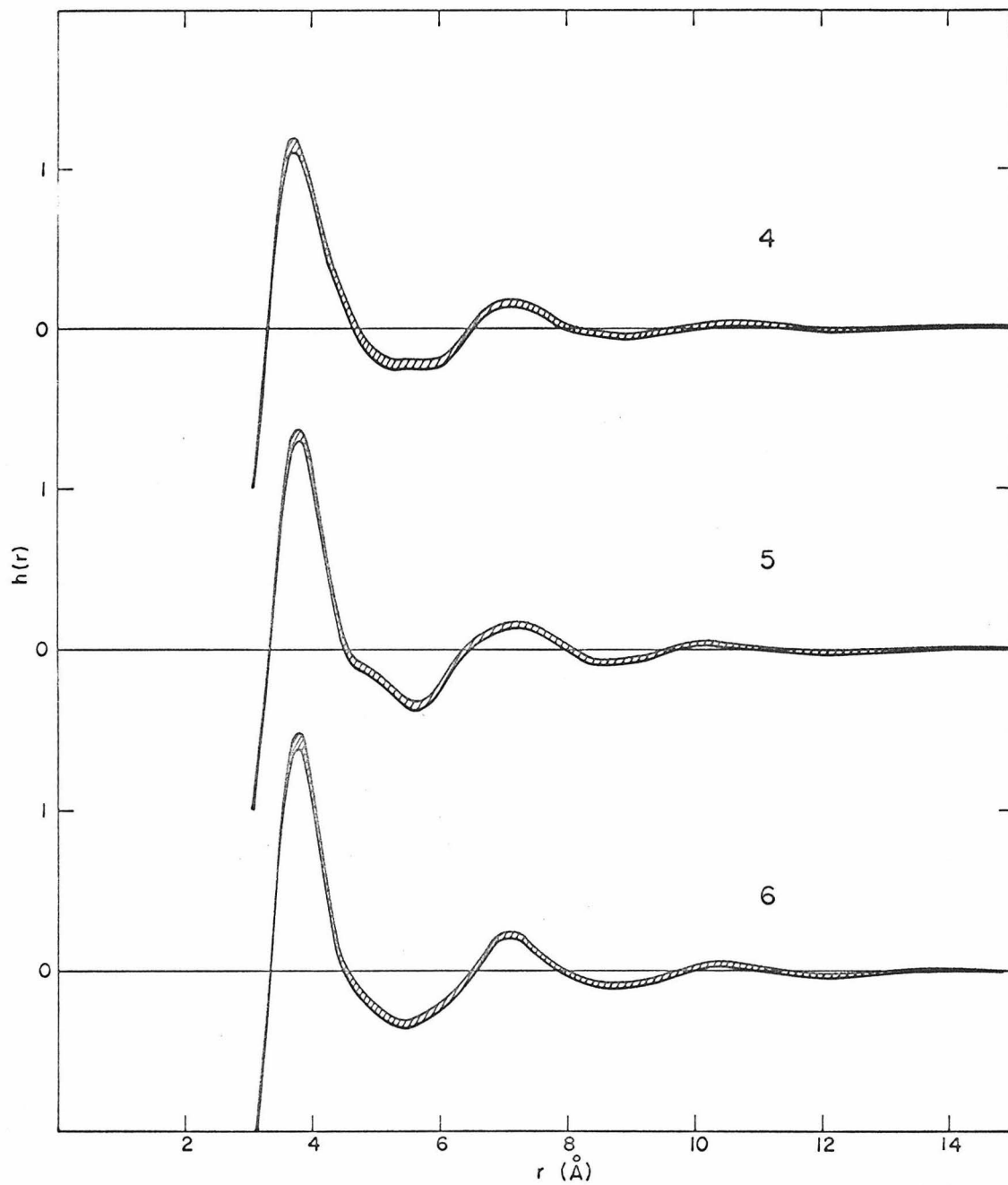


Figure 25. The Estimated Net Radial Distribution Function of Argon for Runs 4, 5, and 6

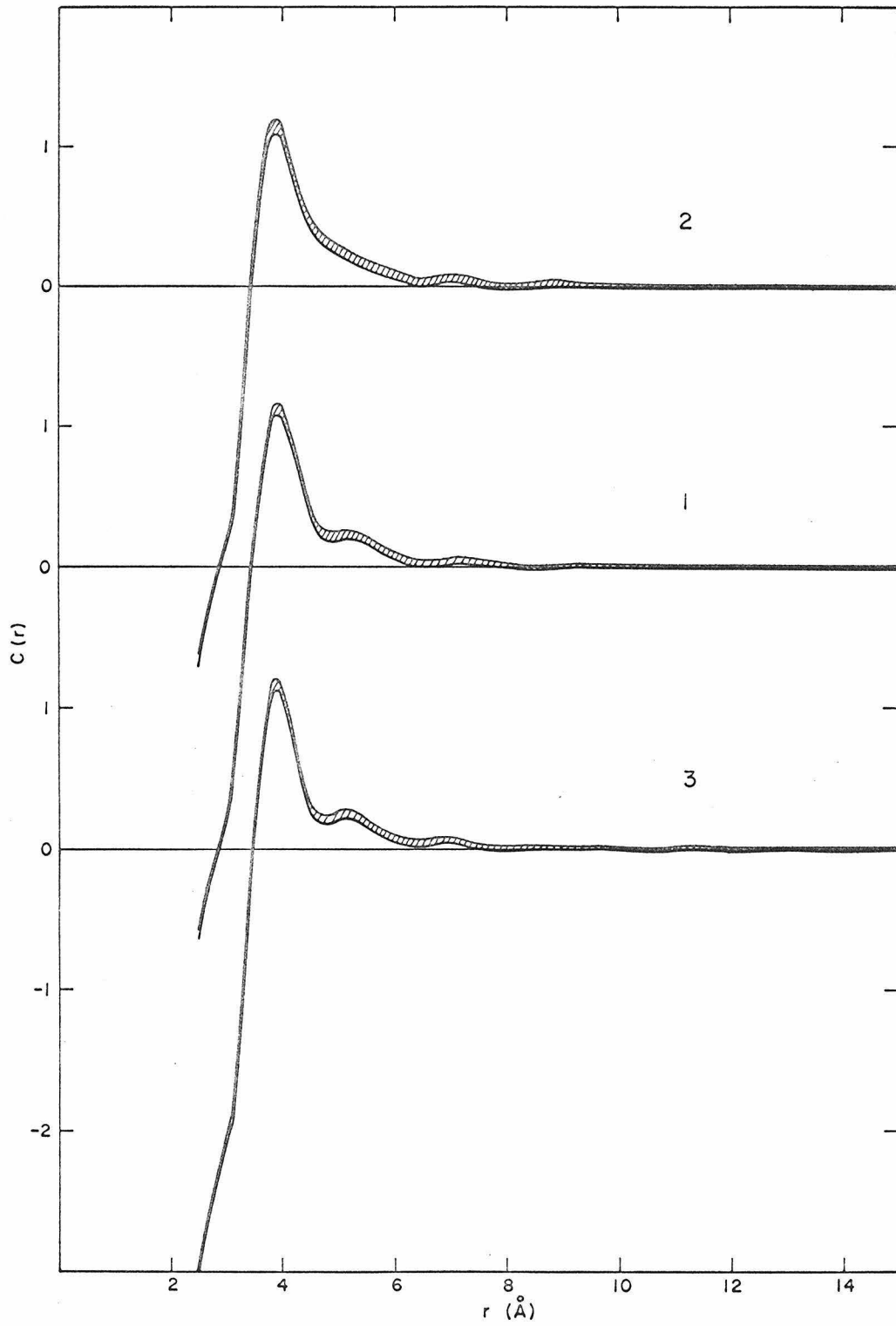


Figure 26. The Estimated Direct Correlation Function of Argon for Runs 1, 2, and 3

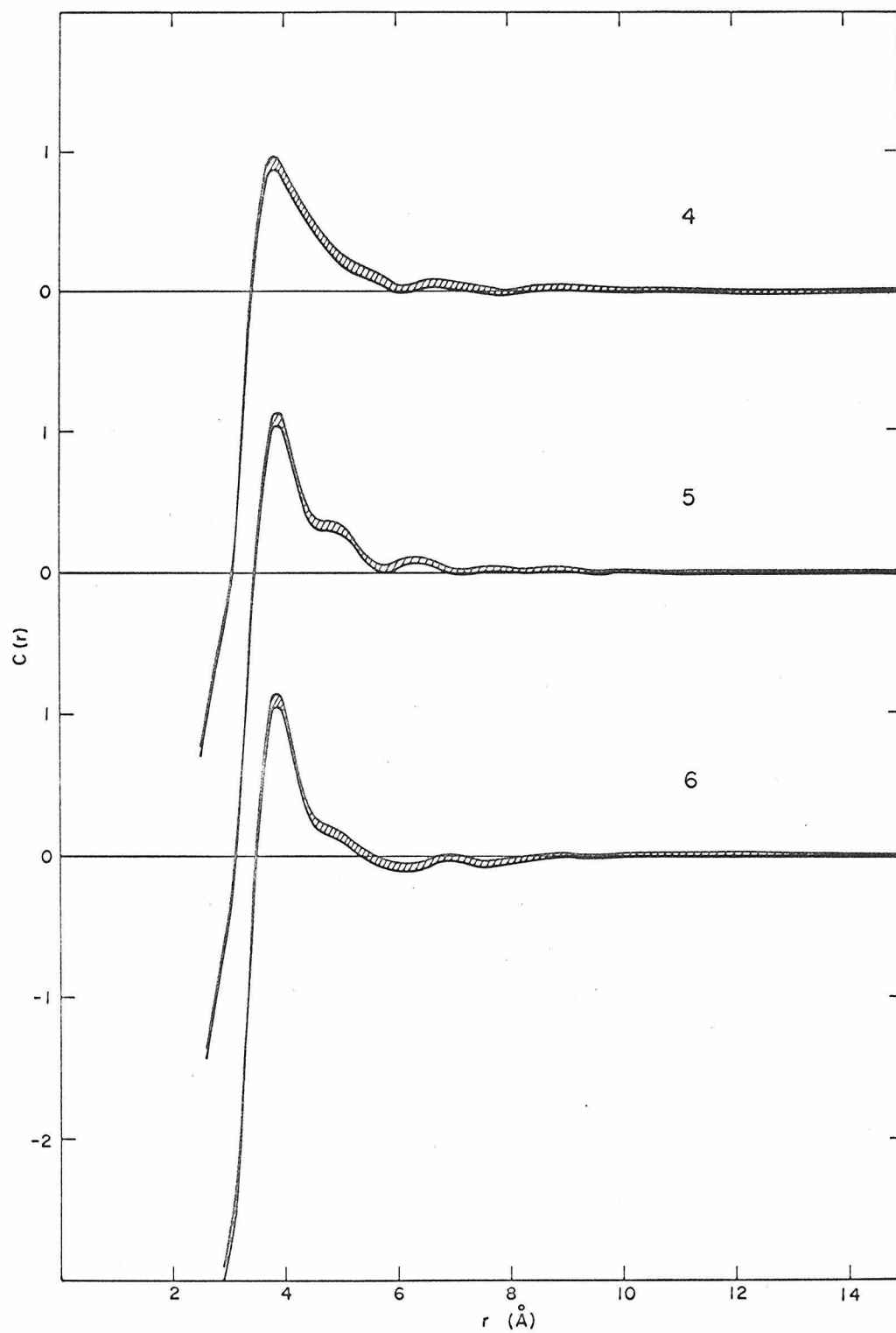


Figure 27. The Estimated Direct Correlation Function of Argon for Runs 4, 5, and 6

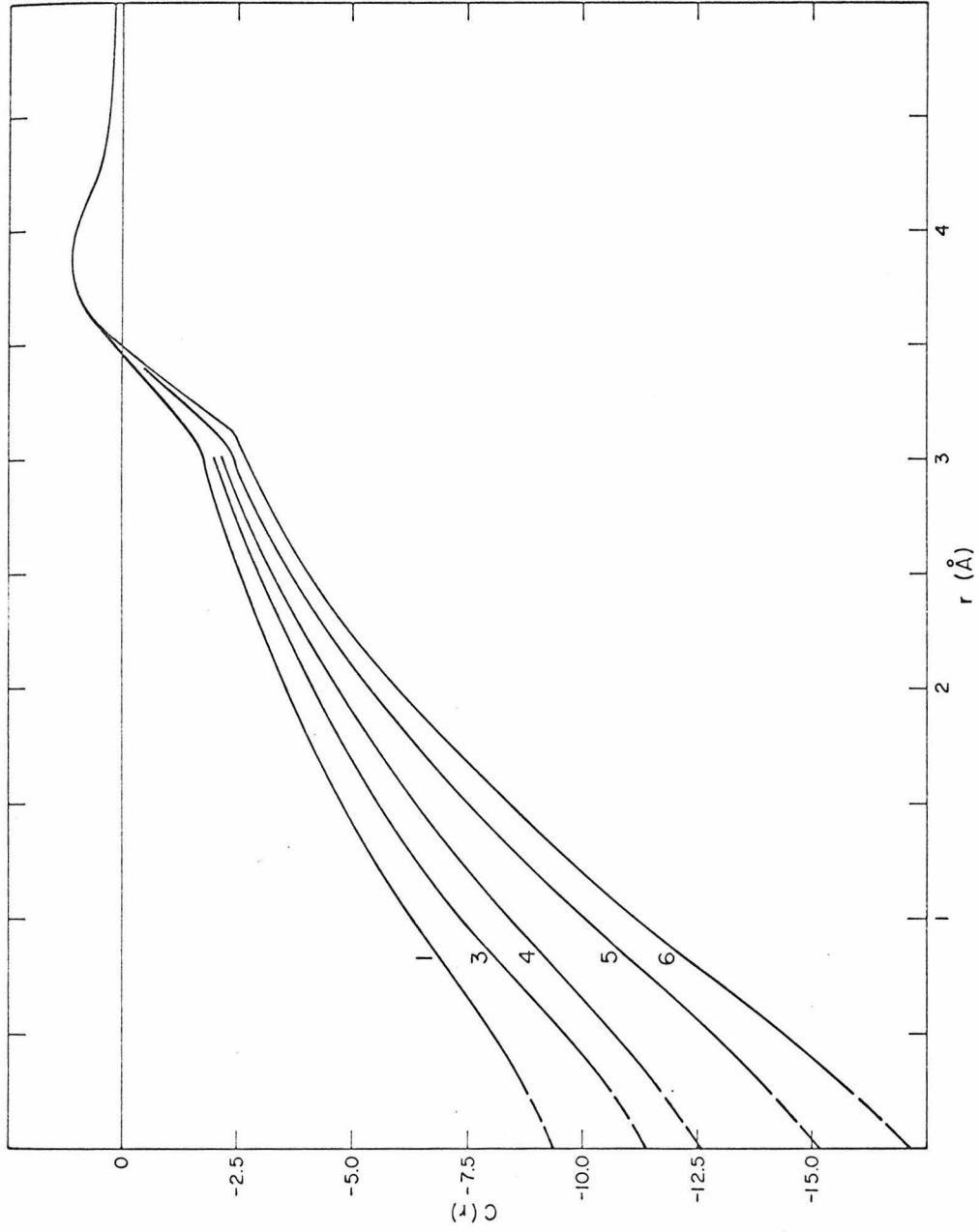


Figure 28. The Estimated Small r Behavior of the Direct Correlation Function of Argon for Runs 1, 3, 4, 5, and 6

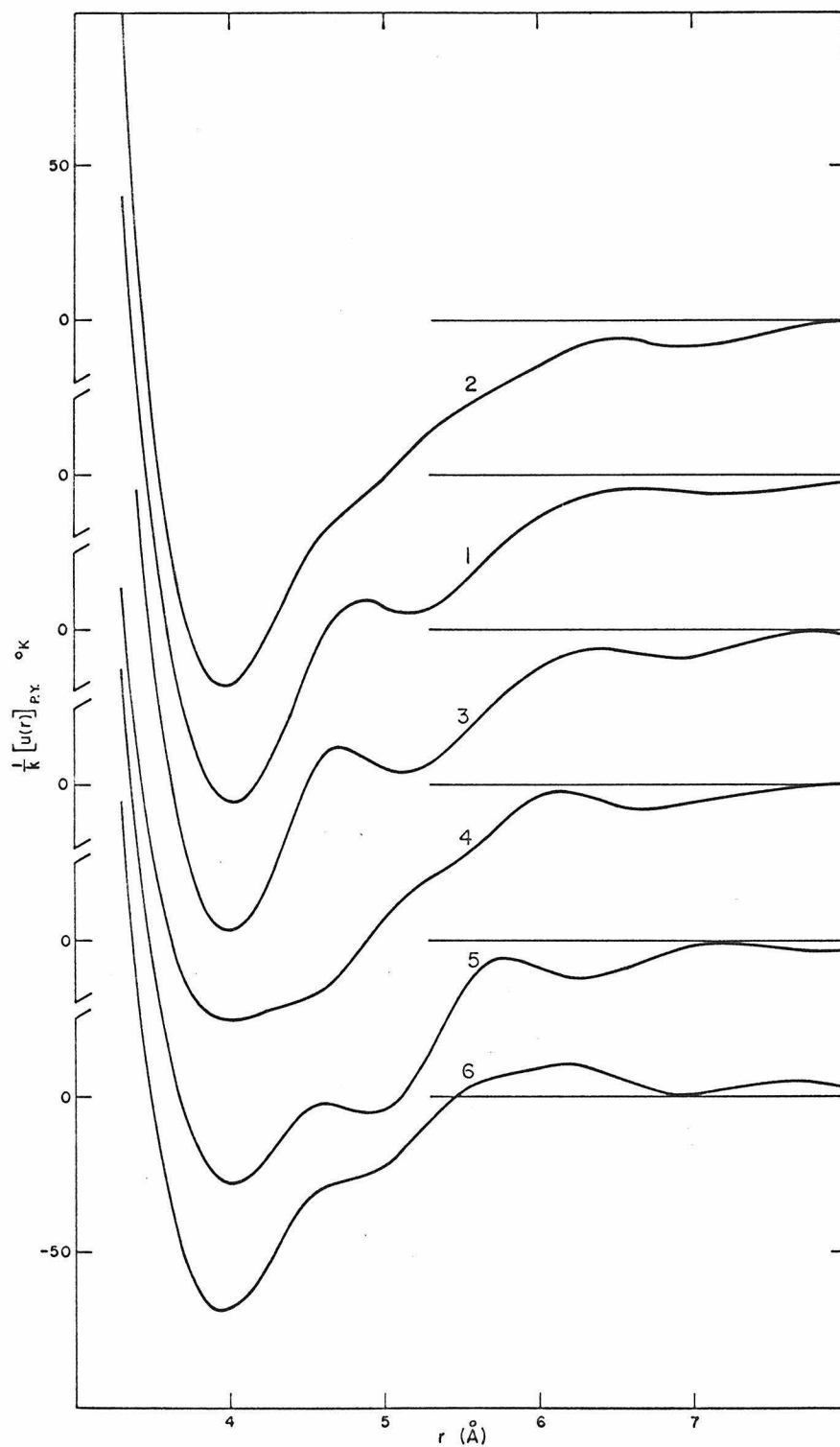


Figure 29. The Potential Function of Liquid Argon Calculated from the Percus-Yevick Equation for the Six States

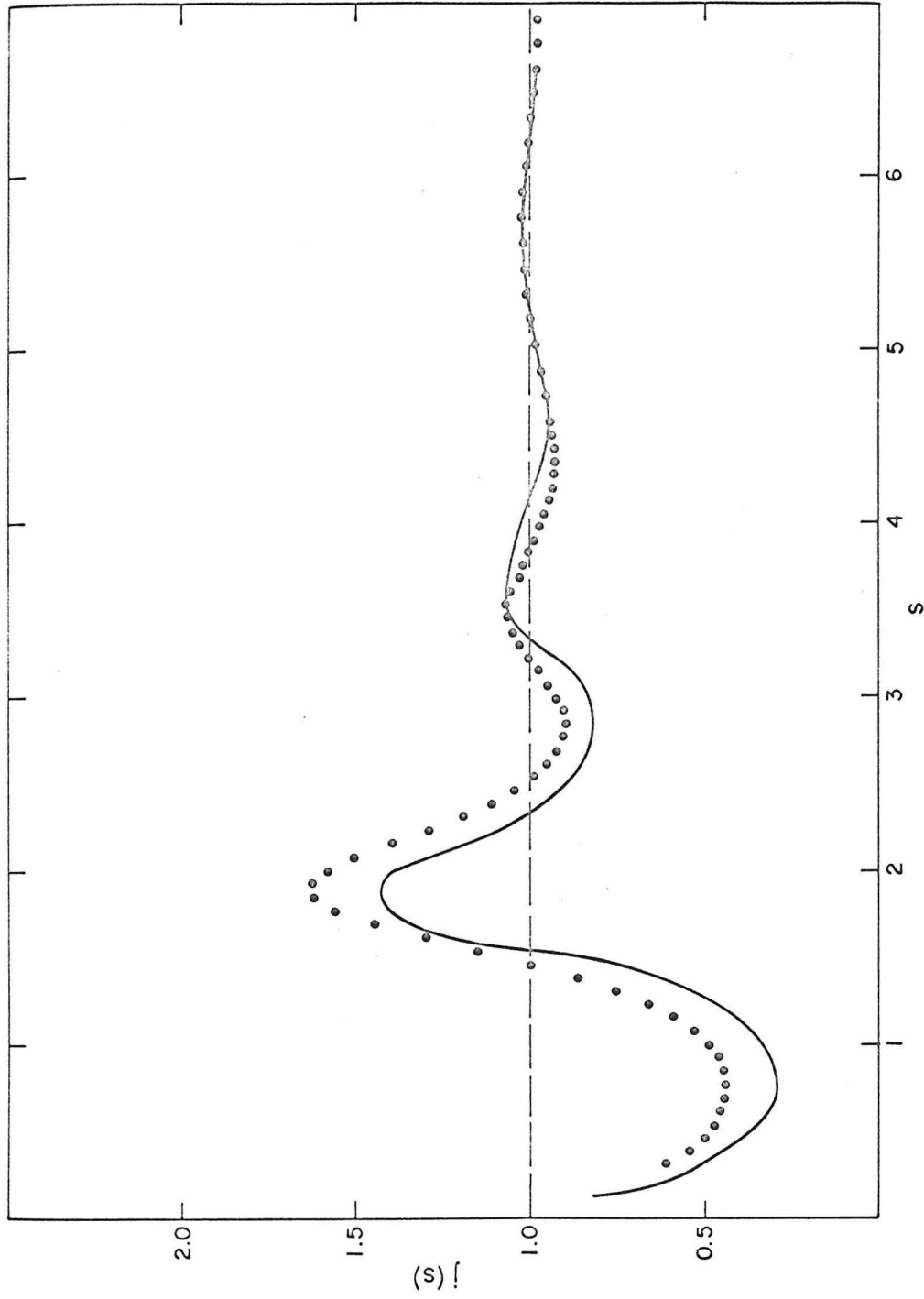


Figure 30. The Argon Intensity Function, $j(s)$ at $\rho = 0.780$ gm/cc and $T = -110$ °C
 (— Verlet's Function Calculated from the P-Y Equation using
 the Leonard-Jones Potential; •, Mikolaj¹⁰) This Figure taken from
 Levesque and Verlet¹⁵

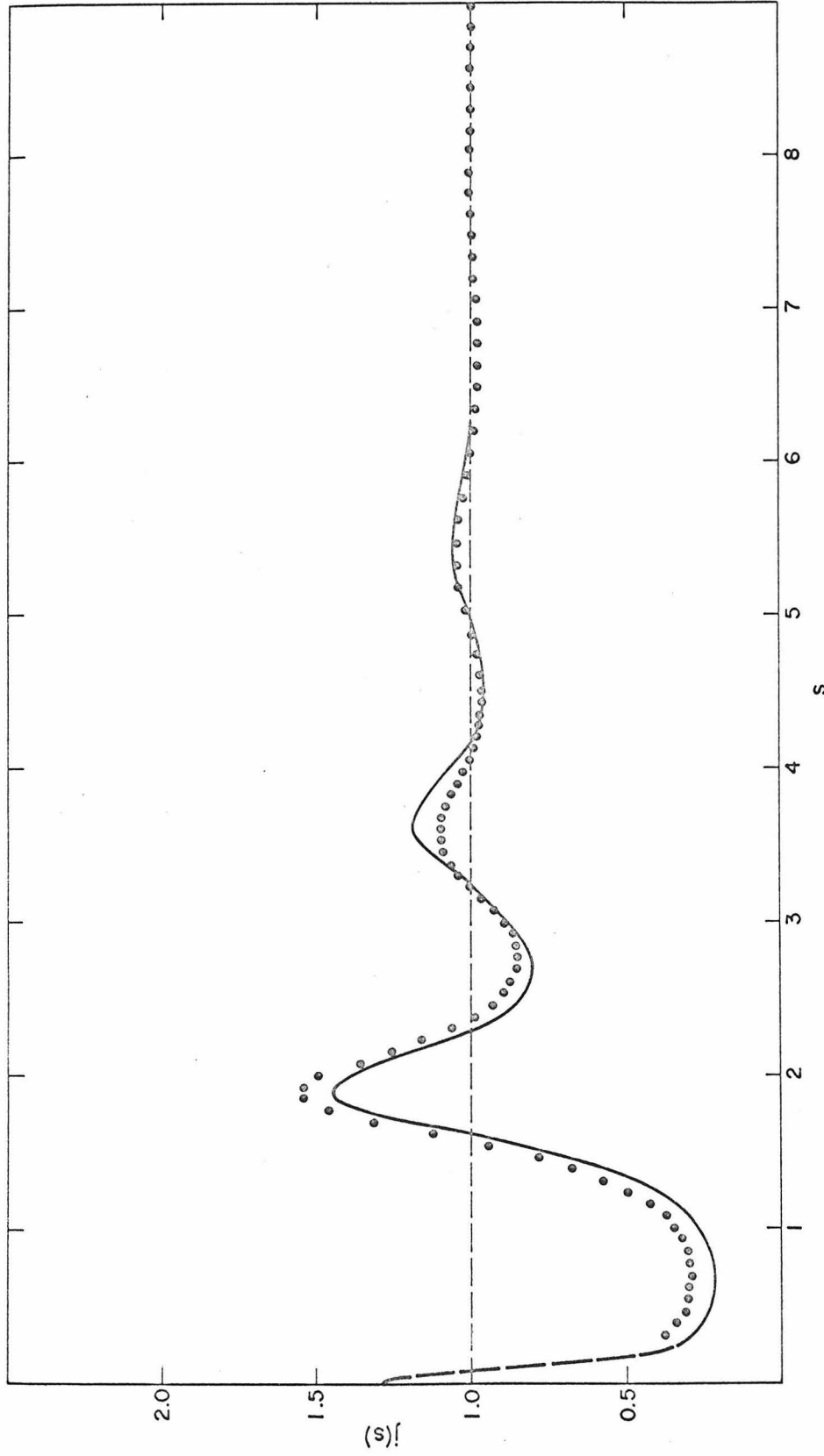


Figure 31. The Argon Intensity Function, $j(s)$ for Run 2 (— this work; •, Mikolaj and Pings¹¹)

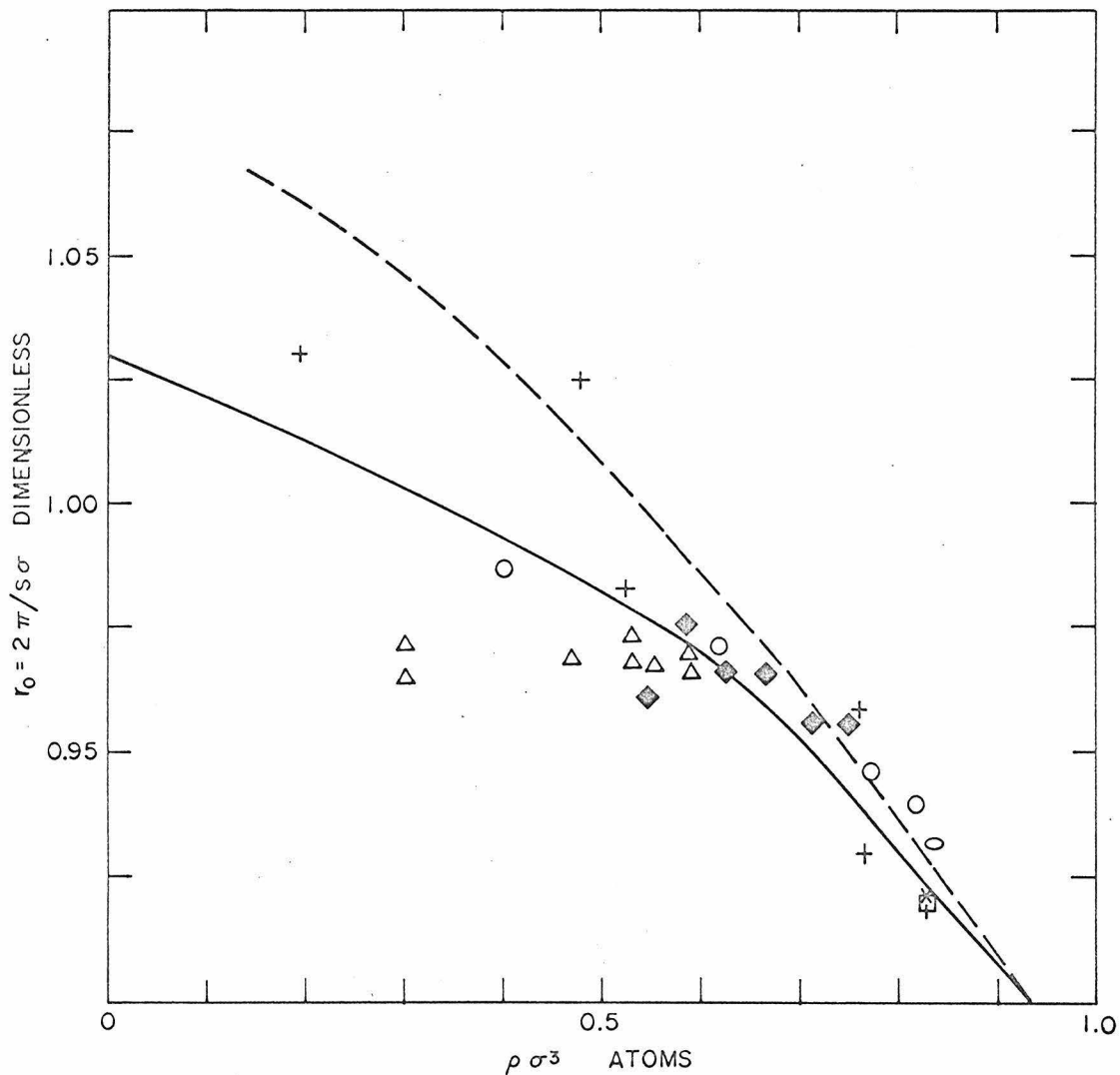


Figure 32. r_0 as a Function of $\rho\sigma^3$. (\diamond this work; All others from Verlet^{17*}) "s" is the value s_{\max} where $j(s_{\max})$ is maximum.

* "Fig. 10. r_0 as a function of $\rho\sigma^3$ for the Lennard Jones potential (———) at the temperature $T=1.35$, and the hard-sphere gas of diameter 1 (— —). Experimental data: \circ neutrons on Krypton, Δ X-Rays on argon¹¹, $+$ X-Rays on Argon⁸, \circ X-Rays on Argon⁶, \square neutrons on argon², \times neutrons on Argon³. The reduction parameters are for Krypton: $\sigma = 4.064 \text{ \AA}$, $\epsilon/k = 224.5^\circ$, and for argon: $\sigma = 3.405 \text{ \AA}$, $\epsilon/k = 119.8^\circ$."

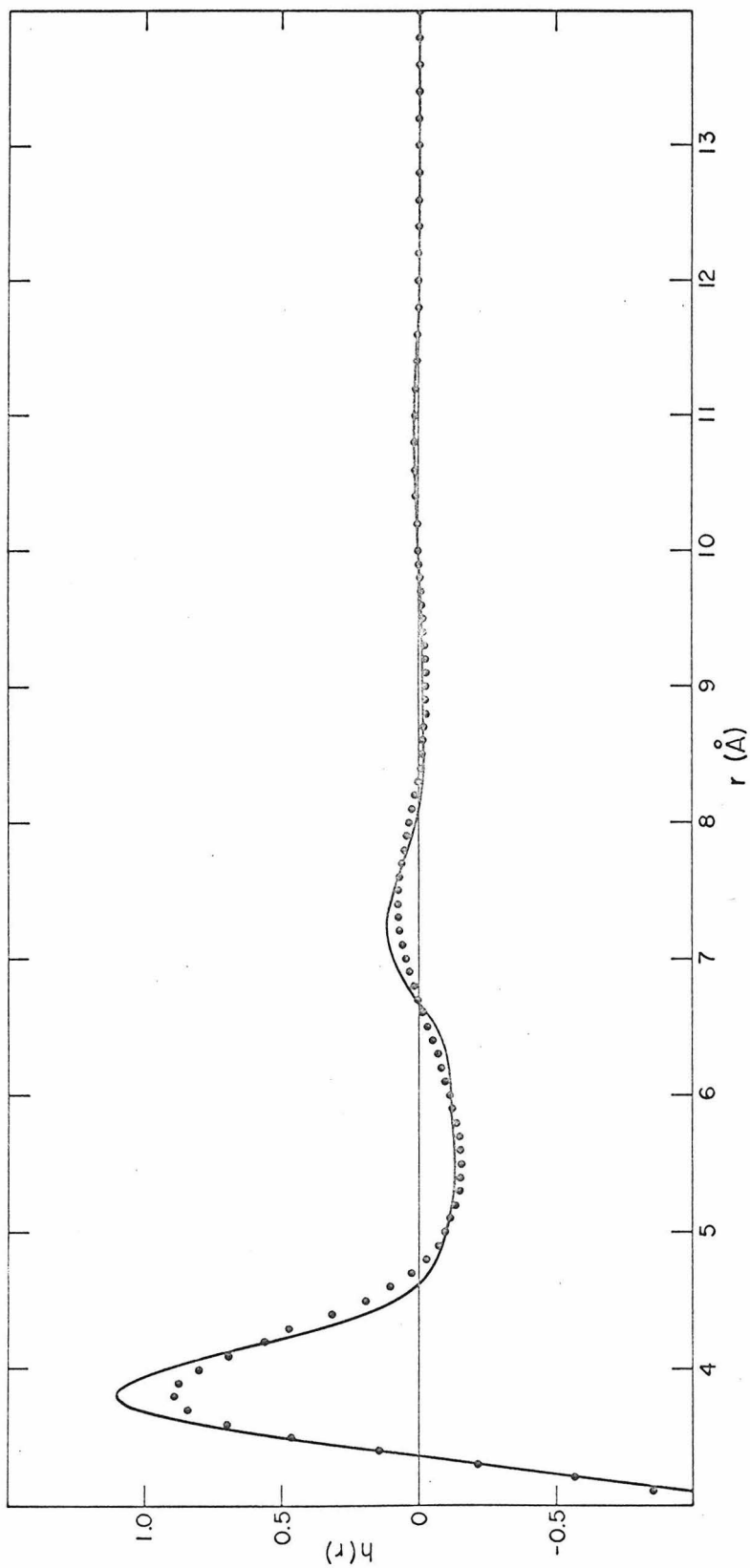


Figure 33. The Net Radial Distribution Function of Argon for Run 2. (——— this work;
•, Mikolaj and Pingsll)

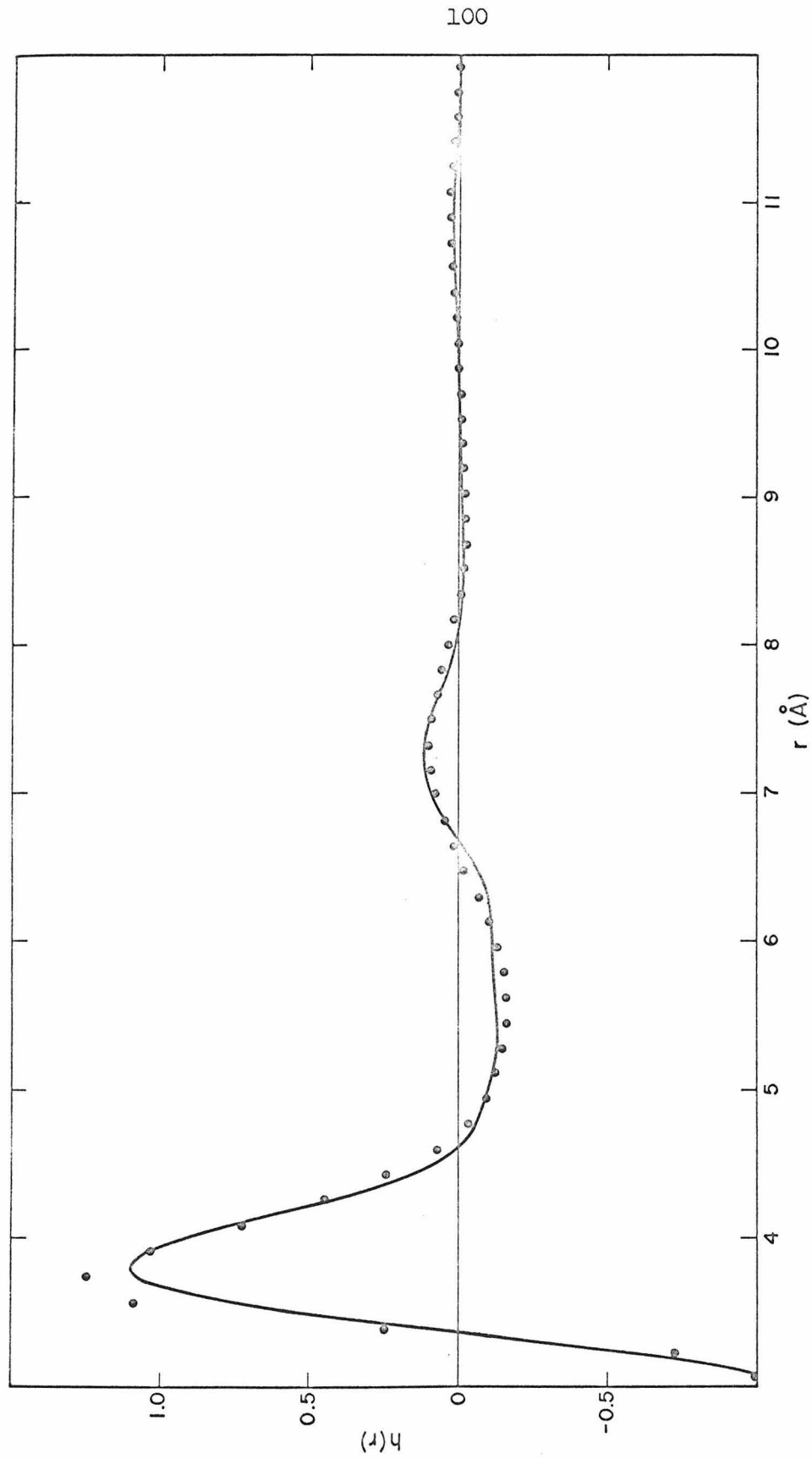


Figure 34. The Net Radial Distribution Function of Argon for Run 2 (——— this work; • Matts¹⁹)

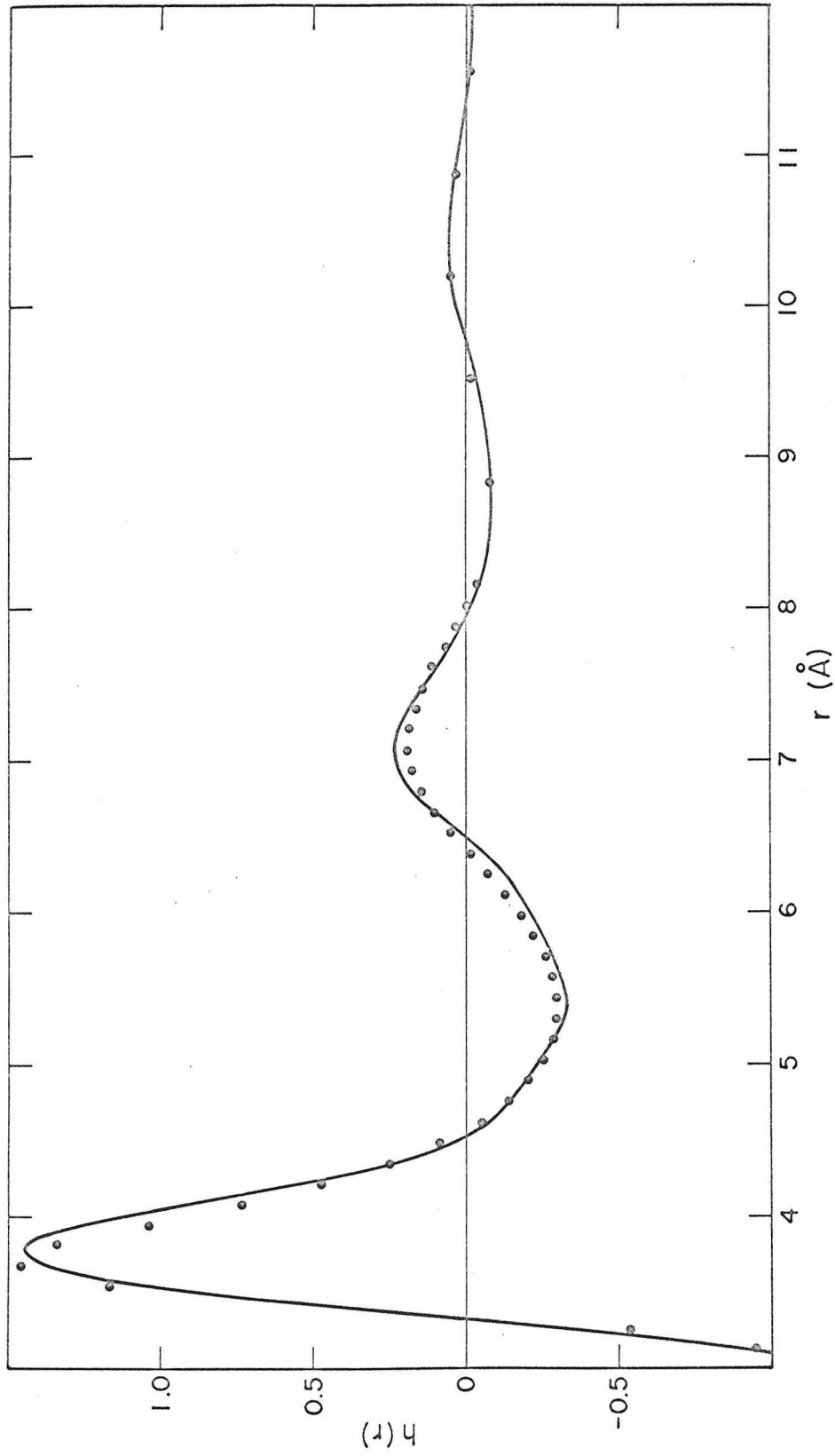


Figure 35. The Net Radial Distribution Function of Argon for Run 6 (——— this work; •••, Molecular Dynamics of Verlet17, same density but a higher temperature)

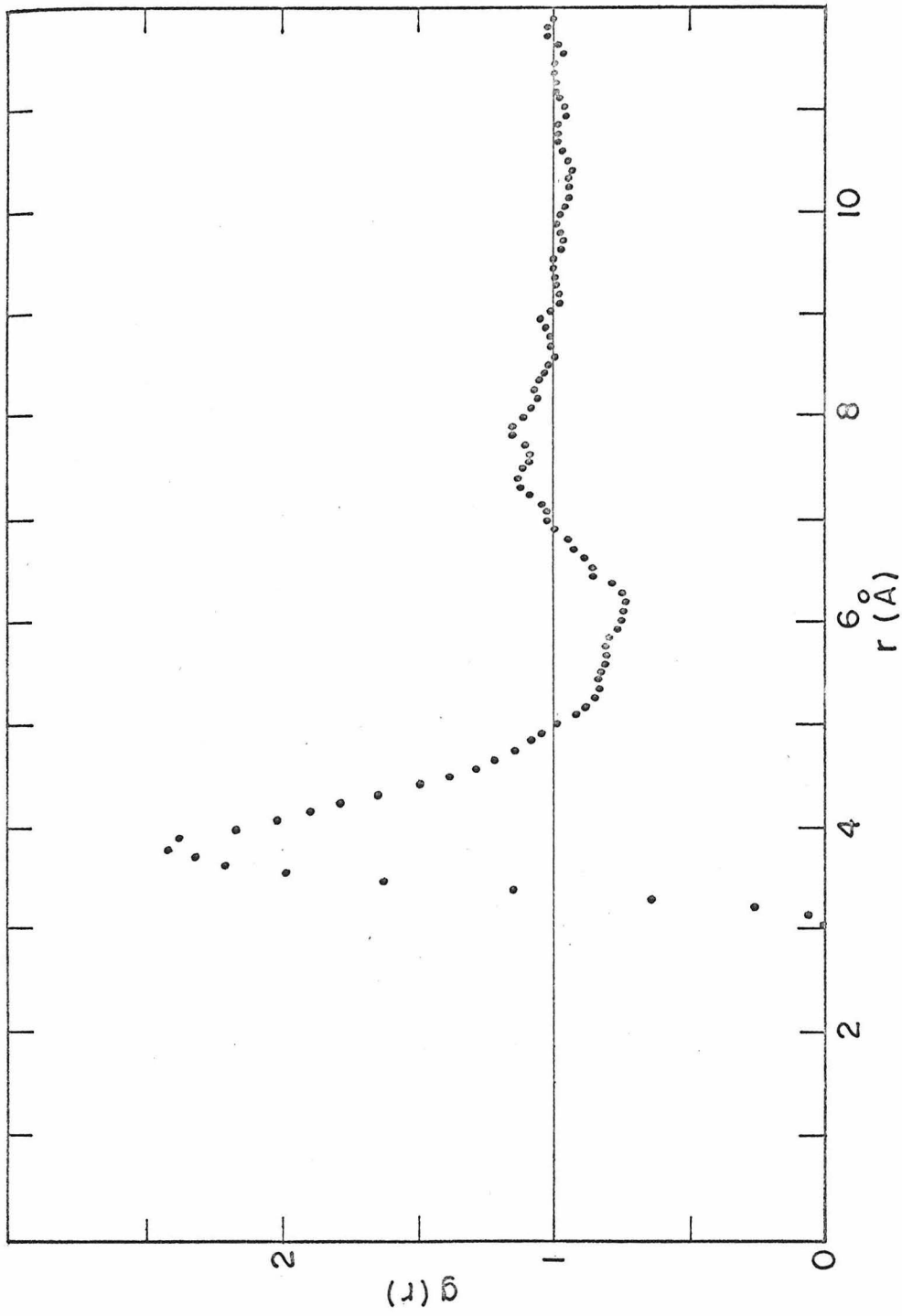


Figure 36. Two Dimensional Molecular Dynamics Calculation of $g(r)$ at a Relative Packing Density of 0.5406 (from Fehder²¹), $T = 137.56$ °K

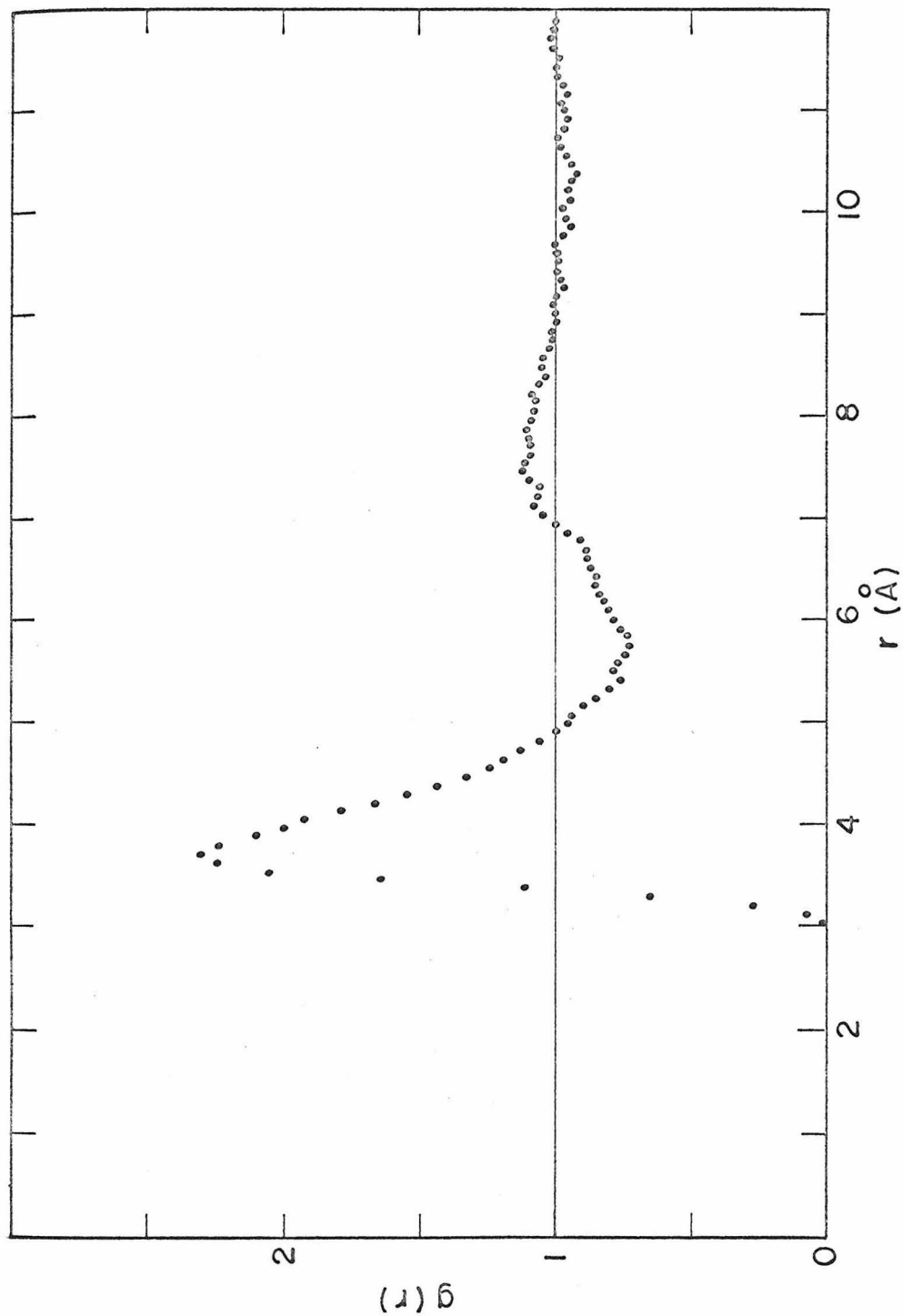


Figure 37. Two Dimensional Molecular Dynamics Calculation of $g(r)$ at a Relative Packing Density of 0.6237 (from Fehder²¹), $T = 132.12 \text{ }^\circ\text{K}$

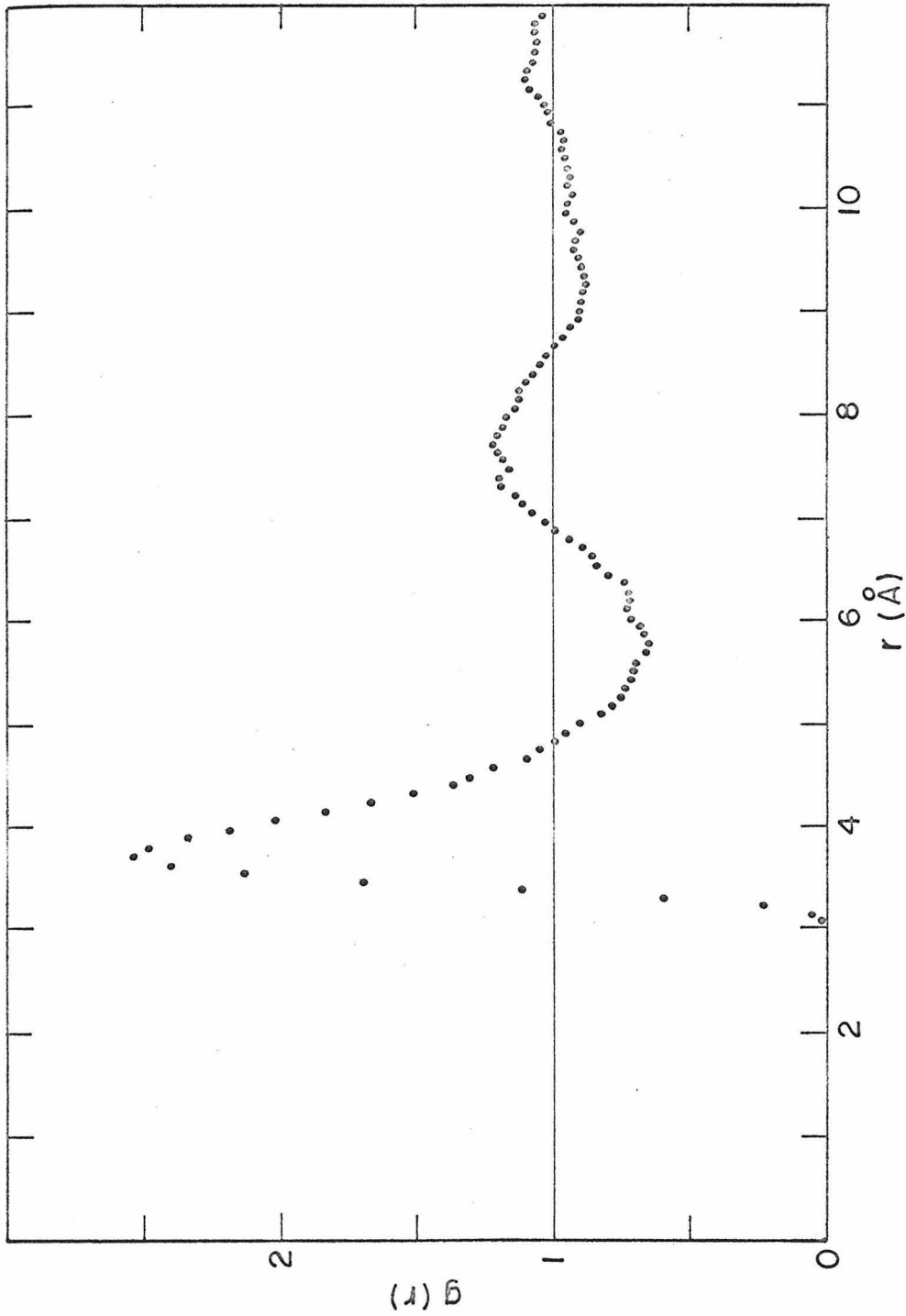


Figure 38. Two Dimensional Molecular Dynamics Calculations of $g(r)$ at a Relative Packing Density of 0.7274 (from Fender²¹), $T = 120.74$ °K

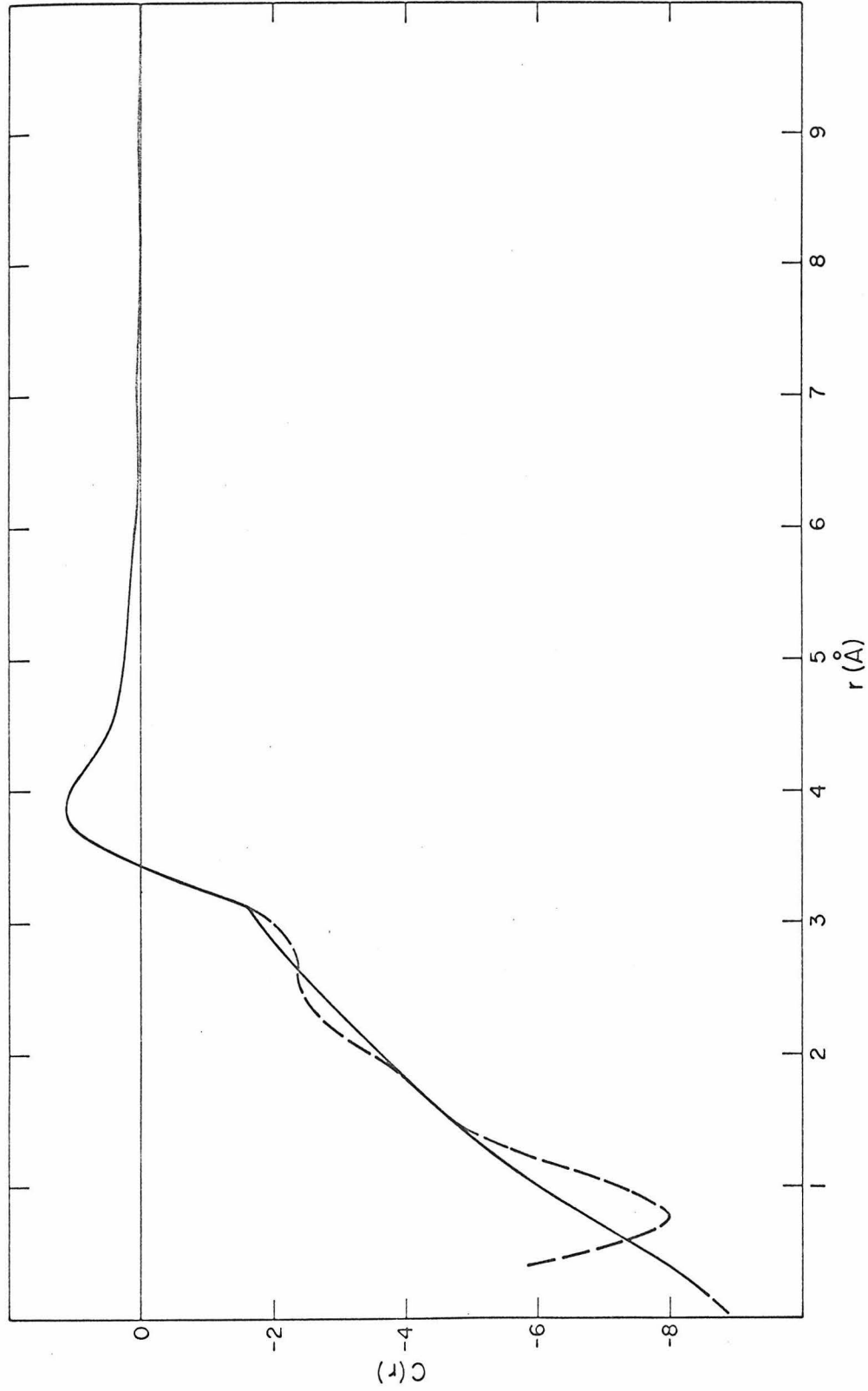


Figure 39. The Direct Correlation Function of Argon Run 2 (——— indicates best estimate of subatomic behavior; - - - Direct Results from Transform of $i(s)$)

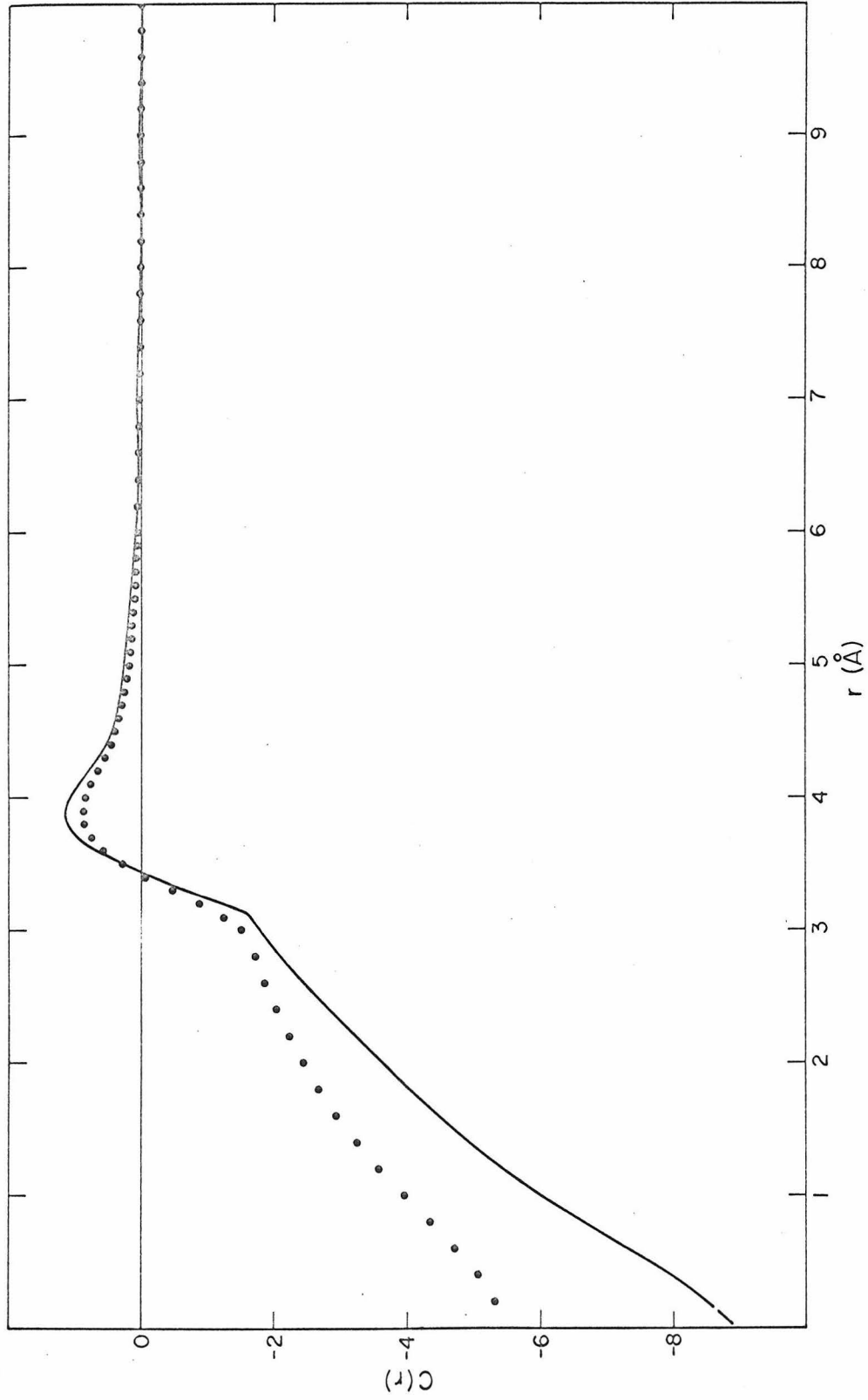


Figure 40. The Direct Correlation Function of Argon, Run 2 (——— this work; • Mikolaj and Pings13)

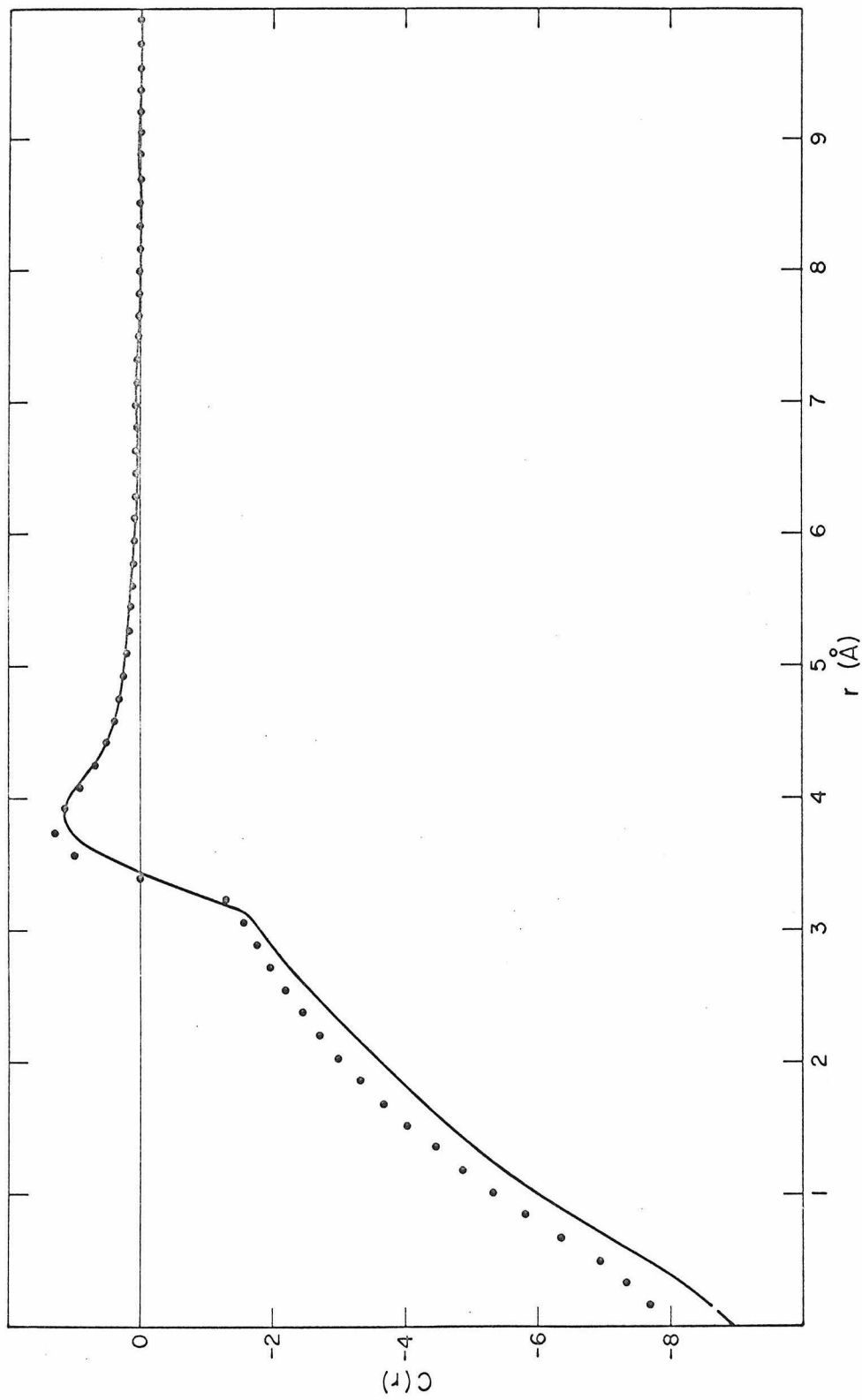


Figure 41. The Direct Correlation Function of Argon, Run 2 (----- this work; •, Leonard-Jones Potential, Percus-Yevick Approximation of Watts19)

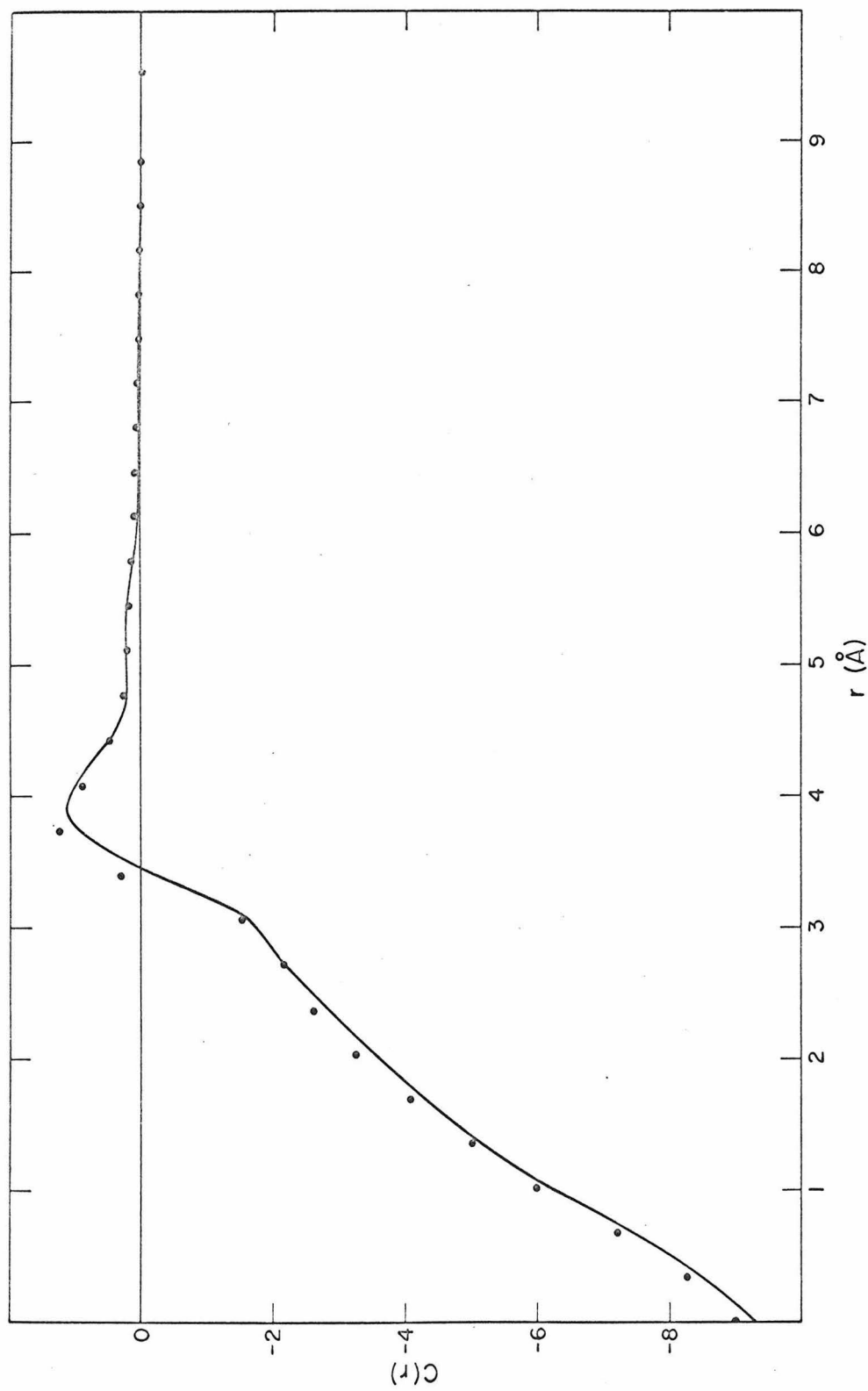


Figure 42. The Direct Correlation Function of Argon (— Run 1, this work; • , Watts¹⁹, same density but 50 higher temperature)

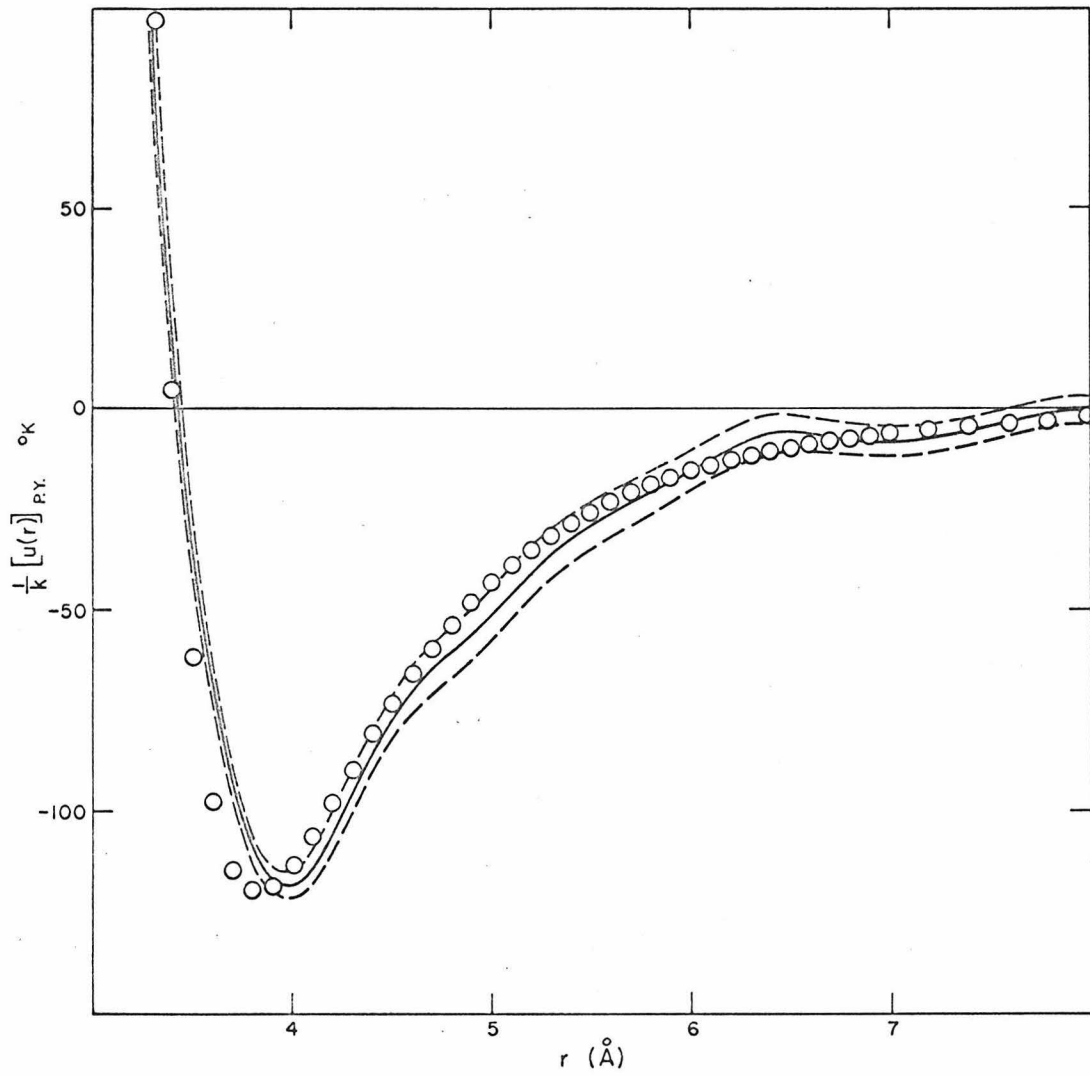


Figure 43. The Calculated Percus-Yevick Potential for Argon 2 with Error Bands vs the Lennard-Jones Potential (O)

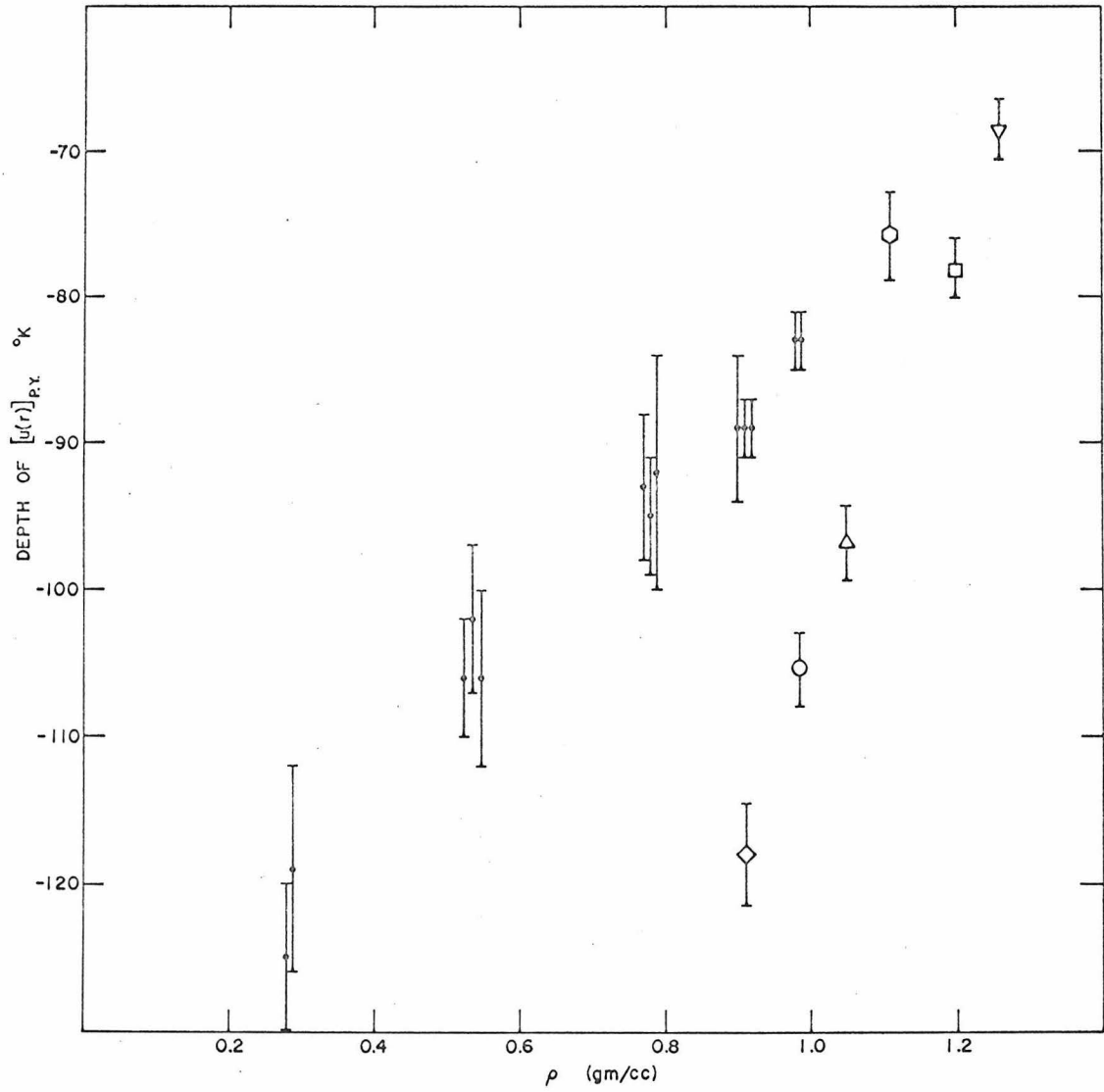


Figure 44. Depth of the Argon Potential Well as Predicted from the Percus-Yevick Equation (Open symbols, this work; •, Mikolaj and Pings¹³)

TABLE I

SUMMARY OF ARGON THERMODYNAMIC STATES AND EXPERIMENTAL UNCERTAINTY LIMITS

<u>Run No.</u>	<u>Temperature (°K)</u>	<u>Density (GM/CC)</u>	<u>Pressure (ATM)</u>
1	138.150 ± .037	0.982 ± 0.003	35.930 ± .035
2	143.150 ± .038	0.910 ± 0.002	39.920 ± .036
3	133.150 ± .038	1.049 ± 0.002	35.380 ± .035
4	127.050 ± .038	1.116 ± 0.002	36.850 ± .034
5	117.093 ± .038	1.200 ± 0.002	31.980 ± .033
6	108.180 ± .038	1.261 ± 0.002	20.690 ± .026

TABLE II

SUMMARY OF THE EXPERIMENTAL ARGON DIFFRACTION DATA

Normalized by the Checkpoint Intensity

<u>θ</u> <u>Degrees</u>	<u>Empty</u> <u>Cell</u>	<u>Argon</u> <u>Run 1</u>	<u>Argon</u> <u>Run 2</u>	<u>Argon</u> <u>Run 3</u>	<u>Argon</u> <u>Run 4</u>	<u>Argon</u> <u>Run 5</u>	<u>Argon</u> <u>Run 6</u>
0.75	0.1989	0.6297	0.7453	0.4579	0.3721	0.2877	0.2118
1.00	0.1647	0.5409	0.6182	0.4161	0.3419	0.2601	0.2006
1.25	0.1549	0.4751	0.5349	0.3721	0.3084	0.2454	0.1935
1.50	0.1527	0.4327	0.4952	0.3583	0.3035	0.2310	0.2032
1.75	0.1567	0.4046	0.4728	0.3394	0.2863	0.2326	0.1940
2.00	0.1636	0.4195	0.4485	0.3311	0.2836	0.2406	0.2133
2.25	0.1825	0.3896	0.4323	0.3408	0.3057	0.2296	0.2207
2.50	0.2034	0.4020	0.4552	0.3409	0.2934	0.2546	0.2368
2.75	0.2340	0.4168	0.4781	0.3721	0.3382	0.2797	0.2603
3.00	0.2513	0.4602	0.4842	0.4123	0.3509	0.2928	0.2543
3.25	0.2314	0.4556	0.4992	0.3990	0.3795	0.3051	0.2627
3.50	0.2530	0.5019	0.5537	0.4808	0.3926	0.3343	0.3038
3.75	0.3003	0.5898	0.6174	0.5007	0.4412	0.3887	0.3480
4.00	0.2743	0.6207	0.6829	0.5845	0.5177	0.4362	0.3806
4.25	0.2740	0.7121	0.7463	0.6744	0.5856	0.4862	0.4151
4.50	0.2803	0.8394	0.8827	0.7719	0.6816	0.5728	0.5005
4.75	0.3103	0.9756	1.0254	0.9369	0.8365	0.7103	0.6195
5.00	0.3098	1.1636	1.1910	1.1192	1.0109	0.9066	0.7565
5.25	0.3255	1.3842	1.3759	1.3462	1.2748	1.1470	0.9755
5.50	0.3497	1.6463	1.5888	1.6679	1.5668	1.4832	1.3046
5.75	0.4692	1.8946	1.7761	1.9159	1.9187	1.8854	1.7434
6.00	0.3441	1.9269	1.7767	2.0697	2.0918	2.1126	2.0424
6.25	0.3447	1.8791	1.7440	2.0555	2.0582	2.1911	2.1927
6.50	0.3806	1.7807	1.6665	1.9002	1.9222	2.0640	2.0587
6.75	0.3678	1.5978	1.5017	1.7126	1.7090	1.7482	1.6971
7.00	0.3745	1.4122	1.3640	1.4848	1.4695	1.4568	1.4407
7.25	0.3839	1.2164	1.2156	1.2632	1.2539	1.2455	1.1779
7.50	0.3878	1.1302	1.0900	1.1385	1.0958	1.0844	1.0012
7.75	0.4013	1.0011	1.0162	1.0245	1.0000	0.9506	0.8972

TABLE II (con't)

<u>θ</u> <u>Degrees</u>	<u>Empty</u> <u>Cell</u>	<u>Argon</u> <u>Run 1</u>	<u>Argon</u> <u>Run 2</u>	<u>Argon</u> <u>Run 3</u>	<u>Argon</u> <u>Run 4</u>	<u>Argon</u> <u>Run 5</u>	<u>Argon</u> <u>Run 6</u>
8.00	0.4283	0.9414	0.9659	0.9435	0.9220	0.8733	0.8248
8.25	0.4293	0.9254	0.9236	0.9099	0.8605	0.8410	0.7991
8.50	0.4513	0.8775	0.8768	0.8443	0.8202	0.7785	0.7373
8.75	0.6532	0.9425	0.9661	0.9137	0.8982	0.8399	0.7861
9.00	0.4535	0.8423	0.8522	0.8082	0.8071	0.7615	0.7120
9.25	0.5885	0.8441	0.9324	0.8463	0.8380	0.7820	0.7437
9.50	0.6631	0.9100	0.9329	0.9104	0.9054	0.8300	0.8042
9.75	0.5455	0.8630	0.9113	0.8619	0.8526	0.8021	0.7712
10.00	0.8963	1.0231	1.0617	1.0042	0.9821	0.9569	0.9097
10.25	2.0247	1.5084	1.6135	1.4846	1.5172	1.4520	1.4447
10.50	0.7813	0.9738	1.0261	0.9862	0.9542	0.9617	0.9146
10.75	0.5144	0.8828	0.8921	0.9111	0.8377	0.8416	0.8153
11.00	0.6046	0.9311	0.9721	0.9733	0.9181	0.8996	0.8531
11.25	1.3890	1.3075	1.3512	1.3356	1.2509	1.2598	1.2329
11.50	4.4631	2.7304	2.8006	2.6919	2.6664	2.6211	2.7265
11.75	6.6110	3.6855	3.8100	3.7012	3.6070	3.5848	3.9979
12.00	1.5882	1.3946	1.4398	1.4465	1.3663	1.3399	1.3502
12.25	0.5353	0.8746	0.9081	0.9152	0.9018	0.8496	0.8246
12.50	0.5311	0.8299	0.8859	0.8777	0.8443	0.8419	0.8136
12.75	0.5276	0.8446	0.8606	0.8673	0.8591	0.8315	0.7991
13.00	0.5495	0.7661	0.8310	0.8507	0.8178	0.8007	0.7355
13.25	0.5260	0.7682	0.8148	0.7585	0.7866	0.7611	0.7202
13.50	0.5186	0.7518	0.7446	0.7538	0.7563	0.7470	0.6816
13.75	0.5134	0.7106	0.7541	0.7112	0.7062	0.6953	0.6536
14.00	0.5112	0.6944	0.7299	0.6680	0.6965	0.6864	0.6538
14.25	0.5219	0.6825	0.7155	0.6825	0.6834	0.6779	0.6459
14.50	0.5163	0.6511	0.6895	0.6771	0.6810	0.6502	0.6166
14.75	0.5418	0.6938	0.7045	0.7098	0.6724	0.6364	0.6229
15.00	0.5548	0.6812	0.7254	0.6803	0.6657	0.6373	0.6070
15.25	0.7213	0.7505	0.7719	0.7761	0.7499	0.7253	0.7097
15.50	2.5971	1.6565	1.7283	1.6485	1.6194	1.6211	1.6387
15.75	0.5926	0.6910	0.7046	0.7049	0.6707	0.6529	0.6449

TABLE II (con't)

<u>θ</u> <u>Degrees</u>	<u>Empty</u> <u>Cell</u>	<u>Argon</u> <u>Run 1</u>	<u>Argon</u> <u>Run 2</u>	<u>Argon</u> <u>Run 3</u>	<u>Argon</u> <u>Run 4</u>	<u>Argon</u> <u>Run 5</u>	<u>Argon</u> <u>Run 6</u>
16.00	0.5501	0.6426	0.6890	0.6855	0.6476	0.6302	0.6237
16.25	0.5281	0.6658	0.6657	0.6622	0.6266	0.6299	0.6195
16.50	0.5473	0.6553	0.6948	0.6662	0.6549	0.6504	0.6368
16.75	0.6155	0.6946	0.7153	0.7105	0.6652	0.6757	0.6781
17.00	0.5295	0.6276	0.6690	0.6758	0.6333	0.6420	0.6322
17.25	0.5339	0.6584	0.6619	0.6620	0.6413	0.6362	0.6011
17.50	0.5651	0.6517	0.6881	0.6514	0.6487	0.6467	0.6486
17.75	0.6688	0.6701	0.7442	0.7205	0.6807	0.7134	0.6905
18.00	1.0133	0.8393	0.8925	0.8700	0.8528	0.8636	0.8808
18.25	1.1483	0.9143	0.9606	0.9277	0.9197	0.8831	0.9518
18.50	0.5650	0.6191	0.6638	0.6334	0.6421	0.6159	0.6365
18.75	0.5228	0.5889	0.6380	0.6348	0.6319	0.5924	0.5965
19.00	0.5455	0.6029	0.6220	0.5899	0.6112	0.5827	0.5935
19.25	0.5364	0.6031	0.6243	0.5898	0.6116	0.5916	0.5877
19.50	0.5410	0.5922	0.6146	0.5875	0.5849	0.5905	0.5856
19.75	0.6100	0.6055	0.6491	0.6275	0.6285	0.6095	0.6128
20.00	0.6879	0.6399	0.6911	0.6495	0.6594	0.6340	0.6620
20.25	2.1217	1.3641	1.4000	1.3362	1.3604	1.3650	1.4068
20.50	1.2289	0.8796	0.9601	0.9003	0.9162	0.8895	0.9437
20.75	0.5958	0.5940	0.6315	0.6121	0.6019	0.5865	0.5956
21.00	0.7576	0.6661	0.6830	0.6438	0.6851	0.6678	0.6678
21.25	0.6299	0.6061	0.6270	0.6203	0.5918	0.5944	0.6103
21.50	0.9180	0.7674	0.7860	0.7332	0.7462	0.7530	0.7626
21.75	1.8854	1.2224	1.2508	1.1998	1.2205	1.2354	1.2665
22.00	1.1569	0.8462	0.8850	0.8421	0.8387	0.8592	0.8768
22.25	0.5608	0.5601	0.5693	0.5501	0.5481	0.5477	0.5521
22.50	0.5375	0.5432	0.5616	0.5382	0.5282	0.5418	0.5388
22.75	0.5565	0.5332	0.5701	0.5258	0.5473	0.5643	0.5504
23.00	0.5541	0.5308	0.5509	0.5251	0.5169	0.5610	0.5539
23.25	0.7118	0.6314	0.6530	0.5915	0.6254	0.6350	0.6542
23.50	0.7012	0.6184	0.6338	0.6141	0.5851	0.6238	0.6283
23.75	0.5376	0.5233	0.5557	0.5351	0.5396	0.5350	0.5351

TABLE II (con't)

<u>θ</u> <u>Degrees</u>	<u>Empty</u> <u>Cell</u>	<u>Argon</u> <u>Run 1</u>	<u>Argon</u> <u>Run 2</u>	<u>Argon</u> <u>Run 3</u>	<u>Argon</u> <u>Run 4</u>	<u>Argon</u> <u>Run 5</u>	<u>Argon</u> <u>Run 6</u>
24.00	0.5305	0.5095	0.5491	0.5113	0.5291	0.5339	0.5195
24.25	0.7366	0.5981	0.6464	0.6065	0.6058	0.6020	0.6497
24.50	0.5325	0.4808	0.5210	0.5207	0.5215	0.5237	0.5059
24.75	0.5194	0.5014	0.5362	0.5046	0.5079	0.5033	0.5005
25.00	0.5163	0.4881	0.5322	0.5072	0.4987	0.4974	0.5020
25.25	0.5077	0.5024	0.5174	0.5023	0.5099	0.5053	0.4864
25.50	0.5209	0.4842	0.5209	0.5073	0.5174	0.5030	0.4889
25.75	0.8097	0.6197	0.6609	0.6214	0.6338	0.6313	0.6702
26.00	0.6230	0.5311	0.5425	0.5462	0.5325	0.5496	0.5509
26.25	0.5102	0.4774	0.5052	0.4805	0.4740	0.4794	0.4747
26.50	0.5064	0.4508	0.4923	0.4730	0.4569	0.4836	0.4787
26.75	0.5057	0.4612	0.4954	0.4875	0.4672	0.4834	0.4743
27.00	0.5151	0.4514	0.4883	0.4732	0.4663	0.4654	0.4731
27.25	0.5024	0.4623	0.4908	0.4815	0.4657	0.4718	0.4665
27.50	0.5271	0.4443	0.4843	0.4718	0.4799	0.4630	0.4700
27.75	1.0182	0.7023	0.7379	0.7089	0.7144	0.7163	0.7416
28.00	0.6995	0.5381	0.5716	0.5246	0.5511	0.5545	0.5475
28.25	0.5630	0.4746	0.5119	0.4818	0.4817	0.4912	0.4836
28.50	0.5515	0.4593	0.4998	0.4587	0.4665	0.4815	0.4651
28.75	0.5286	0.4381	0.4794	0.4489	0.4521	0.4602	0.4526
29.00	1.0901	0.7226	0.7583	0.7337	0.7137	0.7334	0.7763
29.25	0.7179	0.5148	0.5668	0.5487	0.5331	0.5328	0.5635
29.50	0.4951	0.4284	0.4629	0.4510	0.4345	0.4373	0.4392
29.75	0.5004	0.4338	0.4619	0.4321	0.4382	0.4302	0.4467
30.00	0.4948	0.4181	0.4554	0.4180	0.4497	0.4275	0.4560
30.25	0.9372	0.6281	0.6928	0.6687	0.6497	0.6414	0.6913
30.50	0.6296	0.4804	0.5122	0.4940	0.4995	0.5140	0.5273
30.75	0.4917	0.4137	0.4388	0.4203	0.4392	0.4260	0.4232
31.00	0.6044	0.4498	0.4897	0.4622	0.4692	0.4693	0.4851
31.25	0.4925	0.4036	0.4496	0.4380	0.4392	0.4171	0.4428
31.50	0.5012	0.3971	0.4263	0.4159	0.4181	0.4156	0.4113
31.75	0.7824	0.5454	0.5910	0.5658	0.5622	0.5564	0.5745

TABLE II (con't)

<u>θ</u> <u>Degrees</u>	<u>Empty</u> <u>Cell</u>	<u>Argon</u> <u>Run 1</u>	<u>Argon</u> <u>Run 2</u>	<u>Argon</u> <u>Run 3</u>	<u>Argon</u> <u>Run 4</u>	<u>Argon</u> <u>Run 5</u>	<u>Argon</u> <u>Run 6</u>
32.00	0.6420	0.4814	0.5150	0.4986	0.5155	0.4857	0.4941
32.25	0.5280	0.4178	0.4561	0.4085	0.4410	0.4442	0.4439
32.50	0.5769	0.4380	0.4856	0.4364	0.4722	0.4564	0.4777
32.75	0.5158	0.4066	0.4329	0.4202	0.4174	0.4121	0.4186
33.00	0.4422	0.3693	0.4129	0.3790	0.3898	0.3829	0.3788
33.25	0.4613	0.3808	0.4021	0.3965	0.3850	0.3798	0.3854
33.50	0.4599	0.3533	0.3973	0.3833	0.3744	0.3871	0.3721
33.75	0.4658	0.3628	0.3937	0.4007	0.3842	0.3780	0.4165
34.00	0.6867	0.4638	0.5278	0.4930	0.5061	0.4782	0.5222
34.25	0.6047	0.4212	0.4691	0.4350	0.4614	0.4328	0.4413
34.50	0.4513	0.3722	0.3958	0.3683	0.3815	0.3635	0.3758
34.75	0.4419	0.3693	0.3793	0.3792	0.3851	0.3671	0.3786
35.00	0.6054	0.4203	0.4498	0.4439	0.4456	0.4372	0.4624
35.25	0.4660	0.3714	0.4059	0.3765	0.3837	0.3982	0.4043
35.50	0.4205	0.3402	0.3733	0.3518	0.3650	0.3652	0.3451
35.75	0.4159	0.3317	0.3638	0.3661	0.3429	0.3633	0.3501
36.00	0.4110	0.3390	0.3552	0.3489	0.3586	0.3583	0.3630
36.25	0.4208	0.3409	0.3694	0.3643	0.3548	0.3569	0.3524
36.50	0.4313	0.3462	0.3710	0.3640	0.3690	0.3617	0.3618
36.75	0.4174	0.3398	0.3658	0.3535	0.3452	0.3526	0.3564
37.00	0.4284	0.3399	0.3477	0.3497	0.3538	0.3530	0.3462
37.25	0.4286	0.3202	0.3536	0.3412	0.3664	0.3366	0.3401
37.50	0.4238	0.3245	0.3495	0.3539	0.3431	0.3448	0.3346
37.75	0.4941	0.3671	0.3862	0.3835	0.3919	0.3801	0.3900
38.00	0.4751	0.3396	0.3678	0.3618	0.3864	0.3671	0.3842
38.25	0.4535	0.3273	0.3699	0.3547	0.3844	0.3562	0.3594
38.50	0.4329	0.3269	0.3710	0.3567	0.3573	0.3494	0.3606
38.75	0.4142	0.3129	0.3518	0.3266	0.3444	0.3311	0.3428
39.00	0.4145	0.2986	0.3481	0.3367	0.3483	0.3374	0.3418
39.25	0.4063	0.3090	0.3365	0.3283	0.3202	0.3360	0.3485
39.50	0.4123	0.3109	0.3476	0.3185	0.3387	0.3323	0.3328
39.75	0.4128	0.3046	0.3302	0.3131	0.3192	0.3177	0.3181

TABLE II (con't)

<u>θ</u> <u>Degrees</u>	<u>Empty</u> <u>Cell</u>	<u>Argon</u> <u>Run 1</u>	<u>Argon</u> <u>Run 2</u>	<u>Argon</u> <u>Run 3</u>	<u>Argon</u> <u>Run 4</u>	<u>Argon</u> <u>Run 5</u>	<u>Argon</u> <u>Run 6</u>
40.00	0.3924	0.2977	0.3371	0.3183	0.3075	0.3212	0.3197
40.25	0.4108	0.3083	0.3405	0.3317	0.3288	0.3201	0.3263
40.50	0.3907	0.2986	0.3264	0.3124	0.3276	0.3111	0.3202
40.75	0.4660	0.3202	0.3699	0.3585	0.3642	0.3738	0.3614
41.00	0.4329	0.3214	0.3594	0.3380	0.3344	0.3306	0.3466
41.25	0.4192	0.2976	0.3204	0.3211	0.3187	0.3131	0.3255
41.50	0.4025	0.2989	0.3249	0.3020	0.3122	0.3085	0.3039
41.75	0.4038	0.2879	0.3300	0.3095	0.3131	0.3179	0.3221
42.00	0.4475	0.3217	0.3517	0.3421	0.3508	0.3537	0.3660
42.25	0.4373	0.2960	0.3412	0.3384	0.3365	0.3203	0.3582
42.50	0.4261	0.2990	0.3332	0.3296	0.3183	0.3197	0.3374
42.75	0.3940	0.2817	0.3151	0.3139	0.3106	0.3042	0.3047
43.00	0.3930	0.2878	0.3215	0.3127	0.3155	0.3085	0.3100
43.25	0.4706	0.3262	0.3622	0.3587	0.3562	0.3522	0.3428
43.50	0.3994	0.2780	0.3205	0.3114	0.3098	0.3060	0.3073
43.75	0.3998	0.2746	0.3200	0.3103	0.3183	0.2982	0.3064
44.00	0.4104	0.2953	0.3344	0.3282	0.3137	0.3083	0.3090
44.25	0.4007	0.2797	0.3144	0.3244	0.2971	0.2924	0.2990
44.50	0.3844	0.2764	0.3058	0.3229	0.3075	0.2947	0.2910
44.75	0.3838	0.2764	0.3107	0.3041	0.3010	0.3065	0.2973
45.00	0.3875	0.2742	0.2982	0.3014	0.3093	0.2931	0.3018
45.25	0.3887	0.2744	0.3044	0.3019	0.2934	0.2905	0.2964
45.50	0.3910	0.2793	0.3099	0.3124	0.3006	0.2943	0.2987
45.75	0.4441	0.3137	0.3304	0.3417	0.3383	0.3320	0.3344
46.00	0.4068	0.2728	0.3084	0.3038	0.3056	0.3087	0.3070
46.25	0.3904	0.2648	0.3008	0.2991	0.3096	0.3018	0.3121
46.50	0.3922	0.2703	0.3043	0.2867	0.3125	0.2945	0.2979
46.75	0.3931	0.2704	0.3039	0.2930	0.2895	0.2995	0.3020
47.00	0.3892	0.2703	0.2906	0.3004	0.2952	0.2954	0.2853
47.25	0.3797	0.2706	0.2897	0.2952	0.2844	0.2883	0.2917
47.50	0.4131	0.2799	0.3110	0.3114	0.3086	0.3140	0.3177
47.75	0.3923	0.2693	0.2936	0.3032	0.2964	0.2880	0.3194

TABLE II (con't)

<u>θ</u> <u>Degrees</u>	<u>Empty</u> <u>Cell</u>	<u>Argon</u> <u>Run 1</u>	<u>Argon</u> <u>Run 2</u>	<u>Argon</u> <u>Run 3</u>	<u>Argon</u> <u>Run 4</u>	<u>Argon</u> <u>Run 5</u>	<u>Argon</u> <u>Run 6</u>
48.00	0.3900	0.2822	0.3028	0.2926	0.2986	0.2938	0.3112
48.25	0.3908	0.2701	0.3011	0.2973	0.2919	0.2922	0.3132
48.50	0.3860	0.2572	0.2971	0.2991	0.2946	0.2888	0.3049
48.75	0.3724	0.2698	0.2888	0.2940	0.2834	0.2885	0.2895
49.00	0.3857	0.2733	0.3072	0.2955	0.2924	0.2870	0.3085
49.25	0.3889	0.2687	0.2976	0.2963	0.2913	0.2975	0.3154
49.50	0.3989	0.2819	0.3048	0.3034	0.2908	0.2942	0.3159
49.75	0.3996	0.2774	0.2935	0.2959	0.2944	0.2929	0.3129
50.00	0.3803	0.2855	0.3077	0.2934	0.2926	0.2859	0.3077
50.25	0.3894	0.2617	0.2979	0.2901	0.2828	0.2955	0.3048
50.50	0.3869	0.2692	0.2971	0.2875	0.2857	0.2868	0.2981
50.75	0.3887	0.2735	0.2983	0.3065	0.2893	0.2865	0.3181
51.00	0.4098	0.2687	0.3073	0.3032	0.3040	0.2848	0.3212
51.25	0.4201	0.2785	0.3185	0.3084	0.2914	0.3180	0.3341
51.50	0.4162	0.2800	0.3129	0.3020	0.2986	0.2988	0.3109
51.75	0.4135	0.2923	0.3113	0.2949	0.3065	0.2965	0.3091
52.00	0.4222	0.2895	0.3135	0.3098	0.2975	0.3130	0.3295
52.25	0.3953	0.2779	0.3053	0.3074	0.2897	0.2959	0.3093
52.50	0.4141	0.2754	0.3115	0.3151	0.3034	0.2980	0.3237
52.75	0.4043	0.2838	0.3071	0.3077	0.3065	0.2962	0.3170
53.00	0.4029	0.2871	0.2952	0.2978	0.2941	0.2845	0.3097
53.25	0.4246	0.2881	0.3140	0.3197	0.3153	0.2974	0.3267
53.50	0.4040	0.2780	0.3085	0.3020	0.3030	0.2868	0.3199
53.75	0.4279	0.2916	0.3292	0.3178	0.3122	0.3011	0.3361
54.00	0.4111	0.2844	0.3140	0.3073	0.3197	0.2989	0.3158
54.25	0.4347	0.2917	0.3166	0.2950	0.3009	0.3048	0.3420
54.50	0.4365	0.2933	0.3275	0.3049	0.3090	0.3078	0.3392
54.75	0.4270	0.2934	0.3113	0.3071	0.3032	0.3022	0.3243
55.00	0.4370	0.2978	0.3192	0.3071	0.3206	0.3040	0.3352
55.25	0.4351	0.2971	0.3226	0.3120	0.3103	0.3145	0.3386
55.50	0.4290	0.2905	0.3074	0.3031	0.3067	0.3059	0.3200
55.75	0.4365	0.3005	0.3096	0.3079	0.3070	0.3108	0.3319

TABLE II (con't)

<u>θ</u> <u>Degrees</u>	<u>Empty</u> <u>Cell</u>	<u>Argon</u> <u>Run 1</u>	<u>Argon</u> <u>Run 2</u>	<u>Argon</u> <u>Run 3</u>	<u>Argon</u> <u>Run 4</u>	<u>Argon</u> <u>Run 5</u>	<u>Argon</u> <u>Run 6</u>
56.00	0.4301	0.3184	0.3142	0.2999	0.3057	0.3097	0.3384
56.25	0.4308	0.2945	0.3064	0.3167	0.3053	0.3019	0.3241
56.50	0.4418	0.2956	0.3144	0.3131	0.2991	0.3049	0.3408
56.75	0.4606	0.3040	0.3248	0.3047	0.3203	0.3351	0.3344
57.00	0.4524	0.3020	0.3195	0.3266	0.3168	0.3210	0.3431
57.25	0.4632	0.3044	0.3273	0.3199	0.3290	0.3331	0.3540
57.50	0.4457	0.3005	0.3181	0.3129	0.3109	0.3335	0.3410
57.75	0.4713	0.3240	0.3378	0.3398	0.3208	0.3538	0.3540
58.00	0.4442	0.3123	0.3124	0.3236	0.3114	0.3371	0.3305
58.25	0.4847	0.3205	0.3366	0.3179	0.3265	0.3504	0.3742
58.50	0.4526	0.3074	0.3164	0.3110	0.3143	0.3234	0.3629
58.75	0.4504	0.3250	0.3228	0.3134	0.3190	0.3380	0.3595
59.00	0.4533	0.3088	0.3129	0.3122	0.3269	0.3254	0.3507
59.25	0.4671	0.3296	0.3325	0.3248	0.3349	0.3462	0.3766
59.50	0.4591	0.3199	0.3411	0.3329	0.3401	0.3249	0.3628
59.75	0.4587	0.3079	0.3300	0.3098	0.3145	0.3414	0.3420
60.00	0.4513	0.3188	0.3368	0.3187	0.3227	0.3292	0.3611

TABLE III

ATOMIC AND INCOHERENT SCATTERING FACTORS FOR ARGON
 f_d^2 interpolated from values calculated by Berghuis et. al.⁵⁴
 using $\Delta f' = 0.18$, and $\Delta f'' = 0.24$ from Cromer.⁵⁵ I^{inc} interpolated
 from values for Ca^{++} , K^+ and Cl^- calculated by Freeman.⁵²

θ^*	$\frac{\sin \theta}{\lambda}$	s	f_d^2	$(1/B^2) I^{inc}$
0.0	0.0	0.000	330.5700	0.0
1.0	0.0245	0.308	326.7740	.1437
2.0	0.0491	0.617	314.6435	.5719
3.0	0.0736	0.925	296.1972	1.1876
4.0	0.0981	1.233	273.5164	1.9130
5.0	0.123	1.541	248.5668	2.6872
6.0	0.147	1.848	223.0694	3.4651
7.0	0.171	2.155	198.3895	4.2148
8.0	0.196	2.461	175.6541	4.9161
9.0	0.220	2.766	155.6152	5.5587
10.0	0.244	3.070	138.3474	6.1401
12.0	0.292	3.676	111.2861	7.1364
14.0	0.340	4.278	92.1236	7.9994
16.0	0.388	4.874	78.8420	8.7236
18.0	0.435	5.464	69.4318	9.3003
20.0	0.481	6.048	62.3936	9.7628
22.5	0.538	6.767	55.6263	10.2495
25.0	0.594	7.473	50.1294	10.6718
27.5	0.649	8.165	45.3012	11.0416
30.0	0.703	8.841	40.8880	11.3722
35.0	0.807	10.142	33.1093	11.9329
40.0	0.904	11.366	26.7444	12.3804
45.0	0.995	12.503	21.5947	12.7119
50.0	1.077	13.545	17.6515	12.9558
55.0	1.152	14.484	14.7081	13.1352
60.0	1.218	15.313	12.5300	13.2707

* Values for molybdenum K_{α} radiation, $\lambda = 0.7107 \text{ \AA}$.

TABLE IV

ATOMIC AND INCOHERENT SCATTERING FACTORS FOR BERYLLIUM
 f_d^2 interpolated from values calculated by Berghuis et. al.⁵⁴
 using $\Delta f' = 0$ and $\Delta f'' = 0$
 I^{inc} interpolated from values calculated by Freeman.⁵²

θ^*	$\frac{\sin \theta}{\lambda}$	s	f_d^2	$(1/B^2) I^{inc}$
0.0	0.0	0.000	16.0000	0.0
1.0	0.0245	0.308	15.4684	.3961
2.0	0.0491	0.617	13.8090	.7764
3.0	0.0736	0.925	11.6787	1.1255
4.0	0.0981	1.233	9.5495	1.4332
5.0	0.123	1.541	7.6921	1.6942
6.0	0.147	1.848	6.2151	1.9076
7.0	0.171	2.155	5.1352	2.0756
8.0	0.196	2.461	4.3494	2.2032
9.0	0.220	2.766	3.7998	2.2974
10.0	0.244	3.070	3.4125	2.3665
12.0	0.292	3.676	2.9225	2.4646
14.0	0.340	4.278	2.6132	2.5776
16.0	0.388	4.874	2.3696	2.7056
18.0	0.435	5.464	2.1500	2.8273
20.0	0.481	6.048	1.9399	2.9401
22.5	0.538	6.767	1.6875	3.0694
25.0	0.594	7.473	1.4508	3.1828
27.5	0.649	8.165	1.2376	3.2778
30.0	0.703	8.841	1.0503	3.3551
35.0	0.807	10.142	0.7520	3.4659
40.0	0.904	11.366	0.5385	3.5282
45.0	0.995	12.503	0.3931	3.5554
50.0	1.077	13.545	0.2938	3.5613
55.0	1.152	14.484	0.2263	3.5572
60.0	1.218	15.313	0.1804	3.5505

* Values for molybdenum K_{α} radiation, $\lambda = 0.7107 \text{ \AA}$.

TABLE V

ABSORPTION FACTORS

Argon Sample Density = 0.9819 gm/cc

θ	<u>Coherent</u>			<u>Incoherent</u>		
	ASSC	ACC	ACSC	ASSC	ACC	ACSC
0	0.4012	0.9176	0.4420	0.4012	0.9176	0.4420
2	0.4123	0.9170	0.4708	0.4122	0.9170	0.4708
4	0.4233	0.9163	0.5031	0.4231	0.9163	0.5030
6	0.4344	0.9158	0.5359	0.4340	0.9158	0.5357
8	0.4454	0.9154	0.5680	0.4447	0.9154	0.5677
10	0.4562	0.9153	0.5982	0.4552	0.9152	0.5978
12	0.4668	0.9155	0.6240	0.4655	0.9154	0.6236
14	0.4772	0.9162	0.6432	0.4754	0.9160	0.6428
16	0.4871	0.9172	0.6567	0.4849	0.9170	0.6563
18	0.4967	0.9184	0.6662	0.4940	0.9182	0.6658
20	0.5057	0.9197	0.6729	0.5026	0.9195	0.6725
22	0.5142	0.9210	0.6778	0.5105	0.9208	0.6774
24	0.5220	0.9223	0.6813	0.5179	0.9220	0.6810
26	0.5292	0.9236	0.6839	0.5246	0.9232	0.6836
28	0.5357	0.9247	0.6858	0.5306	0.9243	0.6855
30	0.5415	0.9257	0.6873	0.5359	0.9253	0.6870
32	0.5466	0.9265	0.6884	0.5405	0.9262	0.6881
34	0.5509	0.9273	0.6893	0.5443	0.9268	0.6889
36	0.5546	0.9278	0.6899	0.5475	0.9274	0.6896
38	0.5576	0.9283	0.6905	0.5500	0.9278	0.6901
40	0.5600	0.9286	0.6909	0.5519	0.9281	0.6905
42	0.5619	0.9288	0.6912	0.5532	0.9283	0.6908
44	0.5633	0.9289	0.6915	0.5539	0.9283	0.6911
46	0.5641	0.9289	0.6917	0.5542	0.9283	0.6913
48	0.5645	0.9288	0.6918	0.5540	0.9282	0.6913
50	0.5645	0.9286	0.6919	0.5533	0.9279	0.6914
52	0.5640	0.9283	0.6919	0.5520	0.9276	0.6913
54	0.5631	0.9279	0.6918	0.5503	0.9271	0.6912
56	0.5616	0.9273	0.6916	0.5481	0.9264	0.6910
58	0.5597	0.9267	0.6914	0.5454	0.9257	0.6907
60	0.5573	0.9258	0.6910	0.5421	0.9247	0.6903

Table V. (cont.)

Argon Sample Density = 0.9096 gm/cc

θ	<u>Coherent</u>			<u>Incoherent</u>		
	ASSC	ACC	ACSC	ASSC	ACC	ACSC
0	0.4293	0.9176	0.4642	0.4293	0.9176	0.4642
2	0.4401	0.9170	0.4918	0.4401	0.9170	0.4918
4	0.4510	0.9163	0.5228	0.4509	0.9163	0.5227
6	0.4619	0.9158	0.5542	0.4615	0.9158	0.5540
8	0.4727	0.9154	0.5848	0.4720	0.9154	0.5845
10	0.4833	0.9153	0.6135	0.4823	0.9152	0.6131
12	0.4936	0.9155	0.6380	0.4923	0.9154	0.6376
14	0.5037	0.9162	0.6563	0.5020	0.9160	0.6559
16	0.5134	0.9172	0.6691	0.5112	0.9170	0.6687
18	0.5226	0.9184	0.6781	0.5200	0.9182	0.6777
20	0.5314	0.9197	0.6845	0.5283	0.9195	0.6841
22	0.5396	0.9210	0.6891	0.5360	0.9208	0.6888
24	0.5471	0.9223	0.6926	0.5431	0.9220	0.6922
26	0.5541	0.9236	0.6951	0.5496	0.9232	0.6948
28	0.5603	0.9247	0.6970	0.5554	0.9243	0.6966
30	0.5659	0.9257	0.6984	0.5604	0.9253	0.6981
32	0.5707	0.9265	0.6995	0.5648	0.9262	0.6992
34	0.5749	0.9273	0.7003	0.5684	0.9268	0.7000
36	0.5784	0.9278	0.7010	0.5714	0.9274	0.7006
38	0.5812	0.9283	0.7015	0.5738	0.9278	0.7012
40	0.5835	0.9286	0.7020	0.5756	0.9281	0.7016
42	0.5853	0.9288	0.7023	0.5768	0.9283	0.7019
44	0.5866	0.9289	0.7025	0.5774	0.9283	0.7021
46	0.5874	0.9289	0.7027	0.5776	0.9283	0.7023
48	0.5877	0.9288	0.7028	0.5773	0.9282	0.7024
50	0.5876	0.9286	0.7029	0.5766	0.9279	0.7024
52	0.5870	0.9283	0.7029	0.5753	0.9276	0.7023
54	0.5860	0.9279	0.7028	0.5736	0.9271	0.7022
56	0.5846	0.9273	0.7026	0.5713	0.9264	0.7020
58	0.5826	0.9267	0.7023	0.5685	0.9257	0.7017
60	0.5802	0.9258	0.7019	0.5652	0.9247	0.7012

Table V (cont.)

Argon Sample Density = 1.0493 gm/cc

θ	<u>Coherent</u>			<u>Incoherent</u>		
	<u>ASSC</u>	<u>ACC</u>	<u>ACSC</u>	<u>ASSC</u>	<u>ACC</u>	<u>ACSC</u>
0	0.3768	0.9176	0.4227	0.3768	0.9176	0.4227
2	0.3879	0.9170	0.4523	0.3879	0.9170	0.4523
4	0.3991	0.9163	0.4858	0.3989	0.9163	0.4857
6	0.4103	0.9158	0.5199	0.4099	0.9158	0.5196
8	0.4214	0.9154	0.5532	0.4208	0.9154	0.5529
10	0.4324	0.9153	0.5847	0.4315	0.9152	0.5843
12	0.4433	0.9155	0.6117	0.4419	0.9154	0.6112
14	0.4538	0.9162	0.6318	0.4520	0.9160	0.6313
16	0.4640	0.9172	0.6459	0.4618	0.9170	0.6455
18	0.4738	0.9184	0.6557	0.4711	0.9182	0.6553
20	0.4830	0.9197	0.6627	0.4790	0.9195	0.6624
22	0.4917	0.9210	0.6678	0.4881	0.9208	0.6674
24	0.4998	0.9223	0.6714	0.4957	0.9220	0.6711
26	0.5073	0.9236	0.6741	0.5026	0.9232	0.6738
28	0.5140	0.9247	0.6761	0.5088	0.9243	0.6758
30	0.5200	0.9257	0.6776	0.5143	0.9253	0.6773
32	0.5252	0.9265	0.6787	0.5190	0.9262	0.6784
34	0.5297	0.9273	0.6796	0.5230	0.9268	0.6792
36	0.5335	0.9278	0.6802	0.5263	0.9274	0.6799
38	0.5367	0.9283	0.6808	0.5289	0.9278	0.6804
40	0.5392	0.9286	0.6812	0.5309	0.9281	0.6808
42	0.5412	0.9288	0.6816	0.5323	0.9283	0.6812
44	0.5426	0.9289	0.6818	0.5332	0.9283	0.6814
46	0.5436	0.9289	0.6820	0.5335	0.9283	0.6816
48	0.5441	0.9288	0.6822	0.5333	0.9282	0.6817
50	0.5441	0.9286	0.6822	0.5327	0.9279	0.6817
52	0.5437	0.9283	0.6822	0.5315	0.9276	0.6817
54	0.5428	0.9279	0.6822	0.5299	0.9271	0.6816
56	0.5414	0.9273	0.6820	0.5277	0.9264	0.6814
58	0.5395	0.9267	0.6818	0.5250	0.9257	0.6812
60	0.5317	0.9258	0.6815	0.5218	0.9247	0.6808

Table V (cont.)

Argon Sample Density = 1.1162 gm/cc

θ	Coherent			Incoherent		
	ASSC	ACC	ACSC	ASSC	ACC	ACSC
0	0.3540	0.9176	0.4045	0.3540	0.9176	0.4045
2	0.3652	0.9170	0.4350	0.3651	0.9170	0.4350
4	0.3765	0.9163	0.4695	0.3763	0.9163	0.4694
6	0.3877	0.9158	0.5047	0.3873	0.9158	0.5045
8	0.3990	0.9154	0.5393	0.3983	0.9154	0.5390
10	0.4101	0.9153	0.5720	0.4091	0.9152	0.5716
12	0.4211	0.9155	0.6001	0.4198	0.9154	0.5996
14	0.4319	0.9162	0.6210	0.4300	0.9160	0.6206
16	0.4422	0.9172	0.6357	0.4400	0.9170	0.6353
18	0.4522	0.9184	0.6459	0.4494	0.9182	0.6455
20	0.4616	0.9197	0.6532	0.4584	0.9195	0.6528
22	0.4706	0.9210	0.6584	0.4669	0.9208	0.6581
24	0.4789	0.9223	0.6622	0.4747	0.9220	0.6619
26	0.4865	0.9236	0.6649	0.4818	0.9232	0.6646
28	0.4934	0.9247	0.6669	0.4882	0.9243	0.6667
30	0.4996	0.9257	0.6685	0.4939	0.9253	0.6682
32	0.5050	0.9265	0.6696	0.4987	0.9262	0.6693
34	0.5097	0.9273	0.6705	0.5029	0.9268	0.6701
36	0.5136	0.9278	0.6712	0.5063	0.9274	0.6708
38	0.5169	0.9283	0.6717	0.5090	0.9278	0.6714
40	0.5195	0.9286	0.6721	0.5111	0.9281	0.6718
42	0.5216	0.9288	0.6725	0.5126	0.9283	0.6721
44	0.5232	0.9289	0.6728	0.5136	0.9283	0.6724
46	0.5242	0.9289	0.6730	0.5140	0.9283	0.6725
48	0.5247	0.9288	0.6731	0.5139	0.9282	0.6727
50	0.5248	0.9286	0.6732	0.5133	0.9279	0.6727
52	0.5245	0.9283	0.6732	0.5121	0.9276	0.6727
54	0.5236	0.9279	0.6732	0.5105	0.9271	0.6726
56	0.5222	0.9273	0.6730	0.5085	0.9264	0.6725
58	0.5204	0.9267	0.6728	0.5058	0.9257	0.6722
60	0.5181	0.9258	0.6725	0.5026	0.9247	0.6719

Table V (cont.)

Argon Sample Density = 1.1995 gm/cc

θ	Coherent			Incoherent		
	ASSC	ACC	ACSC	ASSC	ACC	ACSC
0	0.3271	0.9176	0.3829	0.3271	0.9176	0.3829
2	0.3382	0.9170	0.4144	0.3381	0.9170	0.4142
4	0.3496	0.9163	0.4500	0.3493	0.9163	0.4500
6	0.3609	0.9158	0.4867	0.3604	0.9158	0.4863
8	0.3722	0.9154	0.5227	0.3715	0.9154	0.5224
10	0.3834	0.9153	0.5567	0.3824	0.9152	0.5563
12	0.3947	0.9155	0.5863	0.3934	0.9154	0.5858
14	0.4056	0.9162	0.6080	0.4036	0.9160	0.6077
16	0.4162	0.9172	0.6236	0.4138	0.9170	0.6234
18	0.4263	0.9184	0.6342	0.4234	0.9182	0.6338
20	0.4360	0.9197	0.6418	0.4328	0.9195	0.6415
22	0.4451	0.9210	0.6472	0.4414	0.9208	0.6469
24	0.4537	0.9223	0.6513	0.4494	0.9220	0.6508
26	0.4616	0.9236	0.6539	0.4567	0.9232	0.6536
28	0.4688	0.9247	0.6559	0.4633	0.9243	0.6558
30	0.4750	0.9257	0.6578	0.4693	0.9253	0.6573
32	0.4805	0.9265	0.6588	0.4743	0.9262	0.6584
34	0.4855	0.9273	0.6597	0.4788	0.9268	0.6592
36	0.4896	0.9278	0.6603	0.4823	0.9274	0.6599
38	0.4932	0.9283	0.6611	0.4851	0.9278	0.6607
40	0.4958	0.9286	0.6612	0.4873	0.9281	0.6609
42	0.4981	0.9288	0.6616	0.4890	0.9283	0.6613
44	0.4997	0.9289	0.6620	0.4899	0.9283	0.6615
46	0.5008	0.9289	0.6622	0.4904	0.9283	0.6617
48	0.5014	0.9288	0.6623	0.4905	0.9282	0.6620
50	0.5015	0.9286	0.6625	0.4899	0.9279	0.6617
52	0.5014	0.9283	0.6625	0.4888	0.9276	0.6620
54	0.5006	0.9279	0.6626	0.4873	0.9271	0.6619
56	0.4991	0.9273	0.6624	0.4854	0.9264	0.6619
58	0.4975	0.9267	0.6621	0.4828	0.9257	0.6614
60	0.4952	0.9258	0.6617	0.4798	0.9247	0.6613

Table V (cont.)

Argon Sample Density = 1.2609 gm/cc

θ	<u>Coherent</u>			<u>Incoherent</u>		
	ASSC	ACC	ACSC	ASSC	ACC	ACSC
0	0.3074	0.9176	0.3669	0.3074	0.9176	0.3669
2	0.3185	0.9170	0.3993	0.3182	0.9170	0.3990
4	0.3301	0.9163	0.4357	0.3295	0.9163	0.4359
6	0.3414	0.9158	0.4735	0.3405	0.9158	0.4728
8	0.3525	0.9154	0.5106	0.3518	0.9154	0.5105
10	0.3637	0.9153	0.5454	0.3626	0.9152	0.5451
12	0.3755	0.9155	0.5764	0.3741	0.9154	0.5757
14	0.3865	0.9162	0.5985	0.3841	0.9160	0.5982
16	0.3970	0.9172	0.6147	0.3945	0.9170	0.6150
18	0.4074	0.9184	0.6255	0.4041	0.9182	0.6252
20	0.4172	0.9197	0.6334	0.4140	0.9195	0.6332
22	0.4263	0.9210	0.6390	0.4228	0.9208	0.6389
24	0.4351	0.9223	0.6435	0.4309	0.9220	0.6426
26	0.4433	0.9236	0.6458	0.4382	0.9232	0.6454
28	0.4506	0.9247	0.6477	0.4449	0.9243	0.6478
30	0.4569	0.9257	0.6501	0.4513	0.9253	0.6493
32	0.4622	0.9265	0.6508	0.4563	0.9262	0.6503
34	0.4676	0.9273	0.6519	0.4611	0.9268	0.6510
36	0.4718	0.9278	0.6523	0.4646	0.9274	0.6518
38	0.4757	0.9283	0.6536	0.4674	0.9278	0.6531
40	0.4782	0.9286	0.6532	0.4696	0.9281	0.6530
42	0.4809	0.9288	0.6536	0.4716	0.9283	0.6533
44	0.4825	0.9289	0.6542	0.4725	0.9283	0.6535
46	0.4835	0.9289	0.6544	0.4730	0.9283	0.6538
48	0.4841	0.9288	0.6545	0.4733	0.9282	0.6543
50	0.4842	0.9286	0.6548	0.4727	0.9279	0.6534
52	0.4847	0.9283	0.6547	0.4714	0.9276	0.6541
54	0.4838	0.9279	0.6550	0.4700	0.9271	0.6541
56	0.4819	0.9273	0.6548	0.4684	0.9264	0.6542
58	0.4805	0.9267	0.6542	0.4658	0.9257	0.6535
60	0.4784	0.9258	0.6536	0.4630	0.9247	0.6538

TABLE VIa

SUMMARY OF THE SMOOTH INTENSITY FUNCTIONS

$$j(s) = i(s) + 1$$

BEFORE DIVERGENCE CORRECTION

<u>θ</u> Degrees	<u>S</u> <u>\AA^{-1}</u>	Argon <u>Run 1</u>	Argon <u>Run 2</u>	Argon <u>Run 3</u>	Argon <u>Run 4</u>	Argon <u>Run 5</u>	Argon <u>Run 6</u>
0.	0.	0.669	1.284	0.373	0.271	0.202	0.109
0.25	0.077	0.602	1.036	0.351	0.261	0.197	0.110
0.50	0.154	0.476	0.666	0.305	0.238	0.184	0.112
0.75	0.231	0.381	0.432	0.267	0.217	0.171	0.114
1.00	0.309	0.329	0.359	0.246	0.200	0.158	0.115
1.25	0.386	0.288	0.308	0.219	0.182	0.149	0.116
1.50	0.463	0.263	0.284	0.207	0.175	0.143	0.119
1.75	0.540	0.246	0.262	0.197	0.169	0.137	0.121
2.00	0.617	0.235	0.251	0.192	0.165	0.138	0.126
2.25	0.694	0.232	0.246	0.190	0.169	0.140	0.130
2.50	0.771	0.233	0.248	0.198	0.176	0.144	0.134
2.75	0.848	0.242	0.257	0.208	0.184	0.155	0.141
3.00	0.925	0.256	0.269	0.224	0.198	0.165	0.148
3.25	1.002	0.280	0.290	0.244	0.214	0.182	0.161
3.50	1.079	0.312	0.321	0.271	0.238	0.205	0.183
3.75	1.156	0.350	0.362	0.317	0.271	0.238	0.210
4.00	1.233	0.411	0.417	0.367	0.323	0.281	0.245
4.25	1.310	0.486	0.490	0.448	0.395	0.337	0.296
4.50	1.387	0.594	0.592	0.538	0.481	0.419	0.371
4.75	1.464	0.710	0.709	0.677	0.614	0.543	0.482
5.00	1.541	0.887	0.859	0.847	0.780	0.739	0.628
5.25	1.618	1.095	1.028	1.059	1.030	0.981	0.857
5.50	1.695	1.349	1.227	1.364	1.316	1.326	1.210
5.75	1.772	1.570	1.380	1.585	1.639	1.721	1.659
6.00	1.848	1.686	1.461	1.814	1.894	2.048	2.080
6.25	1.925	1.684	1.470	1.848	1.910	2.185	2.302
6.50	2.002	1.615	1.414	1.755	1.820	2.058	2.156
6.75	2.078	1.475	1.317	1.582	1.634	1.823	1.895

TABLE VIa (con't)

<u>θ</u> <u>Degrees</u>	<u>S_{0-1}</u> <u>A</u>	<u>Argon</u> <u>Run 1</u>	<u>Argon</u> <u>Run 2</u>	<u>Argon</u> <u>Run 3</u>	<u>Argon</u> <u>Run 4</u>	<u>Argon</u> <u>Run 5</u>	<u>Argon</u> <u>Run 6</u>
7.00	2.155	1.332	1.200	1.412	1.441	1.572	1.603
7.25	2.231	1.180	1.087	1.226	1.246	1.318	1.318
7.50	2.308	1.055	0.989	1.084	1.087	1.134	1.107
7.75	2.384	0.963	0.912	0.974	0.968	0.993	0.961
8.00	2.461	0.903	0.862	0.900	0.885	0.891	0.862
8.25	2.537	0.875	0.824	0.855	0.834	0.838	0.805
8.50	2.614	0.843	0.810	0.823	0.802	0.801	0.766
8.75	2.690	0.834	0.801	0.806	0.796	0.777	0.738
9.00	2.766	0.829	0.808	0.809	0.805	0.781	0.746
9.25	2.842	0.831	0.824	0.815	0.821	0.795	0.762
9.50	2.918	0.850	0.846	0.834	0.851	0.815	0.782
9.75	2.994	0.876	0.880	0.865	0.881	0.858	0.822
10.00	3.070	0.903	0.916	0.898	0.909	0.903	0.868
10.25	3.146	0.936	0.945	0.942	0.938	0.952	0.903
10.50	3.222	0.989	0.986	0.980	0.978	1.008	0.966
10.75	3.298	1.050	1.025	1.046	1.015	1.063	0.993
11.00	3.374	1.120	1.079	1.111	1.065	1.107	1.058
11.25	3.450	1.165	1.131	1.177	1.126	1.148	1.119
11.50	3.525	1.187	1.166	1.205	1.161	1.177	1.174
11.75	3.601	1.199	1.188	1.223	1.198	1.200	1.204
12.00	3.676	1.198	1.183	1.225	1.208	1.214	1.214
12.25	3.752	1.181	1.171	1.208	1.208	1.215	1.216
12.50	3.827	1.144	1.141	1.192	1.196	1.213	1.193
12.75	3.902	1.103	1.113	1.153	1.171	1.188	1.162
13.00	3.978	1.064	1.080	1.112	1.145	1.153	1.085
13.25	4.053	1.044	1.048	1.072	1.096	1.104	1.018
13.50	4.128	1.013	1.018	1.002	1.061	1.072	0.976
13.75	4.203	0.991	0.989	0.978	1.026	1.036	0.939
14.00	4.278	0.968	0.972	0.943	0.993	0.999	0.919
14.25	4.352	0.958	0.965	0.943	0.982	0.979	0.900
14.50	4.427	0.959	0.959	0.946	0.968	0.967	0.888
14.75	4.502	0.959	0.957	0.954	0.959	0.950	0.877

TABLE VIa (con't)

θ Degrees	S_{0-1} A	Argon Run 1	Argon Run 2	Argon Run 3	Argon Run 4	Argon Run 5	Argon Run 6
15.00	4.576	0.962	0.959	0.964	0.949	0.942	0.886
15.25	4.651	0.968	0.963	0.978	0.947	0.938	0.903
15.50	4.725	0.978	0.968	0.986	0.951	0.937	0.919
15.75	4.800	0.998	0.976	1.008	0.956	0.960	0.939
16.00	4.874	1.010	0.985	1.026	0.962	0.993	0.957
16.25	4.948	1.016	1.000	1.045	0.969	1.024	0.977
16.50	5.022	1.024	1.011	1.058	0.978	1.045	1.005
16.75	5.096	1.028	1.026	1.071	0.989	1.061	1.032
17.00	5.170	1.030	1.037	1.084	1.001	1.073	1.055
17.25	5.243	1.032	1.046	1.088	1.014	1.078	1.071
17.50	5.317	1.033	1.055	1.084	1.028	1.077	1.083
17.75	5.391	1.030	1.056	1.080	1.032	1.072	1.097
18.00	5.464	1.027	1.055	1.075	1.042	1.068	1.100
18.25	5.537	1.025	1.053	1.060	1.051	1.058	1.097
18.50	5.611	1.018	1.049	1.057	1.054	1.050	1.095
18.75	5.684	1.009	1.044	1.044	1.057	1.042	1.083
19.00	5.757	1.000	1.037	1.035	1.057	1.031	1.075
19.25	5.830		1.030	1.023	1.055	1.024	1.057
19.50	5.902		1.023	1.012	1.050	1.016	1.044
19.75	5.975		1.015	1.008	1.046	1.009	1.029
20.00	6.048		1.010	1.001	1.043	1.000	1.013
20.25	6.120		1.005	1.000	1.036		1.000
20.50	6.192		1.001		1.028		
20.75	6.265		1.000		1.016		
21.00	6.337				1.001		
21.25	6.409				1.000		

TABLE VIb

SUMMARY OF THE SMOOTH INTENSITY FUNCTIONS
AFTER CORRECTION FOR HORIZONTAL DIVERGENCE

$$j(s) = i(s) + 1$$

<u>θ</u> Degrees	<u>s</u> <u>\AA^{-1}</u>	Argon <u>Run 1</u>	Argon <u>Run 2</u>	Argon <u>Run 3</u>	Argon <u>Run 4</u>	Argon <u>Run 5</u>	Argon <u>Run 6</u>
0.	0.	0.669	1.284	0.373	0.271	0.202	0.109
0.25	0.077	0.571	1.002	0.332	0.247	0.186	0.103
0.50	0.154	0.411	0.596	0.258	0.201	0.154	0.090
0.75	0.231	0.303	0.347	0.216	0.173	0.131	0.086
1.00	0.309	0.266	0.291	0.197	0.159	0.124	0.087
1.25	0.386	0.235	0.252	0.181	0.146	0.120	0.090
1.50	0.463	0.218	0.236	0.171	0.143	0.117	0.095
1.75	0.540	0.207	0.220	0.165	0.141	0.114	0.100
2.00	0.617	0.200	0.214	0.163	0.139	0.116	0.106
2.25	0.694	0.200	0.212	0.163	0.144	0.120	0.111
2.50	0.771	0.204	0.217	0.173	0.153	0.125	0.117
2.75	0.848	0.213	0.228	0.183	0.163	0.136	0.124
3.00	0.925	0.228	0.240	0.199	0.176	0.146	0.131
3.25	1.002	0.253	0.262	0.220	0.192	0.163	0.144
3.50	1.079	0.285	0.293	0.247	0.217	0.187	0.166
3.75	1.156	0.322	0.333	0.291	0.249	0.218	0.193
4.00	1.233	0.381	0.386	0.339	0.298	0.260	0.226
4.25	1.310	0.453	0.458	0.418	0.368	0.314	0.276
4.50	1.387	0.560	0.559	0.506	0.452	0.393	0.348
4.75	1.464	0.675	0.675	0.644	0.583	0.513	0.457
5.00	1.541	0.850	0.825	0.812	0.746	0.706	0.599
5.25	1.618	1.055	0.992	1.019	0.992	0.942	0.822
5.50	1.695	1.308	1.190	1.322	1.273	1.281	1.166
5.75	1.772	1.531	1.346	1.543	1.596	1.674	1.611
6.00	1.848	1.652	1.432	1.777	1.856	2.005	2.034
6.25	1.925	1.657	1.446	1.818	1.879	2.151	2.266
6.50	2.002	1.595	1.396	1.734	1.798	2.033	2.130
6.75	2.078	1.461	1.304	1.567	1.619	1.806	1.878

TABLE VIb (con't)

<u>θ</u> <u>Degrees</u>	<u>σ^S</u> <u>\AA^{-1}</u>	<u>Argon</u> <u>Run 1</u>	<u>Argon</u> <u>Run 2</u>	<u>Argon</u> <u>Run 3</u>	<u>Argon</u> <u>Run 4</u>	<u>Argon</u> <u>Run 5</u>	<u>Argon</u> <u>Run 6</u>
7.00	2.155	1.323	1.192	1.403	1.432	1.562	1.594
7.25	2.231	1.175	1.083	1.222	1.242	1.313	1.313
7.50	2.308	1.053	0.988	1.082	1.086	1.133	1.105
7.75	2.384	0.962	0.911	0.974	0.968	0.992	0.961
8.00	2.461	0.903	0.862	0.900	0.885	0.891	0.862
8.25	2.537	0.875	0.824	0.855	0.834	0.838	0.805
8.50	2.614	0.843	0.810	0.823	0.802	0.801	0.766
8.75	2.690	0.834	0.801	0.806	0.796	0.777	0.738
9.00	2.766	0.829	0.808	0.809	0.805	0.781	0.746
9.25	2.842	0.831	0.824	0.815	0.821	0.795	0.762
9.50	2.918	0.850	0.846	0.834	0.851	0.815	0.782
9.75	2.994	0.876	0.880	0.865	0.881	0.858	0.822
10.00	3.070	0.903	0.916	0.898	0.909	0.903	0.868
10.25	3.146	0.936	0.945	0.942	0.938	0.952	0.903
10.50	3.222	0.989	0.986	0.980	0.978	1.008	0.966
10.75	3.298	1.050	1.025	1.046	1.015	1.063	0.993
11.00	3.374	1.120	1.079	1.111	1.065	1.107	1.058
11.25	3.450	1.165	1.131	1.177	1.126	1.148	1.119
11.50	3.525	1.187	1.166	1.205	1.161	1.177	1.174
11.75	3.601	1.199	1.188	1.223	1.198	1.200	1.204
12.00	3.676	1.198	1.183	1.225	1.208	1.214	1.214
12.25	3.752	1.181	1.171	1.208	1.208	1.215	1.216
12.50	3.827	1.144	1.141	1.192	1.196	1.213	1.193
12.75	3.902	1.103	1.113	1.153	1.171	1.188	1.162
13.00	3.978	1.064	1.080	1.112	1.145	1.153	1.085
13.25	4.053	1.044	1.048	1.072	1.096	1.104	1.018
13.50	4.128	1.013	1.018	1.002	1.061	1.072	0.976
13.75	4.203	0.991	0.989	0.978	1.026	1.036	0.939
14.00	4.278	0.968	0.972	0.943	0.993	0.999	0.919
14.25	4.352	0.958	0.965	0.943	0.982	0.979	0.900
14.50	4.427	0.957	0.959	0.946	0.968	0.967	0.888
14.75	4.502	0.959	0.957	0.954	0.959	0.950	0.877

TABLE VIb (con't)

<u>θ</u> <u>Degrees</u>	<u>S</u> <u>Å^{-1}</u>	<u>Argon</u> <u>Run 1</u>	<u>Argon</u> <u>Run 2</u>	<u>Argon</u> <u>Run 3</u>	<u>Argon</u> <u>Run 4</u>	<u>Argon</u> <u>Run 5</u>	<u>Argon</u> <u>Run 6</u>
15.00	4.576	0.962	0.959	0.964	0.949	0.942	0.886
15.25	4.651	0.968	0.963	0.978	0.947	0.938	0.903
15.50	4.725	0.978	0.968	0.986	0.951	0.937	0.919
15.75	4.800	0.998	0.976	1.008	0.956	0.960	0.939
16.00	4.874	1.010	0.985	1.026	0.962	0.993	0.957
16.25	4.948	1.016	1.000	1.045	0.969	1.024	0.977
16.50	5.022	1.024	1.011	1.058	0.978	1.045	1.005
16.75	5.096	1.028	1.026	1.071	0.989	1.061	1.032
17.00	5.170	1.030	1.037	1.084	1.001	1.073	1.055
17.25	5.243	1.032	1.046	1.088	1.014	1.078	1.071
17.50	5.317	1.033	1.055	1.084	1.028	1.077	1.083
17.75	5.391	1.030	1.056	1.080	1.032	1.072	1.097
18.00	5.464	1.027	1.055	1.075	1.042	1.068	1.100
18.25	5.537	1.025	1.053	1.060	1.051	1.058	1.097
18.50	5.611	1.018	1.049	1.057	1.054	1.050	1.095
18.75	5.684	1.009	1.044	1.044	1.057	1.042	1.083
19.00	5.757	1.000	1.037	1.035	1.057	1.031	1.075
19.25	5.830		1.030	1.023	1.055	1.024	1.057
19.50	5.902		1.023	1.012	1.050	1.016	1.044
19.75	5.975		1.015	1.008	1.046	1.009	1.029
20.00	6.048		1.010	1.001	1.043	1.000	1.013
20.25	6.120		1.005	1.000	1.036		1.000
20.50	6.192		1.001		1.028		
20.75	6.265		1.000		1.016		
21.00	6.337				1.001		
21.25	6.409				1.000		

TABLE VII

EXTRAPOLATION COEFFICIENTS, NORMALIZATION CONSTANTS AND TRUNCATION LIMITS
USED IN THE FOURIER INVERSION

VALUES OF a_2 AND a_4 FOR TABLE VIA

Run No.	K_T	$j(0)$	a_2	a_4	Q	C/N	S_{\max}
1	0.0024	0.66884	19.327	-98.191	1.5300	58.726	5.7567
2	0.0048	1.2841	40.596	-70.345	1.4890	61.095	6.2645
3	0.0013	0.37315	10.801	-62.857	1.5201	55.515	6.1200
4	0.00093	0.27094	6.652	-38.295	1.4737	55.866	6.4804
5	0.00070	0.20198	4.775	-26.936	1.4274	57.401	6.0476
6	0.00039	0.10929	-0.505	-15.441	1.3454	60.747	6.1200

TABLE VII (con't)

EXTRAPOLATION COEFFICIENTS, NORMALIZATION CONSTANTS AND TRUNCATION LIMITS
 USED IN THE FOURIER INVERSION
 VALUES OF a_2 AND a_4 FOR TABLE VIIb

Run No.	$j(0)$	a_2	a_4
1	0.66884	20.430	-128.635
2	1.28407	46.938	64.277
3	0.37315	21.573	-123.066
4	0.27094	17.118	-105.132
5	0.20198	15.283	- 98.176
6	0.10929	11.005	- 91.804

TABLE VIII
 SUMMARY OF FEATURES IN THE EXPERIMENTAL ARGON INTENSITY PATTERNS

Run No.	Location of extrema in $j(s)$ (\AA^{-1})						Main Peak	
	$(s_1)_{\min}$	$(s_1)_{\max}$	$(s_2)_{\min}$	$(s_2)_{\max}$	$(s_3)_{\min}$	$(s_3)_{\max}$	$j(s)_{\min}$	$j(s)_{\max}$
1	0.64	1.89	2.77	3.62	4.46	5.26	0.20	1.61
2	0.69	1.92	2.69	3.62	4.55	5.39	0.21	1.45
3	0.58	1.91	2.75	3.66	4.31	5.27	0.16	1.82
4	0.59	1.91	2.69	3.71	4.65	5.68	0.14	1.89
5	0.55	1.93	2.72	3.74	4.66	5.26	0.11	2.15
6	0.14	1.93	2.72	3.70	4.50	5.50	0.09	2.26
median	—	$1.91 \pm .02$	$2.73 \pm .04$	$3.68 \pm .06$	$4.48 \pm .18$	$5.43 \pm .16$		

TABLE IX

ESTIMATES OF THE NET RADIAL DISTRIBUTION FUNCTIONS, $h(r) = g(r) - 1$

R Å	VALUES IN PARENTHESES ESTIMATES EXPERIMENTAL ERROR (SEE TEXT)					
	Run 1	Run 2	Run 3	Run 4	Run 5	Run 6
	$h(r) \pm (\text{BAND})$	$h(r) \pm (\text{BAND})$	$h(r) \pm (\text{BAND})$	$h(r) \pm (\text{BAND})$	$h(r) \pm (\text{BAND})$	$h(r) \pm (\text{BAND})$
3.0	-1.0500(.0519)	-1.2029(.0630)	-1.1584(.0551)	-1.2215(.0569)	-1.1065(.0526)	-1.2325(.0550)
3.1	-0.8510(.0515)	-1.0083(.0591)	-0.9925(.0505)	-0.8587(.0561)	-0.8537(.0490)	-0.9930(.0504)
3.2	-0.5746(.0494)	-0.6929(.0588)	-0.7070(.0485)	-0.4058(.0564)	-0.5021(.0458)	-0.6091(.0484)
3.3	-0.2406(.0451)	-0.2952(.0587)	-0.3238(.0480)	0.0720(.0547)	-0.0835(.0448)	-0.1283(.0480)
3.4	0.1202(.0430)	0.1302(.0571)	0.1133(.0477)	0.5086(.0505)	0.3545(.0446)	0.3808(.0476)
3.5	0.4704(.0428)	0.5245(.0532)	0.5472(.0463)	0.8507(.0482)	0.7580(.0441)	0.8440(.0462)
3.6	0.7727(.0434)	0.8370(.0505)	0.9203(.0433)	1.0676(.0483)	1.0778(.0422)	1.1977(.0433)
3.7	0.9957(.0429)	1.0342(.0509)	1.1852(.0421)	1.1542(.0490)	1.2785(.0400)	1.4014(.0422)
3.8	1.1195(.0407)	1.1051(.0514)	1.3145(.0421)	1.1279(.0478)	1.3451(.0395)	1.4441(.0422)
3.9	1.1385(.0384)	1.0600(.0504)	1.3042(.0421)	1.0200(.0447)	1.2843(.0395)	1.3430(.0422)
4.0	1.0612(.0376)	0.9264(.0471)	1.1725(.0410)	0.8667(.0430)	1.1213(.0390)	1.1369(.0410)
4.1	0.9082(.0379)	0.7404(.0448)	0.9544(.0386)	0.6998(.0429)	0.8936(.0376)	0.8745(.0385)
4.2	0.7078(.0377)	0.5385(.0449)	0.6931(.0372)	0.5414(.0431)	0.6423(.0354)	0.6037(.0372)
4.3	0.4904(.0364)	0.3509(.0453)	0.4307(.0371)	0.4022(.0419)	0.4044(.0347)	0.3616(.0371)
4.4	0.2838(.0341)	0.1967(.0444)	0.2010(.0370)	0.2836(.0394)	0.2060(.0346)	0.1697(.0370)

TABLE IX (con't)

R Å	Run 1 $h(r)_{\pm}$ (BAND)	Run 2 $h(r)_{\pm}$ (BAND)	Run 3 $h(r)_{\pm}$ (BAND)	Run 4 $h(r)_{\pm}$ (BAND)	Run 5 $h(r)_{\pm}$ (BAND)	Run 6 $h(r)_{\pm}$ (BAND)
4.5	0.1087(.0332)	0.0832(.0418)	0.0247(.0363)	0.1813(.0383)	0.0599(.0344)	0.0330(.0362)
4.6	-0.0231(.0331)	0.0080(.0398)	-0.0916(.0343)	0.0902(.0381)	-0.0343(.0333)	-0.0561(.0342)
4.7	-0.1089(.0334)	-0.0376(.0401)	-0.1536(.0333)	0.0073(.0383)	-0.0870(.0317)	-0.1125(.0332)
4.8	-0.1539(.0329)	-0.0646(.0405)	-0.1748(.0331)	-0.0672(.0373)	-0.1140(.0310)	-0.1521(.0332)
4.9	-0.1680(.0314)	-0.0821(.0402)	-0.1719(.0334)	-0.1304(.0356)	-0.1317(.0312)	-0.1870(.0335)
5.0	-0.1634(.0302)	-0.0963(.0380)	-0.1601(.0329)	-0.1789(.0350)	-0.1525(.0311)	-0.2229(.0329)
5.1	-0.1512(.0296)	-0.1095(.0361)	-0.1505(.0311)	-0.2107(.0346)	-0.1829(.0301)	-0.2596(.0311)
5.2	-0.1398(.0296)	-0.1213(.0359)	-0.1487(.0298)	-0.2268(.0343)	-0.2229(.0286)	-0.2927(.0297)
5.3	-0.1339(.0292)	-0.1299(.0361)	-0.1553(.0296)	-0.2312(.0331)	-0.2674(.0278)	-0.3168(.0295)
5.4	-0.1347(.0284)	-0.1340(.0358)	-0.1678(.0297)	-0.2293(.0319)	-0.3085(.0278)	-0.3279(.0298)
5.5	-0.1409(.0276)	-0.1336(.0346)	-0.1821(.0299)	-0.2268(.0320)	-0.3383(.0282)	-0.3249(.0300)
5.6	-0.1494(.0272)	-0.1298(.0334)	-0.1942(.0288)	-0.2270(.0320)	-0.3505(.0278)	-0.3101(.0288)
5.7	-0.1573(.0273)	-0.1249(.0333)	-0.2015(.0278)	-0.2303(.0317)	-0.3426(.0267)	-0.2876(.0278)
5.8	-0.1619(.0272)	-0.1209(.0335)	-0.2028(.0274)	-0.2341(.0305)	-0.3152(.0258)	-0.2616(.0275)
5.9	-0.1618(.0264)	-0.1189(.0329)	-0.1979(.0274)	-0.2335(.0295)	-0.2720(.0256)	-0.2351(.0274)
6.0	-0.1566(.0250)	-0.1184(.0311)	-0.1873(.0268)	-0.2237(.0290)	-0.2183(.0252)	-0.2087(.0269)
6.1	-0.1463(.0244)	-0.1175(.0301)	-0.1711(.0261)	-0.2012(.0289)	-0.1600(.0250)	-0.1805(.0261)
6.2	-0.1315(.0245)	-0.1137(.0302)	-0.1491(.0252)	-0.1651(.0287)	-0.1022(.0243)	-0.1475(.0251)
6.3	-0.1125(.0247)	-0.1041(.0305)	-0.1213(.0250)	-0.1178(.0277)	-0.0486(.0236)	-0.1069(.0250)
6.4	-0.0896(.0246)	-0.0871(.0304)	-0.0873(.0253)	-0.0638(.0274)	-0.0013(.0236)	-0.0573(.0253)
6.5	-0.0631(.0238)	-0.0624(.0293)	-0.0480(.0251)	-0.0089(.0273)	0.0389(.0236)	-0.0001(.0252)
6.6	-0.0334(.0229)	-0.0315(.0282)	-0.0051(.0245)	0.0417(.0270)	0.0722(.0234)	0.0609(.0245)
6.7	-0.0014(.0226)	0.0029(.0280)	0.0386(.0234)	0.0840(.0265)	0.0993(.0227)	0.1199(.0234)
6.8	0.0314(.0225)	0.0372(.0282)	0.0797(.0231)	0.1162(.0255)	0.1209(.0218)	0.1709(.0231)
6.9	0.0629(.0225)	0.0677(.0280)	0.1145(.0232)	0.1382(.0253)	0.1377(.0217)	0.2085(.0232)

TABLE IX (con't)

R λ	Run 1 $h(r)_{\pm}$ (BAND)	Run 2 $h(r)_{\pm}$ (BAND)	Run 3 $h(r)_{\pm}$ (BAND)	Run 4 $h(r)_{\pm}$ (BAND)	Run 5 $h(r)_{\pm}$ (BAND)	Run 6 $h(r)_{\pm}$ (BAND)
7.0	0.0908(.0219)	0.0917(.0267)	0.1400(.0229)	0.1510(.0250)	0.1498(.0215)	0.2294(.0229)
7.2	0.1275(.0209)	0.1141(.0259)	0.1574(.0217)	0.1550(.0244)	0.1600(.0212)	0.2221(.0217)
7.4	0.1315(.0210)	0.1043(.0262)	0.1349(.0217)	0.1355(.0237)	0.1502(.0203)	0.1693(.0217)
7.6	0.1072(.0204)	0.0744(.0248)	0.0919(.0215)	0.0961(.0237)	0.1199(.0204)	0.1031(.0215)
7.8	0.0686(.0194)	0.0387(.0245)	0.0482(.0201)	0.0461(.0222)	0.0731(.0191)	0.0426(.0201)
8.0	0.0292(.0192)	0.0084(.0234)	0.0135(.0200)	0.0027(.0220)	0.0193(.0187)	-0.0080(.0200)
8.2	-0.0040(.0185)	-0.0100(.0228)	-0.0119(.0192)	-0.0220(.0213)	-0.0281(.0187)	-0.0480(.0192)
8.4	-0.0289(.0182)	-0.0157(.0230)	-0.0300(.0190)	-0.0315(.0209)	-0.0583(.0178)	-0.0735(.0190)
8.6	-0.0437(.0180)	-0.0135(.0217)	-0.0418(.0188)	-0.0379(.0207)	-0.0695(.0178)	-0.0825(.0188)
8.8	-0.0462(.0172)	-0.0110(.0217)	-0.0478(.0179)	-0.0468(.0198)	-0.0690(.0171)	-0.0799(.0179)
9.0	-0.0375(.0172)	-0.0124(.0212)	-0.0488(.0181)	-0.0524(.0199)	-0.0657(.0169)	-0.0735(.0181)
9.2	-0.0239(.0167)	-0.0160(.0205)	-0.0448(.0173)	-0.0474(.0189)	-0.0616(.0167)	-0.0656(.0172)
9.4	-0.0136(.0161)	-0.0170(.0205)	-0.0342(.0170)	-0.0334(.0188)	-0.1513(.0159)	-0.0511(.0170)
9.6	-0.0101(.0161)	-0.0132(.0196)	-0.0172(.0168)	-0.0185(.0185)	-0.0295(.0158)	-0.0258(.0169)
9.8	-0.0098(.0155)	-0.0068(.0194)	0.0020(.0160)	-0.0073(.0177)	0.0009(.0154)	0.0063(.0160)
10.0	-0.0064(.0153)	-0.0013(.0189)	0.0159(.0161)	0.0027(.0179)	0.0294(.0150)	0.0346(.0161)
10.2	0.0026(.0152)	0.0027(.0185)	0.0202(.0157)	0.0148(.0170)	0.0451(.0150)	0.0512(.0156)
10.4	0.0135(.0149)	0.0068(.0187)	0.0172(.0155)	0.0262(.0172)	0.0450(.0146)	0.0555(.0155)
10.6	0.0201(.0146)	0.0121(.0179)	0.0140(.0154)	0.0310(.0168)	0.0351(.0144)	0.0515(.0153)
10.8	0.0200(.0142)	0.0170(.0175)	0.0153(.0144)	0.0276(.0160)	0.0238(.0140)	0.0421(.0144)
11.0	0.0157(.0139)	0.0183(.0174)	0.0195(.0148)	0.0208(.0164)	0.0160(.0138)	0.0278(.0148)
11.2	0.0114(.0138)	0.0147(.0168)	0.0207(.0143)	0.0154(.0155)	0.0111(.0136)	0.0098(.0143)
11.4	0.0087(.0134)	0.0080(.0168)	0.0147(.0139)	0.0110(.0154)	0.0060(.0131)	-0.0072(.0138)
11.6	0.0059(.0131)	0.0013(.0163)	0.0033(.0139)	0.0036(.0152)	-0.0011(.0130)	-0.0181(.0140)
11.8	0.0013(.0132)	-0.0030(.0162)	-0.0083(.0134)	-0.0069(.0149)	-0.0098(.0131)	-0.0222(.0134)

TABLE IX (con't)

R Å	Run 1 $h(r) \pm (\text{BAND})$	Run 2 $h(r) \pm (\text{BAND})$	Run 3 $h(r) \pm (\text{BAND})$	Run 4 $h(r) \pm (\text{BAND})$	Run 5 $h(r) \pm (\text{BAND})$	Run 6 $h(r) \pm (\text{BAND})$
12.0	-0.0042(.0126)	-0.0045(.0157)	-0.0156(.0133)	-0.0156(.0148)	-0.0177(.0124)	-0.0228(.0133)
12.2	-0.0079(.0126)	-0.0038(.0155)	-0.0174(.0133)	-0.0178(.0143)	-0.0222(.0125)	-0.0234(.0132)
12.4	-0.0079(.0125)	-0.0016(.0154)	-0.0148(.0127)	-0.0144(.0143)	-0.0216(.0122)	-0.0236(.0127)
12.6	-0.0052(.0121)	0.0009(.0150)	-0.0096(.0128)	-0.0100(.0138)	-0.0159(.0120)	-0.0203(.0128)
12.8	-0.0027(.0121)	0.0026(.0150)	-0.0033(.0124)	-0.0073(.0138)	-0.0076(.0120)	-0.0120(.0124)
13.0	-0.0021(.0118)	0.0025(.0145)	0.0020(.0123)	-0.0051(.0136)	-0.0002(.0115)	-0.0011(.0123)
13.2	-0.0024(.0114)	0.0007(.0142)	0.0044(.0122)	-0.0013(.0132)	0.0040(.0115)	0.0083(.0122)
13.4	-0.0021(.0115)	-0.0014(.0143)	0.0032(.0118)	0.0028(.0132)	0.0054(.0113)	0.0136(.0118)
13.6	-0.0004(.0111)	-0.0024(.0139)	0.0005(.0118)	0.0042(.0128)	0.0063(.0110)	0.0150(.0119)
13.8	0.0014(.0112)	-0.0016(.0139)	-0.0008(.0117)	0.0029(.0130)	0.0082(.0112)	0.0137(.0116)
14.0	0.0022(.0107)	0.0006(.0130)	0.0008(.0110)	0.0022(.0122)	0.0103(.0103)	0.0109(.0110)
14.2	0.0017(.0103)	0.0032(.0128)	0.0043(.0109)	0.0047(.0119)	0.0104(.0102)	0.0075(.0109)
14.4	0.0013(.0106)	0.0052(.0130)	0.0069(.0108)	0.0088(.0121)	0.0075(.0105)	0.0047(.0108)
14.6	0.0018(.0105)	0.0058(.0129)	0.0068(.0110)	0.0099(.0120)	0.0027(.0102)	0.0036(.0110)
14.8	0.0031(.0102)	0.0050(.0129)	0.0043(.0108)	0.0060(.0120)	-0.0013(.0103)	0.0032(.0108)
15.0	0.0043(.0103)	0.0033(.0127)	0.0012(.0107)	0.0002(.0117)	-0.0031(.0101)	0.0012(.0106)
15.2	0.0047(.0101)	0.0016(.0125)	-0.0012(.0106)	-0.0033(.0116)	-0.0033(.0100)	-0.0038(.0106)
15.4	0.0044(.0100)	0.0005(.0123)	-0.0025(.0102)	-0.0034(.0114)	-0.0035(.0100)	-0.0101(.0102)
15.6	0.0034(.0100)	0.0003(.0121)	-0.0030(.0103)	-0.0025(.0113)	-0.0044(.0096)	-0.0136(.0103)
15.8	0.0015(.0096)	0.0004(.0121)	-0.0032(.0101)	-0.0029(.0112)	-0.0055(.0096)	-0.0119(.0101)
16.0	-0.0017(.0096)	0.0004(.0118)	-0.0032(.0099)	-0.0040(.0109)	-0.0057(.0095)	-0.0063(.0099)
16.2	-0.0051(.0096)	0.0003(.0118)	-0.0028(.0100)	-0.0040(.0110)	-0.0044(.0094)	-0.0003(.0101)
16.4	-0.0069(.0093)	0.0003(.0116)	-0.0019(.0096)	-0.0025(.0107)	-0.0020(.0093)	0.0030(.0096)
16.6	-0.0054(.0091)	0.0004(.0112)	-0.0005(.0095)	-0.0009(.0105)	0.0008(.0089)	0.0034(.0095)
16.8	-0.0013(.0092)	0.0004(.0114)	0.0012(.0096)	-0.0004(.0106)	0.0033(.0090)	0.0028(.0096)

TABLE IX (con't)

° R A	Run 1 h(r) [±] (BAND)	Run 2 h(r) [±] (BAND)	Run 3 h(r) [±] (BAND)	Run 4 h(r) [±] (BAND)	Run 5 h(r) [±] (BAND)	Run 6 h(r) [±] (BAND)
17.0	0.0029(.0090)	0.0002(.0111)	0.0024(.0093)	-0.0001(.0103)	0.0046(.0090)	0.0024(.0093)
17.2	0.0044(.0090)	0.0001(.0111)	0.0027(.0094)	0.0011(.0104)	0.0044(.0088)	0.0027(.0094)
17.4	0.0028(.0087)	0.0004(.0110)	0.0020(.0091)	0.0028(.0100)	0.0031(.0087)	0.0031(.0091)
17.6	-0.0003(.0087)	0.0009(.0108)	0.0009(.0091)	0.0036(.0101)	0.0017(.0086)	0.0033(.0091)
17.8	-0.0022(.0087)	0.0013(.0107)	0.0002(.0090)	0.0028(.0100)	0.0013(.0085)	0.0035(.0091)
18.0	-0.0016(.0084)	0.0012(.0104)	0.0002(.0087)	0.0015(.0097)	0.0017(.0085)	0.0034(.0087)
18.2	0.0005(.0085)	0.0009(.0105)	0.0006(.0089)	0.0011(.0098)	0.0019(.0083)	0.0024(.0089)
18.4	0.0024(.0084)	0.0010(.0103)	0.0008(.0086)	0.0014(.0094)	0.0008(.0082)	0.0004(.0086)
18.6	0.0030(.0082)	0.0016(.0101)	0.0004(.0086)	0.0012(.0095)	-0.0014(.0081)	-0.0020(.0085)
18.8	0.0024(.0082)	0.0024(.0102)	-0.0002(.0086)	-0.0004(.0094)	-0.0035(.0080)	-0.0038(.0086)
19.0	0.0014(.0081)	0.0025(.0099)	-0.0007(.0083)	-0.0021(.0093)	-0.0040(.0081)	-0.0045(.0083)
19.2	0.0005(.0079)	0.0016(.0099)	-0.0009(.0083)	-0.0026(.0092)	-0.0028(.0077)	-0.0043(.0083)
19.4	-0.0003(.0080)	0.0004(.0098)	-0.0011(.0082)	-0.0019(.0089)	-0.0012(.0078)	-0.0034(.0082)
19.6	-0.0010(.0077)	-0.0004(.0096)	-0.0014(.0081)	-0.0013(.0090)	-0.0001(.0077)	-0.0018(.0081)
19.8	-0.0014(.0077)	-0.0005(.0097)	-0.0014(.0082)	-0.0014(.0088)	0.0001(.0076)	0.0002(.0082)
20.0	-0.0012(.0077)	-0.0009(.0079)	-0.0009(.0079)	-0.0014(.0088)	0.0000(.0076)	0.0021(.0078)
20.2	-0.0003(.0076)	0.0005(.0095)	0.0001(.0080)	-0.0005(.0089)	0.0004(.0075)	0.0029(.0080)
20.4	0.0004(.0073)	0.0008(.0093)	0.0013(.0077)	0.0009(.0085)	0.0010(.0073)	0.0022(.0077)
20.6	0.0006(.0073)	0.0006(.0090)	0.0022(.0076)	0.0016(.0084)	0.0014(.0073)	0.0011(.0076)
20.8	0.0003(.0079)	0.0002(.0097)	0.0023(.0082)	0.0011(.0088)	0.0014(.0077)	0.0006(.0082)
21.0	0.0001(.0068)	-0.0002(.0083)	0.0015(.0070)	0.0006(.0078)	0.0012(.0067)	0.0011(.0070)
21.2	0.0002(.0074)	-0.0003(.0093)	0.0002(.0078)	0.0009(.0087)	0.0011(.0074)	0.0015(.0078)
21.4	0.0004(.0074)	-0.0001(.0093)	-0.0010(.0077)	0.0018(.0085)	0.0009(.0073)	0.0010(.0077)
21.6	0.0004(.0069)	0.0005(.0084)	-0.0016(.0070)	0.0019(.0079)	0.0005(.0068)	-0.0003(.0070)
21.8	0.0001(.0070)	0.0009(.0087)	-0.0012(.0073)	0.0008(.0078)	-0.0001(.0068)	-0.0014(.0074)

TABLE IX (con't)

R Å	Run 1 h(r) [±] (BAND)	Run 2 h(r) [±] (BAND)	Run 3 h(r) [±] (BAND)	Run 4 h(r) [±] (BAND)	Run 5 h(r) [±] (BAND)	Run 6 h(r) [±] (BAND)
22.0	-0.0002(.0071)	0.0010(.0088)	-0.0003(.0074)	-0.0007(.0082)	-0.0008(.0071)	-0.0017(.0074)
22.2	-0.0005(.0068)	0.0008(.0087)	0.0004(.0072)	-0.0013(.0080)	-0.0013(.0068)	-0.0014(.0072)
22.4	0.0005(.0067)	0.0006(.0085)	0.0002(.0071)	-0.0009(.0079)	-0.0013(.0067)	-0.0012(.0071)
22.6	0.0009(.0068)	0.0005(.0081)	-0.0004(.0069)	-0.0004(.0077)	-0.0010(.0067)	-0.0013(.0069)
22.8	0.0007(.0068)	0.0006(.0084)	-0.0008(.0071)	-0.0006(.0076)	-0.0004(.0067)	-0.0011(.0072)
23.0	0.0000(.0066)	0.0007(.0083)	-0.0002(.0069)	-0.0012(.0078)	0.0002(.0066)	-0.0002(.0069)
23.2	-0.0005(.0066)	0.0006(.0082)	0.0007(.0068)	-0.0013(.0076)	0.0007(.0065)	0.0011(.0068)
23.4	-0.0004(.0065)	0.0005(.0081)	0.0012(.0068)	-0.0009(.0076)	0.0006(.0064)	0.0017(.0069)
23.6	0.0002(.0065)	0.0004(.0079)	0.0009(.0067)	-0.0003(.0074)	0.0001(.0065)	0.0013(.0067)
23.8	0.0005(.0064)	0.0002(.0081)	0.0003(.0068)	0.0002(.0073)	-0.0006(.0064)	0.0005(.0068)
24.0	-0.0005(.0064)	-0.0002(.0078)	0.0004(.0066)	0.0008(.0074)	-0.0007(.0063)	0.0001(.0066)

TABLE X

SUMMARY OF FEATURES IN THE ATOMIC DENSITY DISTRIBUTION OF ARGON

Run No.	Maxima in the function $4\pi r^2 \rho_h(r)$							
	First		Second		Third		Fourth	
	Position \AA	Height Atoms/ \AA	Position \AA	Height Atoms/ \AA	Position \AA	Height Atoms/ \AA	Position \AA	Height Atoms/ \AA
1	3.91	3.22	7.38	1.33	10.70	0.86	—	—
2	3.88	2.78	7.29	1.05	11.00	0.37	—	—
3	3.91	3.95	7.22	1.63	10.18	0.42	—	—
					11.20	0.51	—	—
4	3.80	3.44	7.19	1.70	10.64	0.75	13.61	0.16
							14.59	0.45
5	3.87	4.45	7.31	1.91	10.30	1.12	14.12	0.48
6	3.80	4.98	7.18	2.75	10.40	1.43	13.60	0.65

TABLE XI

SUMMARY OF FEATURES IN THE ARGON DISTRIBUTION FUNCTION, $h(r)$

Run No.	σ first zero Å	r_{\max} first maximum Å	$h(r_{\max})$	N_1^*
1	3.37	3.72	1.09	5.1 ± 0.3
2	3.36	3.84	1.13	4.3 ± 0.2
3	3.36	3.82	1.31	5.7 ± 0.2
4	3.31	3.72	1.15	5.3 ± 0.2
5	3.33	3.81	1.33	6.4 ± 0.2
6	3.33	3.81	1.44	6.5 ± 0.2
median	$3.34 \pm .03$	$3.78 \pm .06$		

* First coordination number calculated by symmetrizing $r g(r)$ in the function $4\pi r^2 g(r)$

TABLE XII

ESTIMATES OF THE DIRECT CORRELATION FUNCTIONS, $c(r)$

VALUES IN PARENTHESSES ESTIMATE EXPERIMENTAL ERROR (SEE TEXT)

R Å	Run 1	Run 2	Run 3	Run 4	Run 5	Run 6
	$c(r) \pm$ (BAND)					
0.0	-9.37	-8.93	-11.38	-12.58	-15.15	-17.13
0.1	-9.17	-8.74	-11.12	-12.24	-14.74	-16.62
0.2	-8.92	-8.52	-10.80	-11.88	-14.28	-16.09
0.3	-8.6280(.3079)	-8.3092(.3498)	-10.4761(.3994)	-11.5134(.3363)	-13.7512(.3223)	-15.5425(.3737)
0.4	-8.3720(.2415)	-8.0335(.2621)	-10.0920(.2284)	-11.1526(.2486)	-13.3284(.2481)	-15.0145(.2854)
0.5	-8.0661(.1714)	-7.7129(.1729)	-9.6475(.1552)	-10.7315(.1619)	-12.8299(.1715)	-14.4035(.1943)
0.6	-7.7245(.1135)	-7.3662(.1224)	-9.1700(.1076)	-10.2731(.1198)	-12.2810(.1178)	-13.7459(.1345)
0.7	-7.3614(.0936)	-7.0106(.1089)	-8.6841(.0936)	-9.7981(.1091)	-11.7056(.1016)	-13.0738(.1163)
0.8	-6.9899(.0891)	-6.6599(.1041)	-8.2095(.0894)	-9.3228(.1036)	-11.1240(.0974)	-12.4114(.1117)
0.9	-6.6213(.0870)	-6.3238(.0966)	-7.7592(.0846)	-8.8579(.0939)	-10.5507(.0928)	-11.7735(.1062)
1.0	-6.2642(.0812)	-6.0074(.0831)	-7.3394(.0748)	-8.4093(.0793)	-9.9949(.0834)	-11.1657(.0947)
1.1	-5.9243(.0692)	-5.7121(.0726)	-6.9508(.0642)	-7.9786(.0717)	-9.4608(.0710)	-10.5866(.0818)
1.2	-5.6047(.0606)	-5.4367(.0687)	-6.5897(.0598)	-7.5649(.0686)	-8.9485(.0653)	-10.0300(.0760)
1.3	-5.3061(.0576)	-5.1782(.0665)	-6.2505(.0578)	-7.1661(.0659)	-8.4559(.0631)	-9.4888(.0729)
1.4	-5.0273(.0559)	-4.9334(.0623)	-5.9273(.0549)	-6.7805(.0608)	-7.9799(.0606)	-8.9568(.0693)
1.5	-4.7658(.0524)	-4.6993(.0543)	-5.6154(.0492)	-6.4068(.0529)	-7.5179(.0554)	-8.4310(.0625)
1.6	-4.5186(.0468)	-4.4740(.0483)	-5.3120(.0430)	-6.0448(.0487)	-7.0684(.0482)	-7.9118(.0551)
1.7	-4.2825(.0407)	-4.2559(.0457)	-5.0162(.0400)	-5.6946(.0464)	-6.6311(.0438)	-7.4026(.0511)
1.8	-4.0547(.0385)	-4.0442(.0448)	-4.7285(.0392)	-5.3563(.0446)	-6.2067(.0423)	-6.9082(.0495)
1.9	-3.8326(.0384)	-3.8382(.0435)	-4.4500(.0385)	-5.0298(.0418)	-5.7967(.0417)	-6.4337(.0481)

TABLE XII (con't)

R A	Run 1 $c(r) \pm (\text{BAND})$	Run 2 $c(r) \pm (\text{BAND})$	Run 3 $c(r) \pm (\text{BAND})$	Run 4 $c(r) \pm (\text{BAND})$	Run 5 $c(r) \pm (\text{BAND})$	Run 6 $c(r) \pm (\text{BAND})$
2.0	-3.6149(.0377)	-3.6368(.0399)	-4.1816(.0361)	-4.7142(.0382)	-5.4024(.0397)	-5.9829(.0448)
2.1	-3.4007(.0362)	-3.4390(.0375)	-3.9236(.0331)	-4.4085(.0372)	-5.0249(.0366)	-5.5578(.0413)
2.2	-3.1899(.0328)	-3.2436(.0365)	-3.6756(.0314)	-4.1118(.0364)	-4.6647(.0342)	-5.1582(.0394)
2.3	-2.9833(.0303)	-3.0496(.0355)	-3.4367(.0305)	-3.8236(.0350)	-4.3220(.0328)	-4.7823(.0381)
2.4	-2.7822(.0296)	-2.8566(.0342)	-3.2059(.0298)	-3.5448(.0325)	-3.9969(.0321)	-4.4280(.0371)
2.5	-2.5883(.0292)	-2.6652(.0317)	-2.9827(.0285)	-3.2772(.0301)	-3.6893(.0309)	-4.0929(.0353)
2.6	-2.4033(.0285)	-2.4767(.0297)	-2.7677(.0265)	-3.0234(.0293)	-3.3999(.0288)	-3.7761(.0327)
2.7	-2.2293(.0272)	-2.2935(.0297)	-2.5624(.0257)	-2.7864(.0294)	-3.1292(.0275)	-3.4773(.0320)
2.8	-2.0677(.0259)	-2.1181(.0299)	-2.3693(.0258)	-2.5689(.0292)	-2.8785(.0276)	-3.1975(.0322)
2.9	-1.9198(.0253)	-1.9534(.0291)	-2.1911(.0255)	-2.3723(.0276)	-2.6487(.0275)	-2.9379(.0319)
3.0	-1.7860(.0248)	-1.8013(.0271)	-2.0299(.0245)	-2.1966(.0262)	-2.4402(.0269)	-2.6994(.0307)
3.1	-1.5171(.0532)	-1.6712(.0608)	-1.8795(.0521)	-1.8989(.0588)	-2.1062(.0521)	-2.4748(.0552)
3.2	-1.1340(.0512)	-1.2311(.0605)	-1.4691(.0502)	-1.3060(.0591)	-1.5862(.0488)	-1.8932(.0534)
3.3	-0.7046(.0470)	-0.7213(.0606)	-0.9770(.0498)	-0.7007(.0574)	-1.0161(.0476)	-1.2321(.0529)
3.4	-0.2581(.0449)	-0.1945(.0590)	-0.4438(.0495)	-0.1454(.0531)	-0.4400(.0474)	-0.5570(.0524)
3.5	0.1706(.0448)	0.2930(.0550)	0.0778(.0480)	0.3098(.0507)	0.0918(.0468)	0.0608(.0506)
3.6	0.5459(.0451)	0.6922(.0522)	0.5340(.0448)	0.6362(.0504)	0.5334(.0449)	0.5603(.0474)
3.7	0.8385(.0445)	0.9714(.0524)	0.8813(.0434)	0.8298(.0509)	0.8521(.0425)	0.9022(.0460)
3.8	1.0296(.0420)	1.1199(.0527)	1.0941(.0433)	0.9072(.0497)	1.0342(.0418)	1.0757(.0460)
3.9	1.1141(.0397)	1.1478(.0518)	1.1689(.0433)	0.8989(.0466)	1.0866(.0417)	1.0969(.0459)
4.0	1.1005(.0389)	1.0817(.0484)	1.1230(.0422)	0.8393(.0448)	1.0334(.0410)	1.0030(.0446)
4.1	1.0088(.0392)	0.9561(.0461)	0.9890(.0397)	0.7588(.0447)	0.9100(.0397)	0.8410(.0421)
4.2	0.8662(.0390)	0.8064(.0463)	0.8070(.0384)	0.6780(.0450)	0.7553(.0375)	0.6576(.0407)
4.3	0.7019(.0377)	0.6615(.0466)	0.6163(.0382)	0.6070(.0437)	0.6037(.0368)	0.4897(.0406)
4.4	0.5424(.0354)	0.5401(.0456)	0.4483(.0380)	0.5468(.0411)	0.4797(.0366)	0.3594(.0404)

TABLE XII (con't)

R Å	Run 1 $c(r) \pm (\text{BAND})$	Run 2 $c(r) \pm (\text{BAND})$	Run 3 $c(r) \pm (\text{BAND})$	Run 4 $c(r) \pm (\text{BAND})$	Run 5 $c(r) \pm (\text{BAND})$	Run 6 $c(r) \pm (\text{BAND})$
4.5	0.4074 (.0345)	0.4497 (.0430)	0.3223 (.0372)	0.4930 (.0400)	0.3951 (.0363)	0.2731 (.0394)
4.6	0.3081 (.0343)	0.3885 (.0410)	0.2446 (.0354)	0.4409 (.0398)	0.3494 (.0352)	0.2248 (.0373)
4.7	0.2468 (.0346)	0.3488 (.0412)	0.2104 (.0344)	0.3876 (.0400)	0.3329 (.0336)	0.2011 (.0363)
4.8	0.2187 (.0340)	0.3214 (.0416)	0.2077 (.0342)	0.3337 (.0388)	0.3310 (.0329)	0.1874 (.0363)
4.9	0.2141 (.0326)	0.2980 (.0413)	0.2215 (.0344)	0.2826 (.0372)	0.3291 (.0331)	0.1719 (.0366)
5.0	0.2218 (.0313)	0.2740 (.0391)	0.2384 (.0338)	0.2384 (.0366)	0.3164 (.0329)	0.1485 (.0359)
5.1	0.2316 (.0307)	0.2480 (.0372)	0.2487 (.0321)	0.2039 (.0362)	0.2877 (.0319)	0.1169 (.0340)
5.2	0.2362 (.0308)	0.2214 (.0370)	0.2477 (.0308)	0.1794 (.0359)	0.2440 (.0303)	0.0809 (.0327)
5.3	0.2317 (.0304)	0.1966 (.0372)	0.2352 (.0305)	0.1624 (.0346)	0.1909 (.0294)	0.0456 (.0324)
5.4	0.2177 (.0295)	0.1755 (.0368)	0.2138 (.0307)	0.1485 (.0333)	0.1367 (.0294)	0.0154 (.0325)
5.5	0.1964 (.0286)	0.1586 (.0356)	0.1875 (.0307)	0.1334 (.0334)	0.0893 (.0298)	-0.0077 (.0325)
5.6	0.1710 (.0282)	0.1452 (.0343)	0.1601 (.0297)	0.1141 (.0333)	0.0550 (.0294)	-0.0242 (.0314)
5.7	0.1448 (.0282)	0.1333 (.0342)	0.1341 (.0285)	0.0904 (.0330)	0.0364 (.0282)	-0.0364 (.0302)
5.8	0.1205 (.0280)	0.1208 (.0343)	0.1109 (.0281)	0.0647 (.0317)	0.0328 (.0273)	-0.0470 (.0299)
5.9	0.0993 (.0273)	0.1065 (.0338)	0.0908 (.0280)	0.0410 (.0307)	0.0410 (.0270)	-0.0578 (.0298)
6.0	0.0817 (.0258)	0.0903 (.0321)	0.0739 (.0275)	0.0234 (.0301)	0.0558 (.0266)	-0.0688 (.0292)
6.1	0.0672 (.0253)	0.0735 (.0310)	0.0602 (.0269)	0.0149 (.0301)	0.0719 (.0265)	-0.0783 (.0284)
6.2	0.0552 (.0253)	0.0581 (.0311)	0.0501 (.0259)	0.0159 (.0299)	0.0850 (.0257)	-0.0839 (.0274)
6.3	0.0455 (.0255)	0.0463 (.0314)	0.0443 (.0258)	0.0248 (.0289)	0.0920 (.0250)	-0.0832 (.0273)
6.4	0.0379 (.0254)	0.0396 (.0313)	0.0430 (.0259)	0.0378 (.0285)	0.0920 (.0249)	-0.0753 (.0275)
6.5	0.0328 (.0246)	0.0384 (.0301)	0.0462 (.0258)	0.0509 (.0283)	0.0852 (.0250)	-0.0609 (.0274)
6.6	0.0303 (.0237)	0.0419 (.0290)	0.0528 (.0251)	0.0607 (.0281)	0.0733 (.0247)	-0.0430 (.0266)
6.7	0.0306 (.0234)	0.0483 (.0288)	0.0609 (.0240)	0.0651 (.0276)	0.0586 (.0240)	-0.0252 (.0255)
6.8	0.0334 (.0233)	0.0553 (.0289)	0.0682 (.0236)	0.0641 (.0266)	0.0434 (.0231)	-0.0114 (.0251)
6.9	0.0378 (.0233)	0.0608 (.0288)	0.0727 (.0238)	0.0589 (.0263)	0.0298 (.0229)	-0.0044 (.0253)

TABLE XII (con't)

R A	Run 1 $c(r)^{\pm}$ (BAND)	Run 2 $c(r)^{\pm}$ (BAND)	Run 3 $c(r)^{\pm}$ (BAND)	Run 4 $c(r)^{\pm}$ (BAND)	Run 5 $c(r)^{\pm}$ (BAND)	Run 6 $c(r)^{\pm}$ (BAND)
7.0	0.0426(.0227)	0.0633(.0276)	0.0727(.0236)	0.0517(.0261)	0.0193(.0228)	-0.0051(.0250)
7.2	0.0488(.0216)	0.0575(.0267)	0.0584(.0223)	0.0375(.0254)	0.0103(.0223)	-0.0242(.0236)
7.4	0.0459(.0217)	0.0412(.0269)	0.0332(.0223)	0.0262(.0247)	0.0151(.0214)	-0.0471(.0236)
7.6	0.0356(.0210)	0.0227(.0255)	0.0130(.0220)	0.0139(.0246)	0.0243(.0216)	-0.0542(.0233)
7.8	0.0243(.0201)	0.0084(.0252)	0.0064(.0206)	0.0009(.0232)	0.0284(.0202)	-0.0447(.0219)
8.0	0.0157(.0198)	0.0012(.0241)	0.0103(.0206)	-0.0039(.0229)	0.0242(.0198)	-0.0301(.0217)
8.2	0.0088(.0191)	0.0023(.0235)	0.0157(.0197)	0.0054(.0222)	0.0173(.0197)	-0.0187(.0209)
8.4	0.0016(.0189)	0.0103(.0236)	0.0169(.0195)	0.0221(.0218)	0.0158(.0188)	-0.0092(.0207)
8.6	-0.0039(.0186)	0.0206(.0224)	0.0145(.0193)	0.0331(.0215)	0.0216(.0187)	0.0013(.0204)
8.8	-0.0037(.0178)	0.0267(.0223)	0.0109(.0184)	0.0330(.0206)	0.0281(.0181)	0.0097(.0195)
9.0	0.0039(.0178)	0.0258(.0218)	0.0076(.0185)	0.0280(.0207)	0.0266(.0178)	0.0104(.0196)
9.2	0.0141(.0173)	0.0204(.0211)	0.0059(.0178)	0.0260(.0197)	0.0156(.0176)	0.0038(.0188)
9.4	0.0194(.0167)	0.0157(.0211)	0.0071(.0175)	0.0265(.0196)	0.0026(.0168)	-0.0027(.0185)
9.6	0.0160(.0168)	0.0140(.0201)	0.0117(.0174)	0.0233(.0193)	-0.0027(.0168)	-0.0023(.0183)
9.8	0.0077(.0160)	0.0134(.0200)	0.0165(.0166)	0.0147(.0185)	0.0020(.0164)	0.0044(.0175)
10.0	0.0013(.0158)	0.0110(.0195)	0.0162(.0166)	0.0066(.0186)	0.0101(.0159)	0.0110(.0175)
10.2	0.0006(.0157)	0.0070(.0190)	0.0087(.0161)	0.0045(.0177)	0.0130(.0158)	0.0132(.0169)
10.4	0.0035(.0154)	0.0046(.0192)	-0.0020(.0159)	0.0073(.0179)	0.0077(.0155)	0.0129(.0169)
10.6	0.0053(.0151)	0.0059(.0184)	-0.0083(.0158)	0.0094(.0175)	-0.0012(.0152)	0.0140(.0167)
10.8	0.0041(.0147)	0.0098(.0179)	-0.0055(.0148)	0.0083(.0166)	-0.0067(.0148)	0.0167(.0157)
11.0	0.0022(.0144)	0.0128(.0179)	0.0034(.0152)	0.0069(.0170)	-0.0053(.0146)	0.0181(.0160)
11.2	0.0027(.0143)	0.0126(.0173)	0.0111(.0147)	0.0084(.0162)	0.0011(.0144)	0.0161(.0155)
11.4	0.0058(.0138)	0.0095(.0172)	0.0121(.0143)	0.0106(.0161)	0.0078(.0139)	0.0131(.0151)
11.6	0.0085(.0136)	0.0059(.0167)	0.0068(.0143)	0.0088(.0158)	0.0112(.0138)	0.0127(.0151)
11.8	0.0083(.0137)	0.0034(.0166)	-0.0001(.0138)	0.0025(.0156)	0.0106(.0138)	0.0154(.0146)

TABLE XII (cont.)

R \bar{R}	Run 1	Run 2	Run 3	Run 4	Run 5	Run 6
	$c(r)^{\pm}$ (BAND)					
12.0	0.0055(.0130)	0.0026(.0162)	-0.0046(.0137)	-0.0039(.0154)	0.0074(.0132)	0.0174(.0145)
12.2	0.0031(.0130)	0.0034(.0160)	-0.0052(.0136)	-0.0055(.0150)	0.0043(.0133)	0.0157(.0144)
12.4	0.0032(.0130)	0.0054(.0159)	-0.0031(.0131)	-0.0031(.0149)	0.0035(.0129)	0.0111(.0139)
12.6	0.0050(.0125)	0.0076(.0154)	0.0003(.0131)	-0.0009(.0145)	0.0054(.0126)	0.0073(.0140)
12.8	0.0061(.0126)	0.0089(.0154)	0.0037(.0128)	-0.0010(.0144)	0.0082(.0127)	0.0069(.0135)
13.0	0.0051(.0123)	0.0082(.0150)	0.0056(.0126)	-0.0019(.0142)	0.0091(.0122)	0.0086(.0134)
13.2	0.0029(.0119)	0.0058(.0147)	0.0046(.0125)	-0.0011(.0137)	0.0065(.0121)	0.0095(.0133)
13.4	0.0014(.0119)	0.0028(.0147)	0.0010(.0121)	0.0002(.0137)	0.0021(.0120)	0.0080(.0128)
13.6	0.0014(.0115)	0.0009(.0143)	-0.0030(.0120)	-0.0004(.0133)	-0.0009(.0116)	0.0048(.0128)
13.8	0.0019(.0116)	0.0008(.0143)	-0.0044(.0119)	-0.0029(.0135)	-0.0006(.0118)	0.0016(.0126)
14.0	0.0018(.0110)	0.0021(.0134)	-0.0023(.0113)	-0.0039(.0127)	0.0019(.0109)	-0.0009(.0120)
14.2	0.0010(.0107)	0.0042(.0132)	0.0018(.0113)	-0.0007(.0125)	0.0037(.0109)	-0.0021(.0120)
14.4	0.0007(.0108)	0.0060(.0134)	0.0051(.0110)	0.0047(.0126)	0.0029(.0110)	-0.0013(.0117)
14.6	0.0017(.0108)	0.0069(.0133)	0.0061(.0112)	0.0077(.0125)	0.0004(.0108)	0.0017(.0119)
14.8	0.0034(.0106)	0.0067(.0133)	0.0051(.0111)	0.0064(.0125)	-0.0013(.0109)	0.0051(.0117)
15.0	0.0050(.0106)	0.0056(.0130)	0.0039(.0110)	0.0032(.0122)	-0.0008(.0107)	0.0061(.0116)
15.2	0.0059(.0104)	0.0043(.0128)	0.0035(.0109)	0.0021(.0120)	0.0013(.0106)	0.0031(.0116)
15.4	0.0060(.0103)	0.0034(.0126)	0.0038(.0105)	0.0038(.0119)	0.0031(.0105)	-0.0021(.0111)
15.6	0.0054(.0103)	0.0031(.0124)	0.0040(.0105)	0.0057(.0118)	0.0033(.0101)	-0.0055(.0112)
15.8	0.0037(.0099)	0.0029(.0124)	0.0037(.0104)	0.0056(.0117)	0.0024(.0101)	-0.0046(.0110)
16.0	0.0006(.0099)	0.0027(.0121)	0.0029(.0102)	0.0040(.0113)	0.0014(.0100)	-0.0005(.0108)
16.2	-0.0029(.0099)	0.0025(.0122)	0.0022(.0103)	0.0030(.0114)	0.0014(.0099)	0.0034(.0109)
16.4	-0.0050(.0096)	0.0025(.0119)	0.0019(.0099)	0.0032(.0111)	0.0025(.0099)	0.0044(.0105)
16.6	-0.0040(.0094)	0.0027(.0115)	0.0024(.0098)	0.0034(.0109)	0.0043(.0094)	0.0029(.0103)
16.8	-0.0004(.0095)	0.0027(.0117)	0.0033(.0098)	0.0027(.0110)	0.0059(.0095)	0.0012(.0104)

TABLE XII (con't)

R Å	Run 1 $c(r)^{\pm}$ (BAND)	Run 2 $c(r)^{\pm}$ (BAND)	Run 3 $c(r)^{\pm}$ (BAND)	Run 4 $c(r)^{\pm}$ (BAND)	Run 5 $c(r)^{\pm}$ (BAND)	Run 6 $c(r)^{\pm}$ (BAND)
17.0	0.0033(.0093)	0.0026(.0115)	0.0040(.0096)	0.0019(.0107)	0.0067(.0095)	0.0008(.0101)
17.2	0.0046(.0093)	0.0024(.0114)	0.0039(.0097)	0.0020(.0108)	0.0061(.0093)	0.0020(.0102)
17.4	0.0028(.0090)	0.0024(.0112)	0.0029(.0094)	0.0028(.0104)	0.0046(.0092)	0.0037(.0099)
17.6	-0.0003(.0090)	0.0026(.0111)	0.0014(.0094)	0.0028(.0105)	0.0033(.0091)	0.0055(.0099)
17.8	-0.0022(.0090)	0.0026(.0110)	0.0004(.0093)	0.0015(.0103)	0.0031(.0090)	0.0071(.0098)
18.0	-0.0016(.0087)	0.0023(.0107)	0.0003(.0090)	0.0003(.0101)	0.0039(.0089)	0.0081(.0095)
18.2	0.0005(.0088)	0.0020(.0108)	0.0008(.0091)	0.0003(.0102)	0.0045(.0087)	0.0080(.0097)
18.4	0.0024(.0087)	0.0021(.0106)	0.0012(.0089)	0.0014(.0098)	0.0038(.0087)	0.0069(.0094)
18.6	0.0031(.0085)	0.0028(.0104)	0.0011(.0088)	0.0018(.0099)	0.0016(.0085)	0.0052(.0093)
18.8	0.0029(.0085)	0.0036(.0105)	0.0008(.0088)	0.0008(.0098)	-0.0005(.0085)	0.0038(.0093)
19.0	0.0025(.0084)	0.0036(.0101)	0.0003(.0086)	-0.0005(.0096)	-0.0012(.0085)	0.0028(.0091)
19.2	0.0023(.0082)	0.0027(.0102)	-0.0001(.0086)	-0.0003(.0096)	-0.0005(.0082)	0.0018(.0091)
19.4	0.0021(.0083)	0.0013(.0101)	-0.0006(.0084)	-0.0001(.0094)	0.0005(.0082)	0.0008(.0089)
19.6	0.0017(.0080)	0.0001(.0100)	-0.0012(.0084)	0.0003(.0094)	0.0009(.0083)	0.0002(.0090)
19.8	0.0014(.0081)	-0.0002(.0100)	-0.0016(.0084)	0. (.0093)	0.0005(.0081)	0.0003(.0089)
20.0	0.0013(.0080)	0. (.0096)	-0.0015(.0081)	-0.0004(.0091)	-0. (.0080)	0.0008(.0085)
20.2	0.0016(.0078)	0.0004(.0097)	-0.0008(.0081)	0. (.0092)	0. (.0078)	0.0008(.0086)
20.4	0.0017(.0075)	0.0004(.0094)	0.0001(.0078)	0.0009(.0087)	0.0006(.0076)	-0.0003(.0083)
20.6	0.0013(.0075)	0.0001(.0093)	0.0009(.0078)	0.0010(.0087)	0.0012(.0076)	-0.0017(.0082)
20.8	0.0007(.0082)	-0.0005(.0099)	0.0011(.0084)	0.0001(.0091)	0.0015(.0081)	-0.0023(.0090)
21.0	0.0003(.0071)	-0.0011(.0086)	0.0007(.0072)	-0.0007(.0083)	0.0017(.0072)	-0.0019(.0077)
21.2	0.0003(.0077)	-0.0013(.0096)	-0.0001(.0081)	-0.0004(.0091)	0.0018(.0078)	-0.0011(.0086)
21.4	0.0003(.0077)	-0.0011(.0095)	-0.0009(.0080)	0.0005(.0089)	0.0021(.0078)	-0.0008(.0085)
21.6	-0. (.0071)	-0.0006(.0086)	-0.0011(.0072)	0.0008(.0082)	0.0022(.0072)	-0.0010(.0077)
21.8	-0.0008(.0073)	-0.0001(.0089)	-0.0005(.0076)	-0.0002(.0082)	0.0021(.0072)	-0.0009(.0080)

TABLE XII (con't)

R Å	Run 1 $c(r)^{\pm}$ (BAND)	Run 2 $c(r)^{\pm}$ (BAND)	Run 3 $c(r)^{\pm}$ (BAND)	Run 4 $c(r)^{\pm}$ (BAND)	Run 5 $c(r)^{\pm}$ (BAND)	Run 6 $c(r)^{\pm}$ (BAND)
22.0	-0.0014(.0073)	0.0001(.0090)	0.0006(.0076)	-0.0015(.0085)	0.0019(.0074)	-0. (.0079)
22.2	-0.0013(.0071)	0. (.0089)	0.0014(.0075)	-0.0019(.0084)	0.0017(.0072)	0.0010(.0079)
22.4	-0.0006(.0069)	0. (.0087)	0.0015(.0073)	-0.0013(.0082)	0.0017(.0070)	0.0017(.0078)
22.6	0. (.0071)	0.0002(.0084)	0.0010(.0071)	-0.0007(.0080)	0.0017(.0071)	0.0018(.0074)
22.8	0.0002(.0070)	0.0006(.0087)	0.0007(.0073)	-0.0008(.0079)	0.0018(.0070)	0.0018(.0078)
23.0	-0.0001(.0068)	0.0009(.0085)	0.0011(.0072)	-0.0012(.0081)	0.0019(.0070)	0.0024(.0076)
23.2	-0.0003(.0068)	0.0010(.0084)	0.0017(.0070)	-0.0013(.0079)	0.0018(.0069)	0.0031(.0074)
23.4	0. (.0068)	0.0010(.0084)	0.0018(.0070)	-0.0009(.0079)	0.0013(.0068)	0.0031(.0075)
23.6	0.0006(.0068)	0.0009(.0081)	0.0013(.0069)	-0.0004(.0078)	0.0004(.0068)	0.0022(.0073)
23.8	0.0009(.0067)	0.0008(.0083)	0.0004(.0070)	-0. (.0076)	-0.0006(.0067)	0.0010(.0074)
24.0	0.0006(.0065)	0.0005(.0081)	0.0001(.0069)	0.0003(.0077)	-0.0010(.0067)	0.0004(.0072)

TABLE XIII

SUMMARY OF FEATURES IN THE DIRECT CORRELATION FUNCTION OF ARGON

Run No.	r_0 first zero Å	r_{\max} first maximum Å	$c(r_{\max})$	$c(0)^*$
1	3.46	3.96	1.11	- 9.37
2	3.43	3.87	1.15	- 8.93
3	3.49	3.93	1.17	-11.38
4	3.43	3.85	.91	-12.58
5	3.48	3.90	1.09	-15.15
6	3.49	3.87	1.10	-17.13
median	$3.46 \pm .03$		$1.04 \pm .14^{**}$	

* Estimated by extrapolation at small r

** $1.14 \pm .05$ if Run No. 4 is left out

TABLE XIV

SUMMARY OF FEATURES IN THE PREDICTED PY POTENTIAL FUNCTIONS

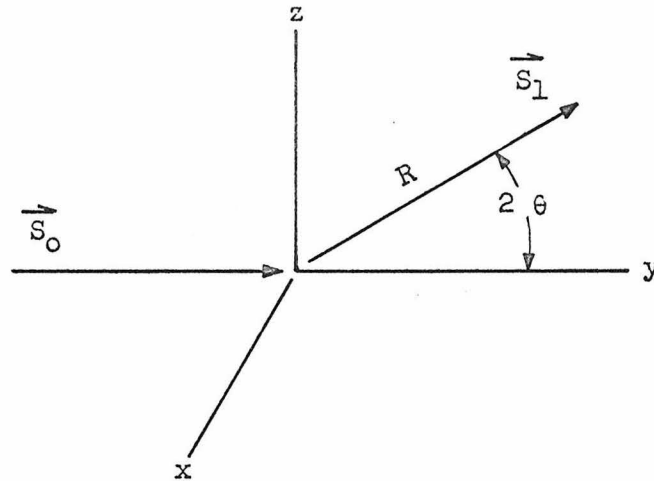
Run No.	σ first zero Å	r_0 first minimum Å	ϵ/k °K
1	3.44	3.98	-105.5 \pm 2.6
2	3.46	4.03	-118.0 \pm 3.5
3	3.48	4.00	- 96.9 \pm 2.6
4	3.43	4.01	- 75.9 \pm 2.9
5	3.48	4.02	- 78.2 \pm 2.2
6	3.49	3.95	- 68.6 \pm 2.1
median	3.46 \pm .03	3.99 \pm .04	

APPENDIX 1

The Basic Scattering Equation

A. COHERENT SCATTERING BY A FREE ELECTRON IN THE DEBYE-SCHERRER GEOMETRY FOR UNPOLARIZED INCIDENT RADIATION. (The problem of the scattering of radiation by a free electron was first solved in terms of classical electrodynamics by J. J. Thompson, a summary of which can be found in James.¹)

Consider a free electron at the origin of a cartesian coordinate system where the incident radiation is propagated toward the origin from the $-y$ direction, and the scattered radiation for the Debye-Scherrer geometry is detected along an arc of radius R in the $y - z$ plane.



The incident beam direction and the scattered beam direction are described by unit vectors \vec{S}_0 and \vec{S}_1 . Let \vec{i} , \vec{j} , and \vec{k} be unit vectors

in the x, y, and z directions, therefore

$$\vec{S}_0 = \vec{j} \quad (1 - 1)$$

$$\vec{S}_1 = \cos 2\theta \vec{j} + \sin 2\theta \vec{k} \quad (1 - 2)$$

The time-varying electric field associated with the plane wave that is propagated in the y direction lies in the x - z plane and can be described

$$\vec{E}_0 (\Psi) = Ae^{i\omega t} (\sin \Psi \vec{i} + \cos \Psi \vec{k}) \quad (1 - 3)$$

where A is the amplitude, ω is the circular frequency and Ψ is the polarization angle with respect to the x axis in the x - z plane. Ψ varies from 0 to π radians.

For a free electron accelerated by this electromagnetic field

$$m\vec{a} = e\vec{E}_0 = m\vec{\ddot{x}}(t) = eAe^{i\omega t} (\sin \Psi \vec{i} + \cos \Psi \vec{k}) \quad (1 - 4)$$

The intensity of the secondary radiation scattered from this accelerated electron in the S_1 direction at a distance R is the vector product²:

$$\vec{E}_s (\Psi) = \frac{e}{c^2 R^3} R \vec{S}_1 \times (R \vec{S}_1 \times \vec{\ddot{x}}(t)) \quad (1 - 5)$$

or

$$\vec{E}_s(\Psi) = \frac{e^2 A e^{i\omega(t - \frac{R}{c})}}{m c^2 R} (\sin \Psi \vec{i} + \cos \Psi \sin 2\theta \cos 2\theta \vec{j} + \cos \Psi \cos^2 2\theta \vec{k}) \quad (1 - 6)$$

The scattered intensity is proportional to the square of the amplitude of this electromagnetic radiation.

$$I_s(\Psi) = \vec{E}_s(\Psi) \cdot \vec{E}_s^*(\Psi) = \frac{e^4 A^2}{m^2 c^4 R^2} (\sin^2 \Psi + \cos^2 \Psi \cos^2 2\theta) \quad (1 - 7)$$

The average of the scattered intensity for all values of the polarization angle Ψ is:

$$I_s = \frac{\int_0^\pi \frac{e^4 A^2}{m^2 c^4 R^2} (\sin^2 \Psi + \cos^2 \Psi \cos^2 2\theta) d\Psi}{\int_0^\pi d\Psi} \quad (1 - 8)$$

$$I_s = \frac{e^4 A^2}{m^2 c^4 R^2} \left(\frac{1 + \cos^2 2\theta}{2} \right) \quad (1 - 9)$$

In a similar manner, the average incident intensity, I_o , is

$$I_o = \frac{\int_0^\pi A^2 d\Psi}{\int_0^\pi d\Psi} \quad (1 - 10)$$

Therefore the total scattering from an electron, I_T , for unpolarized radiation in the Debye-Scherrer geometry is:

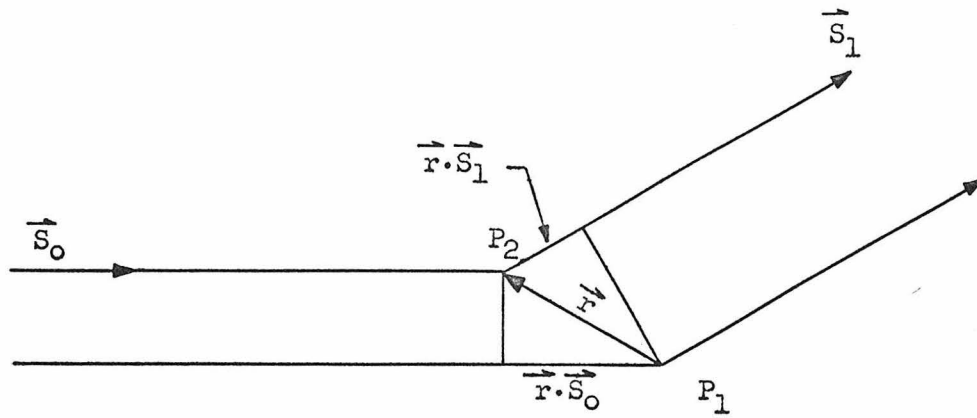
$$I_T = I_s = \frac{e^4 I_0}{m^2 c^4 R^2} \left(\frac{1 + \cos^2 2\theta}{2} \right) \quad (1 - 11)$$

B. COHERENT SCATTERING FROM A MEDIUM WHOSE ELECTRON DENSITY IS $\rho(\vec{R})$.

Let $\rho(\vec{R})$ represent the electron density at the vector position \vec{R} in a medium that is being swept by a plane wave of electromagnetic radiation whose field varies as:

$$\vec{E}_0 = A e^{i\omega t} (\sin \psi \vec{i} + \cos \psi \vec{j}) \quad (1 - 3)$$

Within this medium, consider two different scattering points, P_1 and P_2 , and the vector \vec{r} from P_1 to P_2 . If \vec{S}_0 and \vec{S}_1 are unit



vectors in the incident and diffracted directions respectively, then the difference, l , in path length traveled by the two waves scattered from P_1 and P_2 is:

$$l = (\vec{r} \cdot \vec{S}_1 - \vec{r} \cdot \vec{S}_0) \quad (1 - 12)$$

The phase angle, ϕ , that corresponds to this distance is,

$$\phi = \frac{2\pi}{\lambda} l = \frac{2\pi}{\lambda} (\vec{r} \cdot \vec{S}_1 - \vec{r} \cdot \vec{S}_0) \quad (1 - 13)$$

If the phase angle of the wave scattered from P_1 is taken as zero, then the wave scattered from P_2 is:

$$\vec{E}_2 = \frac{e^2 A e^{i\omega(t-R/c) + i2\pi/\lambda(\vec{r} \cdot \vec{S}_1 - \vec{r} \cdot \vec{S}_0)}}{mc^2 R} (\sin \Psi \vec{i} + \cos \Psi \sin 2\theta \cos 2\theta \vec{j} + \cos \Psi \cos^2 2\theta \vec{k}) \quad (1 - 14)$$

where

$$\vec{E}_1 = \frac{e^2 A e^{i\omega(t-R/c)}}{mc^2 R} (\sin \Psi \vec{i} + \cos \Psi \sin 2\theta \cos 2\theta \vec{j} + \cos \Psi \cos^2 2\theta \vec{k}) \quad (1 - 15)$$

The scattering parameter \vec{s} is defined as:

$$\vec{s} = \frac{2\pi}{\lambda} (\vec{S}_1 - \vec{S}_0) \quad (1 - 16)$$

The resultant amplitude is found by integrating the electronic density times the scattering power of the electron times the phase term over the volume of the medium.

$$\vec{E}_s = \frac{e^2 A e^{i\omega(t-R/c)}}{mc^2 R} (\sin \Psi \vec{i} + \cos \Psi \sin 2\theta \cos 2\theta \vec{j} + \cos \Psi \cos^2 2\theta \vec{k}) \int_V \rho(\vec{R}) e^{i \vec{r} \cdot \vec{s}} dV \quad (1 - 17)$$

From which the intensity averaged over the polarization angle Ψ is:

$$I(s) = \frac{e^4 A^2}{m^2 c^4 R^2} \left(\frac{1 + \cos^2 2\theta}{2} \right) \left| \int_V \rho(\vec{R}) e^{i \vec{r} \cdot \vec{s}} dV \right|^2 \quad (1 - 18)$$

or using equation (1 - 11)

$$I(s) = I_T \left| \int_V \rho(\vec{R}) e^{i \vec{r} \cdot \vec{s}} dV \right|^2 \quad (1 - 19)$$

C. COHERENT SCATTERING FROM A LIQUID COMPOSED OF ONE TYPE OF SPHERICALLY SYMMETRIC ATOMS. (This derivation follows that of Paalman and Pings.³)

If one defines the electron density of an atom as $\rho_i(\vec{R} - \vec{R}_i)$, where \vec{R}_i is a vector to the i^{th} atom in the fluid at time t , and \vec{R} is a vector to a scattering point in the same atom, then the scattering intensity is time-dependent.

$$I(s, t) = I_T \left| \sum_{i=1}^N \int_{V_i} \rho_i(\vec{R} - \vec{R}_i) e^{i \vec{r} \cdot \vec{s}} dV \right|^2 \quad (1 - 20)$$

where N is the total number of atoms in the fluid and each integral in the sum is over the volume of the i^{th} atom (Note: $\rho_i(\vec{R} - \vec{R}_i)$ is zero outside the i^{th} atom). The observed scattering is then the time-average of equation (1 - 20)

$$I(s) = \langle I(s, t) \rangle = I_T \left\langle \left| \sum_{i=1}^N \int_{V_i} \rho_i (\vec{R} - \vec{R}_i) e^{i \vec{r} \cdot \vec{s}} dV \right|^2 \right\rangle \quad (1 - 21)$$

If one picks an origin for scattering points, \vec{r} , and positions in the fluid, \vec{R} , to be at the nucleus of one atom in the fluid, $I(s)$ becomes:

$$I(s) = I_T \left\langle \left| \sum_{i=1}^N \int_{V_i} \rho_i (\vec{r} - \vec{r}_i) e^{i \vec{r} \cdot \vec{s}} dV \right|^2 \right\rangle \quad (1 - 22)$$

Equation (1 - 22) can be rearranged to become:

$$I(s) = I_T \left\langle \left| \sum_{i=1}^N \int_{V_i} \rho_i (\vec{r} - \vec{r}_i) e^{i (\vec{r} - \vec{r}_i) \cdot \vec{s}} e^{i \vec{r}_i \cdot \vec{s}} dV \right|^2 \right\rangle \quad (1 - 23)$$

which when expanded is:

$$I(s) = I_T \left\langle \sum_{i=1}^N \sum_{j=1}^N e^{i \vec{r}_i \cdot \vec{s}} e^{-i \vec{r}_j \cdot \vec{s}} \left[\int_{V_i} \rho_i (\vec{r} - \vec{r}_i) e^{i (\vec{r} - \vec{r}_i) \cdot \vec{s}} dV \right] \left[\int_{V_j} \rho_j (\vec{r} - \vec{r}_j) e^{-i (\vec{r} - \vec{r}_j) \cdot \vec{s}} dV \right] \right\rangle \quad (1 - 24)$$

However, since there is no correlation in time between electrons in different atoms, nor between electrons in an atom with the positions

of atoms in the fluid, Equation (1 - 24) reduces to be:

$$I(s) = I_T \sum_{i=1}^N \sum_{j=1}^N \langle e^{i \vec{r}_i \cdot \vec{s}} e^{-i \vec{r}_j \cdot \vec{s}} \rangle f_i(s) f_j^*(s) \quad (1 - 25)$$

where $f_i(s)$, the atomic scattering factor, is

$$f_i(s) = \left\langle \int_{V_i} \rho(\vec{r} - \vec{r}_i) e^{i(\vec{r} - \vec{r}_i) \cdot \vec{s}} dV \right\rangle \quad (1 - 26)$$

and $f_j^*(s)$ is the complex conjugate of this quantity.

The time averaged atomic scattering factor can be calculated from Hartree-Fock wave equations⁴ for the electron density in the atom. That is,

$$f_i(s) = \int_{V_i} \psi_i e^{i(\vec{r} - \vec{r}_i) \cdot \vec{s}} \psi_i^* dV \quad (1 - 27)$$

where ψ_i is the time-dependent wave function for the i^{th} atom.

For a liquid composed of atoms of one type,

$$f_i(s) = f_j(s) = f(s) \text{ for all } i \text{ and } j \quad (1 - 28)$$

The atomic positions of all the atoms in the fluid at time t can be described by a delta function. That is, the atomic density at time t is:

$$\rho_a(\vec{r}) = \sum_{i=1}^N \frac{\delta(|\vec{r} - \vec{r}_i|)}{4\pi(\vec{r} - \vec{r}_i)^2} \quad (1 - 29)$$

From (1 - 29), it follows that

$$\sum_{i=1}^N e^{i\vec{r}_i \cdot \vec{s}} = \int_V \sum_{i=1}^N \frac{\delta(|\vec{r} - \vec{r}_i|)}{4\pi(\vec{r} - \vec{r}_i)^2} e^{i\vec{r} \cdot \vec{s}} dV \quad (1 - 30)$$

Using (1 - 28), (1 - 29), and (1 - 30), equation (1 - 25) may be rewritten as

$$I(s) = I_T f(s) f^*(s) \int_V \int_V \langle \rho_a(\vec{r}_1) \rho_a(\vec{r}_2) \rangle e^{i(\vec{r}_1 - \vec{r}_2) \cdot \vec{s}} dV_1 dV_2 \quad (1 - 31)$$

Let

$$\vec{r}_1 - \vec{r}_2 = \vec{r} \quad (1 - 32)$$

$$\vec{r}_2 = \vec{r}' \quad (1 - 33)$$

Then equation (1 - 31) can be rewritten as

$$I(s) = I_T f(s) f^*(s) \int_V \left[\int_V \langle \rho_a(\vec{r} + \vec{r}') \rho_a(\vec{r}') \rangle dV' \right] e^{i\vec{r} \cdot \vec{s}} dV \quad (1 - 34)$$

The singular points in the square-bracketed integration are distributed thickly for $\vec{r} \neq 0$. The radial atomic density $\rho(\vec{r})$ is now defined as:

$$\rho(\vec{r}) = \frac{1}{N} \int_V \langle \rho_a(\vec{r} + \vec{r}') \rho_a(\vec{r}) \rangle dV' \quad (1 - 35)$$

for $\vec{r} > 0$. Because of the limited atomic packing

$$\rho(\vec{r}) = 0 \quad \text{for} \quad 0 < |\vec{r}| < \text{one atomic diameter} \quad (1 - 36)$$

The singularity at the origin, that is for $\vec{r} = 0$, is isolated and can be removed. $\vec{r} = 0$ corresponds to those terms in equation (1 - 25) where $i = j$. For $\vec{r} = 0$

$$I(s) = I_T f(s) f^*(s) \sum_{i=1}^N e^{i(\vec{r}_i - \vec{r}_i) \cdot \vec{s}} = I_T f(s) f^*(s) N \quad (1 - 37)$$

Therefore, define

$$\rho(\vec{r} = 0) = \rho(0) = 0 \quad (1 - 38)$$

and then add the value of the singularity to the scattering equation:

$$I(s) = I_T f(s) f^*(s) \left(N + \int_V N \rho(\vec{r}) e^{i \vec{r} \cdot \vec{s}} dV \right) \quad (1 - 39)$$

or

$$I(s) - I_T N f(s) f^*(s) = I_T f(s) f^*(s) \int_V N \rho(\vec{r}) e^{i \vec{r} \cdot \vec{s}} dV \quad (1-40)$$

or

$$\frac{\left[\frac{I(s)}{N I_T} - f(s) f^*(s) \right]}{f(s) f^*(s)} = \int_V \rho(\vec{r}) e^{i \vec{r} \cdot \vec{s}} dV \quad (1-41)$$

Let

$$P(\theta) = (1 + \cos^2 2\theta)/2 \quad (1-42)$$

and

$$C = \frac{m^2 c^4 R^2}{e^4 I_0} \quad (1-43)$$

Then

$$\frac{C I(s)}{P(\theta) N f(s) f^*(s)} - 1 = \int_V \rho(\vec{r}) e^{i \vec{r} \cdot \vec{s}} dV \quad (1-44)$$

It will be of value at this point to discuss some finer points of the derivation. In particular, first consider the definition

of $\rho(\vec{r})$ given in equation (1 - 35). Actually,

$$N \rho(\vec{r}) = \gamma(\vec{r}) \int_V \langle \rho_a(\vec{r} + \vec{r}') \rho_a(\vec{r}') \rangle dV' \quad (1 - 45)$$

where $\gamma(\vec{r})$ corrects for the fact that the time-average of the atomic density functions is integrated only over that volume which contains the head of the vector $\vec{r}' + \vec{r}$. Therefore, $\gamma(\vec{r})$ is

$$\gamma(\vec{r}) = V(\vec{r})/V \leq 1 \quad (1 - 46)$$

where $V(\vec{r})$ is that portion of V which contributes to $\rho(\vec{r})$ for each value of \vec{r} . Furthermore, the atomic density at time t can be written as:

$$\rho_a(\vec{r}, t) = \bar{\rho}_a(\vec{r}) + \Delta \rho_a(\vec{r}, t) \quad (1 - 47)$$

It is constructive to note that $\bar{\rho}_a(\vec{r})$ leads to a diffraction called $I_0(s)$, where,

$$I_0(s) = I_T \int_V \gamma(\vec{r}) \int_{V'} \bar{\rho}_a(\vec{r} + \vec{r}') \bar{\rho}_a(\vec{r}') dV' e^{i \vec{s} \cdot \vec{r}} dV \quad (1 - 48)$$

For experiments where the sample dimensions are greater than 1 mm, the diffraction effects in $I_0(s)$ are concentrated at small values of s . Guinier and Fournet⁵ estimate that $I_0(s)$ is significantly different

from zero only for values of $s < \pi/R_0$, where R_0 is the smallest dimension characteristic of the sample. As a consequence, equation (1 - 44) is more properly written

$$\frac{\frac{C}{N} (I(s) - I_0(s))}{P(\theta) f(s) f^*(s)} - 1 = \int_V \gamma(\vec{r}) (\rho(\vec{r}) - \bar{\rho}(\vec{r})) e^{i \vec{s} \cdot \vec{r}} dV \quad (1 - 49)$$

However, $\rho(\vec{r})$ rapidly approaches $\bar{\rho}(\vec{r})$ for \vec{r} on the order of a few atomic radii, where $\gamma(\vec{r})$ is essentially one. Therefore:

$$\frac{\frac{C}{N} (I(s) - I_0(s))}{P(\theta) f(s) f^*(s)} - 1 = \int_V (\rho(\vec{r}) - \bar{\rho}(\vec{r})) e^{i \vec{s} \cdot \vec{r}} dV \quad (1 - 50)$$

This equation can now formally be integrated over all space since the kernel of the integral vanishes for reasonably small r . Therefore, for a spherically symmetric distribution, $\rho(\vec{r})$ is only a function of the magnitude of $|\vec{r}|$ or r and

$$\frac{\frac{C}{N} (I(s) - I_0(s))}{P(\theta) f(s) f^*(s)} - 1 = \int_0^\infty \int_0^\pi \int_0^{2\pi} (\rho(r) - \bar{\rho}(r)) e^{i sr \cos \theta} r^2 \sin \theta d\theta d\varphi dr \quad (1 - 51)$$

$$\frac{\frac{C}{N} (I(s) - I_0(s))}{P(\theta) f(s) f^*(s)} - 1 = \int_0^{\infty} 4\pi (\rho(r) - \bar{\rho}(r)) r^2 \frac{\sin sr}{sr} dr \quad (1 - 52)$$

This integral may be formally transformed to

$$4\pi r^2 (\rho(r) - \bar{\rho}(r)) = \frac{2r}{\pi} \int_0^{\infty} s \left(\frac{\frac{C}{N} (I(s) - I_0(s))}{P(\theta) f(s) f^*(s)} - 1 \right) \sin sr ds \quad (1 - 53)$$

In an experiment, $I(s) - I_0(s)$ is measured from s_{\min} to s_{\max} . s_{\min} is determined by the fact that forward scattering cannot be measured in the main beam, whereas s_{\max} is bounded above by $4\pi/\lambda$. Over the entire experimental range of s , $I_0(s)$ is insignificant, which means that only $I(s)$ is measured. And, since $I(s) (C/N)/P(\theta)$ rapidly approaches $f(s) f^*(s)$ when s is near $s_{\max}/2$, the infinite limit of the transform in s is satisfied by a zero-valued kernel in the integral. Kinetic theory⁶ shows that the scattering power at zero angle $I(0) - I_0(0)$ is:

$$\frac{\frac{C}{N} (I(0) - I_0(0))}{f(0) f^*(0)} = k T \rho K_T - 1 \quad (1 - 54)$$

Therefore, it remains to extrapolate $I(s_{\min})$ to the theoretical

value at $s = 0$ to form the experimentally attainable relationship between $I (s)$ and $\rho (r)$, namely

$$4\pi r^2 \left(\rho (r) - \bar{\rho} (r) \right) = \frac{2r}{\pi} \int_0^{s_{\max}} s \left[\frac{\frac{C}{N} (I (s) - I_0 (s))}{P (\theta) f (s) f^* (s)} - 1 \right] \sin sr \, ds \quad (1 - 55)$$

Since $I_0 (s)$ has only entered this discussion to formalize the transform and is never measured in an experiment, the above equation is often written as

$$4\pi r^2 \left(\rho (r) - \bar{\rho} (r) \right) = \frac{2r}{\pi} \int_0^{s_{\max}} s i (s) \sin sr \, ds \quad (1 - 56)$$

where

$$i (s) = \frac{\frac{C}{N} I (s)}{P (\theta) f (s) f^* (s)} - 1 \quad (1 - 57)$$

and

$$i (0) + 1 = k T \rho K_T \quad (1 - 58)$$

REFERENCES

1. James, R. W. The Optical Principles of the Diffraction of X-Rays. G. Bell and Sons: London, England, 1962.
2. Panofsky, W. K. H. and M. Phillips. Classical Electricity and Magnetism. Addison-Wesley Publishing Co., Inc.: Reading, Massachusetts, 1956.
3. Paalman, H. H. and C. J. Pings. "Fourier Analysis of X-Ray Diffraction Data from Liquids," Rev. Mod. Phys., 35: 2, 389 (1963).
4. Berghuis, J., I. M. Haanappel and M. Potters. "New Calculations of Atomic Scattering Factors," Acta Cryst., 8, 478 (1955).
5. Guinier, A. and G. Fournet. Small Angle Scattering of X-Rays. John Wiley and Sons, Inc.: New York, 1955.
6. Hill, T. L. Statistical Mechanics. McGraw-Hill Book Co., Inc.: New York, 1956.

APPENDIX 2THE BASIC DATA REDUCTION EQUATION¹

The basic scattering equations that relate $i(s)$ to $\rho(r)$ were derived in the previous appendix for an unconfined monatomic liquid. Absorption corrections were neglected. This appendix will develop the basic data reduction equation to calculate the total (coherent and incoherent) scattering function for liquid argon confined in a hollow beryllium cylinder, namely:

$$I_s(s) = \frac{1}{P(\theta) F(\theta) ASSC(\theta)} \left[I_{c+s}^E(\theta) - G(\theta) \frac{ACSC(\theta)}{ACC(\theta)} I_c^E(\theta) \right] \quad (2 - 1)$$

$$\text{where } s = (4\pi/\lambda) \sin \theta \quad (2 - 2)$$

θ is the Bragg angle

$P(\theta)$ is the correction factor for an unpolarized incident beam

$F(\theta)$, $G(\theta)$ are correction factors for incoherent scattering

s is a subscript which stands for sample

c is a subscript which stands for cell

I_s is the total scattering function

$$I_{C+S}^E(\theta) = I_{C+S}^\beta(\theta) - I_{C+S}^\alpha(\theta) \quad (2 - 3)$$

$$I_C^E(\theta) = I_C^\beta(\theta) - I_C^\alpha(\theta) \quad (2 - 4)$$

The α and β superscripts mean that the associated intensity, whether for the cell or cell and sample data, is the experimental scattering intensity measured at θ for either an α or a β filter on the incident x-ray beam. The net result is the I_{C+S}^E and I_C^E are the scattering intensities for a nearly monochromatic incident beam consisting almost entirely of the K_α doublet of the molybdenum target.

Paalman and Pings² and Kendig and Pings³ have discussed the calculation of absorption coefficients for the cylindrical cell and sample in the Debye-Scherrer scattering geometry, where the narrow incident beam only intercepts a portion of the confined liquid. They define absorption coefficients for this geometry as:

$$\text{ASSC}(\theta) = \frac{1}{V_S} \int_{V_S} e^{-\mu_S l_S(V, \theta) - \mu_C l_C(V, \theta)} dV \quad (2 - 5)$$

$$\text{ACSC}(\theta) = \frac{1}{V_C} \int_{V_C} e^{-\mu_S l_S(V, \theta) - \mu_C l_C(V, \theta)} dV \quad (2 - 6)$$

$$\text{ACC}(\theta) = \frac{1}{V_c} \int_{V_c} e^{-\mu_c} \ell_c(V, \theta) dV \quad (2 - 7)$$

where ASSC (θ) measures the volume-averaged reduction in the sample scattering caused by absorption in both the sample and cell

ACSC (θ) measures the volume-averaged reduction in cell scattering caused by absorption in both the sample and cell

ACC (θ) measures the volume-averaged reduction in cell scattering caused by absorption in the cell

μ_c is the linear absorption coefficient for the cell material (a function of wavelength)

μ_s is the linear absorption coefficient for the sample material (also a function of wavelength)

ℓ_c is the distance traversed in the cell by a ray scattered in dV

ℓ_s is the distance traversed in the sample by this same ray

θ is the Bragg angle

V_c is the volume of cell irradiated

V_s is the volume of sample irradiated

For the experiment where the empty cell diffraction pattern is measured, the cell scattering intensity that is detected is:

$$I_c^E(\theta) = I_o P(\theta) N_c ACC^{coh}(\theta) I_c(\theta) \gamma_c^{coh} t^{coh} + I_o P(\theta) N_c ACC^{inc}(\theta) I_c(\theta) \gamma_c^{inc} t^{inc} \quad (2 - 8)$$

- where I_o is the intensity of the incident beam
- $P(\theta)$ is the polarization correction
- N_c is the number of cell atoms irradiated by the incident beam
- $ACC^{coh}(\theta)$ is the ACC coefficient evaluated for the coherent wavelength over all of the distance traversed, l_c
- $ACC^{inc}(\theta)$ is the ACC coefficient evaluated for the coherent wavelength over the incident portion of l_c and for the incoherent wavelength over the diffracted portion of l_c
- $I_c(\theta)$ is the total or intrinsic scattering power per atom of cell material
- $\gamma_c^{coh}(\theta)$ is the fraction of I_c that is scattered with the same wavelength as the incident radiation
- $\gamma_c^{inc}(\theta)$ is the fraction of I_c that is scattered with the incoherent wavelength shift
- t^{coh} is the electronic transmission efficiency for coherent radiation reaching the detector
- t^{inc} is the electronic transmission efficiency for the incoherent radiation

and similarly,

$$\begin{aligned}
 I_{c+s}^E(\theta) = & I_0 P(\theta) N_c \text{ACSC}^{\text{coh}}(\theta) I_c(\theta) \gamma_c^{\text{coh}}(\theta) t^{\text{coh}} \\
 & + I_0 P(\theta) N_c \text{ACSC}^{\text{inc}}(\theta) I_c(\theta) \gamma_c^{\text{inc}}(\theta) t^{\text{inc}} \\
 & + I_0 P(\theta) N_s \text{ASSC}^{\text{coh}}(\theta) I_s(\theta) \gamma_s^{\text{coh}}(\theta) t^{\text{coh}} \\
 & + I_0 P(\theta) N_s \text{ASSC}^{\text{inc}}(\theta) I_s(\theta) \gamma_s^{\text{inc}}(\theta) t^{\text{inc}}
 \end{aligned} \tag{2 - 9}$$

where $\text{ACSC}^{\text{coh}}(\theta)$, $\text{ACSC}^{\text{inc}}(\theta)$ are the ACSC coefficients evaluated for the coherent wavelength over the incident portions of l_c and l_s and the coherent and incoherent wavelengths, respectively, over the diffracted portions

$\text{ASSC}^{\text{coh}}(\theta)$, $\text{ASSC}^{\text{inc}}(\theta)$ are the ASSC coefficients evaluated for coherent and incoherent diffracted wavelengths

N_s is the number of irradiated sample atoms

I_s is the intrinsic scattering power of the sample atoms

γ_s^{coh} is the fraction of coherent radiation in I_s

γ_s^{inc} is the fraction of incoherent radiation in I_s

In this experiment, the voltage windows on the pulse height analyzer were set to make the electronic transmission efficiency greater than 99.5% and, therefore, was almost independent of wavelength for the coherent and incoherent wavelengths.

$$t^{\text{coh}} \approx t^{\text{inc}} > .995 \sim 1 \tag{2 - 10}$$

For algebraic simplicity these transmission efficiencies will be set to one. Since the final intensity, I_s , is normalized by a constant, the magnitude of these terms will not influence the transform to $\rho(r)$.

Let:

$$FCC(\theta) = \gamma_c^{\text{coh}}(\theta) + \gamma_c^{\text{inc}}(\theta) \frac{ACC^{\text{inc}}(\theta)}{ACC^{\text{coh}}(\theta)} \quad (2-11)$$

$$FCSC(\theta) = \gamma_c^{\text{coh}}(\theta) + \gamma_c^{\text{inc}}(\theta) \frac{ACSC^{\text{inc}}(\theta)}{ACSC^{\text{coh}}(\theta)} \quad (2-12)$$

$$F(\theta) = FSSC(\theta) = \gamma_s^{\text{coh}} + \gamma_s^{\text{inc}} \frac{ASSC^{\text{inc}}(\theta)}{ASSC^{\text{coh}}(\theta)} \quad (2-13)$$

Using equations (2-10), (2-11), (2-12) and (2-13), equations (2-8) and (2-9) become:

$$I_c^E = I_o P(\theta) N_c I_c(\theta) ACC(\theta) FCC(\theta) \quad (2-14)$$

$$I_{c+s}^E = I_o P(\theta) N_c I_c(\theta) ACSC(\theta) FCSC(\theta) \\ + I_o P(\theta) N_s I_s(\theta) ASSC(\theta) FSSC(\theta) \quad (2-15)$$

Substituting equation (2-14) into (2-15), (2-15) within a normalizing factor becomes

$$I_s(\theta) = \frac{1}{P(\theta) F(\theta) ASSC(\theta)} \left[I_{c+s}^E(\theta) - G(\theta) \frac{ACSC(\theta)}{ACC(\theta)} I_c^E(\theta) \right] \quad (2-16)$$

where

$$G(\theta) = \frac{FCSC(\theta)}{FCC(\theta)} \quad (2 - 17)$$

and the coherent superscript for ACC, ACSC and ASSC have been removed for convenience.

For data reduction:

$$\gamma_c^{coh} = \frac{f_c^2(\theta)}{f_c^2(\theta) + \frac{I_{inc_c}}{B^2}(\theta)} \quad (2 - 18)$$

where f_c is the Hartree Fock atomic scattering factor for the cell material

I_{inc_c} is the incoherent scattering factor for the cell material, beryllium

B^2 is the proper Breit-Dirac factor

The fraction, γ_s^{coh} , of coherent scattering from the sample depends on the structure $\rho(r)$ and can be calculated from $I_s(\theta)$. Therefore, an iterative procedure is used. The first estimate is taken to be:

$$\gamma_s^{coh}(\theta) = \frac{f_d^2(\theta)}{f_d^2(\theta) + \frac{I_{inc_s}}{B^2}(\theta)} \quad (2 - 19)$$

where f_d is the dispersion corrected Hartree-Fock atomic scattering factor for the argon sample

I_{inc_s} is the incoherent scattering factor for the sample

Successive values of γ_s^{coh} are calculated from the normalized intrinsic scattering;

$$\gamma_s^{coh} = \frac{\frac{C}{N} I_s(\theta) - \frac{I_{inc_s}}{B^2}}{\frac{C}{N} I_s(\theta)} \quad (2 - 20)$$

(This is repeated until successive $I_s(\theta)$ functions are essentially the same.)

$\frac{C}{N}$ is the normalization factor.

REFERENCES

1. Mikolaj, P. G. "An X-Ray Diffraction Study of the Structure of Fluid Argon." Doctoral thesis, California Institute of Technology, Pasadena, California, 1965.
2. Paalman, H. H. and C. J. Pings. "Numerical Evaluation of X-Ray Absorption Factors for Cylindrical Samples and Annular Sample Cells," J. Appl. Phys., 33, 2635 (1962).
3. Kendig, A. P. and C. J. Pings. "X-Ray Absorption Factors for Cylindrical Samples in Annular Sample Cells Exposed to Incident Beams of Limited Width," J. Appl. Phys., 36, 1692 (1965).

APPENDIX 3DERIVATION OF THE CONFIDENCE INTERVAL FOR THE
BASIC DATA REDUCTION EQUATION

The determination of the sample scattering intensity from a confined sample in a dual filter experiment requires the measurement of six statistical quantities

1. N_C^β , the number of scattered quanta detected from the empty cell with a β filter on the incident beam during a time interval, τ_C .
2. N_C^α , the number of scattered quanta detected from the empty cell with an α filter on the incident beam during the same time interval, τ_C .
3. N_{C+S}^β , the number of scattered quanta detected from the cell and sample with a β filter on the incident beam during a time interval, τ_{C+S} .
4. N_{C+S}^α , the number of scattered quanta detected from the cell and sample with an α filter on the incident beam during the same sample measuring time interval, τ_{C+S} .
5. N_C^n and N_{C+S}^n , the numbers of counts of background noise, for the respective time intervals τ_C and τ_{C+S} .

The intensities or counting rates are calculated from these numbers, namely,

$$I_c^E = \frac{N_c^\beta - N_c^n}{\tau_c} - \frac{N_c^\alpha - N_c^n}{\tau_c} \quad (3 - 1)$$

$$I_{c+s}^E = \frac{N_{c+s}^\beta - N_{c+s}^n}{\tau_{c+s}} - \frac{N_{c+s}^\alpha - N_{c+s}^n}{\tau_{c+s}} \quad (3 - 2)$$

From which

$$I_s = A (I_{c+s}^E - B I_c^E) \quad (3 - 3)$$

where for algebraic simplicity,

$$A = \frac{1}{P(\theta) F(\theta) \text{ASSC}(\theta)} \quad (3 - 4)$$

and

$$B = G(\theta) \frac{\text{ACSC}(\theta)}{\text{ACC}(\theta)} \quad (3 - 5)$$

In the following derivation of the statistical uncertainty, ΔI_s , associated with I_s , the assumption is made that the statistical fluctuation of the background noise, N_c^n and N_{c+s}^n , is negligible compared to the level and fluctuations in N_c^β , N_c^α , N_{c+s}^β , and N_{c+s}^α .

Since all of the counting variables are independent discrete and random, the variance of I_s is expressed as:

$$\text{var } I_s = A^2 \left(\frac{\text{var } N_{c+s}^\beta}{\tau_{c+s}^2} + \frac{\text{var } N_{c+s}^\alpha}{\tau_{c+s}^2} + B^2 \left(\frac{\text{var } N_c^\beta}{\tau_c^2} + \frac{\text{var } N_c^\alpha}{\tau_c^2} \right) \right) \quad (3 - 6)$$

Furthermore, all of the remaining counting variables have Poisson distributions, which means that the variance is equal to the mean.

Therefore

$$\frac{\text{var } N_{c+s}^{\beta}}{\tau_{c+s}} = \frac{N_{c+s}^{\beta}}{\tau_{c+s}} = I_{c+s}^{\beta} \quad (3 - 7)$$

However, for the counting times used in this experiment, the values of the mean are so large that the distributions can be considered Gaussian or normal. Since the counting values for cell and sample measurements were made three times, it is proper to say that

$$\frac{\text{var } N_{c+s}^{\beta}}{\tau_{c+s}} = \frac{1}{3} \frac{\text{var } N_{c+s}^{\beta}}{\tau_{c+s}} = \frac{N_{c+s}^{\beta}}{3 \tau_{c+s}} = \frac{I_{c+s}^{\beta}}{3} \quad (3 - 8)$$

Following (3 - 8), equation (3 - 6) becomes

$$\text{var } I_s = A^2 \left(\frac{I_{c+s}^{\beta}}{3 \times 100} + \frac{I_{c+s}^{\alpha}}{3 \times 100} + B^2 \left(\frac{I_c^{\beta}}{5 \times 300} + \frac{I_c^{\alpha}}{5 \times 300} \right) \right) \quad (3 - 9)$$

where the cell data scans were observed five times for 300 seconds.

For a Gaussian distribution the confidence interval is given by

$$(\Delta I_s)_j = \pm k_j [\text{var } I_s]^{\frac{1}{2}} \quad (3 - 10)$$

where k_j is a constant and the subscript j refers to the confidence interval. Some values of k_j are listed below for various levels of confidence:

<u>j</u>	<u>k_j</u>
50%	0.675
90%	1.645
95%	1.960
99%	2.576

The final, expanded form of the confidence interval is:

$$\Delta I_s = \frac{\pm k_j}{\text{ASSC}(\theta) P(\theta) F(\theta) \sqrt{\tau_{c+s}}} * \left[\frac{(I_{c+s}^\beta + I_{c+s}^\alpha)}{n_{c+s}} + \frac{G^2(\theta) \text{ACSC}^2(\theta) \tau_{c+s} (I_c^\beta + I_c^\alpha)}{\text{ACC}^2(\theta) \tau_c n_c} \right]^{\frac{1}{2}} \quad (3 - 11)$$

where τ_{c+s} is the time interval for each data point in each cell and sample scans

n_{c+s} is the number of cell and sample data scans

τ_c is the time interval for each data point in each cell scan

n_c is the number of empty cell data scans

APPENDIX 4THE BREIT-DIRAC CORRECTION FACTOR FOR INCOHERENT SCATTERING
DETECTED BY A SCINTILLATION COUNTER

Several authors^{1,2,3,4} have stated that the proper Breit-Dirac correction factor for calculating the amount of incoherent scattering should be $1/B^2$ rather than the theoretical^{5,6} recoil correction, $1/B^3$, when the scattered radiation is detected by a scintillation counter that measures quanta per second per steradian. It is the opinion of this author that $1/B^2$ is the correct factor for use with a scintillation counter. This appendix will discuss this point.

The Breit-Dirac factor, $1/B^3$, is the multiplicative factor $(v'/v)^3$ where v and v' are the frequencies of the x-ray photons before and after scattering, respectively.

$$B = v/v' \quad (4 - 1)$$

The recoil corrected Waller-Hartree⁷ equation for incoherent scattering is

$$I_{e.u.} = \left\{ Z - \sum_{j=1} |f_{jj}|^2 - \sum_{\substack{j, k \\ j \neq k}} |f_{jk}|^2 \right\} \left(\frac{v'}{v} \right)^3 \quad (4 - 2)$$

where

$$f_{lm} = \int \psi_l^* (p) \psi_m (p) e^{i \vec{s} \cdot \vec{r}_p} dV_p \quad (4 - 3)$$

The integration extends over all coordinates of any one electron, p.

Walker¹, in his paper on Compton scattering for aluminum, made the following statement concerning the Breit-Dirac factor:

"If the scattered radiation is detected by a counter, so that actually one measures the number of scattered quanta per unit solid angle, the appropriate corrective factor is $(v'/v)^2$ or, i.e., $(1/B^2)$."

Similarly, Chipman and Jennings,² in their paper on the atomic scattering factors of Ne, Ar, Kr and Xe, made this statement:

"The Breit-Dirac correction factor appears here as $(1/B)^2$ rather than $(1/B)^3$ because with scintillation counting we measure power in photons per second rather than in conventional units."

At this point, consider just what the scintillation counter does measure. In a scintillation detector, incident photons are converted to output voltage pulses from a photomultiplier by a sequence of events that follows this basic outline. Incident photons create a number of electron-hole pairs in the host crystal that migrate to a fluorescent center where photons in the visible range are emitted. These secondary photons produce photoelectrons when they impinge on the photocathode. The photoelectrons are multiplied as they cascade through the photomultiplier tube to produce an output current pulse. When this current passes through a resistor to ground it, a voltage pulse is produced which, to a first order approximation, is proportional to the energy of the incident photon.

In a scintillation detector, the number of photoelectrons, n , generated at the photocathode of the multiplier for each incident photon is⁸:

$$n = \frac{E_x}{E_p} C_{xp} T_p C_{pe} \quad (4 - 4)$$

where E_x is the energy of the incident x-ray quantum

E_p is the energy of the fluorescent photon

C_{xp} is the fluorescent efficiency of the phosphor and may have values between 4% and 25%

T_p is the transparency of the phosphor to its own fluorescence and is near unity

C_{pe} is the photoelectric efficiency of the photocathode and is only about 5%

From these values, it will be seen that about 35 photoelectrons are liberated for Mo K_α incident x-radiation. Thus it is reasonable to argue that counting the voltage pulses is equivalent to counting quanta per second per steradian in the Debye-Scherrer geometry.

Figure 4-1 depicts⁹ a comparison between experimental results and theory for total scattering from monatomic gases made by Herzog¹⁰ on Wollan's¹¹ experimental data on helium. The solid line curves depict the values of coherent, incoherent, and total scattering calculated from the Waller-Hartree theory, including the $(1/B^3)$ Breit-Dirac correction

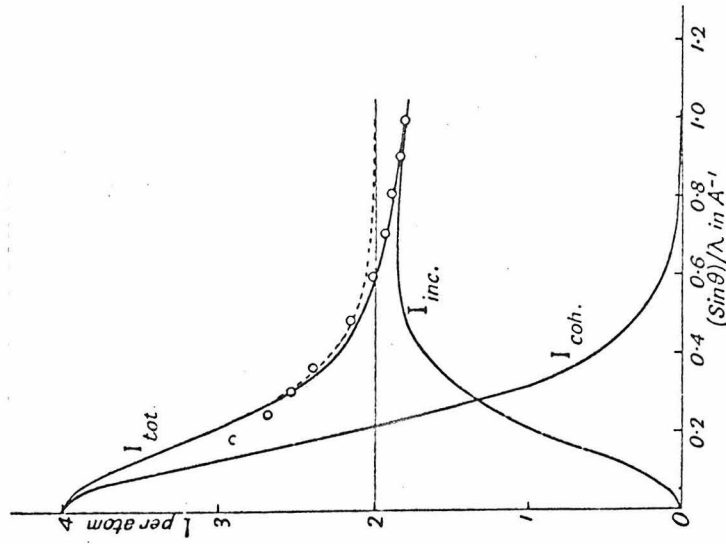


FIG. 4 - 19 . Solid curves represent coherent, incoherent with $1/B^3$ recoil correction, and total scattering from helium. The broken curve represents total scattering with no recoil correction. These theoretical curves are according to Herzog.⁹ The circles indicate experimental values obtained by Wollan.¹⁰

factor. The broken-line curve depicts the total scattering without the Breit-Dirac factor. This figure shows that the agreement between theory and experiment is materially improved by the use of the $(1/B)^3$ factor, and also that $(1/B)^2$ would be inadequate particularly at high values of $\sin \theta/\lambda$ ($\lambda = 0.71$ in this experiment). Wollan's measurements were made with an ionization detector.

At this point, consider just what an ionization detector measures. In an ionization process, the incident energy is converted to electrons that produce a current which passes through a dropping resistor and is converted to a voltage. Note that this voltage is proportional to the incident energy.

$$\frac{h\nu}{E_x} n_\nu e R = V_\nu \quad (4 - 5)$$

where h is Planck's constant

ν is the incident frequency

E_x is the ionization energy of the detector gas

e is the electron charge

R is the dropping resistor

V_ν is the output voltage for frequency ν

n_ν is the quantum rate in counts per second of quanta with energy ν

It will be seen, therefore, that the Wollan experiment means at high $\sin \theta/\lambda$

$$\nu n_{\nu} \propto f^2 \quad (4 - 6)$$

and

$$\nu' n_{\nu'} \propto I_{e.u.} \quad (4 - 7)$$

That is to say that $I_{e.u.}$ and f^2 are in units of energy per unit area perpendicular to the direction of propagation per second.

Therefore, for a scintillation counter the theoretical limits of quanta rate are the theoretical intensity limits divided by the energy of the coherent and incoherent radiations. That is

$$n_{\nu} \propto \frac{f^2}{h\nu} \quad (4 - 8)$$

$$n_{\nu'} \propto \frac{I_{e.u.}}{h\nu'} \quad (4 - 9)$$

Or, the total quanta count rate is:

$$n_{\nu} + n_{\nu'} \propto \frac{f^2}{\nu} + \frac{I_{e.u.}}{\nu'} \quad (4 - 10)$$

This can be rearranged as:

$$n_{\nu} + n_{\bar{\nu}} \propto f^2 + \frac{\nu}{\nu'} I_{e.u.} = f^2 + B I_{e.u.} \quad (4 - 11)$$

Therefore, the proper Breit-Dirac factor for a scintillation counter is $1/B^2$.

REFERENCES

1. Walker, C. B. "X-ray Compton Scattering for Aluminum," Phys. Rev., 103, 558 (1956).
2. Chipman, D. R. and L. D. Jennings. "Measurement of the Atomic Scattering Factor of Ne, Ar, Kr, and Xe," Phys. Rev., 132, 728 (1963).
3. Rodriguez, S. R. "X-ray Diffraction of Stable and Supercooled Liquid Gallium." Ph.D. Thesis. California Institute of Technology, 1964.
4. Mikolaj, P. G. "An X-ray Diffraction Study of the Structure of Fluid Argon." Ph.D. Thesis. California Institute of Technology, 1965.
5. Breit, G. Phys. Rev., 27, 362 (1926).
6. Dirac, P. A. M. Proc. Roy. Soc. (London), 111A, 405 (1926).
7. Waller, I. and D. R. Hartree. Proc. Roy. Soc. (London), 124A, 119 (1929).
8. Peiser, H. S., et al. X-ray Diffraction by Polycrystalline Materials. The Institute of Physics: London, 1955.
9. James, R. W. The Optical Principles of the Diffraction of X-rays. G. Bell and Sons, LTD, 1962.
10. Herzog, G. Z. Physik, 70, 583, 590 (1931).
11. Wollan, E. O. Phys. Rev., 37, 862 (1931).

APPENDIX 5

DUAL FILTER SPECTRUM

The molybdenum x-ray tube used in this experiment was operated at 55 Kv and 20 milliamps. Under these conditions, there is a wide band of white radiation superimposed on the characteristic K_{β} and K_{α} peaks. This appendix will discuss the degree of monochromatization of the incident beam that has been obtained with a dual filter.

The dual filter was two single filters: zirconium and yttrium¹. These elemental filters have absorption edges just less and just greater than the K_{α} doublet of the molybdenum target.

The relative x-ray transmission for each filter throughout the target spectrum depends on the linear absorption coefficient, $\mu(\lambda)$ and the thickness of the filter. The wavelength dependence of the mass absorption coefficients of the two filters is similar except between the K edges:²

$$\text{Zirconium: } \mu/\rho = 477 \lambda^3 - 261 \lambda^4 \text{ for } \lambda < 0.6888 \quad (5 - 1)$$

$$\text{Yttrium: } \mu/\rho = 441 \lambda^3 - 229 \lambda^4 \text{ for } \lambda < 0.7276 \quad (5 - 2)$$

and

$$\text{Zr: } \mu/\rho = 47.9 \lambda^3 - 5.72 \lambda^4 \text{ for } \lambda > 0.6888 \quad (5 - 3)$$

$$\text{Y: } \mu/\rho = 44.1 \lambda^3 - 4.88 \lambda^4 \text{ for } \lambda > 0.7276 \quad (5 - 4)$$

Therefore it is possible to reduce the contribution of white radiation by properly selecting the relative thicknesses of the two filters. Balanced filters attenuate all the wavelengths in the distribution except those between the absorption edges sandwiched around the K_{α} doublet. The net result is nearly monochromatic radiation.

The dual filter was balanced by trial and error until the relative transmissions of each filter at two wavelengths (one on each side of the K_{α} doublet) were similar. The yttrium filter was cold rolled to 5.5 mils. Its transmission was determined to be 37.5% at $\lambda = 0.7611 \text{ \AA}$, and 20.5% at $\lambda = 0.4522 \text{ \AA}$. Then the Zr filter material was cold rolled to several thicknesses near the thickness expected to match these transmissions. The thickness of the closest matching zirconium filter was 3.5 mils. Its transmissions were 37.2% at 0.7611 \AA and 20.5% at 0.4522 \AA .

The net spectrum passed by the dual filter was then measured experimentally by reflection from LiF. The data were taken in the Debye-Scherrer geometry. Vertical soller slits 1-1/4 inches long with a spacing of 0.018 inches and a $1/6^{\circ}$ divergence slit were used on the incident beam. High resolution, horizontal sollers with a spacing of 0.005 inch were used with 0.111 inch receiving slit. The pulse height analyzer was set at 99% transmission of the K_{α} radiation. The wavelength corresponding to data collected at the 2θ -Bragg angle was calculated using a d-spacing of 2.0125 angstroms for LiF.

The results of this work are plotted in Figure 5 - 1. The solid curve in the main portion of the diagram is the zirconium or β -filter spectrum. The circles in the main diagram and the insert are the net dual filter spectrum. For reference tabular data describing the net white radiation, Table 5 - 1, and the net spectrum of the K_{α} and K_{β} peaks, Table 5 - 2, are included.

Ninety per cent of the integrated intensity lies between 0.704 \AA and 0.718 \AA .

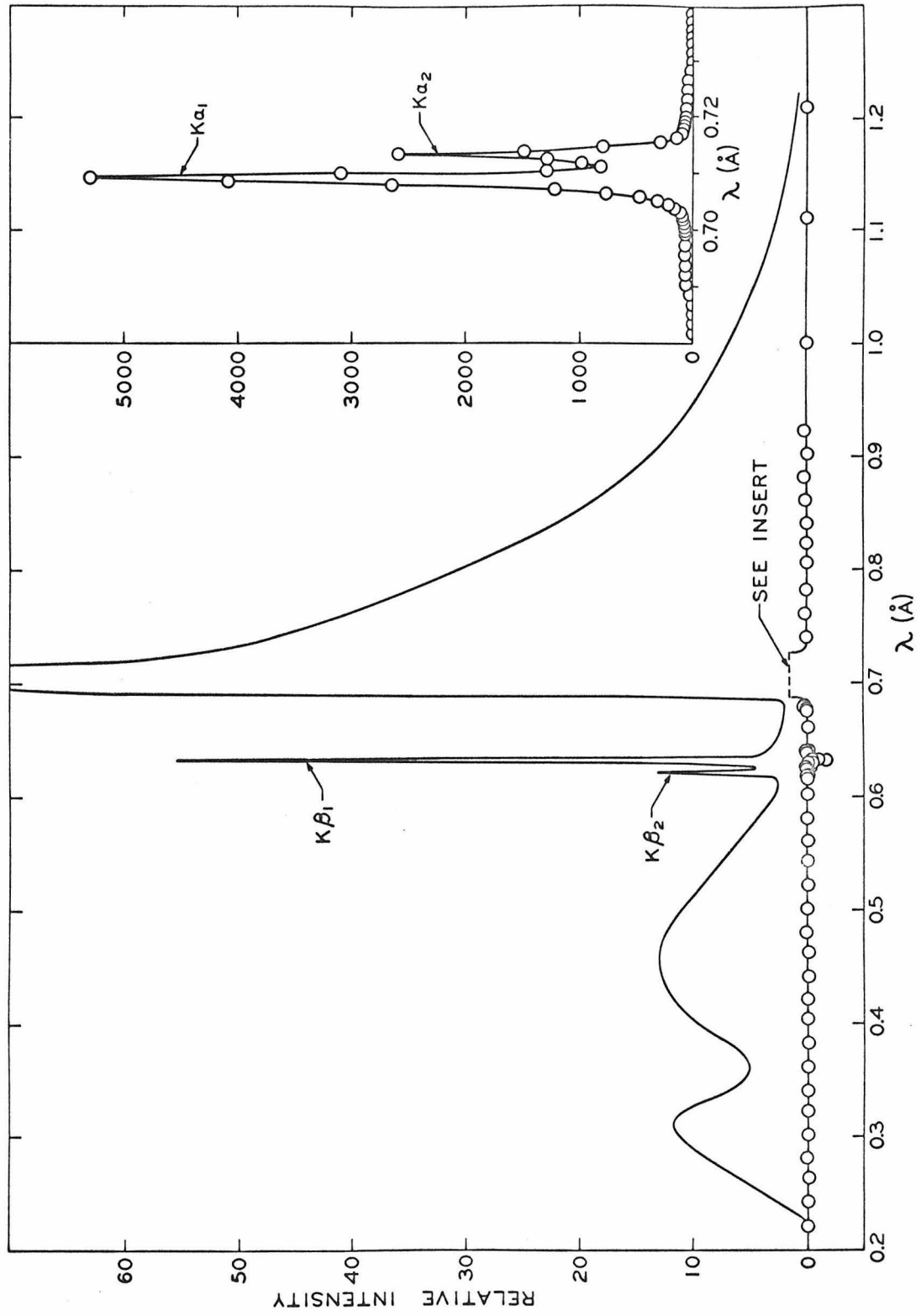


Figure 5 - 1. β Filter and Dual Filter Spectra

TABLE 5 - 1

DUAL FILTER SPECTRUM CORRESPONDING TO CIRCLES IN FIGURE 5 - 1
BACKGROUND RADIATION

λ Angstroms	Relative Intensity	λ Angstroms	Relative Intensity
.2000	0.013	.6019	0.048
.2212	0.027	.6227	-0.126
.2422	-0.001	.6401	0.103
.2632	-0.095	.6609	0.013
.2808	0.148	.6819	0.466
.3018	-0.003	.7404	0.007
.3228	0.010	.7611	0.196
.3403	0.044	.7818	0.853
.3613	-0.007	.8059	0.248
.3823	-0.110	.8231	0.035
.4033	-0.017	.8403	0.002
.4206	-0.016	.8609	-0.361
.4417	-0.110	.8814	0.211
.4626	-0.120	.9020	-0.103
.4801	-0.212	.9225	0.214
.5010	0.027		
.5219	-0.062		
.5418	-0.004		
.5602	-0.029		
.5802	0.302		

TABLE 5 - 2

DUAL FILTER SPECTRUM CORRESPONDING TO CIRCLES IN FIGURE 5 - 1

 K_{α} AND K_{β} REGIONS

K_{α}		K_{β}	
λ Angstroms	Relative Intensity	λ Angstroms	Relative Intensity
.6747	0.193	.6158	0.018
.6782	0.402	.6192	0.129
.6816	0.527	.6199	-0.031
.6851	2.143	.6206	-0.033
.6886	31.152	.6213	-0.254
.6920	71.055	.6220	0.017
.6955	74.329	.6227	-0.157
.6989	73.159	.6234	0.091
.7010	77.536	.6241	0.000
.7024	99.299	.6248	0.090
.7038	163.352	.6255	-0.193
.7052	317.844	.6262	0.044
.7066	782.981	.6269	-0.085
.7079	2655.884	.6276	0.004
.7086	4088.296	.6283	-0.056
.7093	5299.892	.6290	-0.054
.7100	3096.064	.6296	-0.414
.7113	821.938	.6303	-0.102
.7120	985.003	.6310	-0.104
.7127	1293.497	.6317	-0.506
.7134	2603.376	.6324	-1.660
.7141	1493.412	.6331	-0.845
.7148	801.478	.6338	-0.389
.7155	301.826	.6345	-0.021
.7162	150.606	.6352	-0.070

Table 5 - 2 (cont.)

K_{α}		K_{β}	
λ Angstroms	Relative Intensity	λ Angstroms	Relative Intensity
.7169	106.884	.6359	0.089
.7183	82.026	.6366	-0.156
.7197	73.231	.6373	0.016
.7231	55.934	.6380	-0.154
.7266	42.391	.6387	0.022
.7300	2.791	.6394	-0.021
.7355	.221	.6401	0.182

REFERENCE NOTES

- ¹The yttrium was obtained from Dr. Sten Samson of the Chemistry Department at the California Institute of Technology. Cold rolling of both metals was done by the Wilkinson Company of Santa Monica, California. The yttrium was easily worked to 5.5 mils from its initial thickness of 20 mils.
- ²These equations contain only the more important terms in λ . For the complete behavior see Chapter 3 of Volume III of the International Tables for X-ray Crystallography, The Kynoch Press: Birmingham, England, 1962.

APPENDIX 6

CALIBRATION OF THE PRESSURE GAGE

Pressure fluctuations of the confined argon were monitored with a model 141 Texas Instrument Precision Gage. This gage was calibrated against a dead weight tester.

The precision gage is principally a steel spiral called a Bourdon tube. When the tube is pressurized, the spiral unwinds. The degrees of rotation are detected optically. A mirror which reflects light from a fixed source is attached to the free end of the spiral. The sensor, an optical transducer, is mounted on a gear that travels around the Bourdon tube. The position of the transducer is converted to digital readout. The digital-counter reading is then multiplied by a scale factor to determine the pressure.

The model 141 is a servo-nulling gage that can be used in three operating modes: manual nulling, servo nulling, or output to an external recorder. For the argon pressure monitoring, the model 141 was used in the recorder output mode. The digital counter was set at a number corresponding to the desired pressure. The error signal was voltage divided and fed to a microvolt amplifier whose output was fed to a recorder. In this way, large and small error signals could be displayed on the recorder by changing the amplification. The argon pressure was regulated by adjusting the

trimmer injector on the manifold of the cryostat.

The dead weight tester used as a primary pressure standard was the Hart Pressure Balance. The effective area of the piston to be loaded with dead weight was 0.31096 ± 0.00002 square inches as calibrated in February, 1960. A vertical axle is coupled to the lower end of the piston of the measuring cylinder so that weights can be added. The piston is rotated by an electric motor which drives a claw connected to the axle coupled to the top end of the cylinder. To reduce friction between the piston and the cylinder wall, the piston is rotated between 80 and 100 cycles per minute. The motor drive is disengaged for each final calibration reading to eliminate vertical forces associated with the drive linkage. The oil provided with the balance had been developed to minimize viscosity changes between 3 and 300 atmospheres.

The Hart balance and the precision pressure gage were connected as in the schematic diagram (Figure 6 - 1). Nitrogen was used to pressurize the gage. The oil level in the reservoir was 2 inches above the tester pressure tap.

For a typical calibration data point, valves A and C were closed and the gas system vented. (The digital counter was set to zero only once, at the start of the calibration. Before it was set to zero, the Texas Instrument gage was pressurized to full cylinder pressure three times to reduce hysteresis effects. The

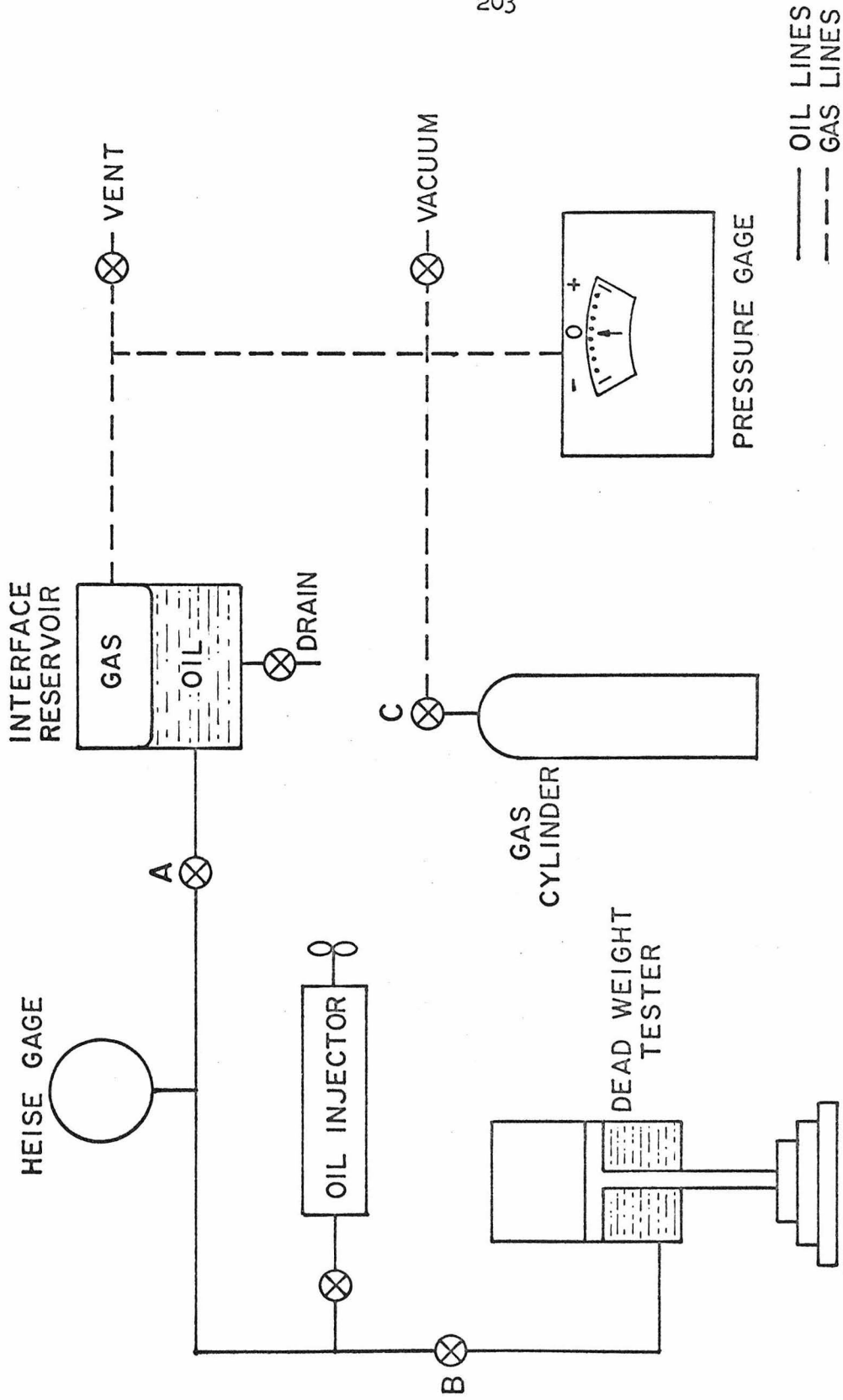


Figure 6 - 1. Schematic Diagram of the Pressure Calibration Equipment

zero shift was 0.004° for 35 pressurizations.) The dead weight tester was loaded with weights and started. With valve B open the pressure indicated by the Heise gage was noted.

Then valve B was closed, isolating the pressure balance. With the vent closed and valve A open, valve C was opened until the gas pressure reached the previous Heise gage reading. Valve B was then opened so that the tester pressure was applied to the TI gage. The TI gage was set in servo-nulling to obtain the coarse setting. After disengaging the pressure balance drive motor, the fine nulling was accomplished manually.

The pressure was calculated from:

- (1) the area of the piston A,
- (2) the total dead weight in pounds mass, W,
- (3) $g_c/g = 1.001116$ for Pasadena,
- (4) 2" oil head correction, h, and
- (5) corrections from the pressure balance manual.

$$P = \left(\frac{W}{A} - \rho_{oil} * h \right) \frac{g}{g_c} \quad (6 - 1)$$

where $\rho_{oil} = 0.880$ gms/cc.

In order to be able to set the digital-counter to the desired pressure, the data were fit to the following equation by least squares:

$$\left(\frac{\sigma}{P}\right) = A + BP + CP^2 \quad (6 - 2)$$

σ is degrees rotation.

The following coefficients were determined for P in psi:

$$A = 0.019706605 \quad (6 - 3)$$

$$B = 0.22031500 * 10^{-6} \quad (6 - 4)$$

$$C = -0.46102648 * 10^{-10} \quad (6 - 5)$$

The scatter of the data from this prediction equation is depicted in Figure 6 - 2. The sensitivity is about 1 part in 10^5 . The data are listed in Table 6 - 1.

The dead-weight tester sensitivity is 1 : 100,000, and is accurate to better than 1 part in 10,000. Since the TI gage is sensitive to 1 : 200,000, an overall accuracy of 1 part in 10,000 is realized.

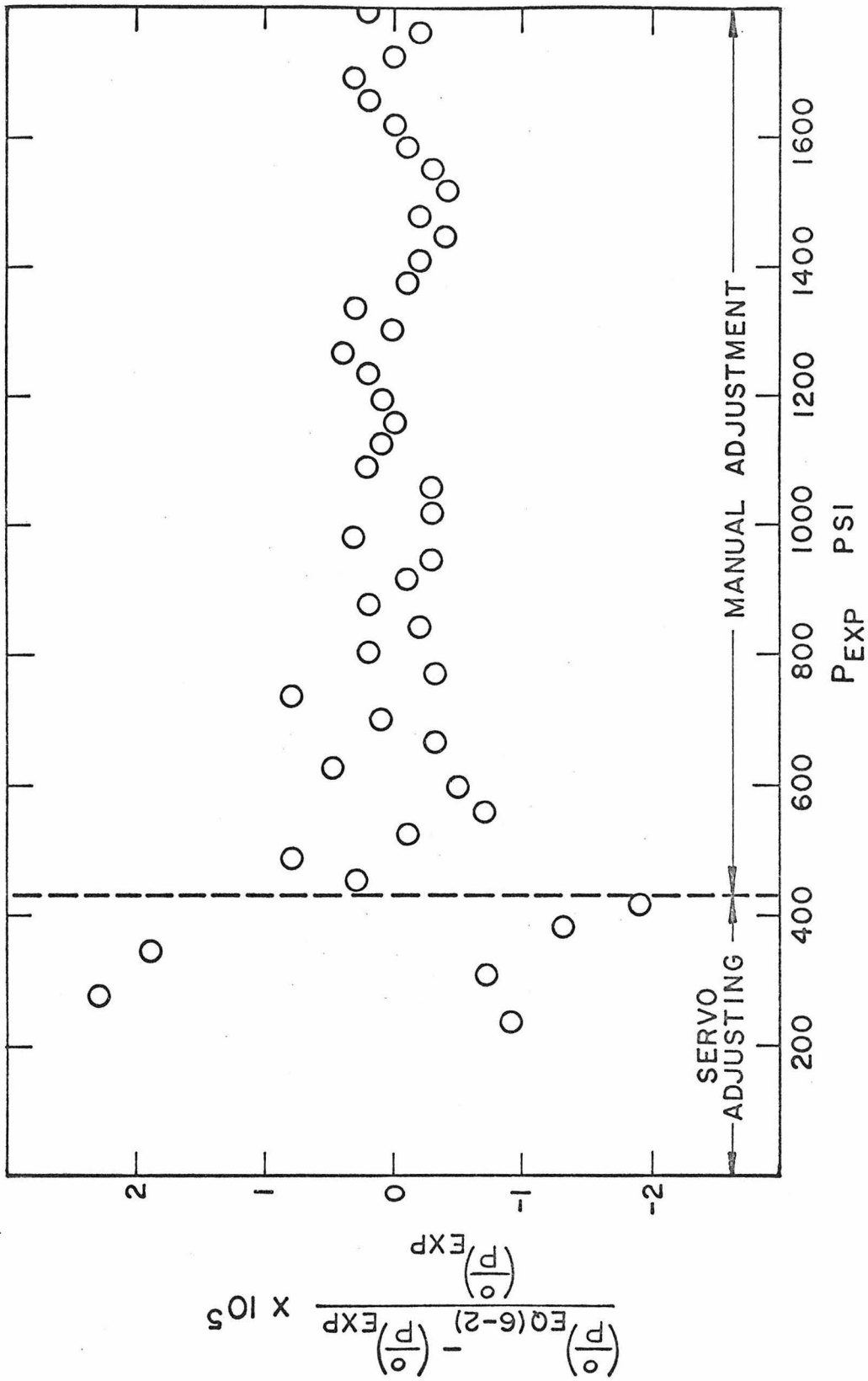


Figure 6 - 2. Deviations from the Least Squares Fit

TABLE 6 - 1

PRESSURE CALIBRATION DATA

<u>Pressure</u> <u>psi</u>	<u>Degrees</u> <u>Texas Instrument</u>	<u>(P_{calc} - P_{exp}/P_{exp})</u> <u>%</u>
239.8296	4.736	-0.0009*
275.2378	5.446	0.0023*
310.6685	6.140	-0.0007*
346.0768	6.851	0.0019*
381.4751	7.542	-0.0013*
416.9743	8.244	-0.0019*
452.3826	8.957	0.0003
487.8134	9.664	0.0008
523.2215	10.364	-0.0001
558.6198	11.065	-0.0007
594.0729	11.772	-0.0005
629.4812	12.484	0.0005
664.9120	13.185	-0.0003
700.3202	13.894	0.0001
735.7184	14.605	0.0008
771.1670	15.304	-0.0003
806.5751	16.016	0.0002
842.0822	16.722	-0.0002
877.4139	17.431	0.0002
912.8122	18.136	-0.0001
948.2597	18.843	-0.0003
983.6571	19.557	0.0003
1019.0977	20.260	-0.0003
1054.5060	20.969	-0.0003
1089.9044	21.683	0.0002
1125.3687	22.392	0.0001
1160.7770	23.100	0.0000
1196.2078	23.811	0.0001
1231.6161	24.522	0.0002
1267.0144	25.234	0.0004
1302.4294	25.940	0.0000
1337.9006	26.654	0.0003
1373.3322	27.359	-0.0001
1408.7395	28.067	-0.0002
1444.1377	28.774	-0.0004

Table 6 - 1 (Cont.)

<u>Pressure</u> <u>psi</u>	<u>Degrees</u> <u>Texas Instrument</u>	<u>(P_{calc} - P_{exp}/P_{exp})</u> <u>%</u>
1479.6175	29.489	-0.0002
1515.0257	30.195	-0.0004
1550.4565	30.908	-0.0003
1585.8647	31.621	-0.0001
1621.2630	32.333	0.0000
1656.7321	33.046	0.0002
1692.1314	33.758	0.0003
1727.5621	34.464	-0.0000
1762.9704	35.170	-0.0002
1798.3686	35.887	0.0002

*Data taken with instrument on servo control.

APPENDIX 7

THERMOMETER CALIBRATION

The temperature sensor used to control the temperature of the argon cell was a platinum resistance thermometer type No. G-20 manufactured by Electric Thermometers, Inc., Kearny, New Jersey. The thermometer element consisted of a doped platinum wire that was wound on a glass core and covered with a thin layer of glass. It was 25 mm long and 2 mm in diameter. Its nominal ice point was 100 ohms.

This thermometer was calibrated by comparison with a Leeds and Northrup 25 ohm, strain-free, platinum resistance thermometer, (serial No. 1612803).¹ This standard thermometer was calibrated at 16 different temperatures between 10 °K and 523 °K by the National Bureau of Standards in 1963. The Callendar-Van-Deusen constants for the standard thermometer were

$$\alpha = 0.0039265_{89} \quad (7 - 1)$$

$$\delta = 1.491_{37} \quad (7 - 2)$$

$$\beta = 0.110_{45} \quad (t < 0 \text{ } ^\circ\text{C}) \quad (7 - 3)$$

$$\beta = 0 \quad (t > 0 \text{ } ^\circ\text{C})$$

$$R_0 = 25.543 \quad (7 - 4)$$

The standard was calibrated using 2 milliamperes. The ice point of water is taken as 273.15 °K (0 °C), and R_0 is the ice point resistance.

Figure 7 - 1² is a schematic of the calibration apparatus,³ which consists principally of a cylindrical, copper, thermal reservoir block, D, that is surrounded by adiabatic shields, G. This assembly is suspended in a vacuum chamber, E. Six thermometers that were to be calibrated were placed in close fitting, silicone oilfilled wells in the copper block. The standard thermometer, H, was mounted with Wood's metal in a tapered copper plug. The plug was pressed, using silicone grease as a lubricant, into a hole in the bottom of the thermal block of copper. The standard thermometer leads were wrapped around the plug to reduce heat transfer effects.

The adiabatic shields, one above and one around the block, were maintained at the temperature of the surface of the block by using the heater wires wrapped on the outer surface of the shields. Differential thermocouples were used as sensors in the shield controller systems. The copper block was suspended from the shield above the block with nylon string. This block and shield assembly was positioned below the brass support lid, A, by three lucite rods. Electrical leads were wrapped and varnished to the handle of the lid with GE 7031 insulating varnish.

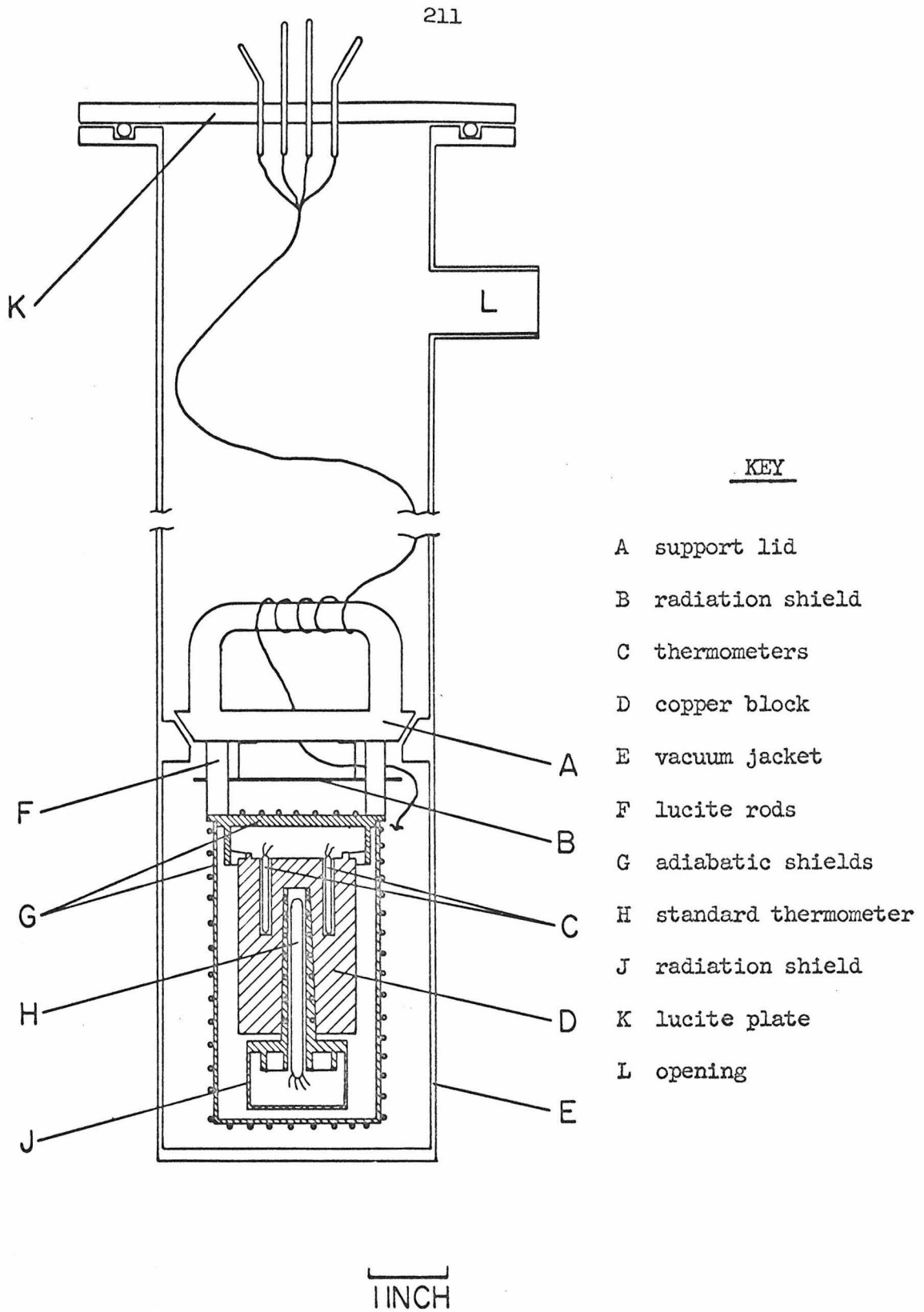


Figure 7 - 1. Schematic of Temperature Calibration Apparatus

The vacuum jacket was sealed with a lucite plate, K, and an O-ring. 1/8 inch threaded copper pins that were epoxy-sealed in position in the plate were used for electrical leadouts. The long leadout wires were spiralled down the walls of the steel vacuum jacket to reduce heat losses. The opening, L, in the jacket was used to connect the vacuum pump, the helium tank and the vent valve.

During the calibration the lower portion of the vacuum jacket was placed in a dewar. After the jacket was evacuated the dewar was filled with liquid N₂. Helium heat exchange gas was introduced into the jacket to speed initial cooling. As the copper block approached the desired calibration temperature the helium was pumped out. After the block had cooled below the desired temperature by radiative transfer, the shield controllers were activated. The final calibration temperature was reached by pulsing current through a heater wire that was wound in a spiral groove on the tapered plug. The jacket vacuum during the calibration was approximately 8×10^{-5} torr.

Figure 7 - 2 shows that the standard thermometer was wired in series with the to-be-calibrated thermometers forming one current loop. The emf leads were taken from each thermometer and also from a 10 ohm standard resistor. All voltages were measured to an estimated sixth significant figure with a Leeds and Northrup Wenner microvolt potentiometer, catalog No. 7559. A

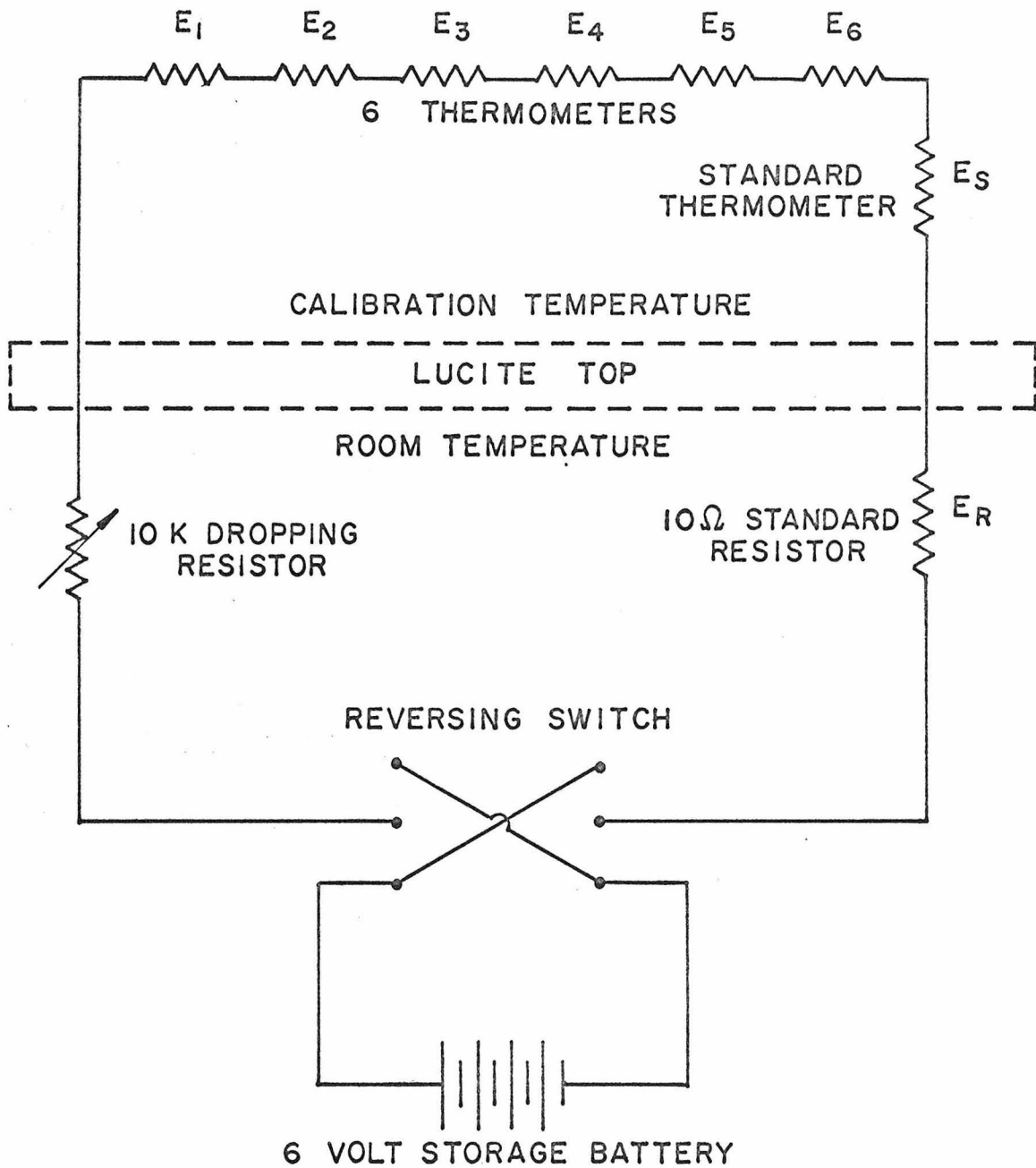


Figure 7 - 2. Wiring Diagram

reversing switch was used to eliminate residual emfs such as thermal emfs. Since the temperature of the block drifted slowly, the emf readings were taken as follows: current, standard thermometer, current, calibration thermometer, current, standard thermometer and current emfs. Interpolation was then used to estimate the current level for the thermometers and again for the temperature at which the resistance of the calibration thermometer was measured.

The resistance of the 10 ohm standard was temperature corrected as follows:⁴

$$R = 10.0000 [1 + \alpha (t - 25) + \beta (t - 25)^2] \quad (7 - 5)$$

$$\alpha = 0.000007 \quad (7 - 6)$$

$$\beta = -0.0000005 \quad (7 - 6)$$

t in degrees centigrade (lab temperature)

The measured voltages (see Figure 7 - 2) were:

E_R the emf across the standard resistor

E_S the emf across the standard thermometer

E_2 the emf across the calibration thermometer

used in the argon experiment.

Therefore:

$$i = \frac{E_R}{R} \quad (7 - 8)$$

$$R_S = \frac{E_S}{i} \quad (7 - 9)$$

$$R_2 = \frac{E_2}{i} \quad (7 - 10)$$

where i is the loop current (near 1 milliamp)

R_S is the resistance of the standard thermometer

R_2 is the resistance of the calibration thermometer.

Using the tabular form of the Callendar-Van-Deusen equation for the thermometer, R_S determined the temperature of the block when the calibration thermometer had resistance R_2 .

The resistance of the thermometer was measured at 10 temperatures (see Table 7 - 1). The temperature-resistance data was least squares fit to the Callendar-Van-Deusen equation:

$$\frac{R - R_{02}}{\alpha R_{02}} = t + \delta \left(1 - \frac{t}{100}\right) \frac{t}{100} + \beta \left(1 - \frac{t}{100}\right) \left(\frac{t}{100}\right)^3 \quad (7 - 11)$$

for t in degrees centigrade.

The following constants were determined:

$$R_{02} = 99.812_{37} \quad (7 - 12)$$

$$\alpha = 0.00382_{75} \quad (7 - 13)$$

$$\beta = 0.091382 \quad (7 - 14)$$

$$\delta = 1.827_{19} \quad (7 - 15)$$

Figure 7 - 3 depicts the error between the prediction equation (7 - 11) and the data, such that for any thermometer temperature and resistance satisfying (7 - 11),

$$T_{\text{STANDARD THERMOMETER}} = T_{\text{THERMOMETER}} + T^* \quad (7 - 16)$$

$T_{\text{STANDARD THERMOMETER}}$ is taken to be the actual temperature of the resistance element. $T_{\text{THERMOMETER}}$ is the temperature predicted from (7 - 11) and T^* is the discrepancy between the two. The root mean square deviation of these discrepancies is 2.2 millidegrees including the data point at $-101\text{ }^{\circ}\text{C}$.

The estimate of the error from the absolute temperature is $\pm 0.024\text{ }^{\circ}\text{C}$.

With the thermometer in situ in the argon diffraction apparatus, the pressure dependence of the resistance element was examined. Within the accuracy obtainable in this situation a data point at $138\text{ }^{\circ}\text{K}$ agreed with the data of Knobler, Honeywell, and Pings.⁵ Therefore, the effect of pressure on the thermometer is assumed to be that described in their paper.

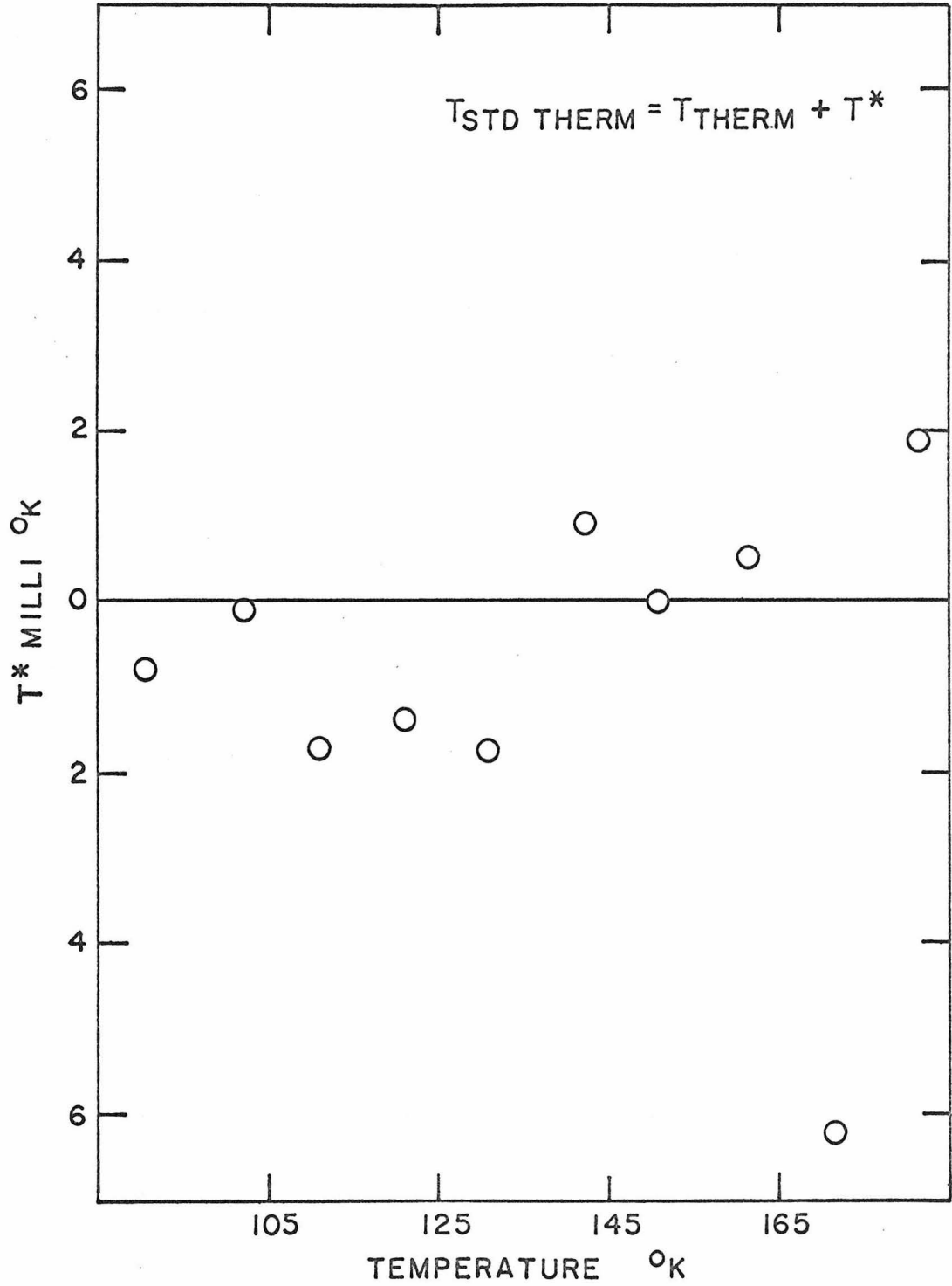


Figure 7 - 3. Deviation from Least Squares Fit

TABLE 7 - 1

<u>Resistance</u> <u>absolute ohms</u>	<u>Temperature</u> <u>°C</u>
25.7645	-182.801
30.7025	-171.177
34.3382	-162.554
38.5512	-152.501
42.6843	-142.574
47.4463	-131.065
50.9393	-122.571
55.1142	-112.367
59.6595	-101.187
63.1982	- 92.453

REFERENCES

1. National Bureau of Standards Certificate for a platinum resistance thermometer serial No. 1612803. Test No. 31./174004, April 1963. Temperature Measurements Section, Heat and Power Division, NBS, U.S. Department of Commerce, Washington.
2. Figure 7 - 1 taken from W. I. Honeywell's thesis: "X-ray Diffraction Studies of Dense Fluids," California Institute of Technology, 1964.
3. The calibration apparatus was designed by Dr. C. M. Knobler.
4. Certificate for Standard Resistor serial No. 1613992. Leeds and Northrup Company, October 1962. Overall accuracy 0.005%.
5. Knobler, C. M., W. I. Honeywell and C. J. Pings. "Thermal and Hydrostatic Behavior of Minature Platinum Resistance Elements," Rev. Sci. Instr., 34 (1963).

APPENDIX 8

CALCULATION OF ABSORPTION CORRECTION FACTORS

The subtraction of empty cell scattering from the sample and cell scattering depends intrinsically upon the mass absorption coefficients of the materials and inherently upon the geometry of the cell, sample, and the irradiating x-ray beam.

When a narrow beam of monochromatic X-rays, with incident intensity I_0 , passes through a layer of homogeneous material of thickness t cm, the emergent intensity, I , is given by

$$I = I_0 e^{-\mu t} \quad (8 - 1)$$

where μ is the linear absorption coefficient in reciprocal centimeters. For a given wavelength, the value of μ is characteristic of the absorbing material in its specific physical state. That is to say, the reduction in intensity is determined, for a given wavelength, by the quantity of matter traversed by the X-rays:

$$I = I_0 e^{-(\mu/\rho) \rho t} \quad (8 - 2)$$

where for a given absorber of density ρ , μ/ρ depends only on the wavelength and t is again the thickness. It follows that, when scattered radiation is detected in the argon diffraction

experiment, it has been attenuated by absorption. The absorption factors are developed to correct the experimental intensities so that the intrinsic scattering from "non-absorbing" argon can be calculated.

This correction procedure has been discussed for the case of an annular sample cell concentric to a cylindrical sample by Paalman and Pings¹ for an incident beam that irradiated all the cell and sample, and by Kendig and Pings² for a narrow incident beam that irradiated only a portion of this cell and sample. Both of these treatments were applicable when the center lines of the annular cell and cylindrical sample coincided, and both were limited to an incident beam of uniform intensity. Neither was developed to calculate absorption corrections for incoherent scattering. It was necessary to extend the concept of Paalman, Kendig, and Pings to cover the following:

- (1) an incident beam whose intensity distribution was trapezoidal in shape,
- (2) parallel, but not coincident cell and sample cell ϕ lines, and
- (3) incoherent scattering.

The geometry is depicted in Figure 8 - 1.

Following Kendig the irradiated portion of the cell and sample was divided into small scattering volumes, and absorption factors were calculated for each scattering element. These element

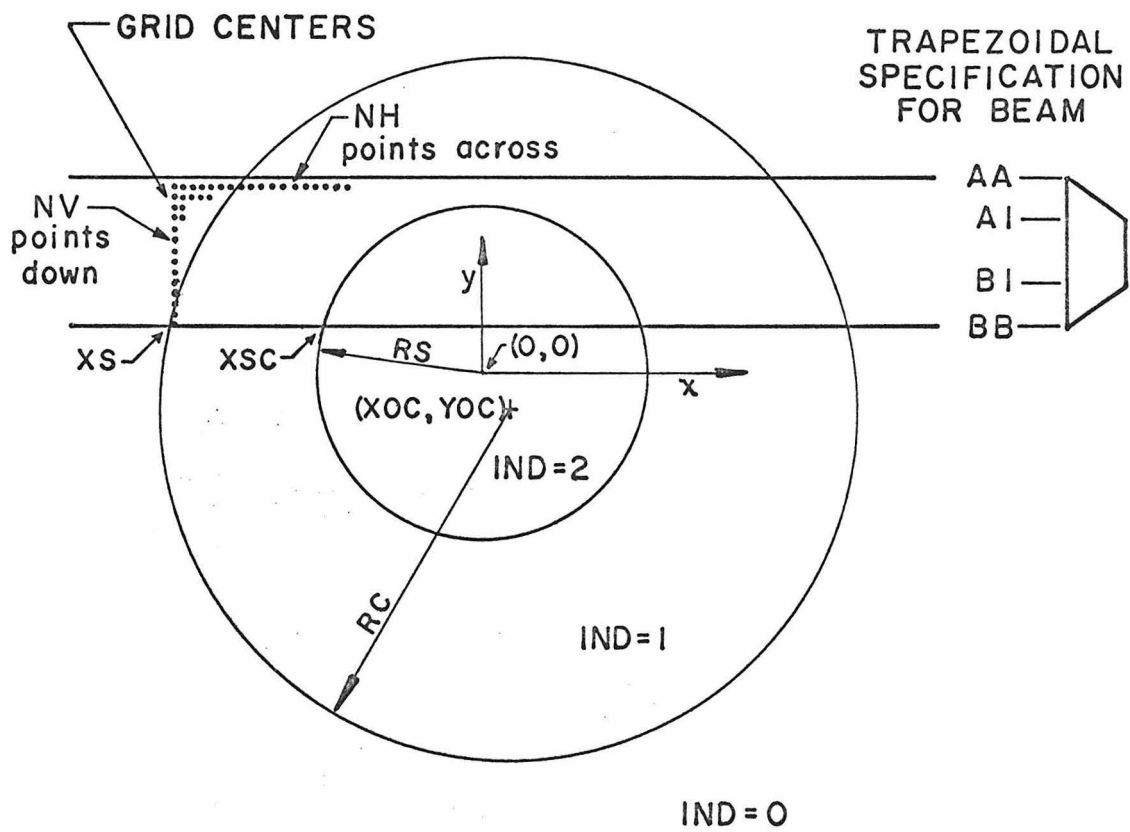


Figure 8 - 1. Cell, Sample and Beam Geometry

factors were then combined to form the total absorption coefficient.

For example, if one considers an element of scattering volume somewhere in the confined liquid several characteristic distances relative to the center of this element can be defined. Let LCI, LSI, LSO, LCO be respectively the distance traversed by the incident X-ray in the cell material, in the sample material, and the distance traversed by the diffracted ray in the sample and cell. Then the intensity scattered from the j^{th} element in the liquid is:

$$\begin{aligned}
 I_j = & P I_0 \frac{I_{0j}}{I_0} \left(\frac{N_s}{V_s} \right) \Delta V_{sj} I_s \gamma_s^{\text{coh}} e^{-\mu_c^{\text{coh}} LCI - \mu_c^{\text{coh}} LCO - \mu_s^{\text{coh}} LSO - \mu_s^{\text{coh}} LSI} \\
 & + P \frac{I_{0j}}{I_0} \left(\frac{N_s}{V_s} \right) \Delta V_{sj} I_s \gamma_s^{\text{inc}} e^{-\mu_c^{\text{coh}} LCI - \mu_c^{\text{inc}} LCO - \mu_s^{\text{inc}} LSO - \mu_s^{\text{coh}} LSI}
 \end{aligned}
 \tag{8 - 3}$$

and for the k^{th} element in the cell is:

$$\begin{aligned}
 I_k = & P I_0 \frac{I_{0k}}{I_0} \left(\frac{N_c}{V_c} \right) \Delta V_{ck} I_c \gamma_c^{\text{coh}} e^{-\mu_c^{\text{coh}} LCI - \mu_c^{\text{coh}} LCO - \mu_s^{\text{coh}} LSO - \mu_s^{\text{coh}} LSI} \\
 & + P I_0 \frac{I_{0k}}{I_0} \left(\frac{N_c}{V_c} \right) \Delta V_{ck} I_c \gamma_c^{\text{inc}} e^{-\mu_c^{\text{coh}} LCI - \mu_c^{\text{inc}} LCO - \mu_s^{\text{inc}} LSO - \mu_s^{\text{coh}} LSI}
 \end{aligned}
 \tag{8 - 4}$$

where μ_c^{coh} , μ_s^{coh} are the linear absorption coefficients for the cell and sample materials evaluated at the incident wavelength,

μ_c^{inc} , μ_s^{inc} are the respective linear absorption coefficients
evaluated at the Compton-shifted wavelength,

I_c , I_s are the intrinsic scattering powers of cell and sample,
 γ^{coh} , γ^{inc} are the fractional portions of I_c and I_s scattered
coherently and incoherently,

ΔV_{sj} , ΔV_{ck} are the volumes of the j^{th} sample element and the
 k^{th} cell element,

I_{oj} , I_{ok} are the intensities of the incident beam that would
irradiate the j^{th} and k^{th} elements were there no absorption
in the cell and sample,

I_o is the total intensity of the incident beam, and

P is the polarization correction.

Now, let:

$$assc_j^{coh} = \frac{I_{oj}}{I_o} \frac{\Delta V_{sj}}{V_s} e^{-\mu_c^{coh} LCI - \mu_c^{coh} LCO - \mu_s^{coh} LSO - \mu_s^{coh} LSI} \quad (8 - 5)$$

$$assc_j^{inc} = \frac{I_{oj}}{I_o} \frac{\Delta V_{sj}}{V_s} e^{-\mu_c^{coh} LCI - \mu_c^{inc} LCO - \mu_s^{inc} LSO - \mu_s^{coh} LSI} \quad (8 - 6)$$

$$acsc_k^{coh} = \frac{I_{ok}}{I_o} \frac{\Delta V_{ck}}{V_c} e^{-\mu_c^{coh} LCI - \mu_c^{coh} LCO - \mu_s^{coh} LSO - \mu_s^{coh} LSI} \quad (8 - 7)$$

$$acsc_k^{inc} = \frac{I_{ok}}{I_o} \frac{\Delta V_{ck}}{V_c} e^{-\mu_c^{coh}} LCI - \mu_c^{inc} LCO - \mu_s^{inc} LSO - \mu_s^{coh} LSI \quad (8 - 8)$$

and when the empty cell data are taken where LSO and LSI are zero, let:

$$acc_k^{coh} = \frac{I_{ok}}{I_o} \frac{\Delta V_{ck}}{V_c} e^{-\mu_c^{coh}} LCI - \mu_c^{coh} LCO \quad (8 - 9)$$

$$acc_k^{inc} = \frac{I_{ok}}{I_o} \frac{\Delta V_{ck}}{V_c} e^{-\mu_c^{coh}} LCI - \mu_c^{inc} LCO \quad (8 - 10)$$

The total experimental intensity observed in the cell and sample diffracton scan is the sum of I_j over the sample elements and I_k over the cell elements:

$$\begin{aligned} I_{c+s}^E &= P I_o N_s I_s \gamma_s^{coh} \sum^{sample} assc_j^{coh} \\ &+ P I_o N_s I_s \gamma_s^{inc} \sum^{sample} assc_j^{inc} \\ &+ P I_o N_c I_c \gamma_c^{coh} \sum^{cell} acsc_k^{coh} \\ &+ P I_o N_c I_c \gamma_c^{inc} \sum^{cell} acsc_k^{inc} \end{aligned} \quad (8 - 11)$$

and for the experimental cell scattering

$$I_c^E = P I_o N_c I_c \gamma_c^{coh} \sum^{cell} acc_k^{coh} + P I_o N_c I_c \gamma_c^{inc} \sum^{cell} acc_k^{inc} \quad (8 - 12)$$

Comparison of (8 - 11) and (8 - 12) with (2 - 9) and (2 - 8) of Appendix 2 leads to the conclusion that the absorption coefficients are:

$$ASSC^{coh} = \sum^{sample} assc_j^{coh} \quad (8 - 13)$$

and similarly for the other five coefficients.

The computer program for calculating these absorption coefficients for the argon sample and beryllium cell consists of seven decks, one main program and six sub-programs. The information fed into the computer is:

- (1) the incident beam specification,
- (2) the cell and sample radii,
- (3) the center of the cell in a coordinate system at the center of the sample,
- (4) the cell and sample densities,
- (5) the grid size for volume elements taken along the incident beam (a maximum of 50 vertical and 200 horizontal),
- (6) the scattering angles for which absorption factors are to be calculated, and

- (7) the wavelength dependence of the linear or mass absorption coefficients.

Subroutine ARRAY is called first. This routine establishes the grid and determines whether the scattering element centers are in the sample (IND = 2), in the cell (IND = 1), or outside the cell (IND = 0). The ordinates of the centers are labeled Y(J) and the abscissas X(J). The intersection of the left limb of the cell XS(J) and sample XSC(J) are found for each row of centers. Since storage requirements prohibit keeping all LSI and LCI distances, calculation of XS and XSC enables efficient recomputation of LSI and LCI as needed.

Subroutine TRIG calculated all the necessary trigonometric values that will be needed to calculate LCO and LSO for a given angle.

The program then calculates the absorptions by row. Subroutine IN establishes LCI and LSI. Subroutine OUT calculates LCO and LSO using a subroutine INTCPT to find the intercepts of the diffracted X-ray with the cell and sample boundaries. Subroutine ABSORB calculates the absorption for a given row for both coherent and incoherent wavelengths. After this has been done for all of the NV rows, the coefficients for each row are multiplied by the intensity for that row to compute the total absorption factors.

In order to check the accuracy of this program, a comparison

was made between values computed and those calculated by Ritter, Harris and Wood.³ For $\mu_s = 13.4 \text{ cm}^{-1}$, $\mu_c = 7.9 \text{ cm}^{-1}$, RS = 0.021 cm, RC = 0.03465 cm, and a 50 x 200 grid, the computed values are compared to Ritter, et al. (see Table 8 - 1). Concentric geometry and a fully exposed cell and sample were used. The machine calculated values agree with Ritter's to within 0.5%.

The wavelength dependence of μ/ρ for argon and beryllium was taken from the International Tables for X-ray Crystallography.⁴ The following was the functional dependence used:

Argon

$$\mu/\rho = -4.18 \lambda^3 + 40.0 \lambda^4 + 0.01352 \lambda + 0.1609 \quad (8 - 14)$$

Beryllium

$$\mu/\rho = -0.00213 \lambda^3 + 0.365 \lambda^4 + 0.01331 \lambda + 0.1584 \quad (8 - 15)$$

TABLE 8 - 1

A COMPARISON OF CALCULATED VALUES WITH RITTER, ET AL.

<u>θ</u> <u>Degrees</u>	ASSC		ACC		ACSC	
	<u>Calculated</u>	<u>Ritter</u>	<u>Calculated</u>	<u>Ritter</u>	<u>Calculated</u>	<u>Ritter</u>
0.0	.4896	.488	.7488	.747	.6010	.599
15.0	.4907	.490	.7494	.748	.6029	.601
30.0	.4940	.494	.7514	.751	.6091	.610
45.0	.4987	.498	.7528	.753	.6202	.621
60.0	.5035	.501	.7541	.754	.6347	.634
75.0	.5073	.504	.7571	.756	.6475	.648

REFERENCES

1. Paalman, H. H. and C. J. Pings. "Numerical Evaluation of X-ray Absorption Factors for Cylindrical Samples and Annular Sample Cells," J. Appl. Phys., 33, 2635 (1962).
2. Kendig, A. P. and C. J. Pings. "X-ray Absorption Factors for Cylindrical Samples in Annular Sample Cells Exposed to Incident Beams of Limited Width," J. Appl. Phys., 36, 1692 (1965).
3. Ritter, H. S., R. L. Harris, and R. E. Wood. "On the X-ray Absorption Correction for Encased Diffractors in the Debye-Scherrer Technique," J. Appl. Phys., 22, 169 (1951).
4. International Tables for X-ray Crystallography. Kynoch Press: Birmingham, England, Vol. 3, p. 161, 1962.

APPENDIX 9

The Correction for Horizontal Divergence

To obtain a qualitative understanding of the horizontal divergence associated with the slit geometry used in this experiment, upper limits to the horizontal divergence will be calculated for the ideal case of a line source, line sample and line detector.

Consider an incident beam of X-rays in the direction \vec{s}_0 and a diffracted beam in the direction \vec{s} . The scattering angle associated with a ray diffracted from a point in a line sample will then be

$$2\varphi = \cos^{-1} \left[\frac{\vec{s}_0 \cdot \vec{s}}{|\vec{s}_0| |\vec{s}|} \right] \quad (9 - 1)$$

In the Debye-Scherrer geometry, the scattering angle for each ray may be different than the nominal angle, 2θ , at which the detector is positioned. To estimate the maximum positive and negative deviations between 2φ and 2θ , consider the three combinations of \vec{s}_0 and \vec{s} depicted in Figure (9 - 1), where

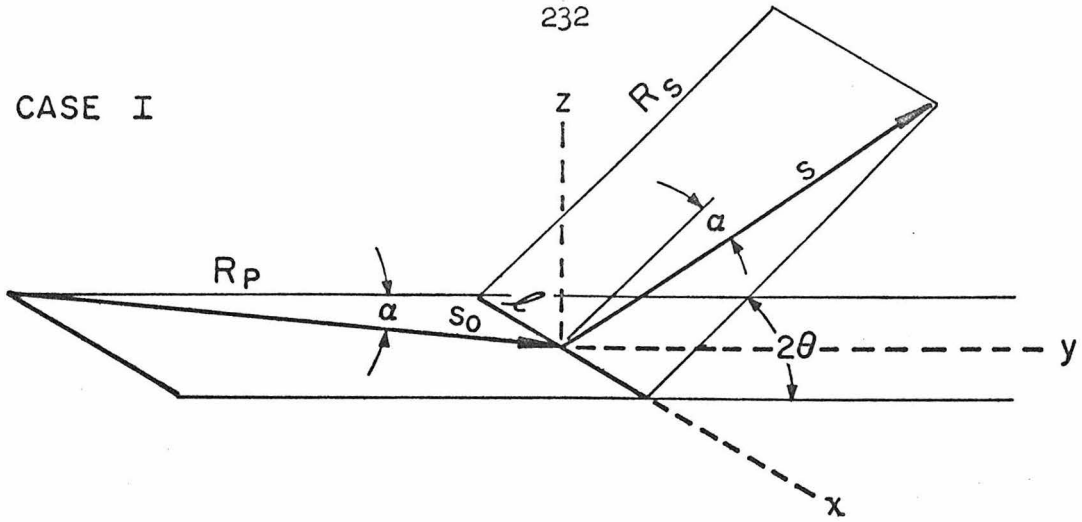
R_p is the distance from the source of X-rays to the sample

R_s is the distance from the sample to the detector

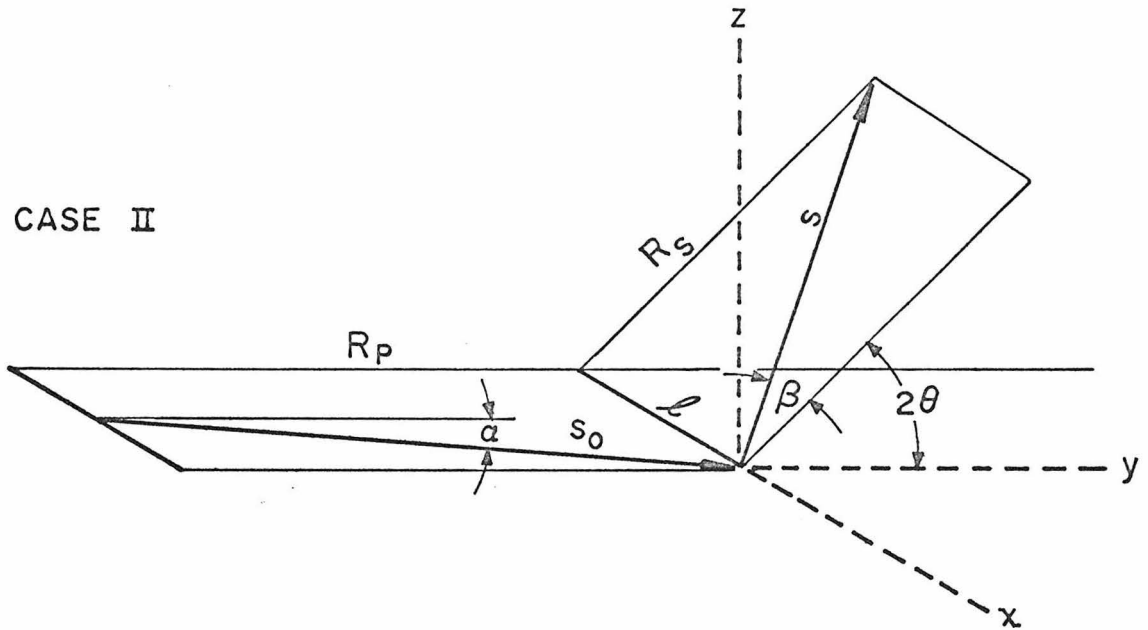
l is the length of the sample

$$\tan \alpha = \frac{\text{vertical soller foil spacing}}{\text{vertical soller foil length}} \quad (9 - 2)$$

CASE I



CASE II



CASE III

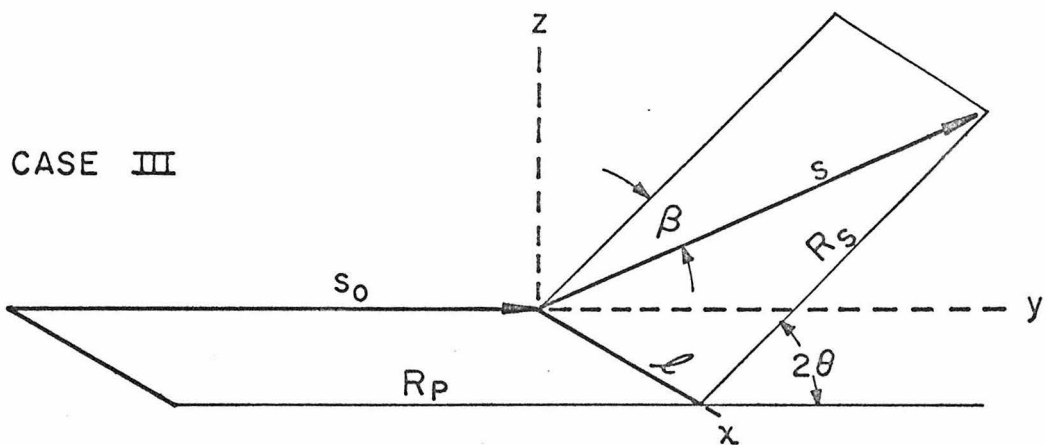


Figure 9 - 1. Three Limiting Cases for Maximum Horizontal Divergence

$$\tan \beta = \frac{1}{R_s} \quad (9 - 3)$$

The following relationships for the scattering angle then hold:

CASE I

$$\vec{s}_o = R_p \tan \alpha \vec{i} + R_p \vec{j} \quad (9 - 4)$$

$$\vec{s} = R_s \tan \alpha \vec{i} + R_s \cos 2\theta \vec{j} + R_s \sin 2\theta \vec{k} \quad (9 - 5)$$

$$\cos (2\varphi_{I}) = \cos^2 \alpha [\cos 2\theta + \tan^2 \alpha] \quad (9 - 6)$$

CASE II

$$\vec{s}_o = R_p \tan \alpha \vec{i} + R_p \vec{j} \quad (9 - 7)$$

$$\vec{s} = -R_s \tan \beta \vec{i} + R_s \cos 2\theta \vec{j} + R_s \sin 2\theta \vec{k} \quad (9 - 8)$$

$$\cos (2\varphi_{II}) = \cos \alpha \cos \beta [\cos 2\theta - \tan \alpha \tan \beta] \quad (9 - 9)$$

CASE III

$$\vec{s}_o = R_p \vec{j} \quad (9 - 10)$$

$$\vec{s} = R_s \tan \beta \vec{i} + R_s \cos 2\theta \vec{j} + R_s \sin 2\theta \vec{k} \quad (9 - 11)$$

$$\cos (2\varphi_{III}) = \cos \beta \cos 2\theta \quad (9 - 12)$$

From the conditions of the experiment the following values were obtained:

$$\alpha = 0.825^\circ \quad (9 - 13)$$

$$\beta = 4.844^\circ \quad (9 - 14)$$

Using these values the following table was obtained:

<u>TABLE (9 - 1)</u>			
2θ	$2\varphi_{\text{I}} - 2\theta$	$2\varphi_{\text{II}} - 2\theta$	$2\varphi_{\text{III}} - 2\theta$
3°	0.000°	3.417°	2.700°
5		2.550	1.967
10		1.495	1.100
15		1.005	0.750
20		0.775	0.550
30	-0.008	.500	0.350
45		.300	0.200
60		.200	0.117
90	-0.017	.067	0.
100		.032	-0.033
120	-0.021	-.033	-0.117

The results of the calculations are plotted in Figure (9 - 2). Case III is of particular interest as it represents the scattering situation that is assumed for the divergence corrections, that is, the incident beam is assumed to be perpendicular to the line sample. It is significant to note that the maximum deviation is not greater than the data-point spacing of 0.50° in 2θ except at low angles. After the correction procedure the maximum deviations are indicated by the

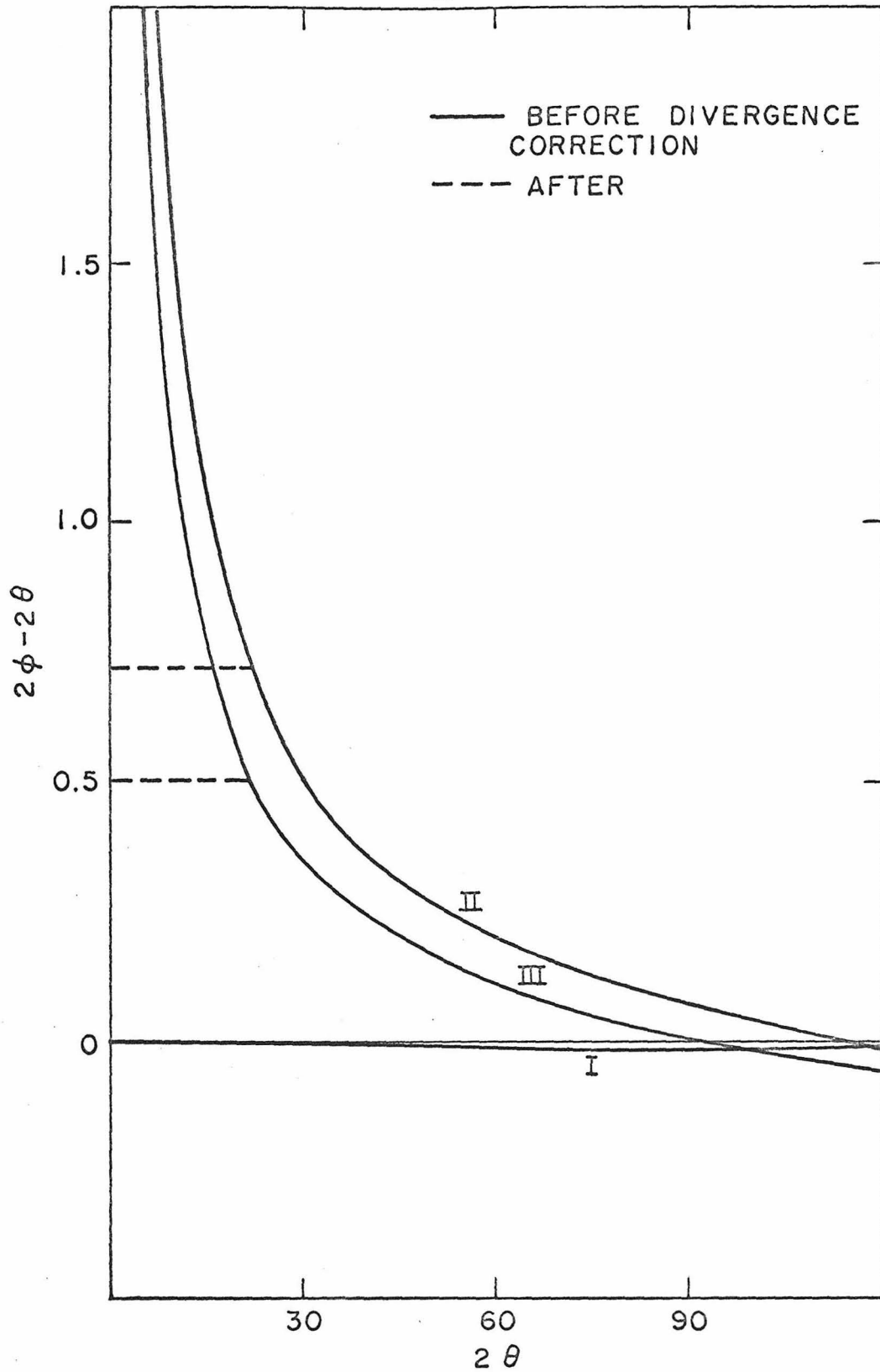


Figure 9 - 2. Upper limits to horizontal divergence for the three situations depicted in Figure 9 - 1.

broken lines in the curves. That is to say, that the correction need only be applied at low scattering angles. Case I shows that horizontal divergence errors due to divergence in the incident beam are negligible.

Note also that the horizontal divergence correction need only be applied to the total scattering from argon as the subtraction of cell scattering from cell and sample scattering eliminates all scattering from beryllium.

Now that limits have been established for the maximum deviations, the quantitative correction procedure will be described. Figure (9 - 3) depicts the Debye-Scherrer scattering geometry for a line sample with the detector positioned at A. R_s is the sample to detector distance. R is the radius of a diffraction cone as would be seen on the plane, AB, which is perpendicular to the plane passing through the sample and 0° , and which passes through the detector window at point A.

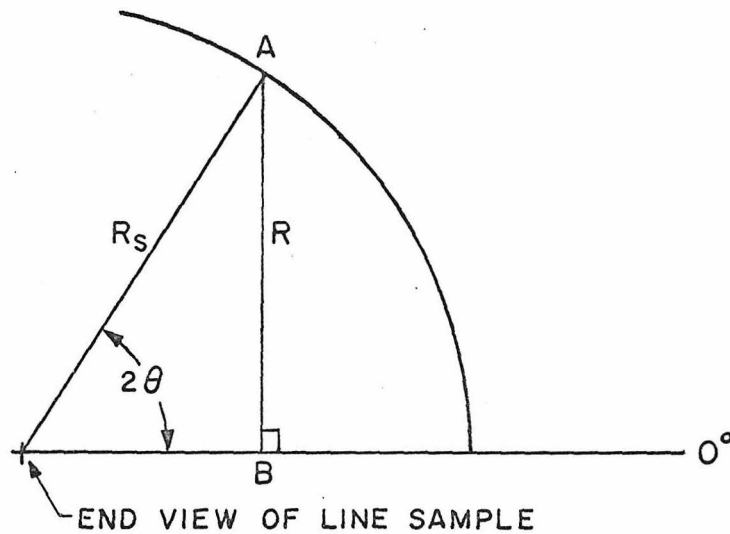


Figure 9 - 3. Scattering geometry as viewed along the axis of the line source

Figure (9 - 4) depicts the base of a typical diffraction cone as would be seen on plane AB of Figure (9 - 3). When the counter is positioned at 2θ it should detect the scattering intensity associated with the intensity per unit length of this rim of the cone. However, the flat horizontal sollar plates also permit a portion of the diffraction cone to be detected at angles which are smaller than the nominal scattering angle, as indicated by the lower window in the figure. In fact, as the radius, R , of the diffraction cones becomes large with respect to the length of the window then the rim of the cone will be seen only at one angular position and will not contribute to the total intensity at any other position. The correction procedure can only reduce the scattering intensities, it can never increase them.

Basically what we are interested in finding is the intensity that would be observed at the nominal scattering angle, 2θ , if the slit system were designed to detect only radiation scattered with a maximum horizontal divergence of 0.5° in 2θ . Let this quantity be denoted by $i(\theta_k)$ where θ_k is the scattering angle.

However, because the slits are not designed to eliminate the horizontal divergence, what we measure is:

$$i^E(\theta_k) = \sum_{l=k}^{k_{\max}} g_{kl} i(\theta_l) \quad (9 - 15)$$

That is, the experimental intensity at θ_k is not only the true scattering but also may include a portion of the scattering from cones where $\theta_l > \theta_k$. For a point sample as represented by the

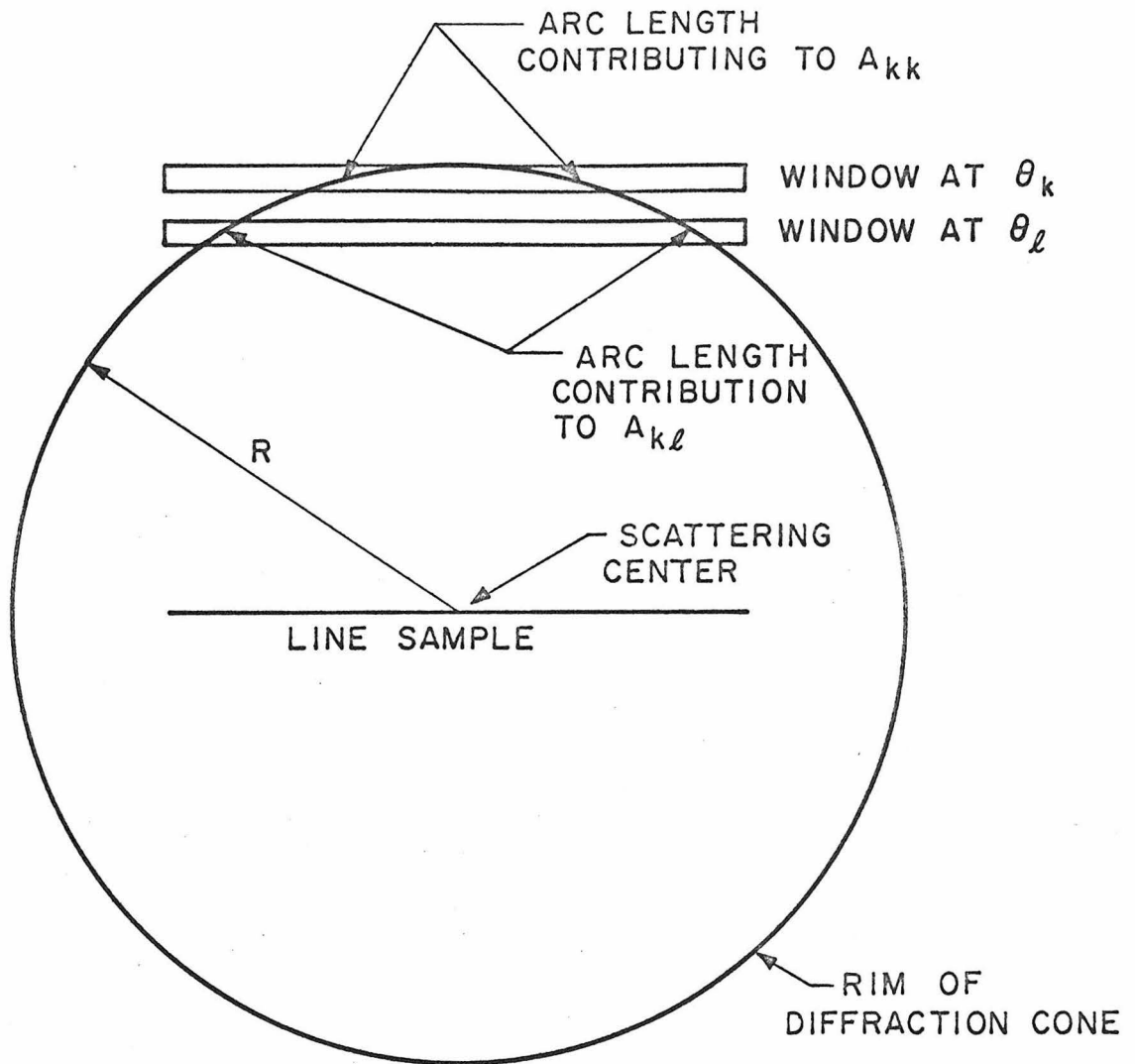


Figure 9 - 4. A typical scattering cone as seen on plane AB

scattering center in Figure (9 - 4),

$$g_{kl} = \frac{A_{kl}}{A_{kk}} \quad (9 - 16)$$

where A_{kk} is the length of arc in the window at θ_k and A_{kl} is the length of arc in the window at θ_l .

Note the following conditions for g_{kl}

$$\theta_l > \theta_k \quad g_{kl} = 0 \quad (9 - 17)$$

$$\theta_l = \theta_k \quad g_{kl} = 1 \quad (9 - 18)$$

$$\theta_l < \theta_k \quad 0 \leq g_{kl} < 1 \quad (9 - 19)$$

A computer program was written to calculate g_{kl} for a line source. All calculations were made on planes like plane AB. A uniform scattering power per unit length of sample was assumed. Whenever an arc length did not intercept the ends of the window its length was calculated rigorously. The upper and lower edges of the window at each angular position are chords of the circle of radius R. Since their positions can be calculated the lengths of the subtended arcs can be calculated. If the arc intercepted the end of the window the portion of arc in the window was assumed to be

$$\left| \frac{X_I - X_E}{X_I - X_O} \right|^{240} * \text{arc}_{TB} \quad (9 - 20)$$

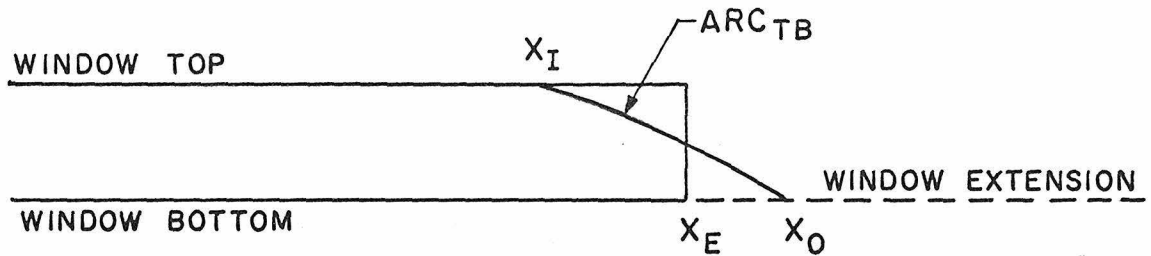


Figure 9 - 5. Diagram of arc length approximation

where

X_I is the value of the x-ordinate common to the arc and the top of the window.

X_O is the value of the x-ordinate common to the arc and the extension of the bottom edge of the window.

X_E is the value of the x-ordinate common to the arc and the end of the window.

Once the values of g_{kl} for all k and l corresponding to each data angle had been calculated, the k_{\max} set of row reducible linear equations were solved for the set of true scattering intensities.

$$i(\theta_k) \leftarrow (g_{kl}, i^E(\theta_k)) \quad (9 - 21)$$

PROPOSITION 1

Whenever accurate data are available, Leibnitz rule and LaGrange Interpolating Polynomials can be used to draw an unbiased curve through data points which represent an average of the dependent variable over a characteristic span of the independent variable.

In the laboratory, most experimental measurements of a dependent variable are made with a device which, in fact, measures an average of the dependent variable over some characteristic span of the independent variable. When the data are presented for publication, a smooth curve is often drawn through the data points while keeping in mind that the smooth curve must represent the "local" data by equal area rules (See Fig. 1). This discussion will present an unbiased way to draw this local curve.

Let $f(x)$ represent the actual local function at x and let $2a$ represent the width of the averaging device, then the average of the function at x is described by:

$$\text{Ave}(x) = \frac{\int_{x-a}^{x+a} f(u) du}{\int_{x-a}^{x+a} du} = \frac{F(x+a) - F(x-a)}{2a} \quad (1)$$

where Ave (x) is the "average" function.¹ If the local function is continuous, then this integral can be differentiated using Leibnitz rule to give:

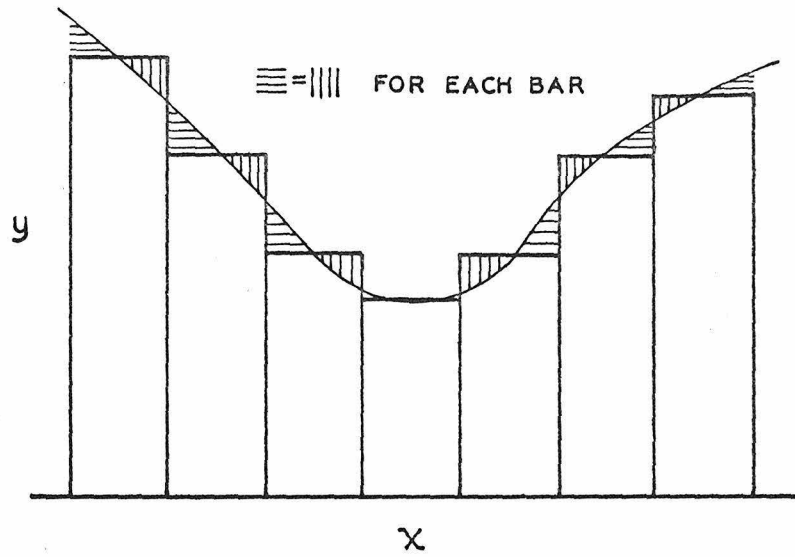
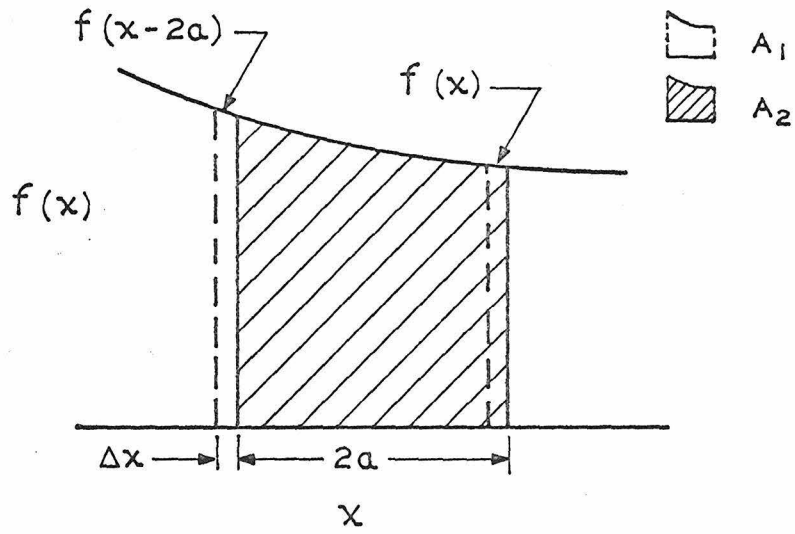


Figure 1. EQUAL AREA RULE



$$\frac{\Delta A}{\Delta x} = \frac{A_2 - A_1}{\Delta x} \cong \frac{A_1 - f(x-2a)\Delta x + f(x)\Delta x - A_1}{\Delta x}$$

$$\frac{\Delta A}{\Delta x} \cong f(x) - f(x-2a)$$

Figure 2. AREA INTERPRETATION

$$\frac{d}{dx} \frac{F(x+a) - F(x-a)}{2a} = \frac{d \text{Ave}(x)}{dx} = f(x+a) - f(x-a) \quad (2)$$

This can be interpreted geometrically; i.e., the rate of change of the area under the local curve is related to the difference in the function at the ends of the interval (See Fig. 2).

If a polynomial can be fit to the average data points so that slopes of the experimental data can be calculated, then a recursion formula can be written which relates the successive local values to the previous ones and the derivatives:

next point	derivative	previous point	
$f(x + 2am) = \frac{d}{dx} A(x + 2am - a) + f(x + 2a(m - 1)) \quad (3)$			
for m = 1, 2 . . .			

The local function can, therefore, be recursively calculated by selecting a value of f at some x . Either the first value of f may be known because it is in a range where the data is nearly linear, (i.e., where the average is equal to the midpoint), or an arbitrary value may be assumed and the calculated function may be integrated and normalized.

The problem with this method in most cases is that "least square" polynomials do not represent experimental data well. For example, the data² of Fig. 3 and Table 1 were subjected to a double precision polynomial fitting subroutine. The results of the fit for polynomials of degrees 9 and 5 are shown respectively in Figs. 3 and 4. Higher degree polynomials could not be fit at all. Intermediate or lower degree

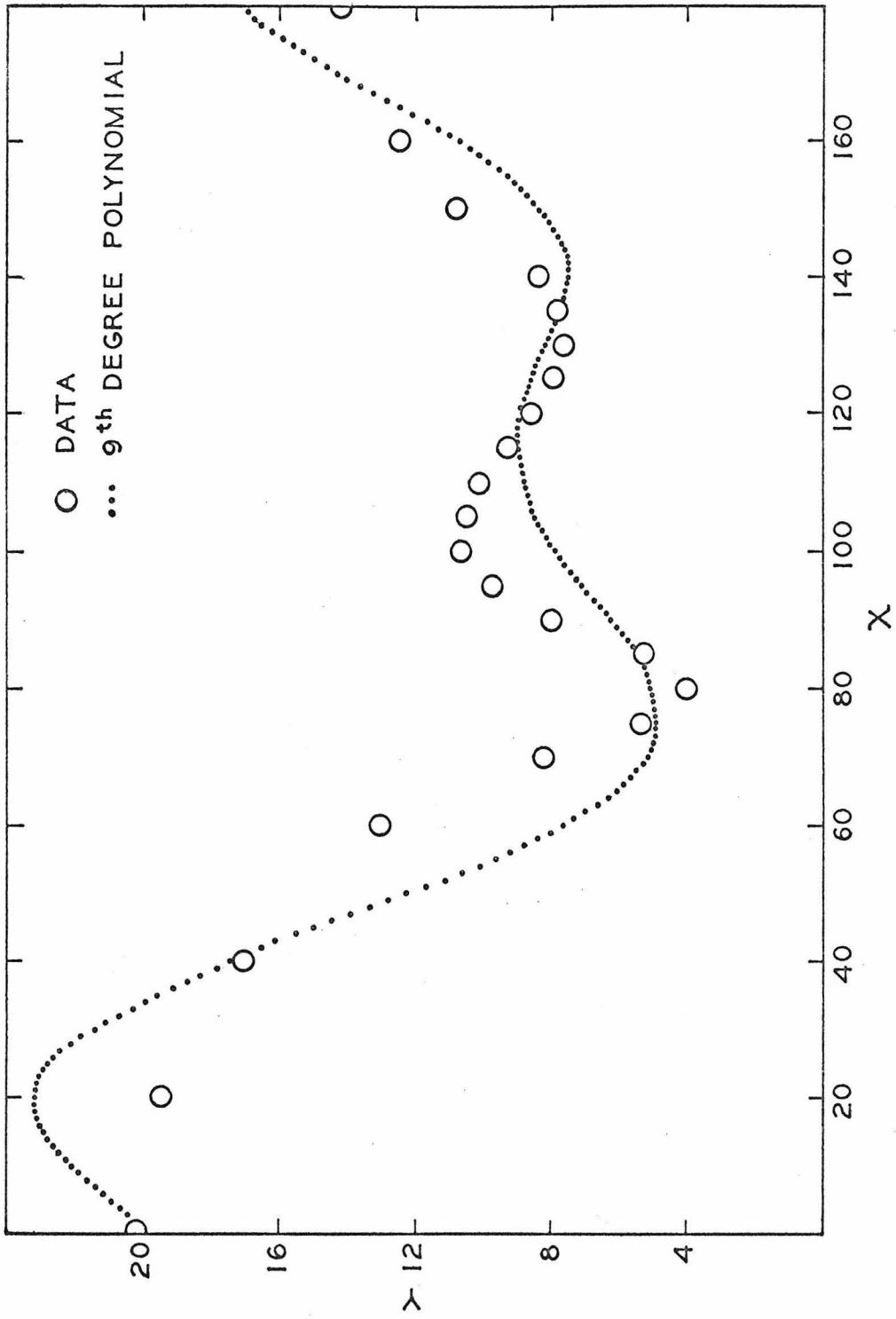


Figure 3. 9th Degree Polynomial Fit by Least Squares

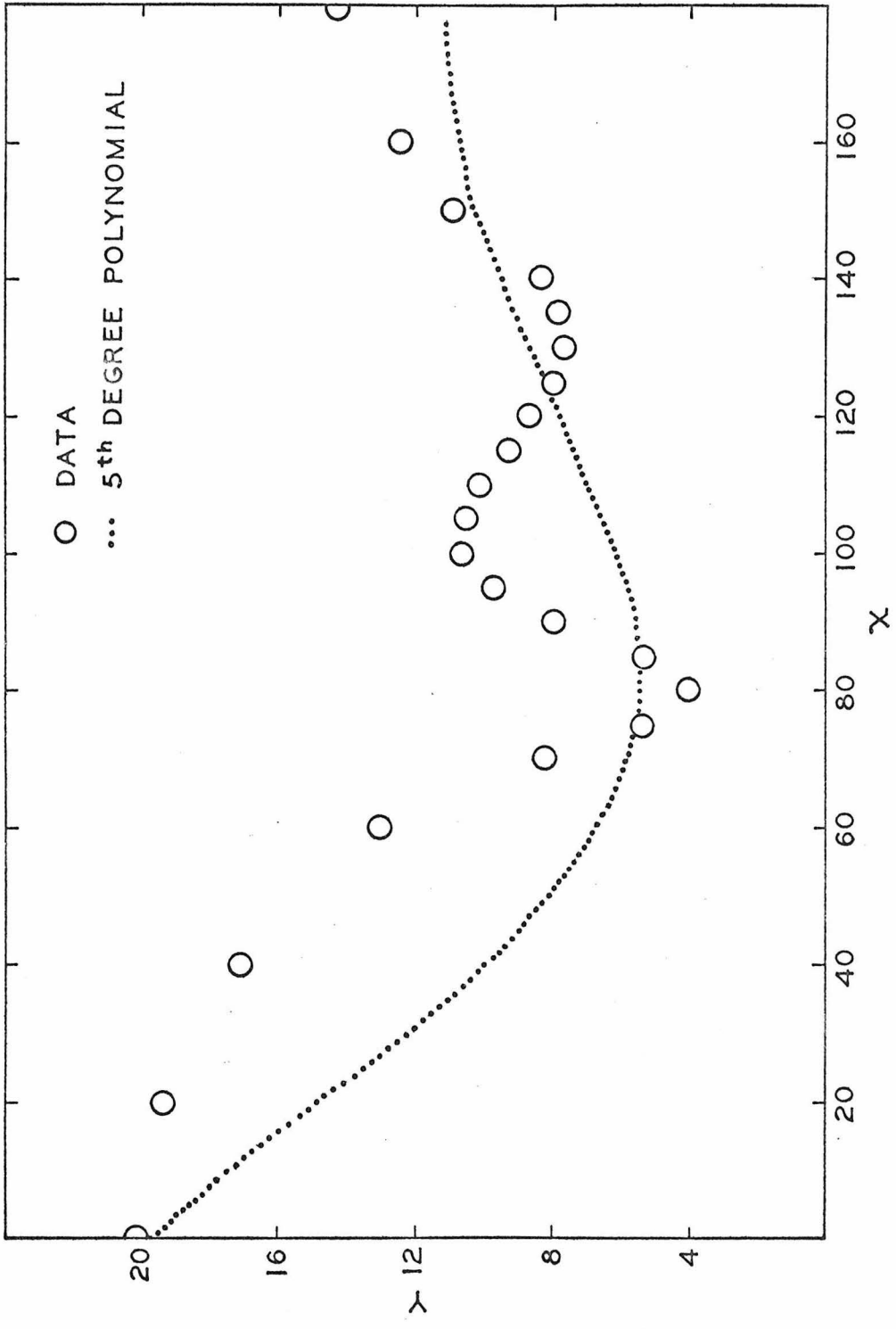


Figure 4. 5th Degree Polynomial Fit by Least Squares

polynomials did not represent the data better than the 9th degree polynomial.

However, an interpolating polynomial can be used to represent the experimental data. In particular, consider the LaGrange Interpolating Polynomial,³ $y_n(x)$:

$$y_n(x) = \sum_{i=1}^N L_i(x) y_i \quad (4)$$

$$L_i(x) = \prod_{\substack{j=1 \\ j \neq i}}^N \frac{x - x_j}{x_i - x_j} \quad (5)$$

where N is the number of x, y pairs used in the interpolation and x is the value of the independent variable for which the interpolated value for y is sought.

These equations can be rearranged to:

$$y_n(x) = A(N)x^{N-1} + \dots + A(1)$$

where:

$$A(N) = \sum_{i=1}^N \frac{y_i}{\prod_{\substack{j=1 \\ j \neq i}}^N (x_i - x_j)} \quad (6)$$

$$A(N-1) = - \sum_{i=1}^N \frac{y_i \sum_{\substack{j=1 \\ j \neq i}}^N x_j}{\prod_{\substack{j=1 \\ j \neq i}}^N (x_i - x_j)} \quad (7)$$

$$A(N-2) = + \sum_{i=1}^N \frac{y_i \sum_{\substack{j=1 \\ j \neq i}}^{N-1} \sum_{\substack{m=j+1 \\ m \neq i}}^N x_m x_j}{\prod_{\substack{j=1 \\ j \neq i}}^N (x_i - x_j)} \quad (8)$$

$$A(N-3) = - \sum_{i=1}^N \frac{y_i \sum_{\substack{j=1 \\ j \neq i}}^{N-2} \sum_{\substack{m=j+1 \\ m \neq i}}^{N-1} \sum_{\substack{L=m+1 \\ L \neq i}}^N x_j x_m x_L}{\prod_{\substack{j=1 \\ j \neq i}}^N (x_i - x_j)} \quad (9)$$

$$\begin{aligned} & \vdots \\ & \vdots \\ A(1) &= \pm \sum_{i=1}^N \frac{y_i \sum_{\substack{j=1 \\ j \neq i}}^2 \sum_{\substack{m=j+1 \\ m \neq i}}^3 \sum_{\substack{S=m+1 \\ S \neq i}}^{N-2} \sum_{\substack{II=S+1 \\ II \neq i}}^{N-1} \sum_{\substack{JJ=II+1 \\ JJ \neq i}}^N x_j \dots x_{JJ}}{\prod_{\substack{j=1 \\ j \neq i}}^N (x_i - x_j)} \end{aligned} \quad (10)$$

In this form, the interpolated data can be easily differentiated to give

$$\frac{d \text{Ave}(x)}{dx} = \frac{1}{2a} \left[(N-1) A(N) x^{N-2} + \dots + A(2) \right]$$

and with this form the recursion formula becomes

$$f(x + 2am) = \frac{1}{2a} \left[(N-1) A(N) (x + 2am - a)^{N-2} + A(2) \right] + f(x + 2a(m-1)) \quad m = 1, 2, \dots \quad (11)$$

For a test of the above method, a computer program was written to calculate interpolating coefficients over six data points at a time. This program was then tested with the aforementioned data. Figure 5 depicts the fit of the interpolated polynomial. Figure 6 shows the interpolated polynomial of Figure 5 and the local data as predicted with this six point interpolation routine.

It is evident in Fig. 6 that the method properly predicts that the local curve does fall below the average curve at 80° . At higher angles than 95° the 6 data point routine shows scatter. This scatter results from accumulative error because the derivatives are not continuous when the 6 point interpolating routine is shifted to the right, across the 26 data points. Figure 7 is a plot of the derivative which clearly shows these discontinuities. When the interpolating routine is expanded to cover more data points at a time, this behavior will be eliminated.

Data must be taken in intervals of less than $2a$ for the local curve to be meaningful. Since a recursion formula is used, "a" must be known to at least three significant figures.

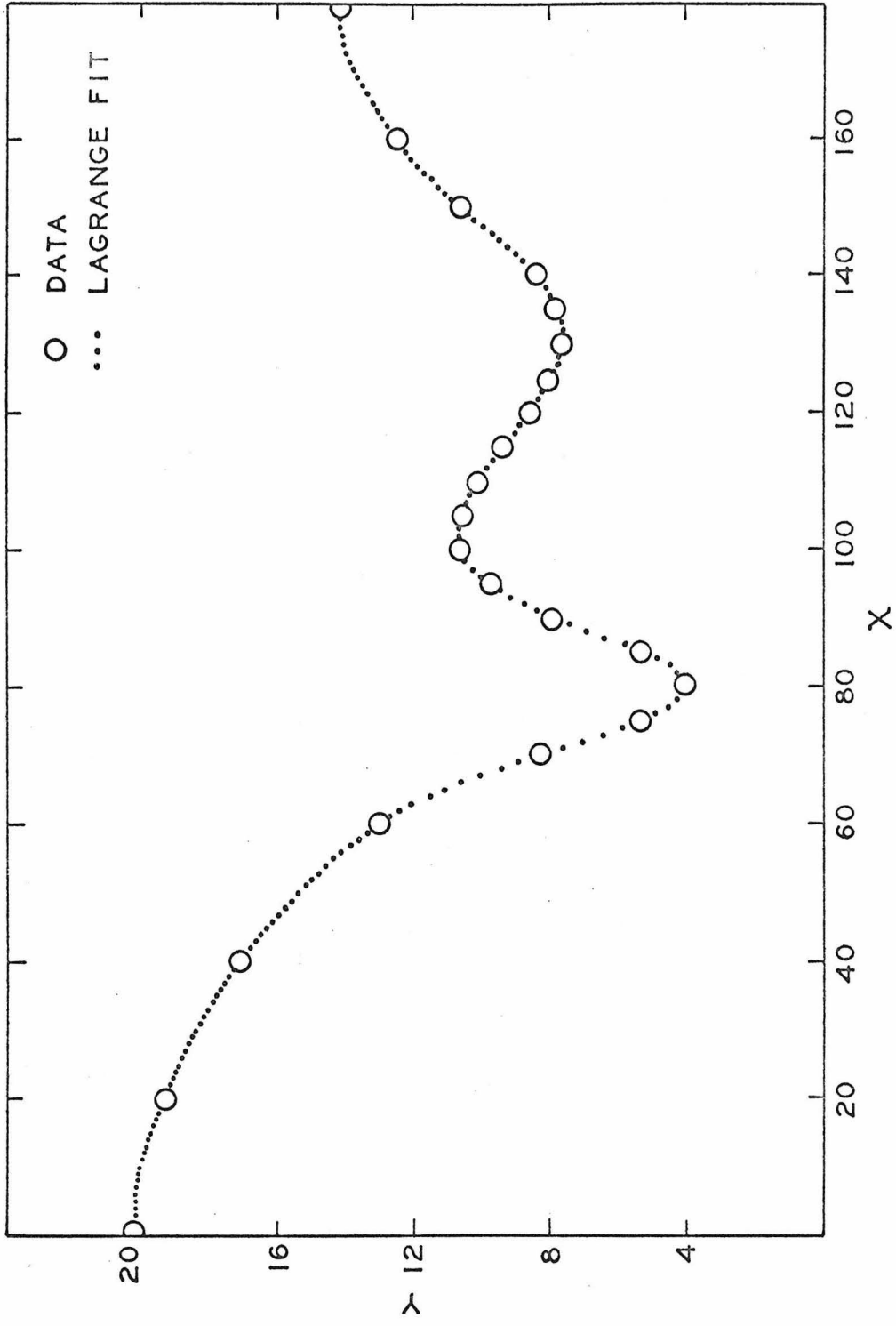


Figure 5. Lagrange Interpolating Polynomial for Six Points at a Time

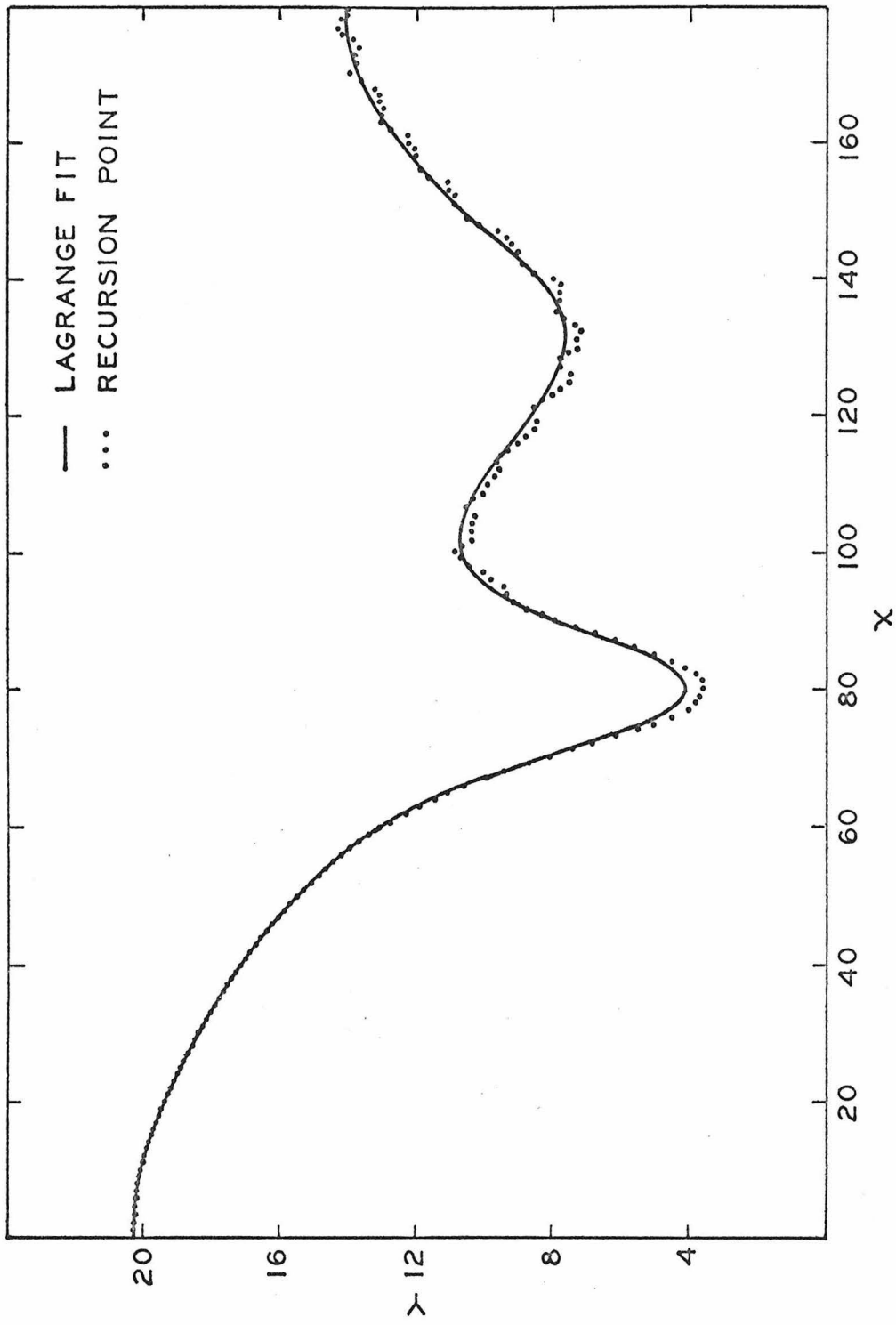


Figure 6. Estimated Local Data Plotted on Top of the Curve Through the Average Data

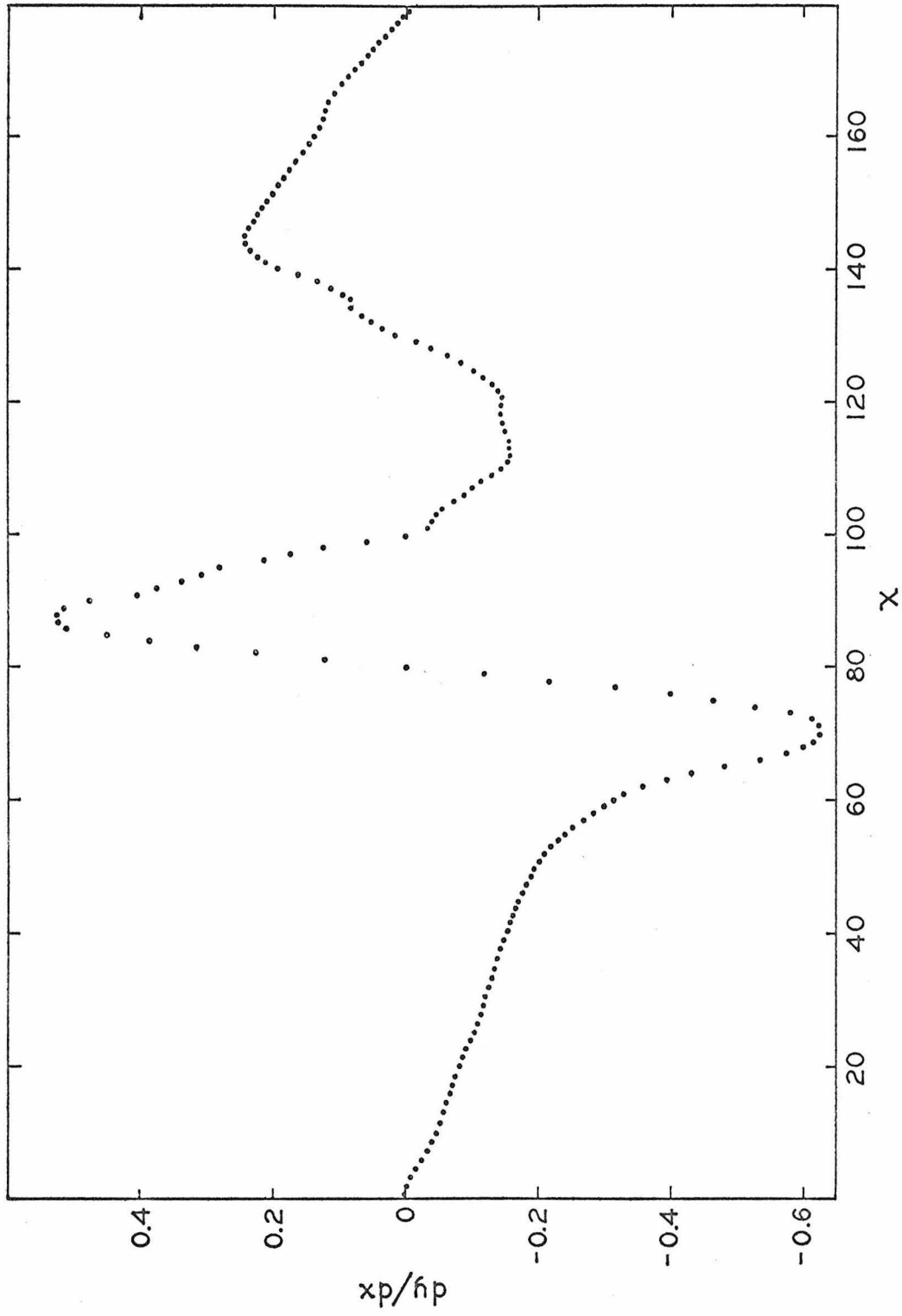


Figure 7. Derivative of the 6 Point Interpolation Function

REFERENCES

1. Wilfred Kaplan, Advanced Calculus, Addison-Wesley Publ. Co., Inc., Reading, Massachusetts, 1952, p. 219.
2. The magnitudes of these data points were taken from: MS 5296, T. R. Galloway and B. H. Sage, Local and Overall Transport from a $1\frac{1}{2}$ " Cylinder in a Turbulent Air Stream.
3. Leon Lapidus, Digital Computation for Chemical Engineers, McGraw-Hill Book Co., Inc., New York, 1962.

NOMENCLATURE

a	One-half the characteristic span of the averaging device
$A(N)$	The n^{th} coefficient of the LaGrange Interpolating polynomial
$\text{Ave}(x)$	The interpolated function that represents the average data point at x
$f(x)$	The local function at x
L_i	The i^{th} LaGrange polynomial
m	The m^{th} step in the recursion formula
N	The number of data points in the LaGrange interpolation
x	The independent variable
x_i	The i^{th} value of the independent variable for which data point y_i is given
y	The dependent variable
y_i	The i^{th} value of the dependent variable, i.e., y_i for x_i in the data
σ	Standard deviation in y values

Table 1Data Points

<u>x</u>	<u>y</u>	<u>σ</u>
- 40.	17.099	+ .026
- 20.	19.371	.032
00.	20.169	.030
20.	19.371	.032
40.	17.099	.026
60.	12.981	.025
70.	8.220	.008
75.	5.316	.005
80.	4.018	.004
85.	5.296	.080
90.	7.879	.008
95.	9.653	.009
100.	10.640	.011
105.	10.514	.010
110.	10.070	.011
115.	9.252	.009
120.	8.607	.008
125.	7.917	.007
130.	7.589	.007
135.	7.816	.008
140.	8.326	.008
150.	10.848	.011
160.	12.407	.013
180.	14.162	.014
200.	12.407	.012
210.	10.848	.011

PROPOSITION 2

The transient behavior of a binary distillation tower during a transition from one steady state to a second steady state using matrix techniques can be extended to a more general case when the partition coefficients for each plate are represented by a straight line, $Y_i = M_i X_i + B_i$.

The transient behavior of distillation columns for a constant partition coefficient ($Y = KX$) has been discussed by Luh C. Tao.¹ This development is severely restricted.

It is sometimes possible to extend the matrix technique presented by Tao when the transient behavior for the transition from one steady state to another steady state can be considered as a small perturbation of the first, (i.e., a change over which the partition function can be approximated by a linear equation). The assumptions of constant molal vaporization and constant molal overflow² are assumed for the calculations.

Consider a distillation tower with n-plates (numbered from the top down), a reboiler and a condenser. For convenience in the derivation presented here, the condenser will be a total condenser, but the method can be extended to a partial condenser with an additional mass balance (see Fig. 1).

In general, n-1 feed streams could enter the tower and n-1 distillate streams could leave. All these streams can be treated in the transient solution when both steady state solutions are available. For a discussion of steady state solutions see Hanson, Duffin and Somerville.³

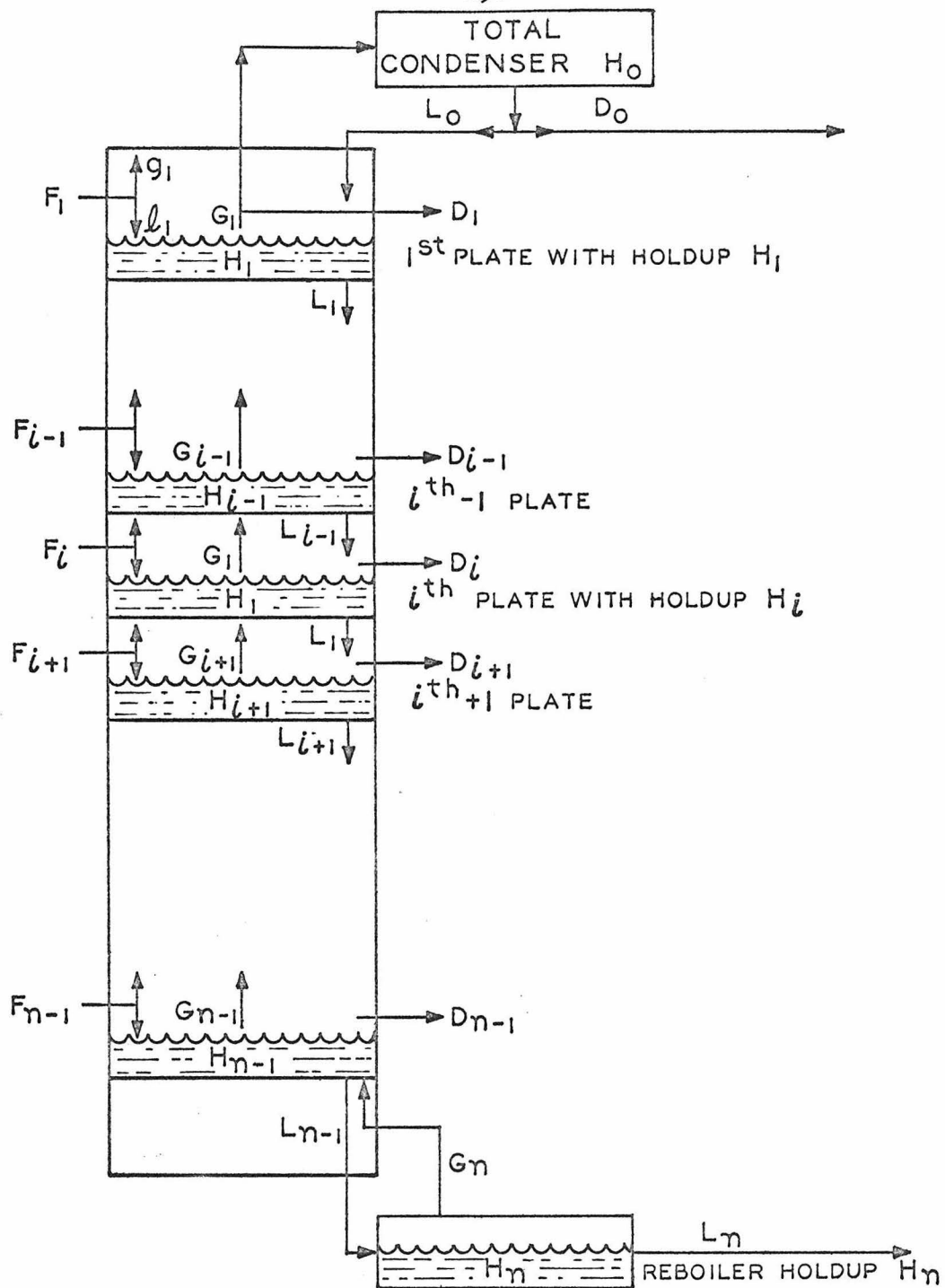


Figure 1. n -Plate Distillation Tower with Reboiler and Total Condenser

In the following equations, it is assumed that the feed stream which enters the i^{th} plate will add its liquid portion to the i^{th} plate and its vapor portion to the $i-1^{\text{th}}$ plate.

Mass balances on the more volatile component can be expressed for the i^{th} plate, the top plate and the reboiler (see Fig. 2). The effects of transients in the vapor space above each plate are neglected. For the i^{th} plate, one has:

For the i^{th} Plate $i = 1, \dots, n-1$:

In

liquid feed + vapor feed + liquid (plate above)

$$L_i X_i + G_{i+1} Y_{i+1} + L_{i-1} X_{i-1}$$

+ gas (plate below)

$$+ (G_{i+1} - D_{i+1}) Y_{i+1} \quad (1)$$

Out

liquid + vapor

$$L_i X_i + G_i Y_i \quad (2)$$

Accumulation

$$\frac{d}{dt} H_i X_i \quad (3)$$

The magnitudes of G_i and L_i are obtained from the degree of superheat of g_{i+1} , the amount of heat required to bring l_i to the

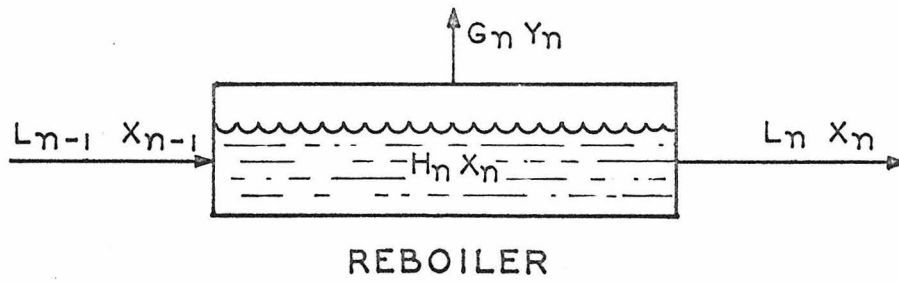
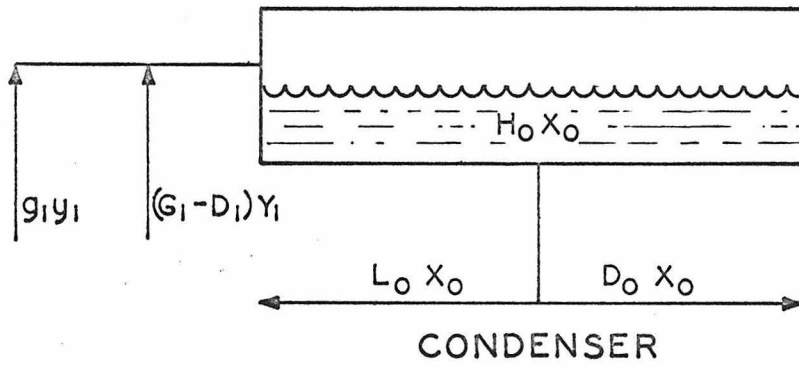
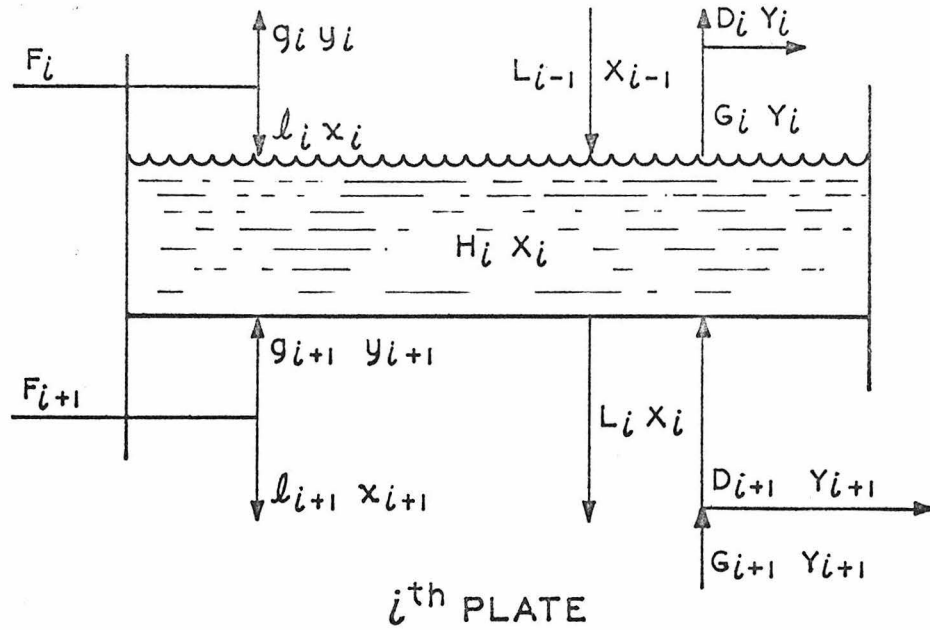


Figure 2. Mass Balance Diagrams

boiling point, and l_i , g_{i+1} , L_{i-1} , D_{i+1} , and G_{i+1} . (The values of the latter variables are taken to be those obtained in the solution of the second steady state problem.)

Therefore:

$$\begin{aligned} \frac{d}{dt} X_i &= \frac{l_i X_i}{H_i} + \frac{g_{i+1}}{H_i} y_{i+1} + \frac{L_{i-1}}{H_i} X_{i-1} \\ &+ \frac{(G_{i+1} - D_{i+1})}{H_i} Y_{i+1} - \frac{G_i}{H_i} Y_i - \frac{L_i}{H_i} X_i \end{aligned}$$

$$i = 1, \dots, n - 1 \quad (4)$$

For the Condenser:

$$\frac{d X_0}{dt} = \frac{g_1}{H_0} y_1 + \frac{(G_1 - D_1)}{H_0} Y_1 - \frac{(L_0 + D_0)}{H_0} X_0 \quad (5)$$

where for a total condenser with a feed stream on the top plate

$$X_0 = \frac{g_1 y_1 + G_1 Y_1}{g_1 + G_1} \quad (6)$$

And for the Reboiler:

$$\frac{d X_n}{dt} = \frac{L_{n-1}}{H_n} X_{n-1} - \frac{G_n Y_n}{H_n} - \frac{L_n}{H_n} X_n \quad (7)$$

Now, referring to the two steady state solutions

$$Y_{1i} = K_{1i} X_{1i} \quad l = 1, \dots, n \quad (8)$$

$$Y_{2i} = K_{2i} X_{2i} \quad i = 1, \dots, n \quad (9)$$

and linearizing these equations

$$\frac{Y_i - Y_{1i}}{X_i - X_{1i}} = \frac{Y_{2i} - Y_{1i}}{X_{2i} - X_{1i}} = M_i \quad (10)$$

or in the shortened slope intercept form derived from the above equation (See Fig. 3):

$$Y_i = M_i X_i + B_i \quad (11)$$

This equation is the basic equation that extends the applicability of the matrix technique.

Equation (11), when introduced into (4), (5), and (7) leads to:

$$\begin{aligned} & \underline{i^{\text{th}} \text{ plate}} \\ \frac{d X_i}{dt} &= \frac{L_{i-1}}{H_i} X_{i-1} - \left(\frac{L_i}{H_i} + \frac{G_i}{H_i} M_i \right) X_i + \frac{(G_{i+1} - D_{i+1})}{H_i} M_{i+1} X_{i+1} \\ &+ \frac{(G_{i+1} - D_{i+1})}{H_i} B_{i+1} - \frac{G_i}{H_i} B_i + \frac{l_i x_i}{H_i} \\ &+ \frac{g_{i+1} y_{i+1}}{H_i} \end{aligned} \quad (12)$$

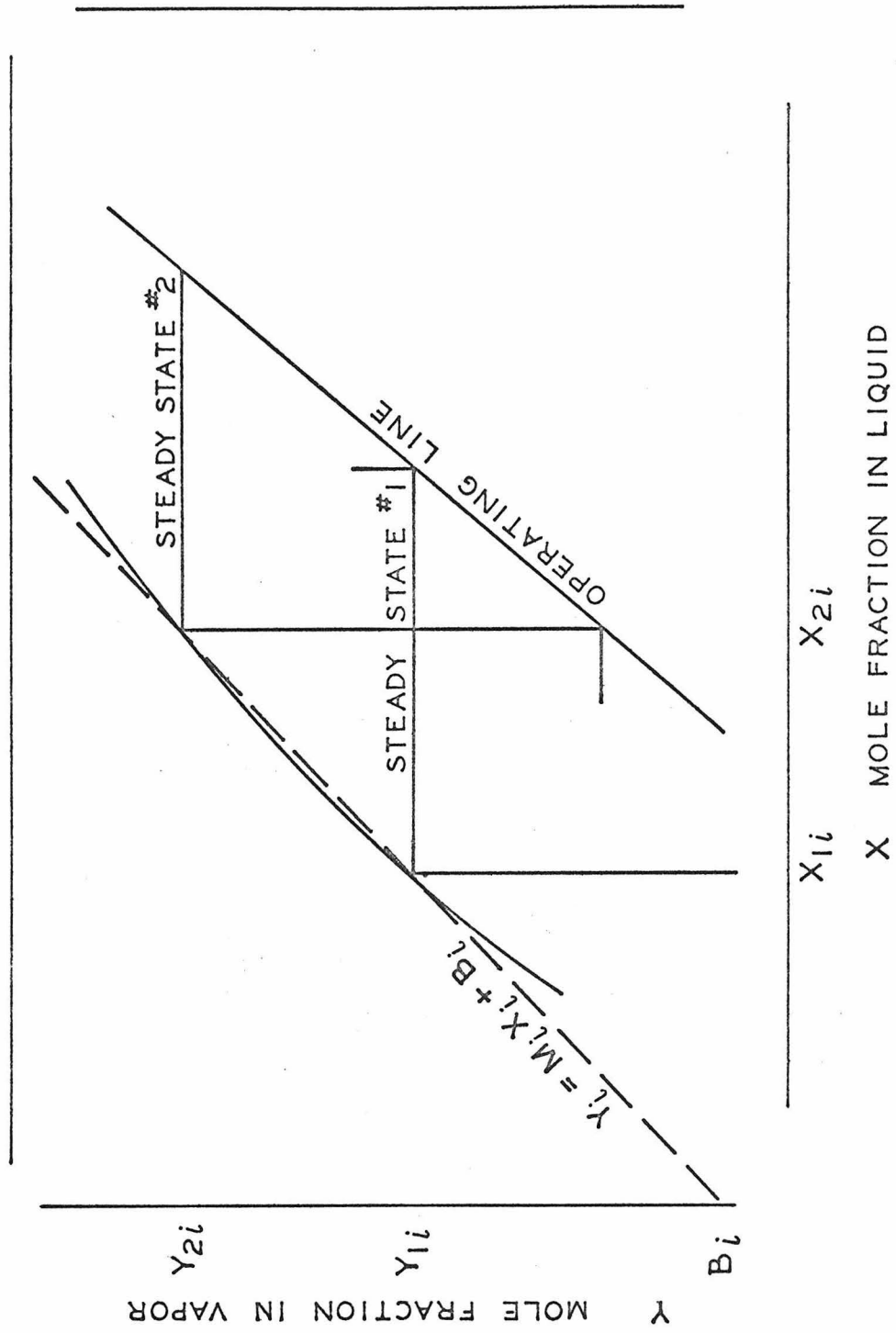


Figure 3. Blow-up of a McCabe Thiele Diagram Showing a Linearized Partition Coefficient Between Steady State #1 and #2 for the i^{th} Plate

condenser

$$\frac{d X_0}{dt} = \frac{-(L_0 + D_0)}{H_0} X_0 + \frac{G_1 M_1}{H_0} X_1 + \frac{G_1 B_1}{H_0} + \frac{g_1 y_1}{H_0} \quad (13)$$

reboiler

$$\frac{d X_n}{dt} = \frac{L_{n-1}}{H_n} X_{n-1} - \left(\frac{L_n}{H_n} + \frac{G_n}{H_n} M_n \right) X_n - \frac{G_n}{H_n} B_n \quad (14)$$

From which the vector equation,

$$\frac{d\vec{x}}{dt} = -A\vec{x} + \vec{z} \quad (15)$$

arises, where A is a tridiagonal matrix. The solution for A positive definite can be written:⁴

$$\vec{x}(t) = e^{-At} [\vec{X}_1(0) + A^{-1} \vec{z}] - A^{-1} \vec{z} \quad (16)$$

where, having solved the eigenvalue problem for A using the power method of von Mises,⁵ e^{-At} and A^{-1} can be expressed:⁴

$$e^{-At} = \sum_{i=0}^n \frac{e^{-\lambda_i t} \prod_{\substack{j=1 \\ j \neq i}}^n (A - \lambda_j I)}{\prod_{\substack{j=1 \\ j \neq i}}^n (\lambda_i - \lambda_j)} \quad (17)$$

and

$$A^{-1} = \sum_{i=0}^n \frac{1}{\lambda_i} \frac{\prod_{\substack{j=1 \\ j \neq i}}^n (A - \lambda_j I)}{\prod_{\substack{j=1 \\ j \neq i}}^n (\lambda_i - \lambda_j)} \quad (18)$$

All the eigenvalues must be positive and distinct or the solution can not be found. If $\lambda_i = \lambda_j$ for $i \neq j$ the expansions fail. If $\lambda_i < 0$ for some i , instability is indicated.⁶ If $\lambda_{\text{largest}} / \lambda_{\text{smallest}} < 100$, the A matrix is well conditioned, and the eigenvalues should accordingly be quite accurate.⁷

When the eigenvalues are known, the calculation scheme reduces to

$$X_i(t) = a_i(t) + X_{2i} \quad (19)$$

where $a_i(t)$ is the transient behavior for the i^{th} plate.

This method can be used for small step changes in l_i , g_i , L_i , G_i , D_i or small step changes in y_i and x_i .

REFERENCES

1. Luh C. Tao, Linear Matrix Differential Equations. Chemical Engineering, May 24, 1965. p. 125.
2. Warren L. McCabe and Julian C. Smith, Unit Operations of Chemical Engineering, McGraw-Hill Book Company, Inc., New York, 1956, p. 690.
3. Donald N. Hanson, John H. Duffin, Graham F. Sommerville, Computation of Multistage Separation Processes, Reinhold Publishing Corp., New York, 1962, p. 20.
4. Tao, op cit., p. 128.
5. Leon Lapidus, Digital Computation for Chemical Engineers, McGraw-Hill Book Co., Inc., New York, 1962, p. 232
6. Richard Bellman, Introduction to Matrix Analysis, McGraw-Hill Book Co., New York, 1960, p. 241.
7. Lapidus, op.cit., p. 240 and 270.

NOMENCLATURE

A	Tridiagonal matrix characteristic of the distillation tower defined in (15)
$a_i(t)$	Transient solution in mole fraction of the more volatile component on the i^{th} plate
B_i	Defined in (11)
D_i	Distillate molal flow rate, i^{th} plate
e	Base of natural logarithms
F_i	Molal feed rate entering i^{th} plate, see Fig. 1
g_i	Gas molal flow rate of F_i as flashed in the tower
G_i	Gas molal flow rate leaving i^{th} plate
H_i	Molal holdup i^{th} plate
i	Indexing subscript for plates
j	Summation index
K	Partition coefficient $K_{\text{EQUILIBRIUM}}$ * Efficiency
K_{1i}	Partition coefficient for i^{th} plate at steady state #1
K_{2i}	Partition coefficient for i^{th} plate at steady state #2
l_i	Liquid molal flow rate in F_i as flashed in the tower
L_i	Liquid molal flow rate leaving plate i
n	Number of actual stages = number of plates plus 1 for the reboiler
X	Mole fraction of lighter component in liquid
x_i	Mole fraction lighter component in l_i
X_{1i}	Mole fraction lighter component on i^{th} plate at steady state #1
X_{2i}	Mole fraction lighter component on i^{th} plate at steady state #2

\vec{x}	Vector containing $X_0 \dots X_n$
$\vec{X}_1(0)$	Vector containing $X_{1i} \dots X_{1n}$
Y	Mole fraction lighter component in gas
y_i	Mole fraction lighter component in g_i
Y_{1i}	Mole fraction lighter component in vapor leaving i^{th} plate at steady state #1
Y_{2i}	Mole fraction lighter component in vapor leaving i^{th} plate at steady state #2
\vec{z}	Constant mole fraction vector defined by (15)
λ_j	j^{th} eigenvalue of A

PROPOSITION 3

A calibration experiment which shows that a single crystal of beryllium can be used as a cell for liquids in x-ray diffraction experiments has been performed. The use of a single crystal would mean a marked improvement in data reduction over the use of a sintered-crystal cell.

In order to study the structure of liquids by x-ray diffraction it is occasionally necessary to confine the liquid to pressurize it. Unfortunately, this means that the detector system will receive radiation not only from the sample, but from this cell. Empty cell scattering measurements are taken so that the portion of the previously mentioned total scattering that originates in the cell may be appropriately subtracted. Thus:

$$I_s(\theta) = \frac{1}{P(\theta) F(\theta) ASSC(\theta)} \left(I_{c+s}(\theta) - \frac{ACSC(\theta)}{ACC(\theta)} I_c(\theta) \right) \quad (1)$$

However, whenever the cell diffraction pattern contains many well-defined Bragg scattering peaks this subtraction is not quantitative. A typical diffraction pattern for a cylindrical sintered Be cell is depicted in Fig. 1. This pattern was obtained in a Debye Scherrer geometry using a 0.0062" divergence slit and a 0.003" receiving slit. The cell was 0.100" in diameter with a 0.059" hole in it. Each point in this diagram (and those to follow) represents ten minutes of counting taken at that angle in three different scans of 200 seconds each. The sintered Be diffraction pattern was taken in a vacuum cryostat at -85 °C.

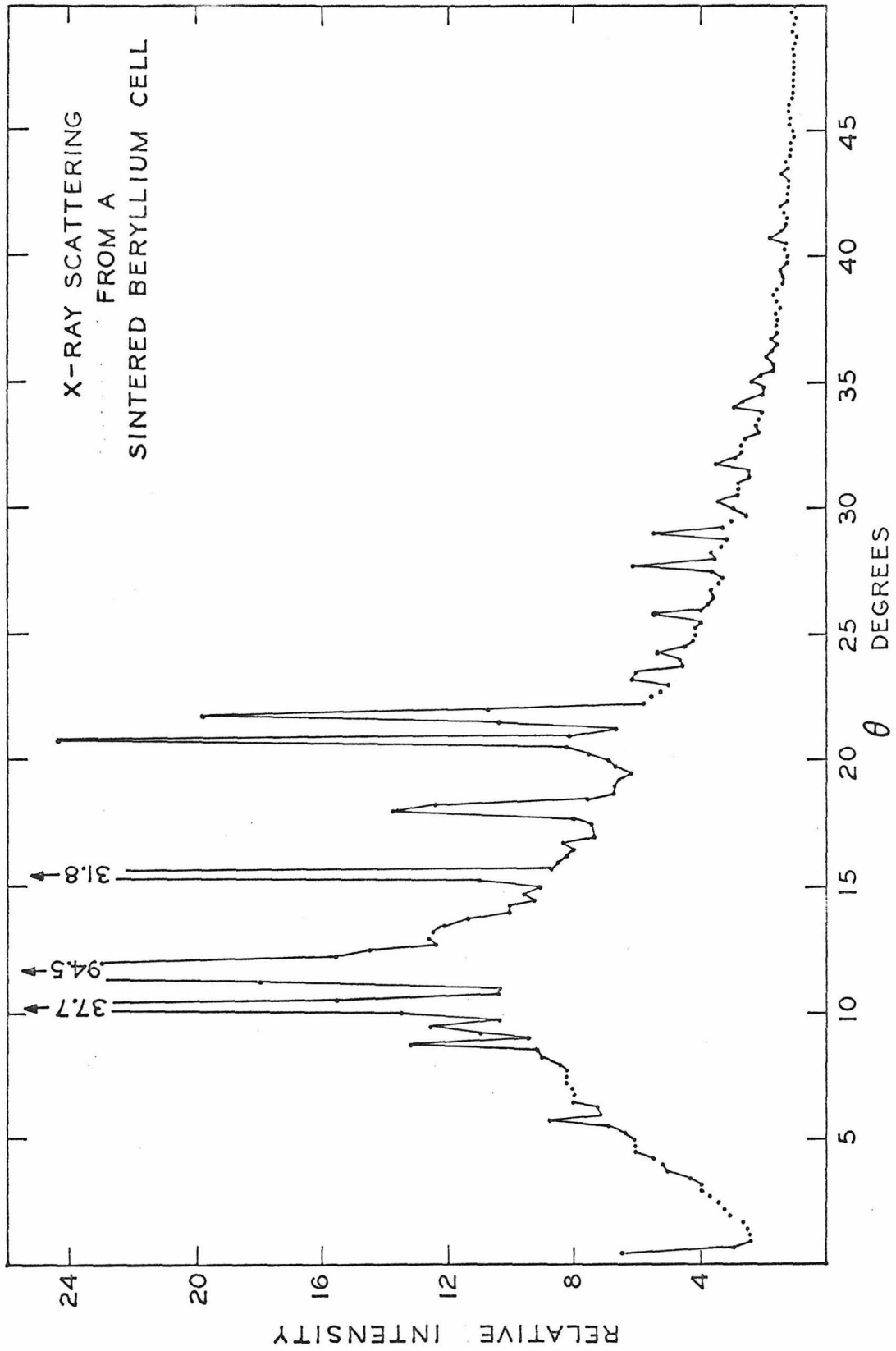


Figure 1. A Typical Diffraction Pattern for a Cylindrical Sintered Beryllium Cell Obtained with a 0.0062" Divergence Slit and a 0.003" Receiving Slit

The calibration experiment consisted of measuring the diffraction pattern of a glass rod confined in the single crystal and subtracting appropriate amounts of cell and air scattering (as the data were taken at atmospheric pressure).

Since the diffraction experiment was performed in air, the argon data reduction scheme¹ is not adequate, since the material that was irradiated included air. In this case, the scattering geometry (see Fig. 2 for cross section of the cell) was defined not only by the incident beam and the Be container but also by the receiving slit.

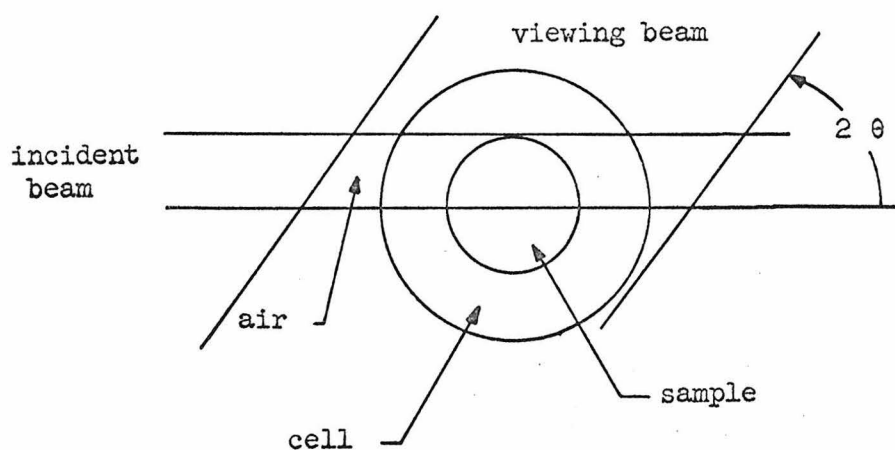


Figure 2. Scattering Geometry: Cross Section of Cell

In fact, the volume of air that contributed to the value of I_{c+a} or I_{c+s+a} now depends on the angle 2θ as follows:

$$V_A = \Delta Z W_I W_D / \sin(2\theta) \quad (2)$$

where

W_I is the width of the incident beam,

W_D is the width of the scattered beam,

ΔZ is the depth of irradiation along the axis of the cell.

Following the example of Paalman and Pings², and neglecting absorption in air as it is small compared to the absorption of Be or SiO₂, one can define absorption coefficients

$$AASC = (1/V_A'') \int_{V_A''} e^{-\mu_s l_s - \mu_c l_c} dV \quad (3)$$

$$AAC = (1/V_A') \int_{V_A'} e^{-\mu_c l_c} dV \quad (4)$$

where:

μ_c , l_c , μ_s and l_s are as defined in the nomenclature;

V_A'' is V_A less the irradiated volume of sample and cell,

V_A' is V_A less the irradiated volume of sample cell.

The calibration experiment provided three sets of data:

$$I_{c+s+a}^E, I_{c+a}^E, \text{ and } I_a^E$$

and I_s^E was taken from P. G. Mikolaj,²

where:

$$I_{c+s+a}^E = I_{c+s}^E + V_A'' I_A^{AASC \text{ coh}} \gamma_A^{\text{coh}} \gamma_t^{\text{coh}} + V_A' I_A^{AASC \text{ inc}} \gamma_A^{\text{inc}} \gamma_t^{\text{inc}} \quad (5)$$

$$I_{c+a}^E = I_c + V_A' I_{AAC}^{coh} \gamma_A^{coh} t^{coh} + V_A' I_{AAC}^{inc} \gamma_A^{inc} t^{inc} \quad (6)$$

$$I_A^E = I_{AA} V_A t^{coh} \gamma_A^{coh} + I_{AA} V_A t^{inc} \gamma_A^{inc} \quad (7)$$

$$I_s^E = I_s \quad (8)$$

From Figure 3, it is evident that the air correction is very small above 10° . But from 0 to 10° almost all the scattered intensity is coherent. In addition, $AASC^{coh} = AASC^{inc}$. Therefore, for the calibration experiment, one can assume that

$$\gamma_A^{coh} = 1 \quad (9)$$

Therefore:

$$I_{c+s} = I_{c+s+a}^E - FCS I_A^E \quad (10)$$

$$I_c = I_{c+a}^E - FC I_A^E \quad (11)$$

$$I_s = I_s^E \quad (12)$$

where

$$FCS = \frac{V_A''}{V_A} AASC \quad (13)$$

and

$$FC = \frac{V_A'}{V_A} AAC. \quad (14)$$

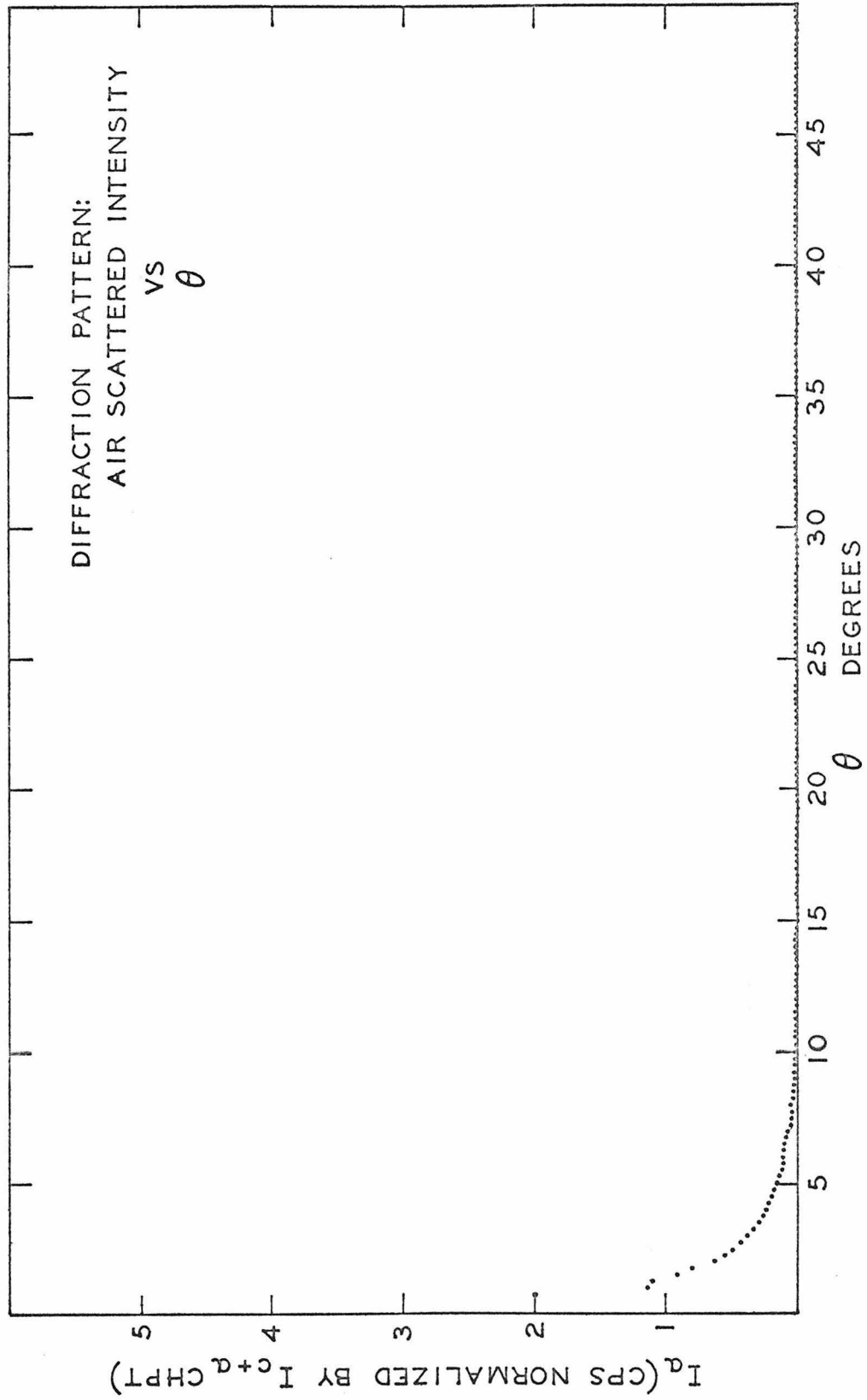


Figure 3. Air Scattering as Experimentally Measured and Normalized to the Empty Cell Checkpoint Intensity

The cell and sample and cell patterns are corrected by subtracting the appropriate portion of air scattering via this method to give the values of I_{c+s} and I_c that would be obtained if the cell and sample patterns were taken in a vacuum. Then these two patterns are subtracted via equation (1) to give the sample diffraction pattern. Thus these two sample intensities, the confined and the unconfined, can be compared.

This experiment has been carried out using a SiO_2 rod 0.059" in diameter placed in the single crystal. The experimental diffraction patterns obtained with a $1/6^\circ$ divergence slit and a 0.111" receiving slit are plotted in Figures 3 to 5.

The cell diffraction pattern in Figure 4 contains two strong peaks, one of which has been used to determine the pulse amplitude distribution. The pattern also contains at least six weak diffraction peaks that are less than $1/3$ of the general background. This low number of peaks compares very favorably to the six very strong, nine intermediate and numerous small peaks of the sintered crystal.

The cell and sample pattern of Figure 5 readily shows the first two maxima of the SiO_2 pattern and also two strong diffraction peaks from the beryllium cell.

After the air scattering corrections had been made using the air diffraction pattern of Figure 3, $I(\theta)$ was calculated and plotted in Figure 6. Except for the regions near 20° , 44° , and 48° , the pattern shows the same features for SiO_2 as $I(\theta)$ obtained by Dr. P. G. Mikolaj². In fact when $I(\theta)$ is multiplied by a linear correction term as in the

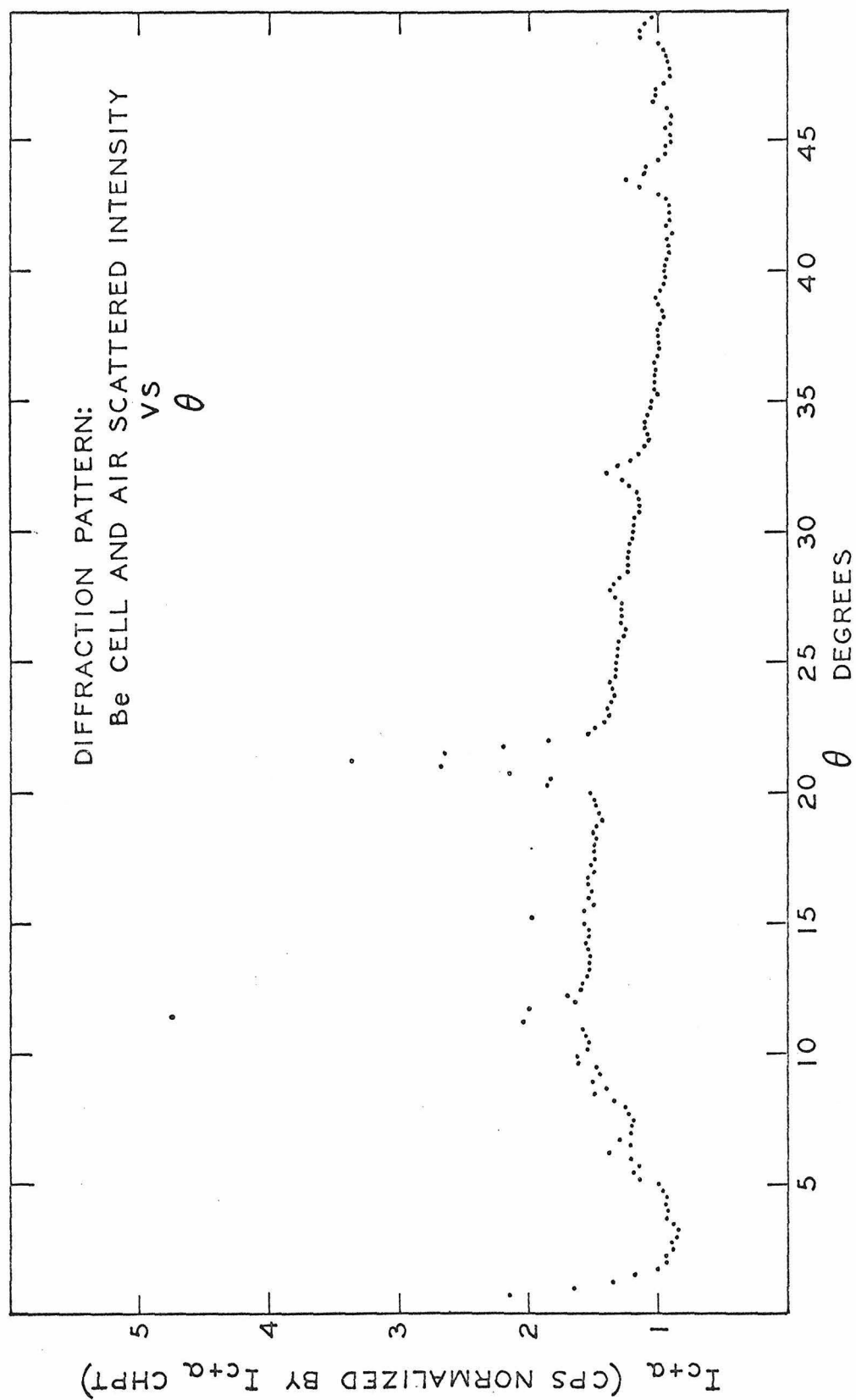


Figure 4. Empty Cell Scattering as Experimentally Measured and Normalized to the Empty Cell Checkpoint Intensity

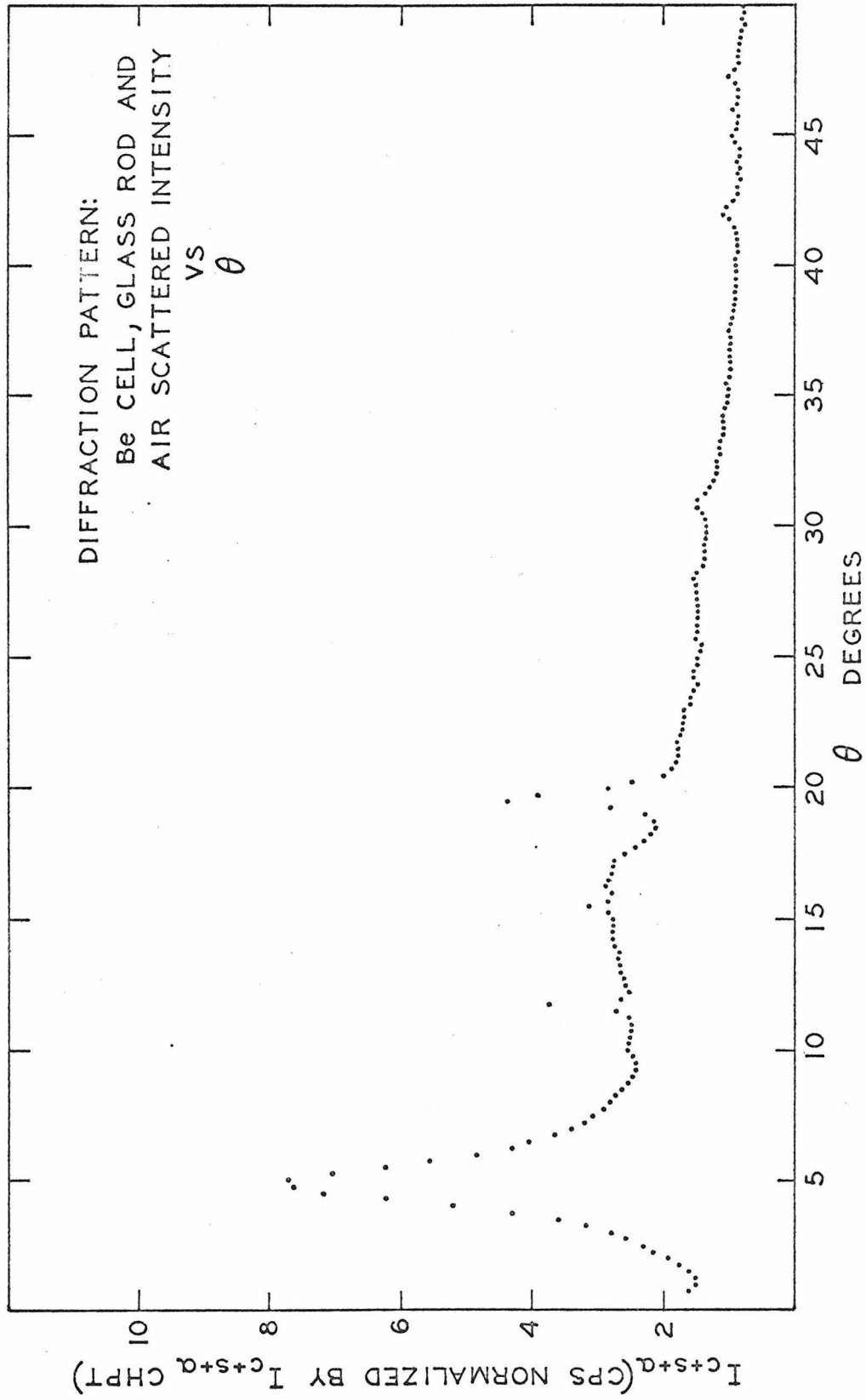


Figure 5. Beryllium Cell, SiO₂ Rod, and Air Scattering as Experimentally Measured and Normalized to the Scan Checkpoint Intensity

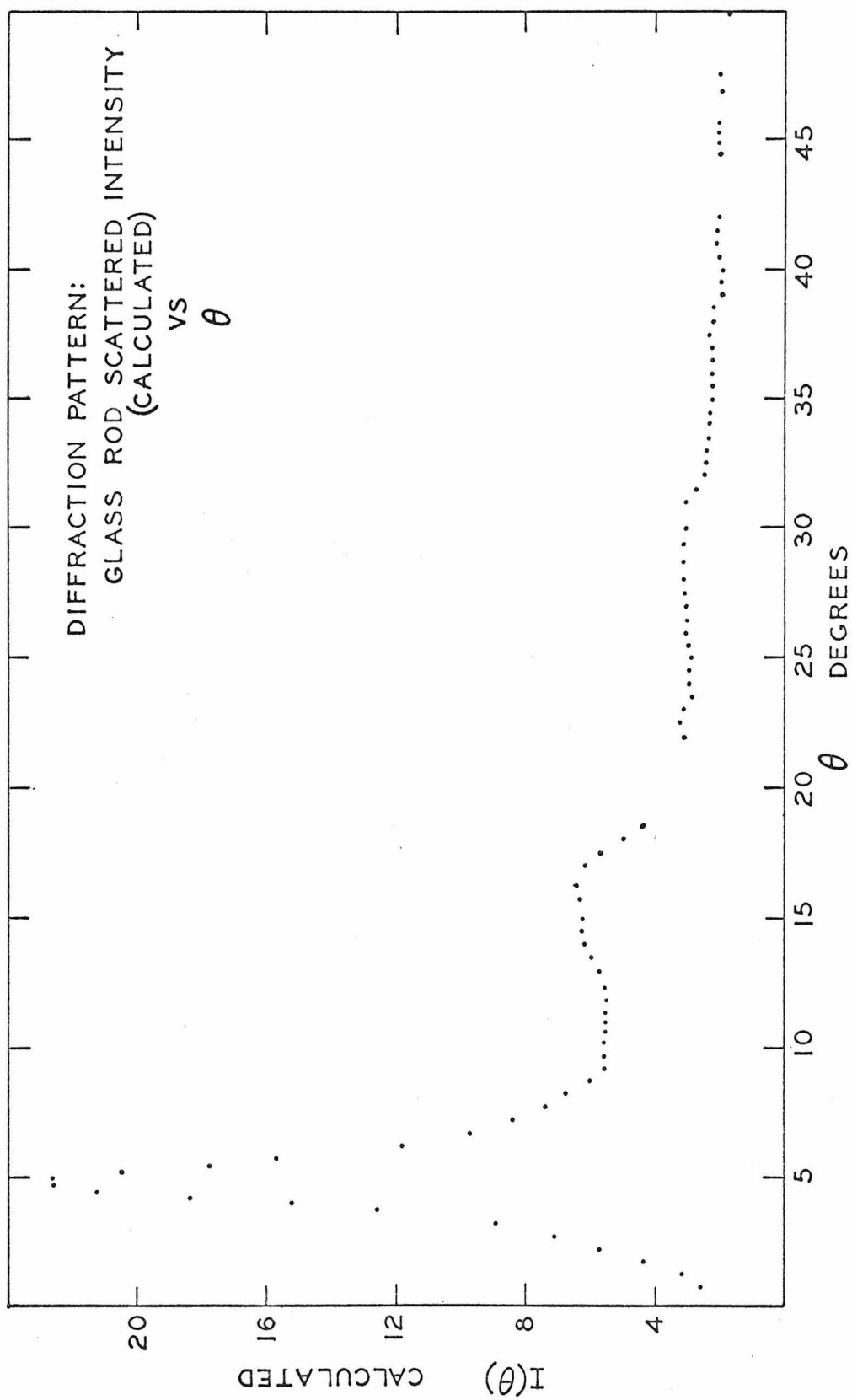


Figure 6. $I_s(\theta)$ as Calculated from Normalized Intensity Data

calibration experiment of Dr. Mikolaj, $I(\theta) (1 + 0.0065 \theta)$ agrees almost identically with $I(\theta)_{\text{Mikolaj}}$. A few of the rotated values of the modified $I(\theta)$ are plotted in Figure 7 for reference.

The incomplete regions in the $I(\theta)$ curve relate to the fact that the single crystal had been rotated accidentally when the glass rod was placed inside it. When the crystal was realigned before the scans of I_{c+s+a} , the peak at 20° was mistaken for the one at 21° when reading the recorder strip chart. As a result, the crystal was several rotational degrees away from its original position, and the two peaks -- one in each pattern -- prevent a meaningful subtraction in the regions.

However, the main features are adequately preserved.

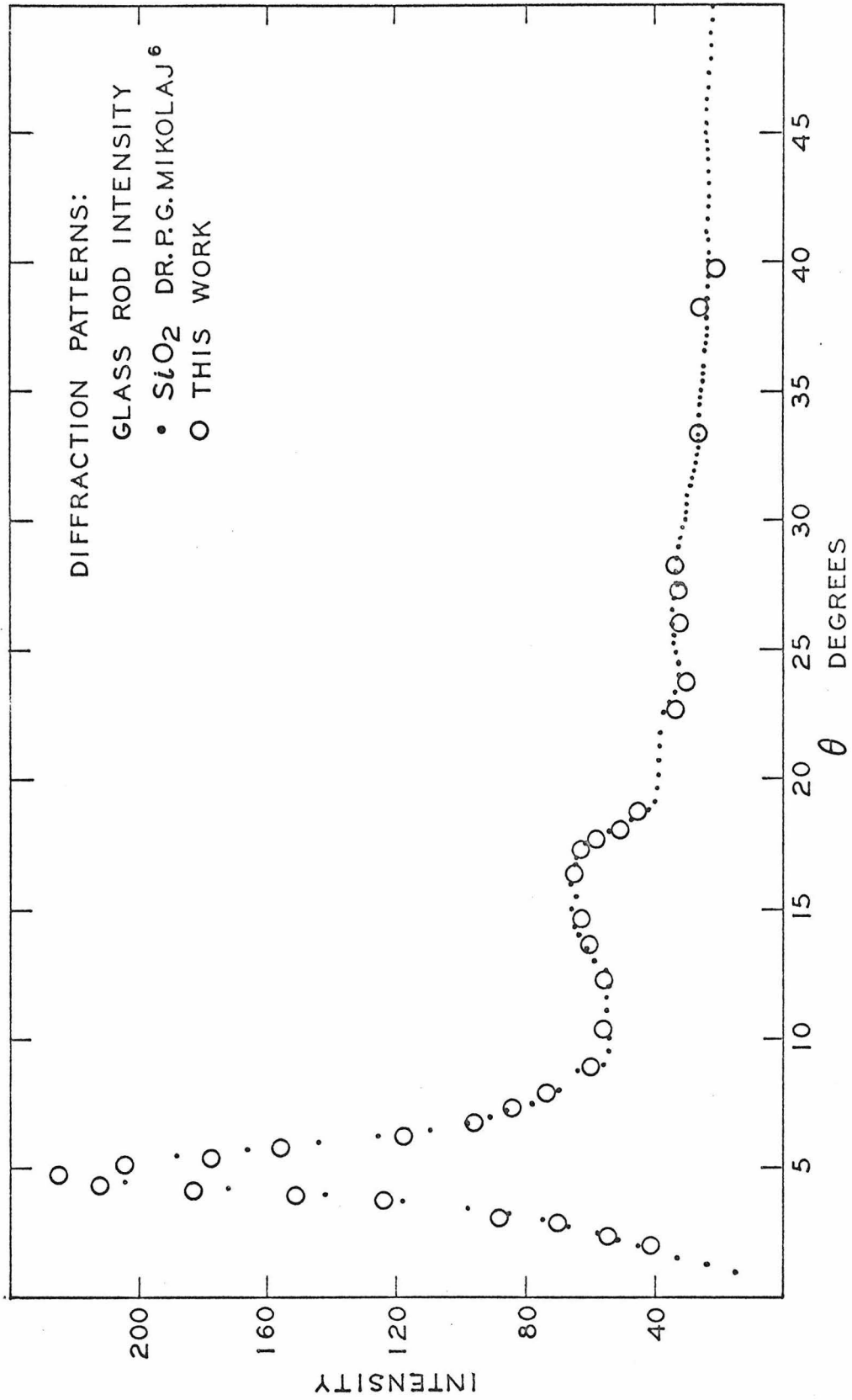


Figure 7. Comparison of P. G. Mikolaj's $I_s(\theta)$ and This Work Normalized to his Experimental Intensities

REFERENCES

1. Mikolaj, P. G., 1965, Thesis: An X-ray Diffraction Study of the Structure of Fluid Argon, California Institute of Technology.
2. Paalman, H. H., and C. J. Pings, 1963, Rev. of Mod. Phys., 35, 389.
3. James, R. W., 1954, The Optical Principles of the Diffraction of X-rays (Bell, London).

NOMENCLATURE

AAC	absorption coefficient for scattering in air and absorption in the cell, defined by equation (4)
AASC	absorption coefficient for scattering in air and absorption in the cell and sample, defined by equation (3)
ACC	absorption coefficient for scattering in the cell and absorption in the cell
ACSC	absorption coefficient for scattering in the cell and absorption in the cell and sample
ASSC	absorption coefficient for scattering in the sample and absorption in the cell and sample
a	subscript denoting air
c	subscript denoting cell
°C	degrees centigrade
c+a	subscript denoting cell and air
c+s	subscript denoting cell and sample
c+s+a	subscript denoting cell, sample and air
CHPT	abbreviation for the beam monitoring checkpoint intensity used to remove incident beam intensity fluctuations from the data
coh	superscript denoting coherent radiation, in this work $\lambda = 0.711 \text{ \AA}$
E	superscript denoting experimentally measured
F	combined correction factor for incoherent scattering (see Mikolaj ¹)
FC	correction factor for air scattering in empty cell measurements, defined by equation (14)
FCS	correction factor for air scattering in the cell and sample measurements, defined by equation (13)

I	intensity in counts per second or dimensionless intensity relative to a checkpoint of 1 count per second
inc	superscript denoting incoherent scattering
c	length of path which radiation follows in the cell
s	length of path which radiation follows in the sample
P	Polarization correction (see James ³)
s	subscript denoting sample
t	transmission correction for electronics (fully discussed in Mikolaj ¹)
V_A	volume of air defined by equation (2)
V_A'	V_A less the irradiated volume of sample
V_A	V_A less the irradiated volume of cell and sample
γ_A	relative fraction of intensity scattered by air that is coherent or incoherent according to the subscript
θ	one/half the scattering angle defined in Figure 2
μ_c	linear absorption coefficient for the cell
μ_s	linear absorption coefficient for the sample

PROPOSITION 4

It is proposed that the list of acceptable monochromators for x-ray diffraction studies of liquids and amorphous materials be restricted to balanced dual filters and curved or flat crystal reflectors; thereby eliminating the β filter with pulse height discrimination as a suitable monochromator.

Liquid structure experiments are designed to measure the coherent scattering from a sample which is being irradiated by a beam of x-rays. The theory which relates the scattering data to the structure requires that the scattering be known as a function of s , where

$$s = 4\pi \sin (\theta)/\lambda \quad (1)$$

When the radiation incident on the scattering material is truly monochromatic, the scattering parameter, s , is uniquely determined by the scattering angle, θ . If monochromatic radiation is used, a measurement of scattering in the geometric scattering plane at θ is readily converted to scattering in s -space. If the incident radiation is not monochromatic, the conversion is very complicated.

Under the high voltage normally used with x-ray tubes,

two types of radiation are generated: a continuous spectrum and superimposed on this, characteristic lines.

The intensity of the continuous spectrum is zero up to a certain wavelength (called the short-wavelength limit), increases rapidly to a maximum, and then decreases on the long wavelength side. When the tube voltage is raised, the intensity of all the continuous spectrum increases, the short-wavelength limit decreases, and the position of the maximum shifts to a lower wavelength. The material of the x-ray tube target affects the total intensity, but not the wavelength distribution of the continuous spectrum.

When the voltage applied to the x-ray tube is raised above the excitation voltages of the target material, sharp intensity peaks occur at certain wavelengths. The wavelengths of the characteristic spectra do not change with increasing tube voltage. However, an increase in the tube voltage increases the intensity of each peak more than the corresponding increase in the continuous spectrum intensity at neighboring wavelengths. The K_{α} lines are usually selected for diffraction studies because they are of high intensity, they are not highly absorbed, and their wavelengths are on the order of atomic diameters.

The x-rays emitted from a target are made more monochromatic by using filters or reflecting crystals. A β filter is a material

whose absorption edge lies between the K_α and K_β wavelengths of the target spectrum. The use of this filter greatly decreases the intensity of undesirable wavelengths relative to the attenuation of the α doublet. A dual filter is a pair of filters whose K edges bridge the α doublet of the target spectrum. Balanced dual filters effectively eliminate all radiation except the characteristic peaks and the continuous spectrum that lie between the two K edges. Crystal reflectors are used as diffractors to select a band of wavelengths about the wavelength which satisfies Bragg's law for the beam incident on the reflector. Curved crystals are used in the same way that flat crystals are used, but the curved crystal is more efficient since it utilizes focusing geometry.

It is evident from this discussion that these monochromatization techniques do not furnish truly monochromatic radiation. The following analysis was used to discover the relative monochromatizing effectiveness of a β filter, a dual filter, a curved-crystal reflector and a flat-crystal monochromator.

The intrinsic scattering power per atom in a fluid depends only on s . Therefore, a scintillation counter positioned at a scattering angle will detect radiation that depends not only upon the intrinsic scattering power of the fluid atoms, but also upon the spectrum of the incident beam. More precisely, for a non-absorbing

scatterer, the total scattering that would be experimentally observed at θ can be calculated:

$$I^E(\theta) = \frac{\int_{\lambda_{LO}}^{\lambda_{HI}} f(\lambda) I^T(s) d\lambda}{\int_{\lambda_{LO}}^{\lambda_{HI}} f(\lambda) d\lambda} \quad (2)$$

where $f(\lambda)$ is the intensity distribution of the incident beam,

$I^T(s)$ is the theoretical scattering power per atom of the fluid, (note that s is $4\pi \sin(\theta)/\lambda$, therefore $I^T(s)$ is actually $I^T(\theta, \lambda)$, and θ is a parameter in the integration),

$I^E(\theta)$ the total scattering that would be observed, per atom,

λ_{LO} is the minimum wavelength in the experimentally measured spectra, $f(\lambda) = 0$ for $\lambda < \lambda_{LO}$, and

λ_{HI} is the maximum wavelength in the experimentally measured spectra, $f(\lambda) = 0$ for $\lambda > \lambda_{HI}$.

Whenever the incident x-rays are sufficiently monochromated, the deviation between the scattering calculated from the spectrum of the incident beam and the scattering from a truly monochromatic source vanishes for all values of θ , i.e.,

$$\frac{I^E(\theta) - I^T(\theta, \lambda^*)}{I^T(\theta, \lambda^*)} \rightarrow 0 \quad (3)$$

where λ^* is the monochromatic wavelength. The degree to which the deviation ratio of Eq. (3) differs from zero is a measure of the degree of monochromatization.

In order to test the four monochromatization techniques by this criteria, it was necessary to know a typical scattering power function. For this purpose, an $I^E(\theta)$ function as measured in a liquid argon experiment performed by Mikolaj¹ was used. It was assumed that this function represented the theoretical scattering power per atom, $I^T(\theta, \lambda^*)$, where λ^* was 0.7107 angstroms. Mikolaj's data are listed versus theta in Table 1.

The spectra for the various monochromators were experimentally determined using a LiF analyzer. The scattering geometry and operating parameters used for the β filter and dual filter data are summarized in Figure 1, for the curved-crystal reflector² in Figure 2 and for the flat-crystal reflector in Figure 3.

The dual filter spectra for 99.5% pulse height transmission and the β filter spectra for 50% and 99.5% pulse height transmission are listed in Tables 2, 3, and 4 respectively. The dual filter and the β filter spectra at 99.5% transmission are depicted in Figure 4, as the series of circles and the solid curve respectively. The insert in this figure is the net K_{α} doublet for the dual filter.

The crystal monochromator data were obtained by Dr. E. H. Henninger.² The flat crystal data are summarized in Table 5, and the curved crystal data in Table 6.

KEY TO FIGURE 1

- S Source: Molybdenum
 55 kilovolts
 3-20 milliamps
 line source: 1.2 mm x 10.0 mm
 take off angle: 5.8°
 K_α 0.7107 Å
- A Vertical Soller slits
 length: 1.125 inches
 foil thickness: 0.0025 inches
 foil spacing: 0.018 inches
- B Divergence slit 0.0062 inches in height
- C Filters
 1. β -filter 0.0035 inches Zr
 2. Dual filter: β -filter 0.0035 inches Zr
 α -filter 0.0055 inches Y
- D LiF analyzer crystal
- E Receiving slit 0.11 inches in height
- F Horizontal Soller slits
 length: 1.31 inches
 foil thickness: 0.0024 inches
 foil spacing: 0.005 inches
- S.C. Scintillation counter ($1/8$ inch Na I (Th))
 (a) β -filter transmissions set at 50% K_α and 99.5% K_α
 (b) dual filter transmission set at 99.5% K_α

Distances

source to divergence slit: 3.31 inches
 divergence slit to LiF: 3.62 inches
 LiF to receiving slit: 5.63 inches

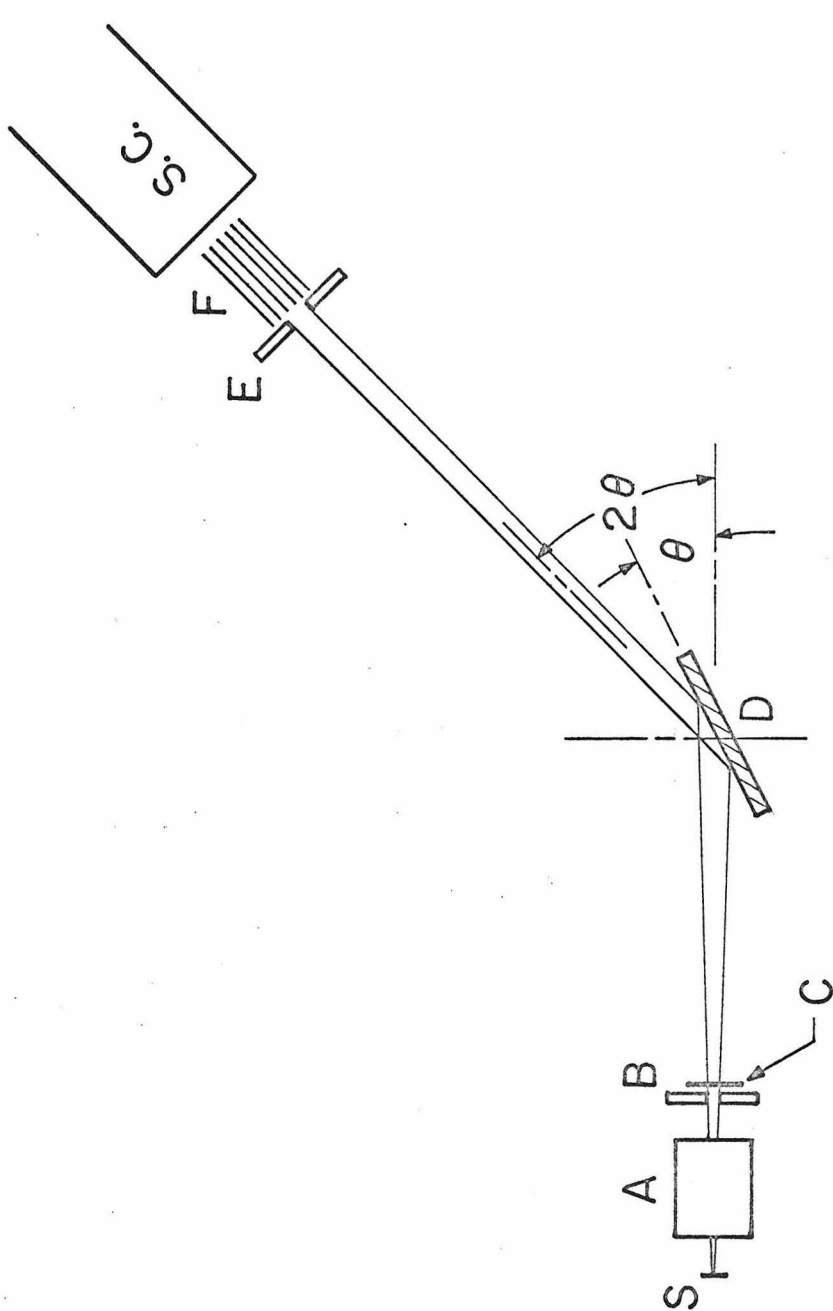


Figure 1. Scattering Geometry for β Filter and Dual Filter Data

KEY TO FIGURE 2

- S Source: Molybdenum
 27 kilovolts
 3 milliamps
 line source: 1.2 mm x 10.0 mm
 take off angle: 5.8°
 K_α 0.7107 Å
- A Divergence slit 0.0025 inches
- B LiF
- C Receiving slit 0.003 inches
- D Advanced Metals Research assembly with a curved-crystal LiF
 monochromator
- S.C. Scintillation counter set at 95% K_α transmission

Distances

source to divergence slit: 2.76 inches
divergence slit to LiF analyzer: 4.17 inches
LiF analyzer to receiving slit: 6.89 inches
receiving slit to curved crystal: 0.75 inches
curved crystal to scintillation counter: 0.75 inches

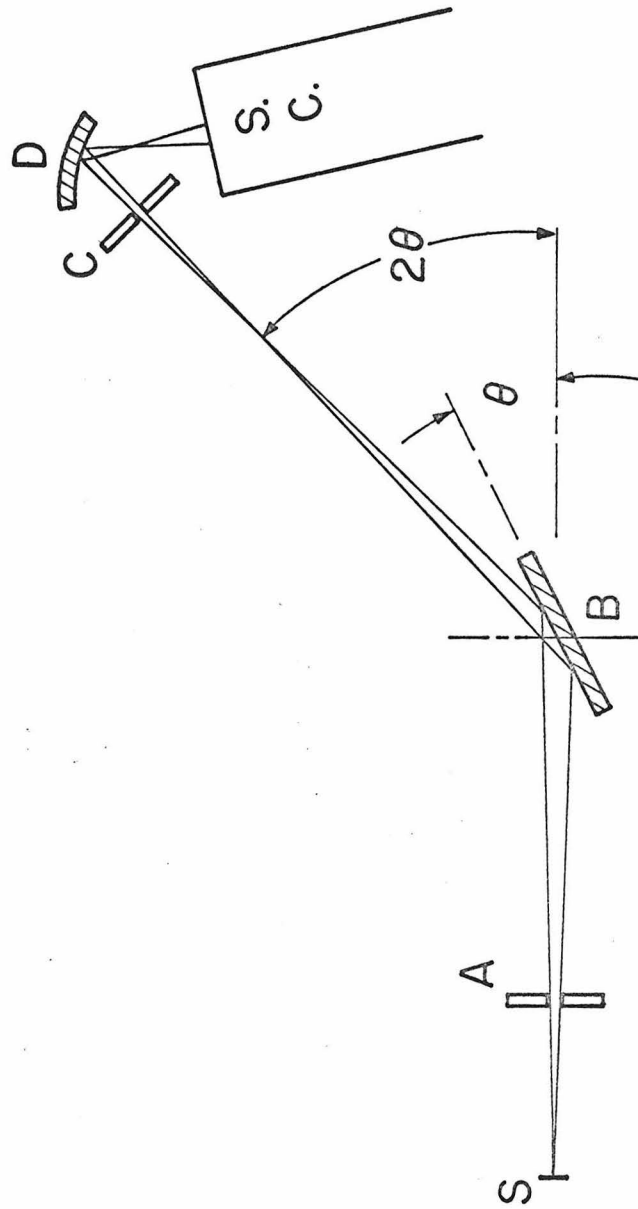


Figure 2. Scattering Geometry for Curved-Crystal Data

KEY TO FIGURE 3

- S Source: Copper
 39 kilovolts
 4 milliamps
 line source:
 take off angle: 4.5°
 K_α 1.543 Å
- A Divergence slit $\sim 1/32$ inch
- B Gypsum flat-crystal monochromator
 2ψ scattering angle set at 11.7°
- C Channel collimator 0.036" x 2" x 0.25"
- D LiF analyzer
- E Receiving slit 0.006 inch
- F Scatter slit $\sim 1/16$ inch
- S.C. Scintillation counter set at 95% K_α transmission

Distances

source to gypsum: 4.30 inches
 gypsum to LiF: 4.50 inches
 LiF to receiving slit: 4.50 inches
 receiving slit to scatter slit: 0.75 inches

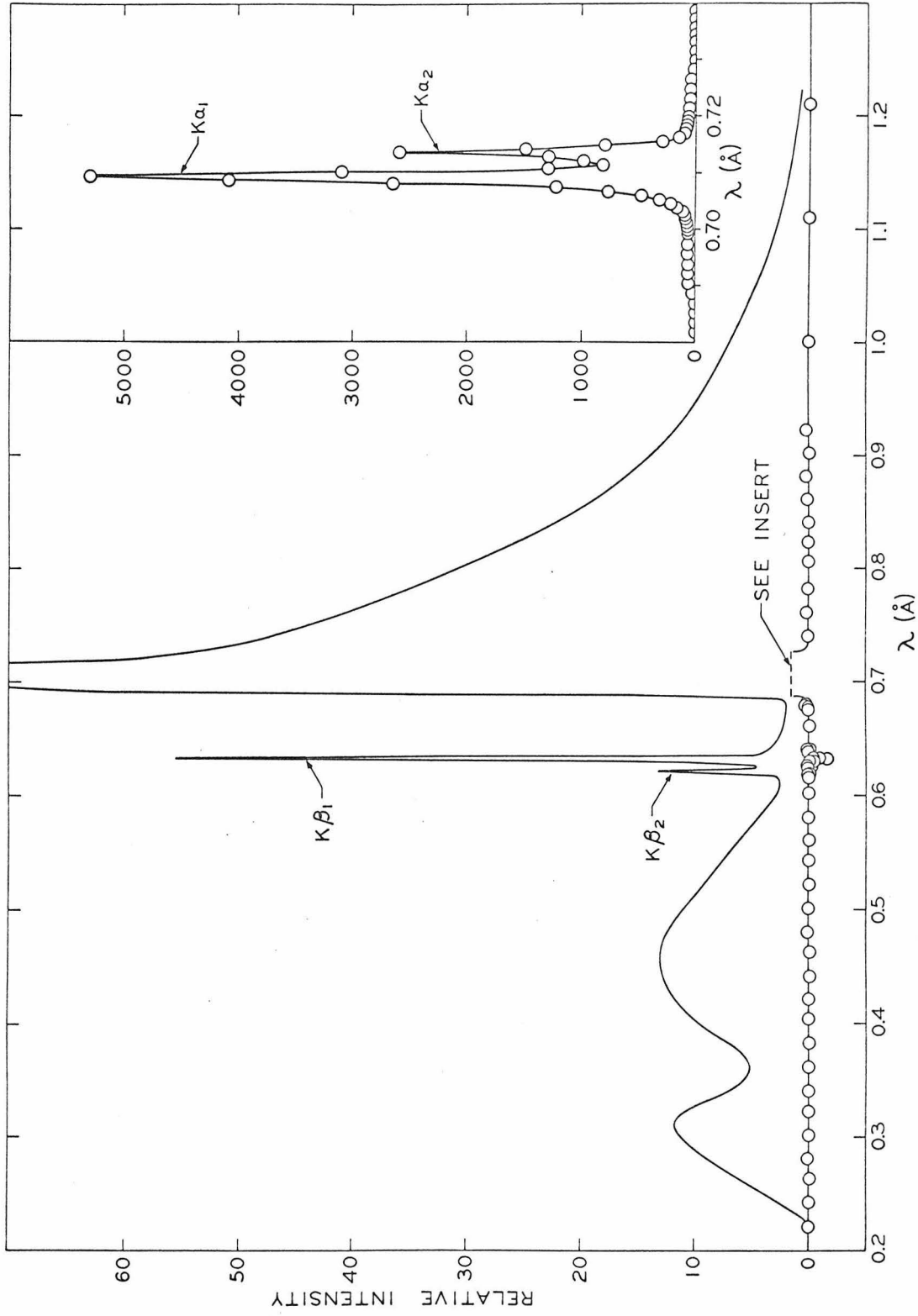


Figure 4. Dual Filter Spectrum (Circles) and β Filter Spectrum at 99.5% Transmission (Solid Curve)

The calculations indicated by Eq. (2) were carried out using the IBM 7094 computer and Simpson's rule integration. A test spectrum, a 0.004 angstroms wide step function, indicated that at least 5 significant figures were obtained by this procedure.

The calculated results are depicted in Figure 5. The results for the β filter are not quantitative beyond s of 4.3.

This figure shows that the dual filter and both crystal monochromators are adequate to within 0.2% over the entire s range shown, whereas the β filter calculations indicate errors as large as 7% for 50% transmission and 12% for 99.5% transmission.

In order to show the trend of the β filter calculations for s greater than 4.3, it was necessary to extrapolate Mikolaj's data beyond $\theta = 60^\circ$ ($s > 15$). The data were extrapolated using

$$IS = Ae^{-Bs} \quad (4)$$

From data at theta of 40° and 60° , B was determined to be 0.115 and A was 106.4. An interpolation at theta of 50° indicated a discrepancy of 2.5%.

When the deviation ratio is calculated at $s = 10$, the extrapolated portion of IS is weighted by less than 10% of the β filter spectrum. At lower values of s the fraction of the spectrum weighting the extrapolation is less. The extrapolation was not needed for s less than 4.3.

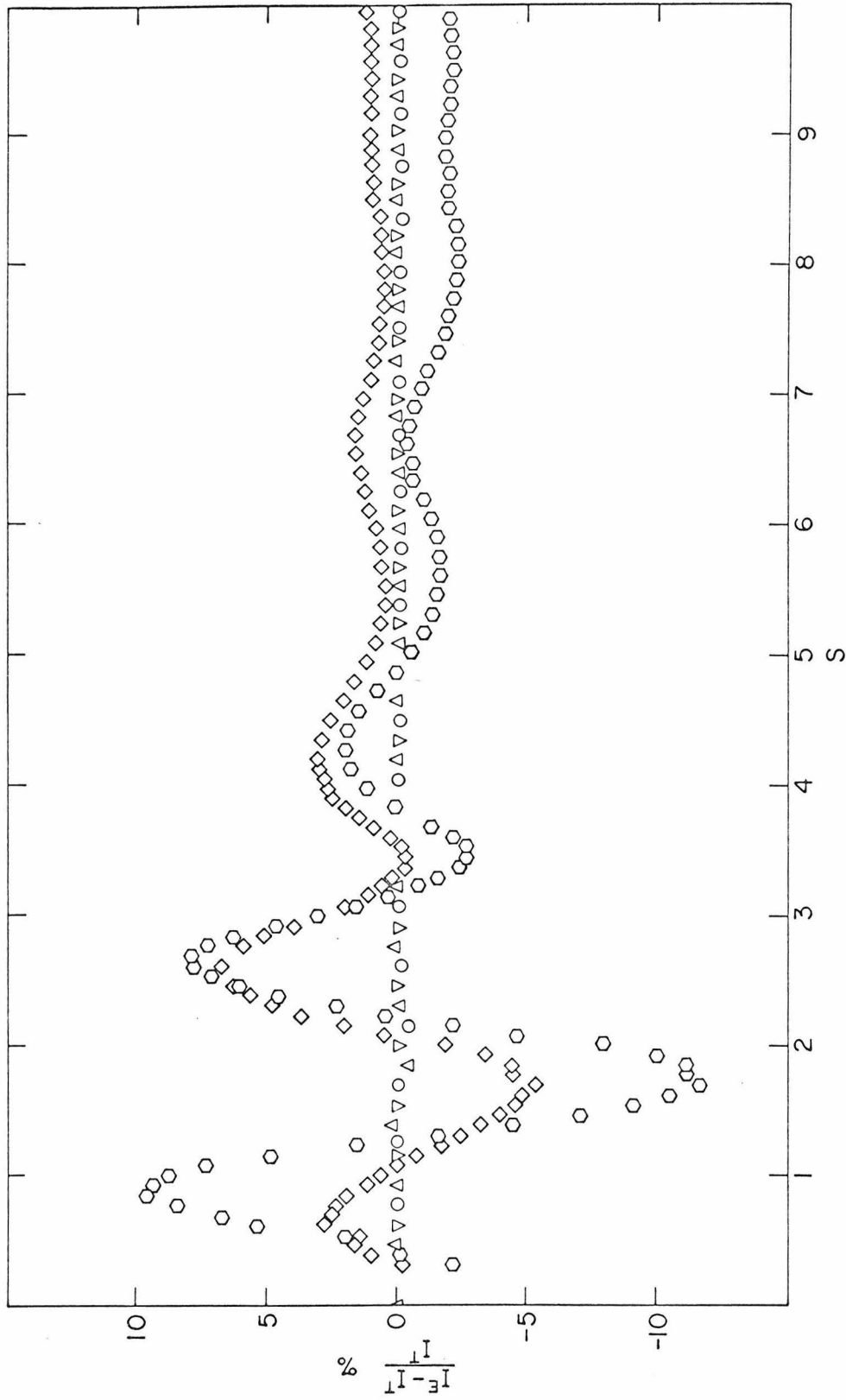


Figure 5. The Deviation Ratio for Flat-Crystal Reflector (▽), Curved-Crystal Reflector (△), Dual Filter (O), 50% Transmission (◇) and 99.5% Transmission (◇)

In addition to the ripple error at low s , it is significant to note that the β filter also introduces error at high s . This discussion indicates that the β filter is not a suitable monochromator.

REFERENCES

1. Mikolaj, P. G. Doctoral Thesis, "An X-ray Diffraction Study of Fluid Argon," California Institute of Technology, 1965.
2. Henninger, E. H. Lab notes, California Institute of Technology, 1968.

TABLE 1
ASSUMED SCATTERING POWER FUNCTION

Theta	IS	Theta	IS	Theta	IS
0	200.0	8.25	129.1	15.75	63.7
1.00	155.1	8.50	119.9	16.00	63.2
1.25	134.3	8.75	113.1	16.25	62.7
1.50	118.0	9.00	108.2	16.50	62.3
1.75	111.1	9.25	104.9	16.75	61.9
2.00	101.7	9.50	103.7	17.00	61.4
2.25	99.7	9.75	103.3	17.25	60.8
2.50	98.1	10.00	102.9	17.50	60.4
2.75	97.5	10.25	102.5	17.75	59.9
3.00	99.6	10.50	102.5	18.00	59.2
3.25	102.8	10.75	102.1	18.25	58.7
3.50	108.6	11.0	101.9	18.50	58.1
3.75	118.1	11.25	100.5	18.75	57.3
4.00	131.6	11.50	98.3	19.00	56.7
4.25	147.6	11.75	95.1	19.25	56.0
4.50	166.5	12.00	91.1	19.50	55.3
4.75	188.6	12.25	87.5	19.75	54.5
5.00	212.2	12.50	84.1	20.00	53.7
5.25	235.6	12.75	80.7	20.25	52.9
5.50	257.9	13.00	78.3	20.50	52.1
5.75	266.8	13.25	76.0	20.75	51.4
6.00	276.6	13.50	73.7	21.00	50.6
6.25	270.8	13.75	71.7	21.25	50.0
6.50	254.3	14.00	70.1	21.50	49.4
6.75	229.0	14.25	68.7	21.75	48.7
7.00	207.8	14.50	67.5	22.00	48.1
7.25	186.8	14.75	66.5	22.25	47.6
7.50	169.2	15.00	65.6	22.50	47.2
7.75	153.6	15.25	64.9	22.75	46.9
8.00	140.3	15.50	64.2	23.00	46.5

Table 1 (cont.)

Theta	IS	Theta	IS	Theta	IS
23.25	46.2	32.00	35.9	40.75	28.2
23.50	45.9	32.25	35.7	41.00	27.9
23.75	45.7	32.50	35.5	41.25	27.7
24.00	45.4	32.75	35.2	41.50	27.5
24.25	45.1	33.00	34.9	41.75	27.4
24.50	45.0	33.25	34.6	42.00	27.2
24.75	44.8	33.50	34.4	42.25	27.0
25.00	44.5	33.75	34.1	42.50	26.8
25.25	44.2	34.00	33.8	42.75	26.6
25.50	43.9	34.25	33.6	43.00	26.4
25.75	43.7	34.50	33.3	43.25	26.2
26.00	43.4	34.75	33.1	43.50	26.0
26.25	43.1	35.00	32.9	43.75	25.8
26.50	42.8	35.25	32.7	44.00	25.6
26.75	42.5	35.50	32.6	44.25	25.4
27.00	42.2	35.75	32.4	44.50	25.3
27.25	41.8	36.00	32.2	44.75	25.1
27.50	41.5	36.25	32.0	45.00	25.0
27.75	41.1	36.50	31.8	45.25	24.8
28.00	40.8	36.75	31.5	45.50	24.6
28.25	40.4	37.00	31.3	45.75	24.4
28.50	39.9	37.25	31.0	46.00	24.2
28.75	39.5	37.50	30.8	46.25	24.1
29.00	39.2	37.75	30.6	46.50	23.9
29.25	38.9	38.00	30.4	46.75	23.8
29.50	38.6	38.25	30.2	47.00	23.6
29.75	38.3	38.50	30.0	47.25	23.4
30.00	37.9	38.75	29.8	47.50	23.3
30.25	37.7	39.00	29.6	47.75	23.1
30.50	37.3	39.25	29.4	48.00	23.0
30.75	37.1	39.50	29.2	48.25	22.8
31.00	36.9	39.75	29.0	48.50	22.7
31.25	36.7	40.00	28.8	48.75	22.5
31.50	36.4	40.25	28.6	49.00	22.4
31.75	36.2	40.50	28.4	49.25	22.2

Table 1 (cont.)

Theta	IS	Theta	IS
49.50	22.1	55.75	19.4
49.75	22.0	56.00	19.3
50.00	21.8	56.25	19.2
50.25	21.7	56.50	19.1
50.50	21.6	56.75	19.0
50.75	21.4	57.00	19.0
51.00	21.3	57.25	18.9
51.25	21.2	57.50	18.8
51.50	21.1	57.75	18.8
51.75	21.0	58.00	18.7
52.00	20.8	58.25	18.6
52.25	20.7	58.50	18.6
52.50	20.6	58.75	18.5
52.75	20.5	59.00	18.5
53.00	20.4	59.25	18.4
53.25	20.3	59.50	18.4
53.50	20.2	59.75	18.3
53.75	20.1	60.00	18.3
54.00	20.0		
54.25	19.9		
54.50	19.8		
54.75	19.7		
55.00	19.6		
55.25	19.5		
55.50	19.4		

TABLE 2

DUAL FILTER SPECTRUM

λ Angstroms	Relative Intensity
.6747	0.193
.6783	0.402
.6816	0.527
.6851	2.143
.6886	31.152
.6920	71.055
.6955	74.329
.6989	73.159
.7010	77.536
.7024	99.299
.7038	163.352
.7052	317.844
.7066	782.981
.7079	2655.884
.7086	4088.296
.7093	5299.892
.7100	3096.064
.7113	821.938
.7120	985.003
.7127	1293.497
.7134	2603.376
.7141	1493.412
.7148	801.478
.7155	301.826
.7162	150.606
.7169	106.884
.7183	82.026
.7197	73.231
.7231	55.934
.7266	42.391
.7300	2.791
.7355	.221

TABLE 3

 β FILTER SPECTRUM WITH PHA SET AT 50%

λ Angstroms	F Relative Intensity	λ Angstroms	F Relative Intensity
0.2000	13	0.3053	1851
0.2036	9	0.3088	1437
0.2071	17	0.3123	1166
0.2107	22	0.3158	883
0.2142	15	0.3193	699
0.2177	12	0.3228	559
0.2212	21	0.3263	461
0.2247	26	0.3298	448
0.2282	64	0.3333	376
0.2317	114	0.3368	317
0.2352	218	0.3403	328
0.2387	401	0.3438	316
0.2422	669	0.3473	327
0.2457	1029	0.3508	311
0.2492	1452	0.3543	310
0.2527	2083	0.3578	336
0.2562	2469	0.3613	311
0.2597	3134	0.3648	343
0.2632	3548	0.3683	327
0.2667	3983	0.3718	265
0.2702	4278	0.3753	235
0.2738	4490	0.3788	235
0.2773	4545	0.3823	244
0.2808	4447	0.3858	241
0.2843	4153	0.3893	224
0.2878	3921	0.3928	275
0.2913	3497	0.3963	291
0.2948	3056	0.3998	325
0.2983	2563	0.4033	328
0.3018	2197	0.4068	348

Table 3 (cont.)

λ Angstroms	F Relative Intensity	λ Angstroms	F Relative Intensity
0.4102	383	0.5949	1011
0.4137	406	0.6019	924
0.4172	419	0.6088	833
0.4207	446	0.6158	1012
0.4242	487	0.6192	4052
0.4277	507	0.6227	1795
0.4312	523	0.6296	6905
0.4374	566	0.63310	14181
0.4417	687	0.6366	1437
0.4487	759	0.6401	1186
0.4556	805	0.6435	1093
0.4626	897	0.6504	1043
0.4696	997	0.6539	942
0.4766	986	0.6609	892
0.4836	1038	0.6643	864
0.4905	1122	0.6712	822
0.4975	1197	0.6782	833
0.5045	1221	0.6816	897
0.5114	1232	0.6851	2633
0.5184	1305	0.6886	31895
0.5254	1417	0.6920	49192
0.5323	1474	0.6955	49919
0.5393	1436	0.6989	47945
0.5463	1439	0.6996	47059
0.5532	1313	0.7003	47524
0.5602	1365	0.7010	50860
0.5671	1306	0.7017	55874
0.5741	1194	0.7024	68000
0.5810	1147	0.7031	87625
0.5880	1115	0.7038	122189

Table 3 (cont.)

λ Angstroms	F Relative Intensity	λ Angstroms	F Relative Intensity
0.7045	174004	0.7439	33062
0.7052	269791	0.7542	30117
0.7059	438824	0.7680	27006
0.7066	757987	0.7852	22884
0.7073	1180298	0.8025	19470
0.7079	1759474	0.8197	16193
0.7086	2326653	0.8368	13306
0.7093	2150814	0.8540	10953
0.7100	1010552	0.8712	8954
0.7107	570481	0.8883	7438
0.7113	672623	0.9054	6317
0.7120	981844	0.9225	5343
0.7127	1765146	0.9396	4051
0.7134	1130341	0.9567	2968
0.7141	488704	0.9737	1957
0.7148	161723	0.9908	1548
0.7155	79352	1.0078	1132
0.7162	59280	1.0418	583
0.7169	53501	1.0756	368
0.7176	49287	1.1095	244
0.7183	46853	1.1432	168
0.7190	43516	1.1768	126
0.7197	41383	1.2104	112
0.7231	41215	1.2438	225
0.7335	35946		

TABLE 4

 β FILTER SPECTRUM WITH PHA SET AT 99.5%

λ Angstroms	F Relative Intensity	λ Angstroms	F Relative Intensity
0.2000	66	0.3053	14258
0.2036	69	0.3088	14404
0.2071	82	0.3123	14437
0.2107	70	0.3158	14005
0.2142	79	0.3193	13693
0.2177	66	0.3228	13492
0.2212	87	0.3263	13006
0.2247	169	0.3298	12224
0.2282	307	0.3333	11688
0.2317	605	0.3368	10756
0.2352	1086	0.3403	10270
0.2387	1600	0.3438	9560
0.2422	2039	0.3473	9168
0.2457	3099	0.3508	8431
0.2492	4159	0.3543	8168
0.2527	4806	0.3578	8006
0.2562	5785	0.3613	7682
0.2597	6506	0.3648	7527
0.2632	7522	0.3683	7389
0.2667	8352	0.3718	7643
0.2702	9215	0.3753	7988
0.2738	10140	0.3788	8199
0.2773	11031	0.3823	8896
0.2808	11736	0.3858	9435
0.2843	12369	0.3893	10078
0.2878	12593	0.3928	10707
0.2913	13346	0.3963	11198
0.2948	13823	0.3998	11632
0.2983	13989	0.4033	12115
0.3018	14348	0.4068	12521

Table 4 (cont.)

λ Angstroms	F Relative Intensity	λ Angstroms	F Relative Intensity
0.4102	13208	0.5149	9475
0.4137	13435	0.5184	9119
0.4172	13562	0.5219	8797
0.4207	14329	0.5254	8566
0.4242	14500	0.5288	8167
0.4277	14998	0.5323	7892
0.4312	15146	0.5358	7621
0.4347	15395	0.5393	7068
0.4382	15441	0.5428	6970
0.4417	15515	0.5463	6607
0.4452	15651	0.5497	6262
0.4487	15252	0.5532	5875
0.4522	15545	0.5567	5679
0.4556	15815	0.5602	5460
0.4591	14848	0.5637	5172
0.4626	14629	0.5671	4762
0.4661	14310	0.5706	4546
0.4696	14037	0.5741	4570
0.4731	13635	0.5775	4235
0.4766	13457	0.5810	4026
0.4810	12956	0.5845	3819
0.4836	12665	0.5880	3571
0.4870	11869	0.5915	3571
0.4905	11689	0.5949	3252
0.4940	11345	0.5984	3152
0.4975	11060	0.6019	2904
0.5010	10786	0.6054	2784
0.5045	10406	0.6088	2729
0.5080	10080	0.6123	2679
0.5114	9628	0.6158	2789

Table 4 (cont.)

λ Angstroms	F Relative Intensity	λ Angstroms	F Relative Intensity
0.6192	9279	0.7038	246725
0.6227	5186	0.7045	357287
0.6262	5019	0.7052	595602
0.6296	19293	0.7059	931561
0.6331	19417	0.7066	1518000
0.6366	4037	0.7037	2502000
0.6401	3573	0.7079	3481000
0.6435	3229	0.7086	4571000
0.6470	3026	0.7093	4091000
0.6504	2925	0.7100	2023000
0.6539	2745	0.7107	1088000
0.6574	2599	0.7113	1337000
0.6609	2541	0.7120	1880000
0.6643	2136	0.7127	2468000
0.6678	1975	0.7134	2126000
0.6712	1983	0.7141	821000
0.6747	1971	0.7148	300000
0.6782	2110	0.7155	173000
0.6816	2035	0.7162	121000
0.6851	4483	0.7169	106000
0.6886	47226	0.7176	97000
0.6920	90801	0.7183	91000
0.6955	93074	0.7190	85000
0.6989	97576	0.7197	80000
0.6996	93439	0.7231	77006
0.7003	96939	0.7266	72893
0.7010	102873	0.7300	69910
0.7017	120451	0.7335	67466
0.7024	142648	0.7369	65213
0.7031	183851	0.7404	63602

Table 4 (cont.)

λ Angstroms	F Relative Intensity	λ Angstroms	F Relative Intensity
0.7439	61532	0.8471	26847
0.7473	60003	0.8506	26246
0.7507	58398	0.8540	25206
0.7542	56822	0.8574	24657
0.7577	55683	0.8609	24500
0.7611	53911	0.8643	23595
0.7645	52813	0.8677	22963
0.7680	51523	0.8712	22179
0.7715	49894	0.8746	21482
0.7749	48788	0.8780	20798
0.7784	47362	0.8814	20151
0.7818	46029	0.8849	19655
0.7852	44569	0.8883	19157
0.7887	43162	0.8911	18488
0.7921	41784	0.8952	18275
0.7956	41036	0.8986	17585
0.7990	39965	0.9020	17114
0.8025	38979	0.9054	16612
0.8059	37876	0.9088	15958
0.8093	36831	0.9123	15688
0.8128	35879	0.9157	15055
0.8162	35066	0.9190	14833
0.8197	33632	0.9225	14036
0.8231	32824	0.9260	13620
0.8265	31441	0.9294	13109
0.8300	30807	0.9328	12647
0.8334	29648	0.9362	12280
0.8368	28614	0.9396	11879
0.8403	27821	0.9430	11394
0.8437	27164	0.9464	11077

Table 4 (cont.)

λ Angstroms	F Relative Intensity
0.9499	10671
0.9533	10139
0.9567	10087
0.9601	9617
0.9635	9227
0.9669	9037
0.9703	8585
0.9737	8418
0.9771	8144
0.9806	7937
0.9839	7837
0.9874	7644
0.9908	7283
0.9942	7434
0.9976	7035
1.001	6639
1.004	6479
1.007	6245
1.041	4327
1.0756	3129
1.109	2040
1.143	1462
1.176	1023
1.210	698
1.243	787

TABLE 5

FLAT CRYSTAL MONOCHROMATOR SPECTRUM

λ Angstroms	Relative Intensity	λ Angstroms	Relative Intensity
1.5201	2	1.5404	10238
1.5207	5	1.5416	11172
1.5214	3	1.5422	10961
1.5220	3	1.5429	10121
1.5227	4	1.5435	8464
1.5233	12	1.5442	6947
1.5240	13	1.5448	5642
1.5253	15	1.5455	4928
1.5266	14	1.5461	4437
1.5272	29	1.5468	3734
1.5279	37	1.5474	2442
1.5285	29	1.5481	1524
1.5292	27	1.5485	660
1.5298	48	1.5492	382
1.5305	46	1.5498	189
1.5312	71	1.5505	103
1.5318	124	1.5511	66
1.5325	114	1.5518	49
1.5331	159	1.5524	42
1.5338	183	1.5531	30
1.5344	250	1.5537	16
1.5351	318	1.5544	14
1.5357	633	1.5550	6
1.5364	1128	1.5557	9
1.5370	2083	1.5563	7
1.5377	3067		
1.5383	4629		
1.5390	5863		
1.5396	7019		
1.5403	8644		

TABLE 6

CURVED-CRYSTAL MONOCHROMATOR SPECTRUM

λ Angstroms	Relative Intensity	λ Angstroms	Relative Intensity
.6188	3	.6778	19
.6223	3	.6812	23
.6257	2	.6847	19
.6275	9	.6882	35
.6292	7	.6899	118
.6310	12	.6916	637
.6327	37	.6933	1725
.6344	5	.6951	2813
.6292	9	.6968	3645
.6299	5	.6985	4029
.6306	18	.7003	4093
.6313	19	.7020	4221
.6320	34	.7037	4157
.6327	39	.7055	4669
.6334	25	.7065	5757
.6341	19	.7068	7037
.6348	6	.7072	9149
.6362	8	.7075	13693
.6396	15	.7079	20669
.6379	9	.7082	32701
.6396	12	.7086	47229
.6414	8	.7089	59005
.6431	5	.7093	65917
.6500	5	.7096	64637
.6570	11	.7100	49405
.6604	13	.7103	34813
.6639	18	.7106	23933
.6674	18	.7113	9405
.6708	25	.7120	12349
.6743	18	.7124	16893

Table 6 (cont.)

λ Angstroms	Relative Intensity
.7127	24829
.7131	31933
.7134	39229
.7138	40765
.7141	36861
.7144	27133
.7148	19197
.7151	12989
.7158	5949
.7165	4349
.7172	3901
.7179	3709
.7186	3453
.7193	3261
.7210	3069
.7227	2685
.7245	2493
.7262	1789
.7297	509
.7331	189
.7400	30